Thèse en cotutelle

University of Science and Technology of China

Université de Lille 1 – Sciences et Technologies

Hydrogen diffusion in NAMs : andradite garnet and zircon

by

Peipei Zhang

In partial fulfillment of the requirements for the degree of

Doctor of Philosophy at USTC

and

Docteur de l'Université Lille I

Discipline : Science des Matériaux

Supervisors : Qunke Xia and Jannick Ingrin

28 February, 2015

N° d'ordre : 41691

Université de Lille 1

UMR CNRS 8207 Unité Matériaux Et Transformations

THÈSE

Pour obtenir le grade de

Docteur de l'Université Lille I

Spécialité : Science des Marétriaux

par

Peipei ZHANG

Hydrogen diffusion in NAMs : andradite garnet and zircon

Soutenue le 28 février 2015

Présentée devant la commission d'examen composée de :

M. Etienne DELOULE	Président, Rapporteur
M. Rucheng WANG	Rapporteur
M. Itsván KOVACS	Examinateur
M. Xiaozhi YANG	Examinateur
M. Yongfei ZHENG	Invité
M. Jannick INGRIN	Directeur de these
M. Qunke XIA	Directeur de thèse

Acknowledgements

I would like to express my gratitude to my PhD advisors, Dr. Qunke Xia and Dr. Jannick Ingrin. Dr. Qunke Xia has been my advisor for over seven years. I thank him sincerely for having recruited me as his student and his trust. He provided me the opportunity to go to France as a co-educational student where I gained fruitful knowledge. His fartherly care for both my study and life and his great patience were a great help. I thank greatly Dr. Jannick Ingrin, who taught me how to do experimental research from the basic experimental operation to data processing and writing of a paper. The talk and discussion with him were always pleasant and enjoyable. From him, I learned the right attitude of research: carefulness, seriousness, honesty and patience. I really thank him a lot for his help and time during my thesis revision. Without the help of my two advisors, this thesis would have been difficult to achieve.

I thank also Christophe Depecker and Isabelle De Waele for their help and guidance in FTIR measurement. The help and encouragement of Patrick Cordier, the head of the team of Mineralogy, when I was in deep despair really touched me. I don't know how to express my gratitude to my friends, Eric Vigouroux and Caroline Bollinger; their kindness and the numerous help they offered me will remain always in my heart. Carole, Christophe, Francois, Nils, Boris and Lise were also kind and helpful. The time I spent with the whole group is a good memory for me.

I am also grateful to my Chinese friends in France, Yingchong Ma, Hui Wang, Jingkui Wang and many others, I cannot list all here. I am so grateful to had them when I was abroad and I had a really happy time with them.

I would like to thank the professors, who have contributed greatly to my geological education at the university (USTC): Yongfei Zheng, Shuguang Li, Jiangfeng Chen, Daogong Chen, Xiachen Zhi, Xiaoyong Yang, Min Feng, Zhi Xie, Yican Liu and Jian Hong. I thank Jia Liu and Yan Yang, for the discussion of scientific issues with them. It always inspired me. The kindly help from Pei Li always

benefits me. I thank also the other members of our group in china: Bo Zhao, Yantao Hao, Huan Chen, Shaochen Liu, Zubing Jia, Zizhen Wang, Zhenzhen Tian, Yao Bi and Bing Yang. They provided the support and friendship I needed. I enjoyed a lot the homey atmosphere in the group, thanks to Dr. Qunke Xia who allows it. The talks with Dr. Youxue Zhang and Dr. Huaiwei Ni benefited me also. The kind suggestions for my research from my classmate Lei Liu were helpful.

I thank Henrik Skogby and an anonymous reviewer for their helpful suggestions to improve the manuscript of the submitted paper, which is part of this thesis.

I thank very much the China Scholarship Council for the opportunity and support they provided for me to study in France.

I am full of gratitude to my boyfriend Deli Jiang, who took so much care of me and always supports me especially during the thesis writing. His love really warms me and encourages me. My parents, that raised me and provided me guidance, I love them so much that I can only repay for their love with the rest of my life. I thank also my parents for bringing me lovely younger sisters and brother, whom I am very happy to live with. I love all of them so much, and I would not have made it this far without them.

Finally, I appreciate the great love from the Lord my God. His guidance, his grace and his discipline all benefit me. I thank sincerely the brothers and sisters in the church who keep praying for me out of God's love.

Résumé

Cette thèse présente les résultats d'une étude de la mobilité de l'hydrogène dans l'andradite entre 400 et 700 °C et dans le zircon entre 900 et 1150 °C. Les expériences ont été réalisées dans un four horizontal à 1 atmosphère sous un flux gazeux $Ar/D_{2(10\%)}$ et $Ar/H_{2(10\%)}$. L'échange H-D a été suivit par analyse infrarouge, réalisé après chaque recuit. Les monocristaux d'andradite utilisés proviennent d'un skarn de l'île de Serifos (Grèce) tandis que les monocristaux de zircons sont originaires de Madagascar.

Contrairement à ce qui est généralement observé dans ce type d'expériences, il n'a pas été possible de remplacer par du deutérium tous les hydrogènes présent dans la structure cristalline sous la forme de défauts ponctuels. A la fin de l'échange 15% à 35% des H dans l'andradite et 25% à 40% des H dans le zircon restent présent. Cependant, un état d'équilibre étant atteint, nous avons pu déterminer les lois de diffusion relative à ces échanges.

Dans l'andradite, toutes les bandes infrarouges suivent la même cinétique d'échange aussi bien au cours du remplacement de H par D (H-D) que pour le remplacement de D par H (D-H):

$$D = D_0 \exp\left[-\frac{(96 \pm 11) kJ/mol}{RT}\right] \text{avec } \log D_0 \text{ (in } m^2/s) = -5.9 \pm 0.7.$$

L'énergie d'activation est comparable à l'énergie d'activation de diffusion de l'hydrogène dans le grossulaire (102 kJ/mol), mais avec une diffusion deux ordres de grandeur plus rapide. Nos résultats montrent que la composition joue un rôle majeur sur la diffusion d'hydrogène dans la série grossulaire-andradite et celle-ci doit impérativement être prise en compte dans toute interprétation des données de δD dans les grenats. Pour les grenats proches du pôle andradite, ces données ne peuvent rendre compte que d'événements métamorphique ou métasomatiques brefs, à des

températures inférieures à 400 °C.

Dans le zircon, la diffusion de l'hydrogène est anisotrope, avec une diffusion selon [001] légèrement plus rapide que celle selon [100] et [010] :

$$D_{[100][010]} = D_0 \exp\left[\frac{-(374 \pm 39)kJ/mol}{RT}\right] \text{avec log } D_0 \text{ } (m^2s^{-1}) = 2.24 \pm 1.57.$$

$$D_{[001]} = D_0 \exp\left[\frac{-(334 \pm 49)kJ/mol}{RT}\right] \text{avec log } D_0 \text{ } (m^2s^{-1}) = 1.11 \pm 0.22.$$

De tous les minéraux nominalement anhydres (MNA), le zircon est celui qui a la diffusion d'hydrogène la plus lente et qui présente la plus forte énergie d'activation. Lors des expériences d'échange H-D le zircon incorpore également du deutérium parallèlement à la réduction de l'uranium présent dans la structure en suivant la réaction d'hydratation $U^{5+} + OH^- = U^{4+} + O^{2-} + 1/2H_2$. La cinétique d'incorporation associée est très légèrement plus lente que la cinétique d'échange H-D, suggérant que l'incorporation est ici limitée par la mobilité de l'hydrogène. Ces résultats montrent que le zircon est le MNA qui a le meilleur potentiel de préservation de sa signature isotopique de l'hydrogène. A 500 °C, un zircon de 300 μm de rayon peut préserver une signature en δD pendant plus d'un million d'années.

Abstract

The hydrogen mobilities in andradite and zircon were investigated by performing H-D exchange experiments under ambient pressure in a horizontal furnace flushed with a gas mixture of $Ar/D_{2(10\%)}$. The temperature range investigated was 400-700 °C for andradite and 900-1150 °C for zircon. The andradite samples are single crystals from an iron-skarn deposit on Serifos island, Greece, while the zircon samples are single crystals from Madagascar. FTIR analyses were performed before and after each annealing run. At contrary to the same type of experiments performed in NAMs, it was not possible to replace all hydrogen atoms in the structure by deuterium, 15% to 35% for andradite and 25% to 40% for zircon of OH remaining after completion of the exchange. However, a steady-state equilibrium was reached at the end of the experiments and it was possible to determine the diffusion law of the exchange process.

In andradite, all bands follow the same kinetics regarding exchange of H by D (H-D exchange) or D by H (D-H exchange), with diffusion law:

$$D = D_0 \exp\left[-\frac{(96 \pm 11) kJ/mol}{RT}\right] \text{with } \log D_0 \text{ (in } m^2/s) = -5.9 \pm 0.7.$$

The activation energy is similar to those of hydrogen diffusion in grossular, but the diffusivity is more than 2 orders of magnitude faster. Our results demonstrate that, composition has a major effect on H diffusion and it must be considered in any discussion of δD signatures in garnets. In andradite-rich garnets, hydrogen isotope data can only be used to record short, low-grade metamorphic or metasomatic events, at temperatures lower than 400 °C.

In zircon, hydrogen diffusion is anisotropic, slightly faster along [001] than along [100] and [010]:

$$D_{[100][010]} = D_0 \exp\left[\frac{-(374 \pm 39) kJ/mol}{RT}\right] \text{with log } D_0 \text{ } (m^2 s^{-1}) = 2.24 \pm 1.57.$$

$$D_{[001]} = D_0 \exp\left[\frac{-(334 \pm 49) kJ/mol}{RT}\right] \text{with log } D_0 \text{ } (m^2 s^{-1}) = 1.11 \pm 0.22.$$

H diffusion in zircon has much higher activation energy and slower diffusivity than other NAMs.

During H-D exchange zircon incorporates also deuterium. For the first time, the hydration reaction $U^{5+} + OH^- = U^{4+} + O^{2-} + 1/2H_2$, involving uranium reduction is observed. The kinetics of deuterium incorporation is just slightly slower than hydrogen diffusion, suggesting that the reaction is limited by hydrogen diffusion. It confirms that hydrogen isotopic memory of zircon is higher than other NAMs. Zircons will be moderately retentive of H signatures at mid-crustal metamorphic temperatures. At 500 °C, a zircon with a radius of 300 μm would retain its H isotopic signature over more than a million years.

Table des matieres – Table of contents

List of illustrations and figures

Chapter 2

Chapter 6

Chapter 7

List of tables

Chapter 1.

Introduction

H species in nominally anhydrous minerals (NAMs), which occur as a minor or trace constituents in the crystal structure, have received growing interests during the past decades because of its disproportionately large effect on the physical and chemical properties of minerals/rocks (Rossman and Aines 1991; Bell and Rosssman 1992a, b; Thompson 1992; Ingrin and Skogby 2000). Hydrogen is also an important marker of the nature of fluids present during metamorphic and metasomatic events (Matveev et al. 2001; Xia et al. 2005; Sheng et al. 2007; Chen et al. 2011). The OH content of some crustal minerals has been employed for genetic interpretation (Arredondo et al. 2001; Johnson 2003; Xia et al. 2005). For example, garnets has been used as indicators of fluid evolution of igneous and metamorphic rocks since the concentrations of OH in garnet may record the evolution of fluid and their spatial distributions during crystallization and later metamorphic/metasomatic events. From OH analysis in spessartine, Arredondo et al. (2001) found evidence of a general increase of water content in coexisting melt from wall to core zone in two pegmatites and a record of a magma reinjection event from in a third pegmatite. Knowledge of hydrogen diffusivity is essential for the interpretation of these indicators, and for the understanding of the origin of hydrogen and its speciation.

1.1 The kinetics of hydrogen diffusion in andradite

1.1.1 Background

Numerous studies have shown that hydroxide is a common trace or minor component in garnets (e.g., Aines and Rossman 1984, 1985; Rossman and Aines 1991; Amthauer and Rossman 1998). A large amount of OH can be incorporated in both

natural and synthetic andradite (Kobayashi and Shoji 1987; Armbruster and Geiger 1993; Armbruster 1995). High OH content was also reported for Fe^{3+}-rich garnets such as melanite and schorlomite (Lager et al. 1989; Locock et al. 1995). Armbruster and Geiger (1993) proposed that incorporation of OH into Ca-Fe garnet can reduce the internal strain in the structure of Ca-Fe^{3+} garnets. The hydrogarnet substitution [$(O_4H_4)^{4-} = (SiO_4)^{4-}$], which was first established for hydrogrossular (Cohen-Addad et al. 1967; Lager et al. 1987, 1989), was also confirmed in andradite (Armbruster 1995), although other kinds of OH defects may also occur in that mineral (Cho and Rossman 1993).

A few studies on the diffusion of hydrogen in garnets have been published (pyrope: Wang et al. 1996, Blanchard and Ingrin 2004a, b; grossular: Kurka et al. 2005; andradite: Kurka 2005, Ingrin and Blanchard 2006, Phichaikamjornwut et al. 2012). These studies have shown that the activation energies of the extraction laws are much higher than those in most ferromagnesian silicates; they range between 200 and 350 kJ/mol and the diffusion coefficients cover two orders of magnitude for temperatures in the range of 700–1050 °C. The difficulty to model the evolution of H concentration with time by a simple diffusion process was mentioned by different authors (Kurka 2005; Phichaikamjornwut et al. 2012). Particularly for andradite garnets, where frequently it was not possible to achieve a complete extraction with 10 to 20% of the original H content remaining in the crystal after annealing (Kurka 2005; Phichaikamjornwut et al. 2012). Several explanations were proposed for this behavior but no definitive solution was really found. Furthermore, the mechanisms involved in H extraction in garnets remain largely questioned. Although the redox-reaction $Fe^{2+} + OH^- = Fe^{3+} + O^{2-} + 1/2H_2$ seems a possible candidate for pyrope and grossular (Blanchard and Ingrin 2004b; Forneris and Skogby 2004; Kurka 2005; Kurka et al. 2005), this process is not available for H extraction in andradites, which dominantly contains Fe^{3+} (Phichaikamjornwut et al. 2012).

Complete H-D exchange studies have only been performed in Dora Maira pyrope and grossular (Blanchard and Ingrin 2004a; Kurka et al. 2005). The knowledge of H

mobility in andradite would provide useful information for identifying the mechanisms of H exchange in this type of garnet.

1.1.2 Aim of this study

The aim of this study is to determine the mobility of hydrogen in andradite from H-D exchange experiments.

The data will be used to elucidate the role of H mobility in the extraction/incorporation kinetics in andradite and propose mechanisms able to explain previous observations (Kurka 2005; Phichaikamjornwut et al. 2012).

Finally, the knowledge of H mobility laws in andradite will provides a quantitative framework for the interpretation of data on natural andradites and their use to identify the nature of fluids rock interactions.

1.2 The kinetics of hydrogen diffusion in zircon

1.2.1 Background

Zircon is a ubiquitous accessory mineral found in crustal rocks. It can incorporate a variety of minor and trace elements, such as U, Th and REE, upon growth from melts and during metamorphism. Zircon is relatively insoluble in crustal melts and fluids and has general resistance to chemical and physical breakdown, largely due to its closed-packed crystal structure. Kinetic studies on cations (U, Th, Hf, Ti, Pb and REE) and oxygen diffusion in zircon reveal that these elements have extraordinarily sluggish diffusion rates with the exception of oxygen diffusion in wet conditions. The chemical integrity and isotopic information provided by these elements make them useful as geochemical tracers. Ti geothermometer (e.g., Watson and Harrison 2005; Cherniak and Watson 2007) or isotopes of the U-Th-Pb system used for dating (Bowring and Schmitz 2003; Davis et al. 2003) are good examples of such elements.

Several studies have reported the presence of hydrous component in natural zircon, especially those suffered radiation-induced amorphization (e.g., Frondel 1953; Woodhead et al. 1991b; Nasdala et al. 2001). In contrast to Ti-thermometry and

U-Th-Pb geochronology, OH in zircon has received relatively little attention, probably due to the low abundance of zircon in the Earth and its consequently limited contribution to the water budgets of the Earth's reservoirs, as well as the low OH content found in natural non-metamict zircons. However, due to the strong resistance of zircon to diffusive re-equilibration (Cherniak et al 1997; Watson and Cherniak 1997), the OH content in zircon may be a useful tool to access water activity during crystal growth, with caution that trace elements requiring charge compensation may significantly alter the OH content (Trail et al. 2011). Since deuterium may also be incorporated into zircon at the time of crystallization or during later metamorphic events, the D/H ratios may provide important information about zircon history similarly or in complement to information provided by oxygen and lithium isotopes (Wilde et al. 2001; Trail et al. 2007, 2009; Ushikubo et al. 2008), on condition that the hydrogen isotope fractionation behavior between zircon and melt/fluid is known. If the information of core and rims of zircon are preserved, the metamorphic history of a terrain could be inferred in combination with U-Pb dating. In order to constrain the conditions under which H signatures in zircon would be retained or lost through diffusion, kinetics data of H diffusion in zircon is of crucial importance. Nevertheless, numerous studies referring to H diffusion have been conducted on NAMs, such as olivine, pyroxene, garnet, feldspar and quartz (Kats et al. 1962; Kronenberg et al. 1986; Mackwell and Kohlstedt 1990; Ingrin et al. 1995; Kronenberg et al. 1996; Wang et al. 1996; Kohlstedt and Mackwell 1998; Hercule and Ingrin 1999; Woods et al. 2000; Stalder and Skogby 2003, 2007; Johnson 2003; Demouchy and Mackwell 2003, 2006; Blanchard and Ingrin 2004a, 2004b; Kurka et al. 2005; Kurka 2005; Stalder and Behrens 2006; Stalder et al. 2007; Sundvall et al. 2009a, 2009b; Phichaikamjornwut et al. 2012; Du Frane and Tyburczy 2012; Johnson and Rossman 2013), but no kinetics data yet are available for H diffusion in zircon.

Comparisons between kinetics of H incorporation/extraction and H-D exchange have been reported for several NAMs. A redox-reaction mechanism ($Fe^{3+} + 1/2H_2 + O^{2-} = Fe^{2+} + OH^-$) through which H is incorporated or extracted has been suggested for Fe-bearing minerals, such as olivine and pyroxene (Kohlstedt and Mackwell 1998;

Hercule and Ingrin 1999). It is generally assumed that, the incorporation/extraction diffusion is rate limited by electron holes linked to Fe atoms when Fe content is below a critical value; it will reach a value of H self-diffusion that defined by H-D exchange when the critical value of Fe content is reached and the diffusion property will be the same as H self-diffusion since protons will be the limiting factor (Kohlstedt and Mackwell 2006; Hercule and Ingrin 1999; Ingrin and Blanchard 2006). Since trace amounts of multivalent elements, such as uranium and cerium that can change its valence with different oxygen fugacity, are usually incorporated in zircon, such mechanism may also be involved during H diffusion.

1.2.2 The aim of this study

The aim of zircon study is to acquire a better understanding of the following points:

1) Determine the kinetics of hydrogen diffusion in zircon, and compare them with kinetics data of diffusion of other elements in zircon and kinetics data of H diffusion in other NAMs.

2) Identify the existence of any redox-reaction mechanism for hydrogen incorporation in zircon.

3) Provide constraints on the incorporation mechanisms of hydrogen into the zircon structure. FTIR spectra of hydrogen species in minerals can provide structural information about the local atomic environment of hydrogen species within the crystal. Studies of the hydrogen species in zircon have not yet provided full understanding of the complex OH absorption spectra. The stability of hydrogen species during diffusion experiments (high-temperature annealing) may provide additional information on the nature of the incorporation mechanisms.

1.3 Structure of this study

The thesis has been organized in seven chapters, starting with the introduction presented here, followed by other chapters.

Chapter 2: What do we know about Hydrogen defects and Hydrogen diffusion in NAMs and especially in Garnet and Zircon?

In this chapter, the nature of H-defects and its speciation in NAMs is introduced, followed by the significant influence of water on the chemical and physical properties of minerals/rocks. Then, the two kinds of diffusivities (chemical diffusivity and self-diffusivity) of H in NAMs are briefly described, with an example of H diffusion in olivine shown after. In the second part, the cases of garnet and zircon are particularly introduced, individually, in detail. The crystal chemistry is given first, followed by water content in garnet (zircon) and the H incorporation mechanism proposed in previous works. In case of garnet, it is followed by H diffusion kinetics in pyropes and garnets of the grossular-andradite series reported in previous studies. While in case of zircon, the following existing diffusion studies limited only to cations, oxygen and helium, since no kinetics data involving hydrogen diffusion in zircon have been reported so far to the best of our knowledge.

Chapter 3: Theory and application

The theory of diffusion and Fick's law, on which our numerical analysis of the experimental results based, is briefly reviewed in this chapter. The diffusion mechanisms and the Arrhenius law the diffusion process follows are introduced subsequently. The application of analytical solution for diffusion to our experimental approach to hydrogen in minerals is presented at last. It is considered that our experimental conditions are close to the simple case of diffusion in a solid bounded by two infinite parallel planes.

Chapter 4: Experimental, analytical methods and samples

The experimental methods are described in this chapter, followed by the analytical methods used for this thesis (EMPA, LA-ICP-MS, Raman and FTIR). A particular attention is dedicated to FTIR spectroscopy, the main tool of this thesis. A general

description and preparation of the samples (andradite garnet and zircon) are also presented.

Chapter 5: Kinetics of hydrogen diffusion in andradite

In this chapter, the results of hydrogen mobility in andradite garnet are presented. The chemical compositions measured by different approaches are given first, and then followed by IR absorption features and the water content. A particular attention is paid to bands transfer occurring during annealing. Then we present the results of diffusion kinetics and the deduced diffusion law. A detailed comparison between hydrogen mobility in andradite and that in other NAMs is discussed. Finally, the geological application of the deduced diffusion kinetics of hydrogen in andradite is proposed.

Chapter 6: Kinetics of hydrogen diffusion in zircon

In this chapter, the results of hydrogen mobility in zircon are presented. The chemical compositions measured by different approaches are given first, and then followed by the water content and Raman/IR absorption features. A new correlation relating the frequency shift (ν_{OH}/ν_{OD}) due to the isotopic replacement to the OH stretching frequency (ν_{OH}) is deduced. The uranium redox reaction, which introduces extra H species during H-D exchange, is specifically described including the IR absorption features of uranium and the rate of reaction. Then, the results of diffusion kinetics and the deduced diffusion law are presented. A detailed comparison between hydrogen mobility in zircon and that in other NAMs is discussed. Then, the geological application of the deduced diffusion kinetics of hydrogen in zircon is proposed. Finally, the incorporation mechanism of hydrogen in zircon is discussed.

Chapter 7: Conclusion and perspectives

This chapter gives a general summary of the results and final conclusions in this study. Then, the perspectives of present study are provided.

Chapter 2

What do we know about Hydrogen defects and Hydrogen diffusion in NAMs and especially in Garnet and Zircon?

2.1 H-defects and H diffusion in NAMs

2.1.1 Hydrogen defects

Hydrogen is the most abundant chemical element in the solar system, while liquid water covers more than 70% of the Earth's surface but constitute only 0.025% weight percent to the whole Earth (Keppler and Smith 2006). It is not surprising that the quantity of water within the Earth's interior could be greater than this amount, with the presence of "water" in nominally hydrous and anhydrous minerals (Keppler and Smith 2006).

Hydrogen can be present as a major constituent in a wide variety of minerals both in the crust and in the upper mantle, such as hydrate (e.g., gypsum), oxide and hydroxide (e.g., brucite), and rock-forming silicates (e.g., amphibole, phlogopite, lawsonite). Nominally hydrous minerals (NHMs) are named for these minerals since H is an important element of their structural formula. H is usually bonded to oxygen forming H_2O molecules or OH groups. It can also form H_3O^+, $H_3O_2^-$ and $H_5O_2^+$ units in very rare cases (Libowitzky and Beran 2006).

Hydrogen can also occur as a minor or trace constituent in most common rock-forming minerals throughout the crust (such as feldspar and quartz) and the mantle (such as olivine, pyroxene, garnet, wadsleyite and ringwoodite). Usually H is

associated to point defects (as defect associates for charge compensation) in the crystal lattice of these minerals and bonded to oxygen forming OH groups. In this case H is a point defect in nominally anhydrous minerals (NAMs; Libowitzky and Beran 2006). Point defects refer to defects occurring within range of one or several atomic distances. Three kinds of main point defects can be present in the crystal structure: (expressed with the Kroger-Vink notation: x denote neutral charges, ′ negative charges and •positive charges; Kroger and Vink 1956): 1) vacancies on the cation and anion sites, e.g., $V^{''''}_{si}$ and $V^{''}_{Me}$ denote vacant Si and metalic sites, respectively; 2) interstitials of intrinsic and extrinsic ions, e.g., $O^{''}_{i}$ and $Fe^{\bullet\bullet\bullet}_{i}$ denote O^{2-} and Fe^{3+} interstitials, respectively; 3) substituted impurity ions, e.g., $Al^{'}_{Si}$ denote Al^{3+} ions in Si tetrahedral sites like in garnet and $U^{\bullet}_{Zr}$ denote U^{5+} ions in Zr sites in zircon.

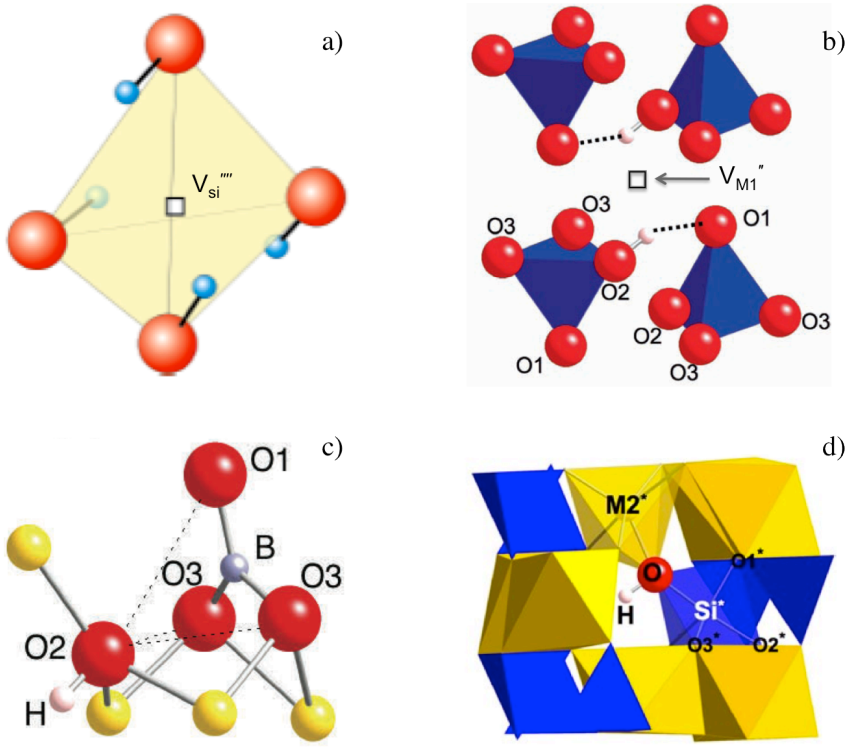

Figure 2.1. Theoretical models of H-defects present in NAMs. a) $[V_{si}''''4H^{\bullet}]^{x}$; b) $[V_{Me}''2H^{\bullet}]^{x}$ (in forsterite, from Balan et al. 2011); c) $[B_{Si}'H^{\bullet}]^{x}$ (in olivine, from Ingrin et al. 2014); d) $[H_i^{\bullet}O'']'$ (in forsterite, from Balan et al. 2014).

Then H-defects present in NAMs are in the form of: 1) clusters of H on silicon or metal vacancies, e.g., $[V_{si}^{''''}4H^{\cdot}]^{x}$, $[V_{Me}^{''}2H^{\cdot}]^{x}$ (Rossman and Aines 1991; Balan et al. 2011); 2) proton coupled with a substituted ion with lower valence to maintain charge balance, e.g., $[B_{Si}^{'}H^{\cdot}]^{x}$ like in olivine (Ingrin et al. 2014) and $[Y_{Zr}^{'}H^{\cdot}]^{x}$ like in zircon (Botis et al. 2013); 3) proton interstitials associated with oxygen ions, e.g., $[H_i^{\cdot}O^{''}]^{'}$ like suggested in forsterite (Balan et al. 2014; Fig. 2.1).

NHMs dominate the water content of most crustal rocks since the OH concentrations in these minerals are orders of magnitude greater than that in NAMs. Most of NHMs are stable in the range of P-T conditions prevailing in subduction zones, but will break down at the high temperature in the mantle. Although the stability ranges of a few of them, like K- or Na-bearing amphiboles, persist into the mantle, their abundance is limited by the low K and Na content in the upper mantle (Thompson 1992). In contrast, NAMs have a wide P-T stability range and no particular compositional requirement. Although only trace concentrations of H are present in NAMs, due to the large volume of these minerals in the Earth's mantle, a significant reservoir of water can be formed (Smyth et al. 1991; Bell and Rossman 1992; Ohtani 2005; Ingrin and Skogby 2000). Such a large reservoir of water in the mantle would affect many geologic processes and has several implications for the evolution of the Earth.

During the last decades, an increasing number of studies have been undertaken to investigate hydrogen in NAMs, especially in upper-mantle minerals, due to its disproportionately large effect on the chemical and physical properties of minerals/rocks. Water is important in weathering and alteration of minerals at the Earth's surface. Water affects the physical properties of minerals and rocks, including plastic deformation (Kronenberg and Wolf 1990; Mei and Kohlstedt 2000a, 2000b; Kohlstedt 2006), lowering of melting temperature (Gaetani and Grove 1998; Green 1973; Hirose and Kawamoto 1995). It facilitates phase transformations and may help to stabilize defects created by radiation damages by compensating for local charge imbalance (Woodhead et al. 1991b; Mosenfelder et al. 2005; Lathe et al. 2005),

increases diffusion rate of major elements such as Fe, Si and O which in turn affect exsolution processes and geochemical signatures (Farver and Yund 1990, 1991; Farver 1994; Hier-Majumder et al. 2005;Costa and Chakraborty 2008), enhances electrical and heat conductivity (Hofmeister 2004; Karato 1990; Wang et al. 2006; Wang et al. 2008 and Yoshino et al. 2006) and may also affect attenuation of seismic waves (Jung and Karato 2001; Karato 2004, 2006). The studies of hydrogen speciation in minerals and its link with crystallographic defects, melt composition, oxygen fugacity, trace element composition and so on, is an ongoing field of interest in Earth science, particularly in mineralogy and geophysics.

2.1.2 Hydrogen diffusion in NAMs

To study hydrogen diffusion in minerals, experiments performed so far involve H-extraction/incorporation and H-D exchange experiments. The diffusivity obtained from H-extraction/incorporation experiments corresponds to a chemical diffusivity, depending on the diffusivity of the H species and the other diffusion species involved in the reaction. The diffusivity deduced from H-D exchange experiments corresponds to D and H diffusivity through the lattice. It is generally assumed that H diffusivity is around 1.4 times of D diffusivity considering the mass difference (Le Claire 1966). It is generally largely below the average experimental uncertainty of diffusion measurements. Thus, H-D exchange is assumed to represent H or D “self-diffusivity”. It is generally assumed that H moves as interstitial in the crystal structure of NAMs during H-D exchange. Olivine is a good example of mineral with different hydrogen diffusion laws, from the H-D diffusion rate that measure mobility of H in the olivine lattice, to chemical diffusion rates that depend directly on the mechanism involved and the nature of H-defects. The kinetics of hydrogen diffusion of these species will be briefly reviewed, in the following.

By extensive studies of H-incorporation in olivine (chemical diffusion), two diffusion mechanisms were proposed by authors (Mackwell and Kohlstedt 1990;

Kohlstedt and Mackwell 1998; Demouchy and Mackwell 2003, 2006; Ingrin and Blanchard 2006):

1) a relatively fast exchange process (with an activation energy around 145 kJ/mol; $Olivine_{H\text{-}h}$, Fig. 2.2a) through a Fe redox-reaction, involving protons ($H^{\cdot}$) and polarons (electron holes $h^{\cdot}$) localized on iron atoms, following the reaction:

$$Fe^{x} + H^{\bullet}_{i} = Fe^{\bullet} + 1/2H_2 \text{or } Fe^{2+} + OH^{-} = Fe^{3+} + O^{2-} + 1/2H_2 \qquad (2.1)$$

2) a slower exchange process with higher activation energy (around 220 kJ/mol; $Olivine_{H\text{-}VMe}$, Fig. 2.2a) involving protons and metal vacancies, following the reaction:

$$MeO + V''_{Me} + 2H^{\bullet}_{i} = Me^{x} + H_2O \qquad (2.2)$$

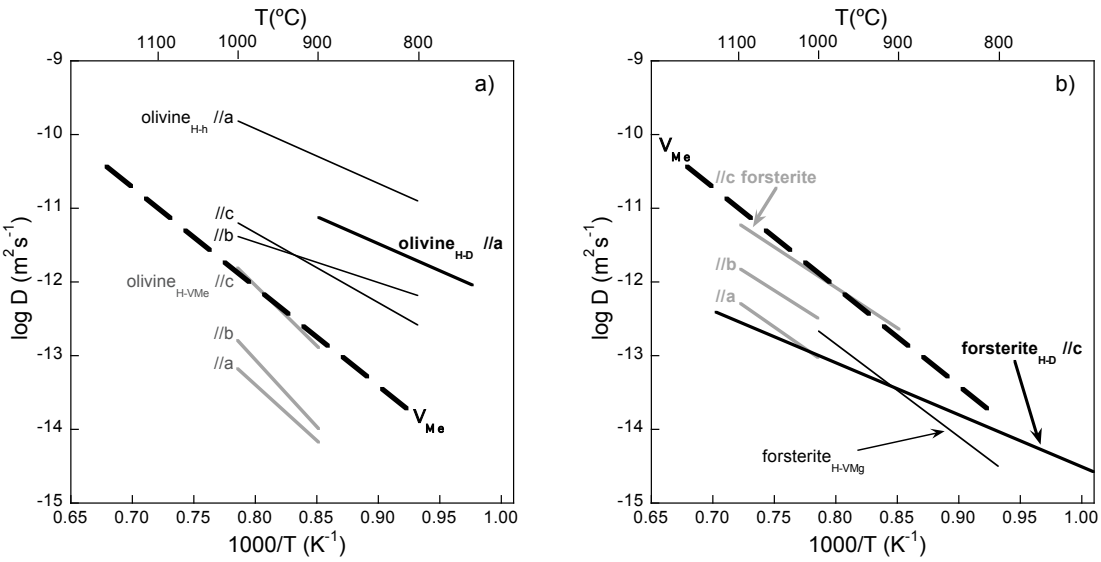

Figure 2.2. Compilation of chemical diffusivities of H in a) olivine and b) forsterite along the three crystallographic directions, as well as one data for H-D exchange. In a), thin black lines are for redox-exchange reactions while light gray lines are for exchange involving metal vacancies in olivine (Kohlstedt and Mackwell 1998); the dashed line is for vacancy diffusion in Fe-bearing olivine (Demouchy and Mackwell 2003); the heavy black line is for H diffusivity along the *a* axis deduced from H-D exchange (Du Frane and Tyburczy 2012). In b), gray lines are for exchange involving metal vacancies in forsterite and (Demouchy and Mackwell 2003); the thin black line

is for the diffusivity of hydrous defects associated with Mg vacancies in forsterite (Padrón-Navarta et al. 2014); the heavy balck line is for H diffusivity along the *c* axis deduced from H-D exchange (Ingrin and Blanchard 2006).

For the first type of exchange, it was proposed that the effective diffusivity (D_{eff}), obtained from diffusion experiments performed at low temperature for short duration, is related to the diffusivity of protons (D_H) and polarons (D_h) by the relation:

$$D_{eff} = \frac{(X_H + X_h)D_H D_h}{X_H D_H + X_h D_h} \text{ or } D_{eff} = \frac{(1 + \frac{X_h}{X_H})D_H D_h}{D_H + \frac{X_h}{X_H} D_h} \quad (2.3)$$

Assuming $X_H \approx X_h$, the above reaction was simplified as (Kohlstedt and Mackwell 1998):

$$D_{eff} = \frac{2D_H D_h}{D_H + D_h} \quad (2.4)$$

If the diffusivity of polarons is far greater than that of protons ($D_h >> D_H$), then the effective diffusivity acquired is roughly twice the diffusivity of protons ($D_{eff} \approx 2D_H$). This interpretation was not confirm by Du Frane and Tyburczy (2012), who performed H-D exchange for olivine along the *a* axis and found that $D_{eff} \approx 7D_H$ (Fig. 2.2a), with D_{eff} deduced by Demouchy and Mackwell (2006). The proposed explanation was that the difference was due to the pressure difference between the two experiments (2 GPa versus 0.3 GPa; Du Frane and Tyburczy 2012). However, this is just a hypothesis, with no real demonstration; the whole model proposed by Kohlstedt and Mackwell (1998) remains hypothetical.

For the second type of exchange reaction, it was proposed that the effective diffusivity, obtained from diffusion experiments performed for longer duration, is related to the diffusivity of protons and metal vacancies (D_{VMe}) by the relation:

$$D_{eff} = \frac{3D_H D_{VMe}}{2D_{VMe} + D_H} \quad (2.5)$$

Assuming $X_H \approx X_h$ and the diffusivity of protons far greater than that of metal vacancies ($D_H >> D_{VMe}$), the same authors deduce that the effective diffusivity is three times the diffusivity of metal vacancies ($D_{eff} \approx 3D_{VMe}$).

Demouchy and Mackwell (2003) obtained H diffusivities in synthetic forsterite similar to that in olivine involving metal vacancies (Fig. 2.2b). Besides, Padrón-Navarta et al. (2014) investigated H-extraction kinetics in synthetic forsterite with consideration of different types of H-defects related to Mg-vacancies, Si-vacancies, and Ti-clinohumite point defects, respectively. They suggested different kinetics for different H-defects giving rise to different IR bands, where the diffusivity of H-defects associated with Mg vacancies lies in the same range of diffusivities in forsterite and in olivine involving vacancy mechanism. A vacancy mechanism was suggested by all of them. The diffusivity deduced from H-D exchange in natural forsterite along *c* axis (Ingrin and Blanchard 2006) shows lower values compared to the diffusivity of H-extraction in synthetic forsterite from Demouchy and Mackwell (2003) (Fig. 2.2b).

2.2 Specific cases of garnet and zircon

2.2.1 Garnets

2.2.1.1 Crystal chemistry

The garnets comprise an important and widespread group of rock-forming minerals distinguished by their chemical variability, structural similarity, physical properties and geological implications. The general chemical formula of garnets can be written as $X_3Y_2(ZO_4)_3$ with eight formula units per unit cell, where generally X denotes divalent cations, Y denotes trivalent cations and Z denotes tetravalent silicon ions:

$X = Ca^{2+}, Mg^{2+}, Fe^{2+}, Mn^{2+}, (Y^{3+}, K, Na)$

$Y = Al^{3+}, Fe^{3+}, Cr^{3+}, V^{3+}, Mn^{3+}, Ti^{3+,4+}, Zr^{3+,4+}$

$Z = Si^{4+}, (Al^{3+}, Fe^{3+}, Ti^{4+}, 4H)$

The ionic radius of Y cations is close to each other, isomorphism is easily occurring, while the radius of Ca^{2+} is much greater than other X cations, it is difficult for Ca^{2+} to realize isomorphous substitution with these cations, such as Mg^{2+}, Fe^{2+} and Mn^{2+}. Therefore, garnets has been divided into two groups (Winchell, 1958): 1) the ugrandites, with X site occupied by Ca^{2+} and Y site alternatively occupied by Al^{3+}, Fe^{3+}, Cr^{3+}, etc., forming end-members grossular, andradite, uvarovite and intermediate compositions; 2) the pyralspites, with Y site predominantly occupied by Al^{3+} and X site alternatively occupied by Mg^{2+}, Fe^{2+}, Mn^{2+}, etc., forming end-members pyrope, almandine, spessartine and intermediate compositions. The main physical constants for the most abundant end-members of the garnet group are shown in Table 2.1. The ion radius of X-cations follows: $r(Mg^{2+}) < r(Fe^{2+}) < r(Mn^{2+}) < r(Ca^{2+})$, while the ion radius of Y-cations follows: $r(Al^{3+}) < r(Fe^{3+}) < r(Mn^{3+}) < r(V^{3+})$. Therefore, the unit cell dimension of pyraspites are generally smaller than that of ugrandites, and the unit cell dimension decreases with increasing Mg^{2+}, Fe^{2+} and Al^{3+} content, increases with increasing Ca^{2+}, Fe^{3+} and V^{3+} content (Table 2.1; Meagher 1980).

Table 2.1. The main physical constants for garnet end-members (unit cell dimension, refraction index and density; after Meagher 1980).

Series	Name	Composition	A_0 (Å)	n	Density ($g.cm^{-2}$)
Pyralspites	Pyrope	$Mg_3Al_2Si_3O_{12}$	11.459 (1)	1.714 (2)	3.582
	Almandine	$Fe_3Al_2Si_3O_{12}$	11.528 (1)	1.829 (3)	4.315
	Spessartite	$Mn_3Al_2Si_3O_{12}$	11.614 (1)	1.799 (3)	4.197
Ugrandites	Grossular	$Ca_3Al_2Si_3O_{12}$	11.851 (1)	1.734 (2)	3.594
	Andradite	$Ca_3Fe_2Si_3O_{12}$	12.048 (1)	1.887 (2)	3.859
	Uvarovite	$Ca_3Cr_2Si_3O_{12}$	11.996 (2)	1.865 (3)	3.85

Most of the garnets crystallize in the cubic system, with space group symmetry *Ia*3*d*. Menzer (1926) first solved the crystal structure of grossular using powder

methods, and later established the isostructuralism of other ugrandites and pyralspites with grossular. He found that the X-, Y- and Z-cations are in special positions with site symmetry D_2, S_6 and S_4, respectively, while oxygen is in a general position with variable coordinates, x, y and z. There are three kinds of coordination polyhedra present in the structure: the triangular dodecahedron (XO_8) consists of eight oxygens coordinating the X-cations, which can also be described as a distorted cube; the octahedron (YO_6) consists of six oxygens coordinating the Y-cations, which is slightly distorted; the tetrahedron (ZO_4) consists of four oxygens coordinating the Z-cations, which are slightly distorted and can be accurately described as tetragonal disphenoids.

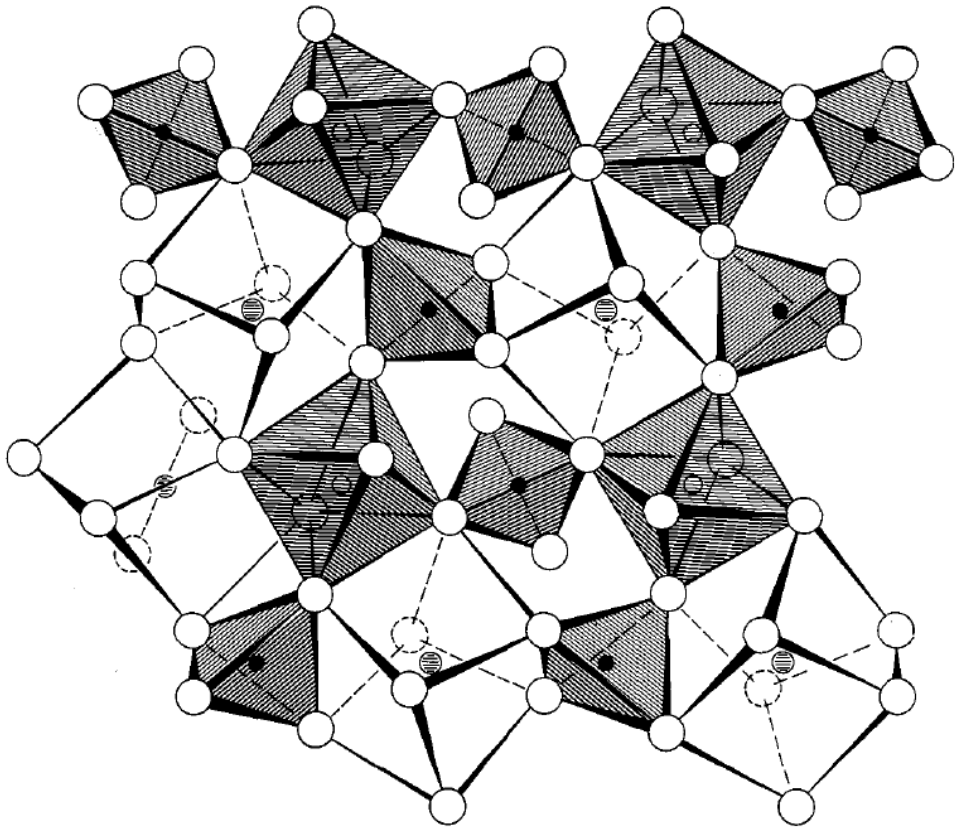

Figure 2.3. Portion of the garnet structure projected down z showing the framework of alternating ZO_4 tetrahedra and YO_6 octahedra (shaded portion) and the spaces occupied by X-cations forming XO_8 triangular dodecahedra (distorted cubes). Large open circles denote oxygens, smaller open circles the Y-cations, solid black circles the Z-cations, and the hatched ones X-cations (from Novak and Gibbs 1971). In case

of andradite X sites are occupied mainly by Ca^{2+}.

Two descriptions can be used to show the crystal structure of garnet. First, the crystal structure can be seen as framework of alternating ZO_4 tetrahedra and YO_6 octahedra, where the two kinds of polyhedra share corners with each other. The X-cations occupy the remaining spaces, forming XO_8 dodecahedra (Fig. 2.3). The crystal structure of garnet can also be described as chains of alternating edge-sharing ZO_4 tetrahedra and XO_8 dodecahedra, paralleling the three mutually perpendicular directions. The remaining spaces are occupied by Y-cations, forming YO_6 octahedra, which share edges with ZO_8 dodecahedral (Fig. 2.4). Each oxygen atom is coordinated by two X-, one Y- and one Z-cations in a nearly tetrahedral coordination.

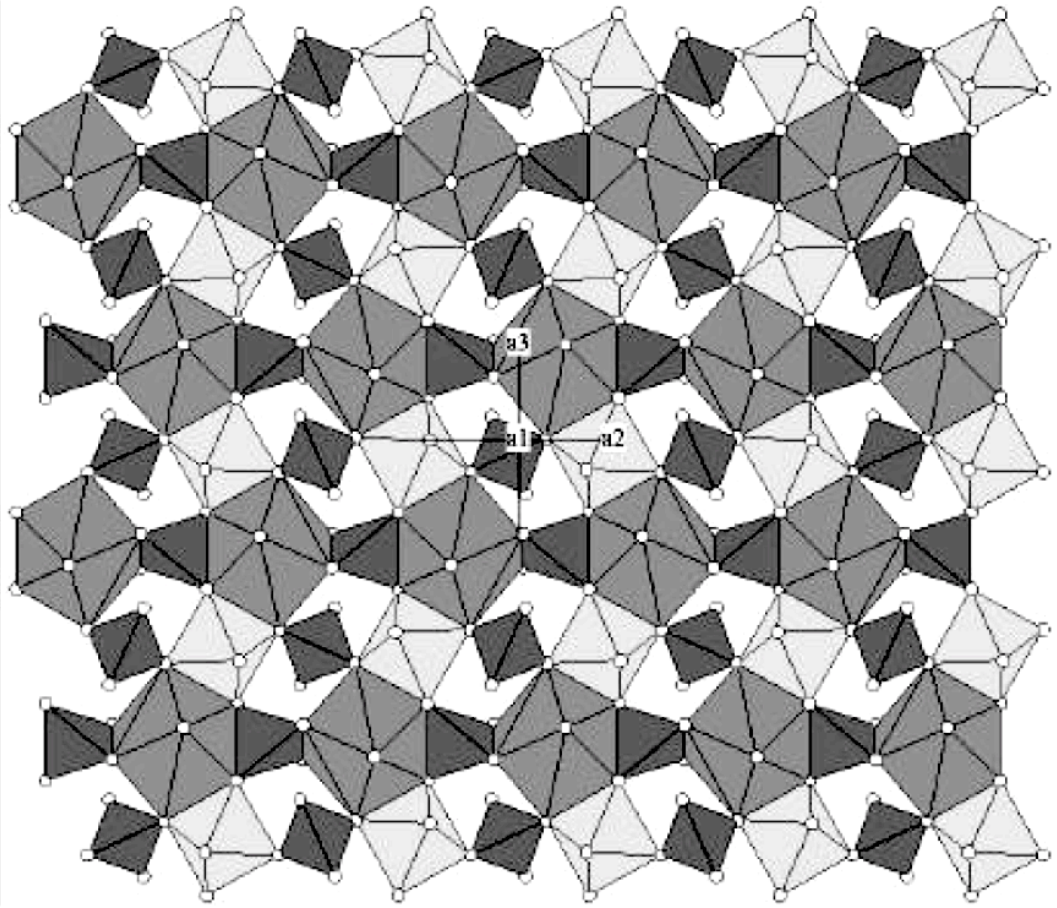

Figure 2.4. Portion of the garnet structure showing chains of alternating edge-sharing ZO_4 tetrahedra (dark) and XO_8 dodecahedra (heavy gray), in parallel in the three mutually perpendicular directions (a1, a2 and a3; a1 is perpendicular to the plane).

The remaining spaces is occupied by Y-cations forming YO_6 octahedral (gray), which also share edges with neighboring dodecahedra (from Kurka 2005).

It is generally known that increasing temperature reduces the coordination number of cations, while increasing pressure raises the coordination number of cations. The X-cations show progressively decreasing ionic radius from Ca^{2+} to Mg^{2+}: Ca^{2+}(0.112 nm), Mn^{2+}(0.096 nm), Fe^{2+}(0.092 nm), Mg^{2+}(0.089 nm). There is no need for high pressure for Ca^{2+} to incorporate as 8-coordinated. Hence, grossular and andradite are commonly found in contact metamorphic rocks. However, increasing pressure is necessary for Mn^{2+}, Fe^{2+} and Mg^{2+} to be stable in the 8-coordinated site since these ions tend to be 6-coordinated. Therefore, spessartine forms under conditions of low-grade regional metamorphism at slightly higher pressure, e.g., in granite and associated pegmatite; almandine forms under conditions of intermediate grade regional metamorphism at even higher pressure; pyrope forms only under greater pressure, e.g., in elcogite and deep peridotites. Uvarovite is relatively rare and limited to chromite deposits within untramafic rock bodies.

Specifically, andradite is typically found in skarns, which are often mined as ore deposits and found in contact metamorphic assemblages, like serpentine. The information of the stability of andradite and andradite-bearing assemblages, have been used to elucidate the physicochemical conditions of skarn formation (Zhang and Saxena 1991). Ti-bearing andradite, was the most extensively studied andradite garnet (Kühberger et al. 1989; Lager et al. 1989; Locock et al. 1995; Armbruster et al. 1998; Amthauer and Rossman 1998). It is commonly described through the name of melanite, $1 < TiO_2 \leq 5$ wt%, and schorlomite or morimotoite, $TiO_2 > 5$ wt%, depending on the Ti substitution mechanism (Deer et al. 1982).

2.2.1.2 Hydrogen defects in garnets

Numerous studies have shown that hydroxide is a common trace or minor component in granets: ugrandites and pyraspites (e.g., Aines and Rossman 1984, 1985; Rossman and Aines 1991; Amthauer and Rossman 1998). The most established type

of OH defect in garnet is the hydrogarnet (or hydrogrossular) substitution, where $(SiO_4)^{4-}$ can be partially or fully replaced by $(OH)_4^{4-}$, the O-H vectors project outside the volume of the tetrahedron (Lager et al. 1987, 1989). This substitution is shown schematically in Figure 2.5, where the shared edge with dodecahedron (O1-O2) is shorter than the unshared edge (O1-O3).

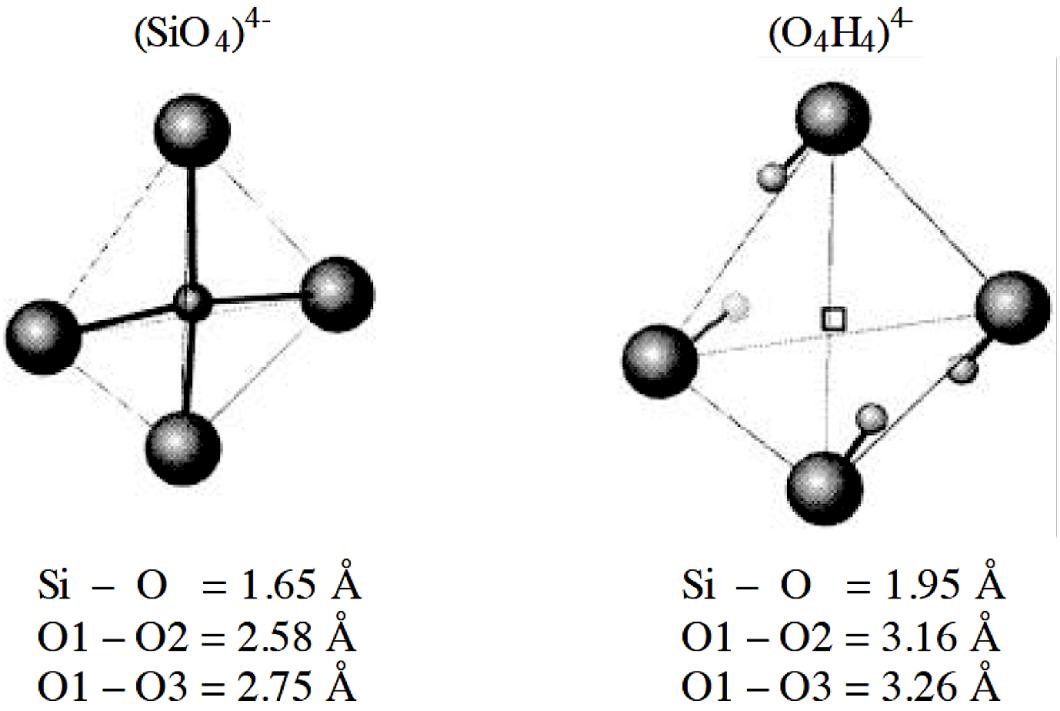

Figure 2.5. Schema of the hydrogarnet substitution: $(SiO_4)^{4-}$ = $(OH)_4^{4-}$. The protons are located outside of the tetrahedron between two unshared edges (modified from Prandl 1966; Cohen-Addad et al. 1967; Kurka 2005).

The hydrogarnet substitution was first experimentally suggested by Cohen-Addad et al. (1967) in grossular, and has been confirmed with IR, X-ray and neutron diffraction (Aines and Rossman 1984, 1985; Foreman 1968; Sacerdoti and Passaglia 1985; Lager et al. 1987, 1989). Hydrogrossulars form a solid solution between the end-member grossular ($Ca_3Al_2Si_3O_{12}$) and Katoite [($Ca_3Al_2(O_4H_4)_3$). Katoite exists only as a synthetic material while the natural OH-rich varieties are called Hibbschite, with a formula $Ca_3Al_2[(SiO_4)_{3-x}(O_4H_4)_x]$, $x < 1.5$. The hydrogarnet substitution is not limited in grossular, but is also common in other garnets, e.g. it has been confirmed

by diffraction studies for a hydrous andradite with 50% Si deficiency and high OH content (Armbruster 1995). However, the extent to which hydrogen can incorporate into the garnet is apparently related to the composition. Garnets belonging to the ugrandites usually contain more hydrous component than those belonging to the pyraspites group, the former ones can incorporate up to 20 wt% H_2O, while the latter can only incorporate less than 0.5 wt% H_2O (Wilkins and Sabine 1973; Lager et al. 1987; Lager et al. 1989; Rossman and Aines 1991; Armbruster and Geiger 1993; Armbruster 1995).

Many explanations for this difference have been proposed by authors from various points of view. Sacerdoti and Passaglia (1985) have suggested that the degree of hydration in garnets may be controlled by the length of the shared and unshared octahedral edges. The shared octahedral edge is longer than the unshared edge for grossular and andradite, while it is opposite in the case of pyrope and almandine. Lager et al. (1989) found by distance-least-squares (DLS) calculations that, the OH substitution will decrease the length of the shared edge and increase that of the unshared edge. The garnet structure will be unable to accommodate more OH if the length of the shared edge approaches some lower limit. The limit would be sooner approached in garnets in which the shared edge is shorter than the unshared edge, such as pyrope and almandine, therefore, the capability of incorporating OH of pyraspites is generally lower than in ugrandites. Zabinski (1966) also proposed another argument by comparing the mean X-O distance in the dodecahedron and the sum of the ionic radii of X cation and oxygen (e.g., 2.405 Å versus 2.50 Å in grossular). He argued that, since Ca is too large for the X site, the OH incorporation in grossular would increase the size of the dodecahedron and thus lead to a more energetically favorable environment for the Ca ion. By contrast, Mg is too small for the X site, thus OH incorporation in pyrope would be limited due to the destabilization of the structure resulting from the expansion of the dodecahedron. Nobes et al. (2000) provided support for this interpretation from an energy point of view by *ab inito* study of hydrogarnets.

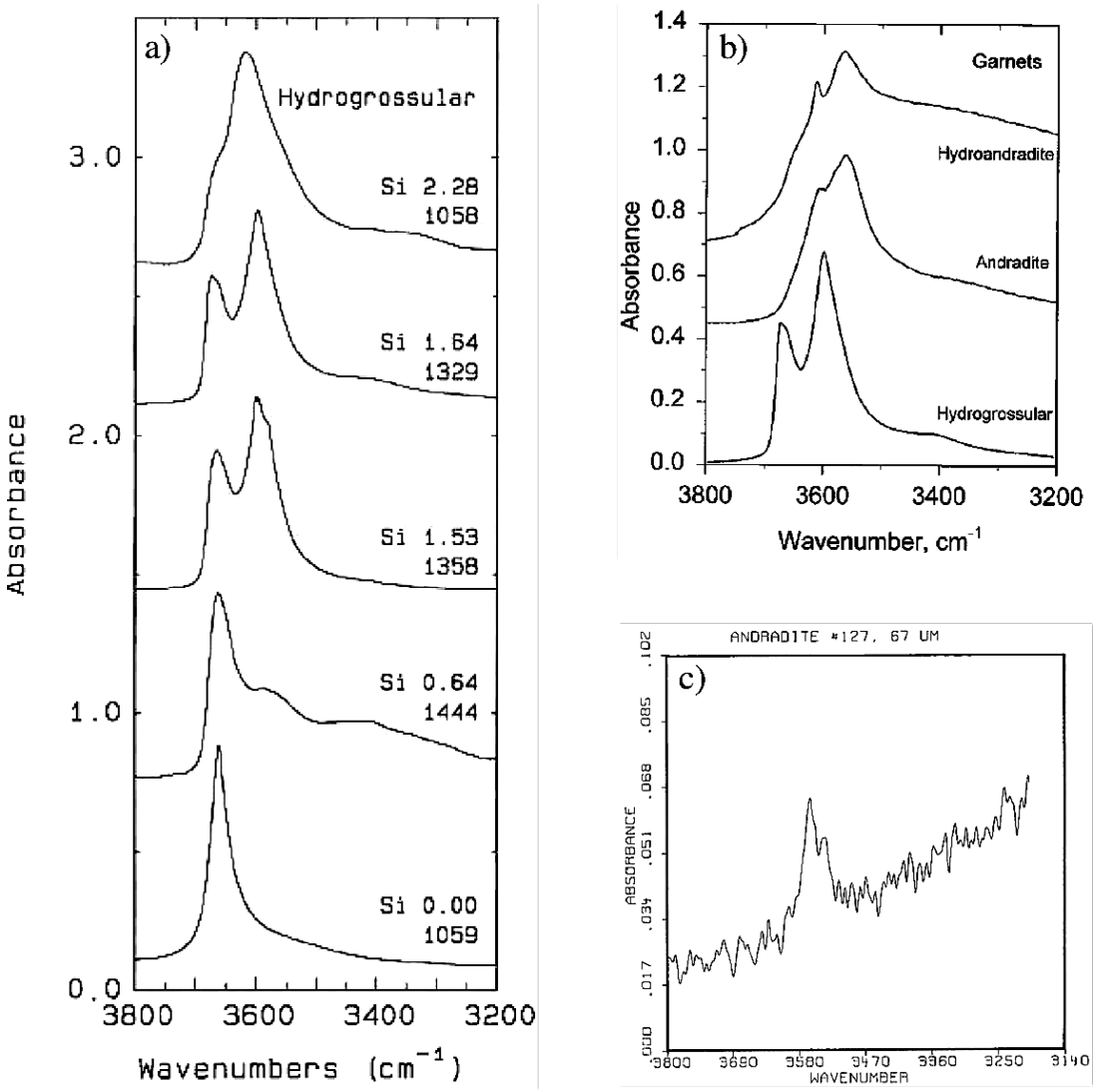

Figure 2.6. a) Compilation of the OH spectra of natural and synthetic hydrogrossular samples with OH contents increasing from top to bottom (from Rossman and Aines 1991). b) Comparison of the OH IR spectra of natural hydrous andradite, synthetic hydroandradite and natural hydrogrossular (from top to bottom; Amthauer and Rossman 1998). c). IR spectrum of a single-crystal andradite synthesized from glass (Armbruster and Geiger 1993).

The hydrogrossulars, natural and synthetic, with varying high OH content (more than 5 wt% H_2O), exhibit IR absorption features composed of two broad overlapping bands centered around 3660 and 3600 cm^{-1} (Rossman and Aines 1991). The higher the OH content is, the greater the relative intensity of the 3660 cm^{-1} band is (Fig. 2.6a).

Thus, the author attributed 3660 cm^{-1} band to $(O_4H_4)^{4-}$ groups surrounding by other $(O_4H_4)^{4-}$ groups, and 3600 cm^{-1} band to the $(O_4H_4)^{4-}$groups adjacent to $(SiO_4)^{4-}$ groups. Similar IR absorption features of both natural and synthetic hydroandradite, show broad bands centered around 3610 and 3560 cm^{-1} (Amthauer and Rossman, 1998) (Fig. 2.6b). These authors proposed that the lower frequencies of absorption bands in hydroandradite (3610 and 3560 cm^{-1}) compared with that in hydrogrossular (3660 and 3600 cm^{-1}) may be related to the greater average tetrahedral cation-cation distance in the former compared to the latter. However, near end-member natural andradite and synthetic andradite exhibit also absorption bands located around 3560 and 3530 cm^{-1} (Fig. 2.6c; Armbruster and Geiger 1993; Amthauer and Rossman 1998), and so do synthetic Ti-andradite and natural melanite and schorlomite (Kühberger et al. 1989; Locock et al. 1995; Amthauer and Rossman 1998). The general appearance of these two bands is similar to the OH absorption spectra observed for synthetic pyrope (3638 and 3614 cm^{-1}; 78 K) and almandine (3617 and 3595 cm^{-1}; 78 K), where the hydrogarnet substitution is suggested (Geiger et al. 1991). Therefore, Armbruster and Geiger (1993) argued that the hydrogarnet substitution is also the main incorporation behavior in andradite since the frequence separation between the two bands in the andradite is similar to that in pyrope and almandine.

However, the majority of garnets, with much lower OH content, show much more complex spectroscopic characteristics. Grossular with less than 0.3 wt% H_2O, the broad hydrogrossular bands are generally not observed (Beran and Libowitzky 2006). The great variability of IR spectra of these garnets has been reported by many authors, especially for the grossular-andradite group, (e.g., up to 20 and 9 distinct bands were reported for grossular and andradite, respectively; Aines and Rossman 1984; Rossman and Aines 1991; Amthauer and Rossman 1998; Kurka 2005; Fig. 2.7). The variability and complexity of the IR spectra indicate that the hydrogarnet substitution is not the only mechanism through which hydrogen incorporate into the crystal structure, other incorporation mechanisms must exist.

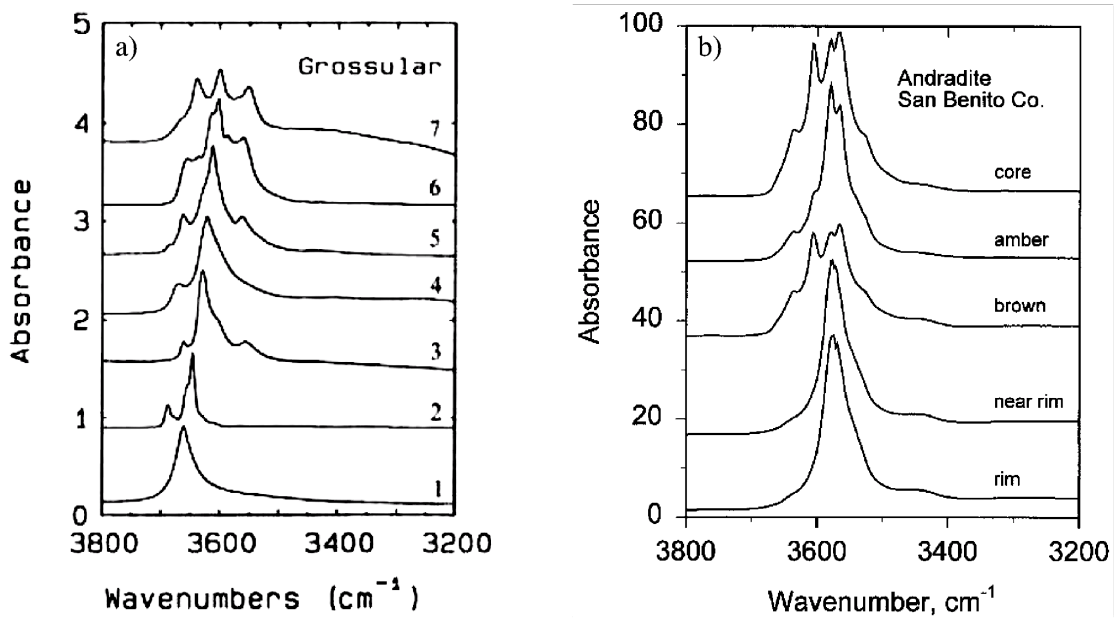

Figure 2.7. a) Compilation of the OH absorption spectra of the least complicated spectrum from the seven classes of spectra of grossular (modified from Rossman and Aines 1991). b) The increase of complexity of IR spectrum from the rim to the core, with increasingly deep color, of a melanite from Santa Rita Peak, San Benito Country, California (Amthauer and Rossman 1998).

A number of authors have proposed that H can enters into garnet through substitution mechanisms other than the classic hydrogarnet substitution, namely vacancies of the octahedral and dodecahedral cations (Andrut et al. 2002; Geiger et al. 1991), octahedral or dodecahedral cation substituted by lower valent cations (Kühberger et al. 1989; Lu and Keppler 1997), tetrahedral cation substituted by lower valent cations (Lu and Keppler 1997), incomplete hydrogarnet substitution (Khomenko et al. 1994; Kurka 2005), and Ti-related hydrogarnet substitution (Khomenko et al. 1994; Johnson 2003; Armbruster et al. 1998).

In an infrared study of a non-cubic garnet with composition close to uvarivite-grossular, Andrut et al. (2002) suggested that the band doublet at 3652 and 3602 $cm^{-1}$and the single band at 3640 cm^{-1} are associated with vacancies on octahedral and dodecahedral cation sites, leading to [SiO_3(OH)] tetrahedral occurring as structural elements. Furthermore, these author concluded that in garnets containing

only hydrogen traces the [$SiO_3(OH)$] substitution mode plays an essential role as OH incorporation mechanism. In addition to hydrogarnet substitution, an octahedral (Al^{3+}) vacancy charge balanced by three H^+ or by two H^+ associated with a Fe^{3+} atom replacing a Ca^{2+} in a nearby X site, was also suggested by Geiger et al. (1991) for a synthetic pyrope with four OH bands ($[3H_{Al}]^x$ or $[2H_{Al}{}'Fe_{Ca}{}^{\cdot}]^x$).

It was also demonstrated that OH incorporation can be charge balanced through a divalent cation such as Fe^{2+} substituting for a trivalent cation such as Fe^{3+}, on the octahedral site, [$FeO_5(OH)$], following $Fe^{3+} + O^{2-} = Fe^{2+} + OH^-$ (Kühberger et al. 1989). Lu and Keppler (1997) concluded in nearly pure natural pyrope that there are two sites, with different compressibility and thermal expansivity, giving rise to two groups of OH bands. They suggested that the 3641, 3651 and 3661 cm^{-1} group of IR bands are associated with Li substituting in a dodecahedral site, [$LiO_7(OH)$], while the band at 3602 cm^{-1} would be associated with B substituting in tetrahedral site, [$BO_3(OH)$]. Considering previous numerous studies on Ti-rich andradite, Kühberger et al. (1989) argued that, in the case of silicon deficiency, other cations can also occupy tetrahedral site with the site preference of Al^{3+}> Fe^{3+}> Ti^{4+}, and so does Fe^{2+} if low oxygen fugacity is present. Charge balance through Fe^{2+} substituting for tetrahedral Si^{4+} was suggested by these authors to account for the incorporated OH species, $[V_{si}^{''''}2H^{\cdot}Fe^{\cdot\cdot}]^x$, following $Si^{4+} + 2O^{2-} = Fe^{2+} + 2OH^-$.

Incomplete hydrogarnet substitution may also be possible in a way that, only three OH^- and one O^{2-} atom are arranged around a Si vacancy, with local charge balance achieved by a tetravalent cation, such as Ti^{4+} and V^{4+}, replacing a octahedral cation, such as Al^{3+} and Fe^{3+}, or by a trivalent cation, such as Al^{3+} and Cr^{3+}, replacing a dodecahedral cation, such as Ca^{2+} and Mg^{2+} (Khomenko et al. 1994; Kurka 2005). OH absorption bands at 3685, 3570 and 3530 cm^{-1} were observed by Khomenko et al. (1994) for hydrothermally grown Ti-bearing pyropes, and an [$O(OH)_3$] incomplete hydrogarnet substitution was proposed to compensate for the higher valence of Ti^{4+} substitution in octahedral site. Representative OH spectra of mantle garnets show either one or two major bands in the range 3660-3645, 3585-3560, and 3525-3515

cm^{-1} (Fig. 2.8; Beran and Libowitzky 2006). Bands in the range 3525-3515 cm^{-1} occur only in Ti-rich granets with TiO_2 greater than 0.4 wt%, and are considered as Ti-related defects (Bell and Rossman 1992b; Bell et al. 2004a; Beran and Libowitzky 2006).

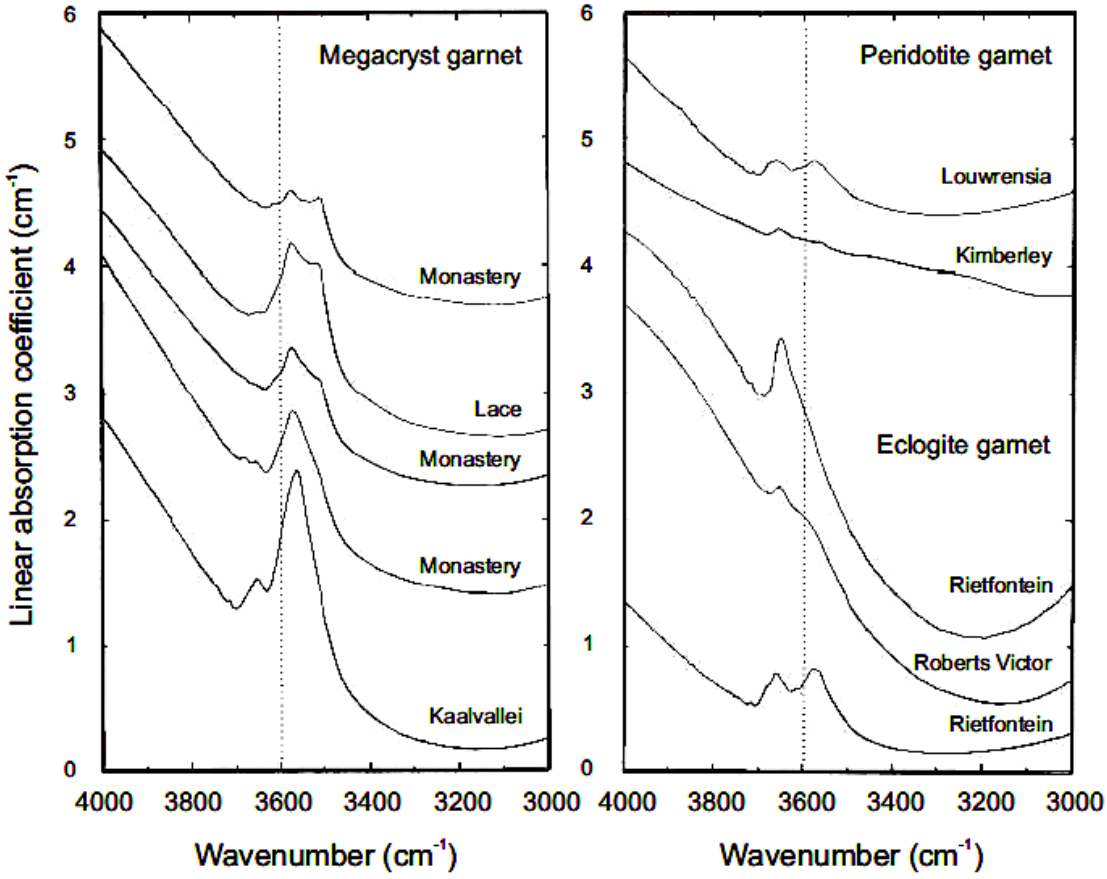

Figure 2.8. Representative IR absorption features in the region of OH stretching frequencies of garnets from kimberlitic xenoliths from South Africa (from Beran and Libowitzky 2006).

Ti-related hydrogarnet substitution is very common in Ti-bearing andradite, such as schorlomite and morimotoite (Khomenko et al. 1994; Johnson 2003). In schorlomite, Ti^{4+} can occupy the octahedral sites, with charge balance achieved by Fe^{3+}, Fe^{2+} or Al^{3+} substituting for Si^{4+} on the tetrahedral sites, e.g., $[Ti_{Fe}^{\cdot}Fe_{Si}^{\prime}]^{x}$, following $Fe^{3+[6]} + Si^{4+[4]} = Ti^{4+[6]} + Fe^{3+[4]}$ (end-member $Ca_3Ti_2Fe_2SiO_{12}$; Henmi et al. 1995). In morimotoite, charge balance is achieved by a coupled substitution of

$Ti^{4+}$and Fe^{2+} for the octahedral Fe^{3+}, $[Ti_{Fe}^{\cdot}Fe_{Fe}^{'}]^{x}$, following $2Fe^{3+} = Fe^{2+} + Ti^{4+}$ (end-member $Ca_3FeTiSi_3O_{12}$). Crystals with dominant schorlomite substitution show only a low degree of additional hydrogarnet substitution (in the same range as pyraspites), while a pronounced hydrogarnet substitution (up to few wt% H_2O) occurs in crystals with Ti^{4+} substitution following the morimotite mechanism (the main bands are located around 3630, 3610, 3575, 3560 and 3520 cm^{-1}; Fig. 2.9; Armbruster et al. 1998). Whatever mechanism Ti^{4+} substitution follows in the Ti-andradite, schorlomite or morimotoite mechanism, the tetrahedron is always expanded for all Ti-andradites compared with end-member andradite, which is due to repulsion between dodecahedron cations (Ca^{2+}) and octahedron cations (Ti^{4+}) decreasing the shared octahedron-dodecahedron edge and increasing the shared tetrahedron-dodecahedron edge. Then, the expansion of tetrahedron results in a structural stress, which can be released by incorporating large cations on the tetrahedron site. In this case, $(O_4H_4)^{4-}$ can substitutes for SiO_4^{4-}, leading to higher OH content in Ti-andradite, or Fe^{3+} and Fe^{2+} can also substitute for Si^{4+}, depending on geochemical environment.

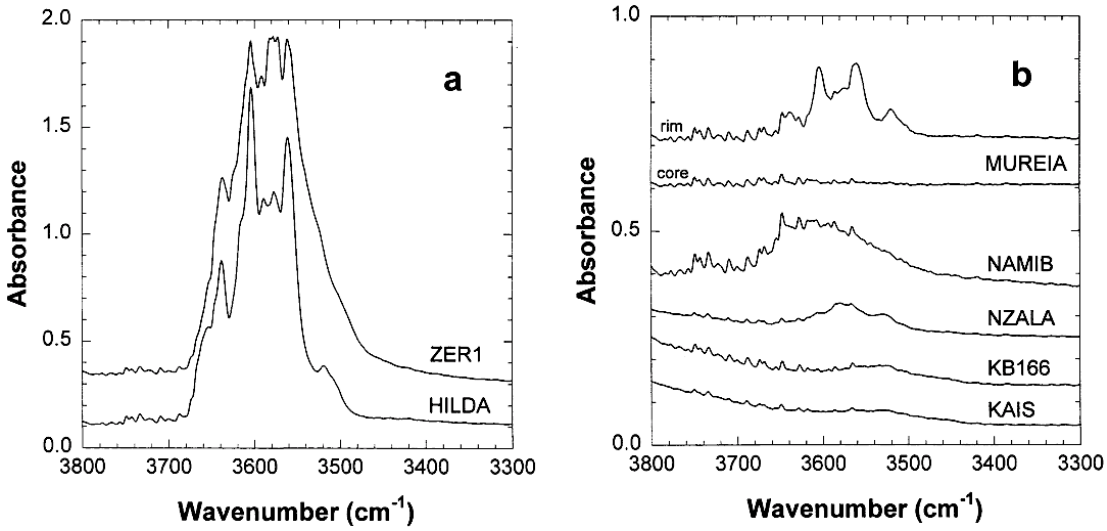

Figure 2.9. IR OH absorption spectra of Ti-bearing andradites. a) Crystals with morimotoite substitution coupled with a pronounced hydrogarnet substitution. b) Crystals with schorlomite substitution coupled with minor hydrogarnet substitution (from Armbruster et al. 1998).

For the complexity of the OH spectra in natural garnets with complicated composition, one has to consider that there is only one symmetrically independent O coordinated by two X-, one Y- and one Z-cation. Thus, the OH element in garnets, while taking hydrogarnet substitution in andradite as example, may be influenced by neighboring dodecahedral cations (Ca^{2+}, Mn^{2+}, etc.) and octahedral cations (Fe^{3+}, Fe^{2+}, Al^{3+}, Ti^{4+}, etc.), which leads to multiple OH absorption bands.

2.2.1.2 Hydrogen diffusion in garnets

Studies of hydrogen diffusion in garnets have been conducted by far mainly on pyrope (Wang et al. 1996; Blanchard and Ingrin 2004a, 2004b) and grossular-andradite series (Kurka et al. 2005; Kurka 2005; Phichaikamjornwut et al. 2012).

H-extraction experiments performed on mantle pyropes lead to two single diffusion laws for two crystals (py1 and py4), respectively (Wang et al. 1996). The kinetics are from comparable to that of olivine along the *a* axis following Fe-redox reaction to nearly two orders of magnitude slower, and higher activation energies are observed, around 250 kJ/mol (Fig. 2.10). H-extraction experiments performed on pyrope of metamorphic origin (Dora Maira pyrope; Blanchard and Ingrin 2004b), with lower Fe^{2+} content than mantle pyropes, reveal a slightly lower diffusivity but comparable activation energies, around 300 kJ/mol (Fig. 2.10). In spite of certain Fe^{2+} ion present in the crystal, a vacancy diffusion mechanism was suggested for H-extraction in Dora Maira pyrope by Blanchard and Ingrin (2004b), while there is no definite explanation for mantle pyrope. Like for olivine, garnets and Dora Maira pyrope show extraction kinetics that are different for different OH bands (The OHa triplet centered on 3651 cm^{-1} show kinetics at least five times faster than the OHb band at 3602 cm^{-1}). Another feature is that in Dora Maira pyrope the diffusivity depends also on oxygen partial pressure. The diffusivities deduced under reducing conditions (OHa, b, Ar/H_2; Fig. 2.10) are smaller than the diffusivities measured in air

(OHa, b air; Fig. 2.10). The dependence of the diffusivities on oxygen partial pressure is expressed with an exponent between 1/8.5 and 1/7

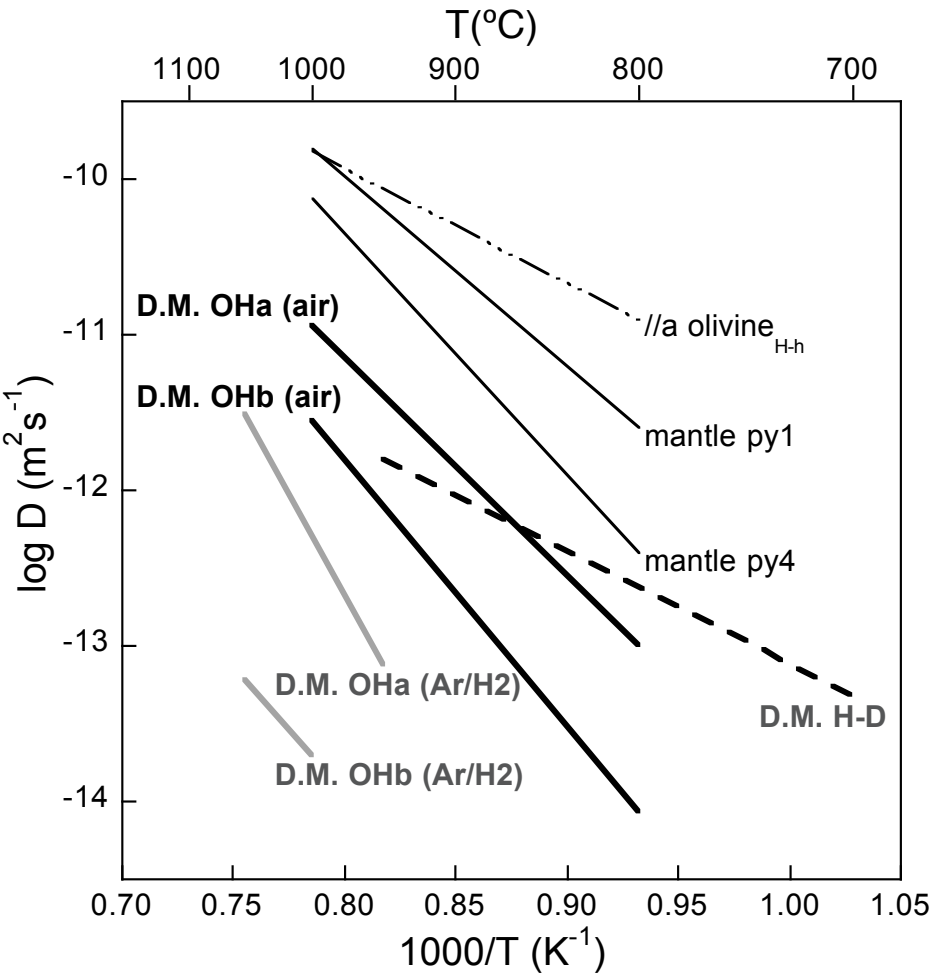

Figure 2.10. Compilation of H-extraction and H-D exchange kinetics in pyrope compared to the incorporation kinetics in olivine. Plain lines are for H-extraction kinetics: thin black lines are for extraction in two mantle pyropes in oxidizing conditions (py1 and py4; Wang et al. 1996), thick black lines are for Dora Maira pyrope (D.M.) in oxidizing conditions (D.M. OHa, b, air; Blanchard and Ingrin 2004b), and thick gray lines are for Dora Maira pyrope in reducing conditions (D.M. OHa, b, Ar/H_2; Blanchard and Ingrin 2004b); Dash line is for H-D exchange kinetics of Dora Maira pyrope (Blanchard and Ingrin 2004a); Dash-dotted line is for incorporation kinetics of olivine along a axis following Fe-redox reaction (Kohlstedt and Mackwell 1998).

The Hydrogen diffusion law deduced from H-D exchange experiments in Dora Maira pyrope has an activation energy of 140 kJ/mol, much lower than for extraction kinetics (Blanchard and Ingrin 2004a; Fig. 2.10). Comparable values of activation energy were reported for olivine and pyroxene (Du Frane and Tyburczy, 2012; Hercule and Ingrin 1999).

For hydrogen diffusion studies of garnets of the grossular-andradite series, Kurka (2005) performed both H-extraction and H-D exchange experiments in two grossulars, with composition of $Gr_{83}An_{14}$ and $Gr_{73}An_{23}$, as well as H-extraction experiments on a nearly end-member andradite, An_{99}; Phichaikamjornwut et al. (2012) performed H-extraction/incorporation experiments for a series of grossulars with increasing andradite component (An_{20}, An_{21}, An_{29}, An_{32}, An_{45} and An_{54}, which are assigned to group An_{20}–An_{54}; An_{99} which is assigned to group An_{99}). For grossular $Gr_{83}An_{14}$, the H-D law shows lower activation energy compared with H extraction diffusion (102 kJ/mol versus 323 kJ/mol) and faster kinetics like in olivine and pyroxene (Fig. 2.11a). However, for grossular $Gr_{73}An_{23}$ with more Fe^{3+} ion content than $Gr_{83}An_{14}$, a comparable diffusivity of extraction and H-D exchange was observed (Fig. 2.11a), and a simultaneous decrease of Fe^{2+} was found during hydrogen extraction measured by Mössbauer. It confirmed the occurrence of a redox-reaction process like in olivine and pyroxene. Probably the Fe content is large enough in grossular $Gr_{73}An_{23}$, leading to greater diffusivity of polarons than that of protons and thus H diffusivity becomes the rate-limiting factor. But the influence of Fe content has not been unambiguously illustrated. H-D exchange diffusivity of andradite would provide important information to understand the influence of Fe content on H diffusion and thus it is in need. The difference in hydrogen extraction kinetics for different OH bands was also observed in almost pure andradite An_{99}: The lower wavenumber group I, with most prominent band at 3560 cm^{-1}, show kinetics about one order of magnitude faster than the higher wavenumber group II, with most prominent band at 3611 cm^{-1} (Fig. 2.11a) The dependence of extraction kinetics on oxygen partial pressure was also found for the two grossulars (Fig. 2.11b; Kurka 2005): $D_{H-extr} \propto pO_2^{0.22\pm0.04}$.

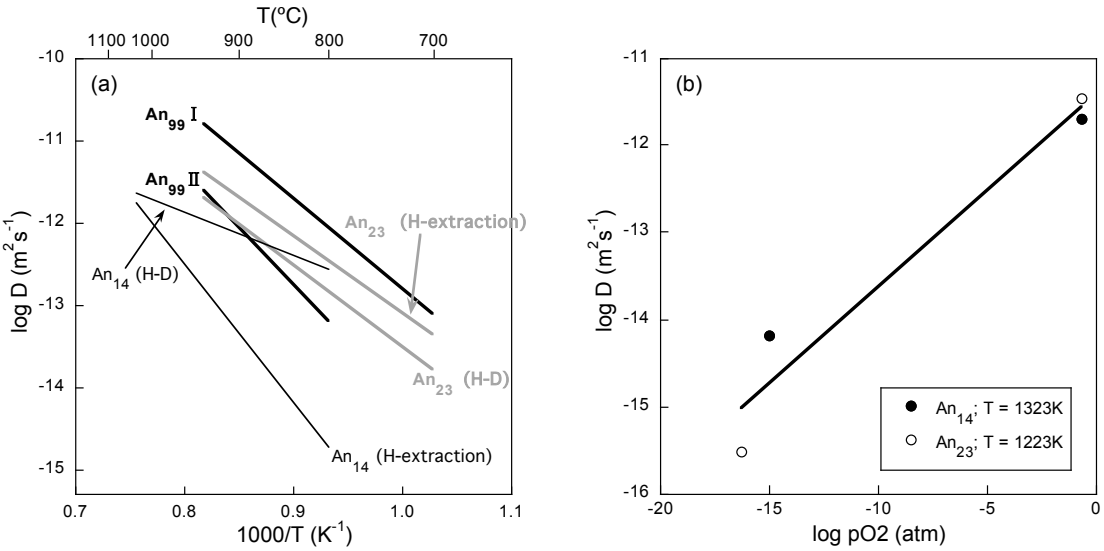

Figure 2.11. a) Compilation of kinetics of H-D exchange and H-extraction in garnets of the grosssular-andradite series from Kurka (2005). Thin black lines are for the two kinds of diffusion laws of grossular $Gr_{83}An_{14}$; Gray lines are for the two kinds of diffusion laws of grossular $Gr_{73}An_{23}$; Thick black lines are for extraction kinetics of the almost pure andradite An_{99}, with An_{99} I for the faster kinetics corresponding to OH bands at lower frequencies and An_{99} II for the slower kinetics corresponding to OH bands at higher frequency bands. b) Kinetics of H-extraction of the two grossulars plotted versus oxygen partial pressure.

In study of Phichaikamjornwut et al. (2012), an increase of effective diffusivities for H-extraction was found roughly with increase of Fe^{3+} ions content and two different kinetics were also observed for the samples with higher Fe^{3+} content like in the Kurka (2005) study. For instance for An_{99}, the distinct data when separating OH bands into higher-frequencies and lower-frequencies bands fall on the diffusion laws deduced by Kurka 2005 (Fig. 2.12). Surprisingly, the incorporation kinetics is about an order of magnitude faster than extraction kinetics (Fig. 2.12). A clear explanation of these features and the diffusion mechanisms involved in H-extraction/incorporation was not provided by these authors and it remains an open question.

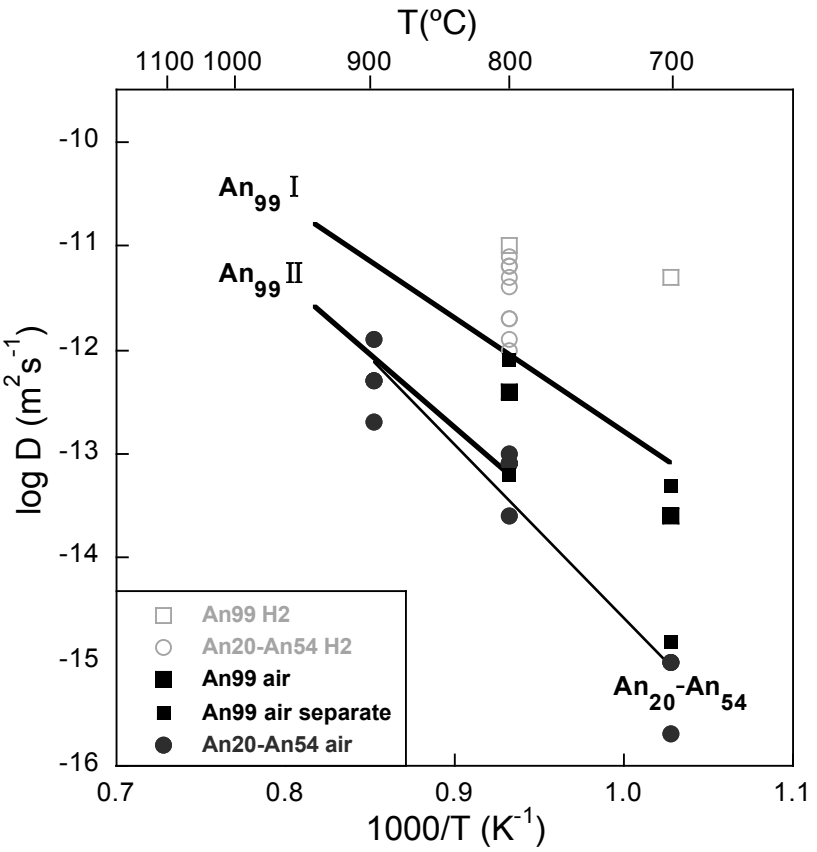

Figure 2.12. Compilation of kinetics of H-extraction/incorporation in garnets of the grosssular-andradite series deduced by Phichaikamjornwut et al. (2012). Solid symbols represent H-extraction data: circles are for An_{20}-An_{54}, squares are for An_{99} with the larger ones the original data when taking overall OH bands as a whole and smaller ones the distinct data when separating OH bands into higher-frequency and lower-frequency bands. Empty symbols represent H-incorporation data: circles are for An_{20}-An_{54}, squares are for An_{99}. An_{99} I, II are the diffusion laws for the lower-frequencies bands and higher-frequencies bands, respectively (Kurka 2005).

2.2.2 Zircon

Zircon is a ubiquitous accessory mineral found in crustal rocks. It can occur in a wide range of settings: sediments, soils and sedimentary rocks, ultrabasic to acidic igneous rocks, weakly metamorphized to ultrahigh-pressure rocks, and also meteorites and lunar rocks (e.g., Belousova et al. 2002; Bell et al. 2004; Page et al. 2007; Liu et al. 2010). Zircon can incorporate a variety of minor and trace elements, such as U, Th

and REE, upon growth from melts and during metamorphism. Although the radioactive decay of these elements will damage the structure of zircon, zircon seems to survive but the harshest conditions, for instance, survive physical breakdown during weathering, resist high-temperature diffusive re-equilibration (e.g., Cherniak et al. 1997), has a slow kinetics of dissolution in crustal melts (e.g., Watson 1996), preserves its chemical integrity (e.g., U/Th and Pb content), isotopic information (e.g., $^{18}O/^{16}O$) and structural properties. Therefore, zircon is used in a wide range of geochemical investigations, including as Ti geothermometer (e.g., Watson and Harrison 2005; Watson et al. 2006; Cherniak and Watson 2007), oxygen, hafnium and lithium isotope studies indicating genetic environment of ancient rocks (Wilde et al. 2001; Valley et al. 2003; Trail et al. 2007, 2009; Ushikubo et al. 2008; Harrison et al. 2008), U-Th-Pb isotropic dating (e.g., Williams 1992; Bowring et al 1998; Bowring and Schmitz, 2003; Ireland and Williams, 2003; Davis et al. 2003), zircon-melt rare earth element partition coefficients (Thomas et al. 2002; Luo and Ayers 2009), studies on the evolution of the Earth's crust and mantle (e.g., Bowring 1995; Vervoort et al. 1996; Hoskin and Schaltegger 2003; Valley 2003). Zircon also is proposed as a potential candidate host for long-term geological repository of high-activity radioactive waste, for example, plutonium from dismantled nuclear weapons (Ewing and Lutze 1997; Burakov et al. 2002; Ewing et al. 2003).

The chemical and physical properties of zircon, its ability to incorporate and preserve trace elements are largely depended on its crystal structure.

2.2.2.1 Crystal chemistry

Zircon is an orthosilicate, with nominal chemical formula of $ZrSiO_4$. It is tetragonal and crystallizes in space group $I4_1/amd$. The zircon structure can be described as chains of alternating edge-sharing SiO_4 tetrahedra and ZrO_8 triangular dodecahedra running parallel to the *c* axis, which are laterally connected by edge-sharing ZrO_8 dodecahedra, in a zigzag pattern, along the crystallographically equivalent *a* and *b* axis (Fig. 2.13; Finch and Hanchar 2003; Robinson et al. 1971).

Therefore, each ZrO_8 dodecahedron shares two edges with two neighboring SiO_4 tetrahedra, and shares four edges with four neighboring ZrO_8 dodecahedral, two along each of the *a* and *b* axis. The zircon structure is relatively open, with unoccupied small voids between the SiO_4 tetrahedra and ZrO_8 dodecahedra running parallel to the *c* axis. The strongly connected feature in the structure of zircon accounts for its many physical properties, including prismatic habit, indistinct cleavage along {110}, high birefringence (Speer 1982), anisotropic thermal expansion (Bayer 1972; Subbarao et al. 1990) and compression (Hazen and Finger 1979; van Westrenen et al. 2004).

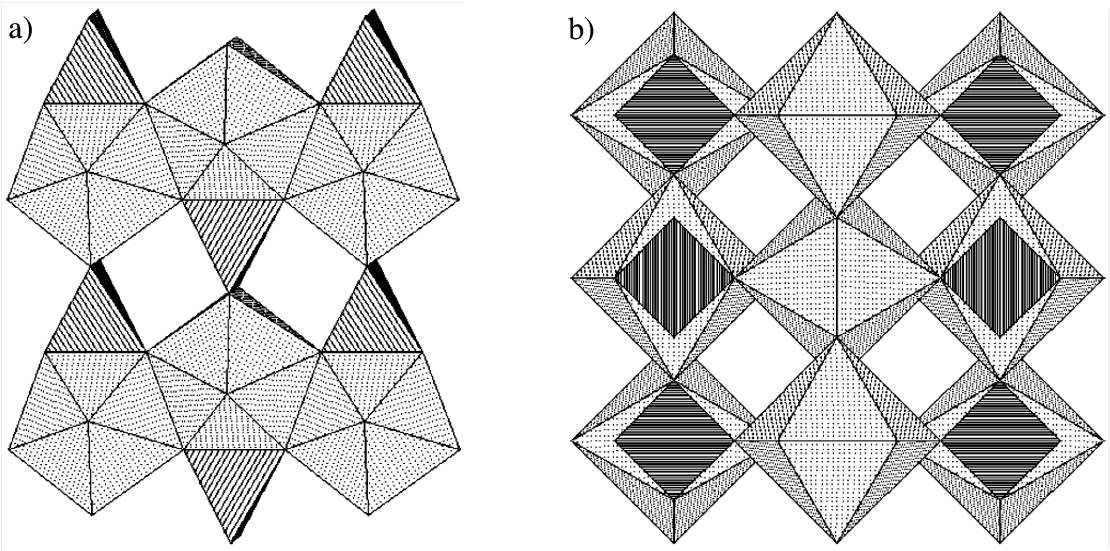

Figure 2.13. Zircon structure projected a) on (100), with *c* axis vertical and *b* axis horizontal; and b) on (001), showing view down the [001] channels. ZrO_8 dodecahedral are shaded light gray SiO_4 tetrahedral are stripped (from Finch and Hanchar 2003).

The O atom occupies a site with symmetry *m* in the zircon. The *y* and *z* coordinates of O atom are: $y = 0.066$, $z = 0.195$ (Hazen and Finger 1979; Finch and Hanchar 2003). Each O atom is coordinated in a planar array by one Si atom at 1.62 Å, and two Zr atom at 2.13 and 2.27 Å (Robinson et al. 1971; Hazen and Finger 1979), so that each Zr atom is coordinated by four O atoms at 2.13 Å and another four at 2.27 Å (Fig. 2.14).

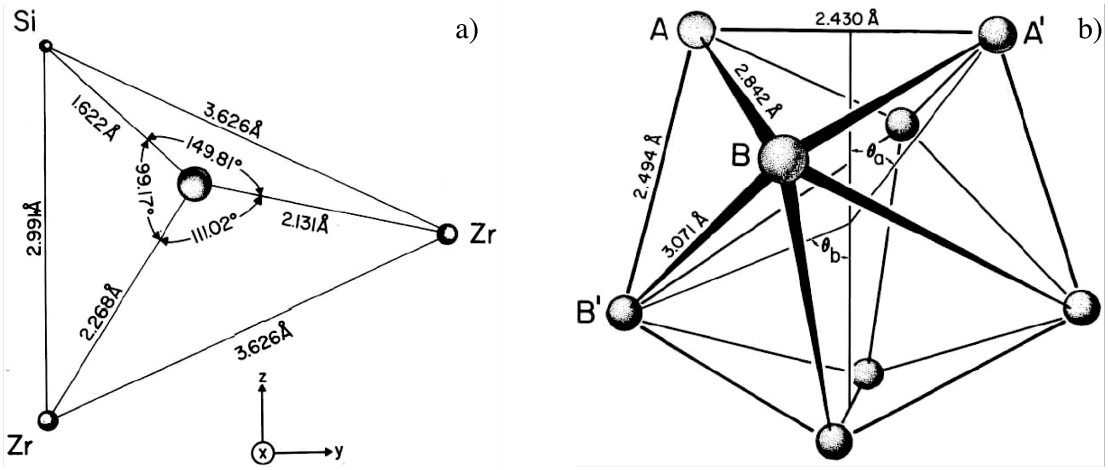

Figure 2.14. a) The coordination of O atom, showing with inter-atomic distances and angles; b) The *42m* symmetry of ZrO_8 triangular dodecahedron, showing with O-O distances. AA′, shares edge with SiO_4 tetrahedron, 2.43 Å; AB′, shares edge with ZrO_8 dodecahedron, 2.49 Å; AB, short unshared edge, 2.84 Å; BB′, longer unshared edge, 3.07 Å (from Robinson et al. 1971).

In zircon, the SiO_4 tetrahedron is tetragonal disphenoid elongated parallel to the *c* axis, while ZrO_8 dodecahedron can best be described as triangular dodecahedron. Both of them have site symmetry *42m*. For SiO_4 tetrahedron, the two O-O edges shared with the ZrO_8 dodecahedron are shorter (2.43 Å, opposite the small O-Si-O angle of 97.0°) than the two unshared edges (2.75 Å, opposite the larger O-Si-O angle of 116°) (Robinson et al. 1971; Hazen and Finger 1979). The repulsion between Zr and Si atoms across the shared edges are probably responsible for the elongation of the SiO_4 tetrahedron along the *c* axis. In the case of ZrO_8 dodecahedron, two edges are shared with SiO_4 tetrahedra, at 2.43 Å, and four with neighboring dodecahedra, at 2.49 Å. There are two sets of unshared edges, eight are shorter at 2.84 Å, and four are longer at 3.07 Å (Fig. 2.14b; Robinson et al. 1971). The ZrO_8 dodecahedron can be described as two interpenetrating ZrO_4 tetrahedral: one elongated along the *c* axis (ZrO_4^e), and the other compressed along the *c* axis (ZrO_4^c) (Fig. 2.15; Nyman et al. 1984; Finch and Hanchar 2003). The four short Zr-O bond distances are related to the

compressed ZrO_4^c tetrahedral, while the longer Zr-O distances are related to the elongated ZrO_4^e tetrahedral.

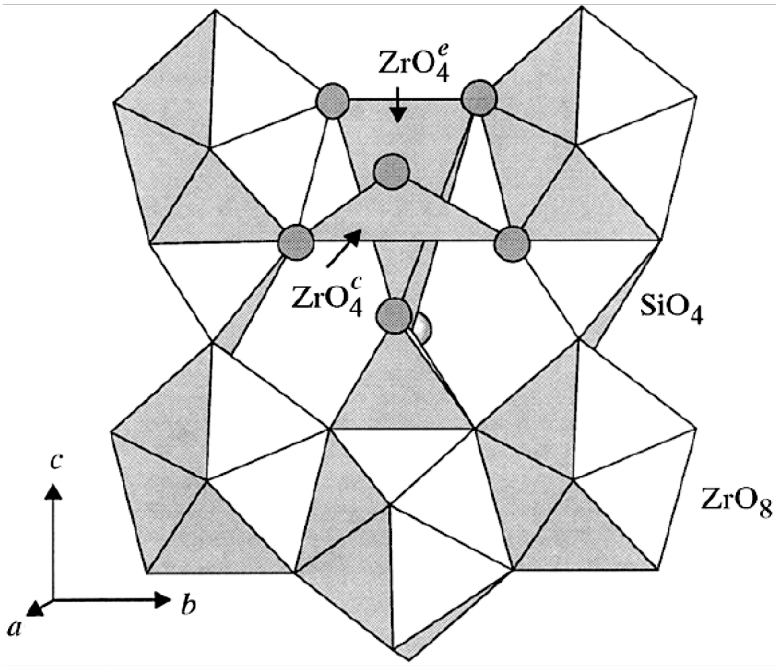

Figure 2.15. Zircon structure projected on (100), showing ZrO_8 dodecahedra composed of interpenetrating elongated ZrO_4^e and compressed ZrO_4^c tetrahedra (from Finch and Hanchar 2003).

There are two kinds of small voids in the zircon crystal structure running parallel to the *c* axis. One is a distorted six-coordinated octahedron that shares two faces with neighboring ZrO_8 dodecahedra and SiO_4 tetrahedra, respectively. It lies approximately 1.87 Å from two O sites and 2.08 Å from four O sites. The other one is a four-coordinated tetrahedron (Fig. 2.13b), adjacent to the octahedral void, sharing two faces with neighboring ZrO_8 dodecahedra. It lies 1.84 Å from four O sites (Finch and Hanchar 2003). These structural voids are potential interstitial sites that could incorporate impurities, providing that excess structural strain introduced by impurities incorporating into the voids is not too high. Generally, large cations, such as U, Th and REE, substitute Zr in the dodecahedral site, while smaller cations may be incorporated into the octahedral void (Váczi 2009). Si in the tetrahedral site can be

substituted by P (Hanchar et al. 2001) or four protons (Frondel 1953; Mumpton and Roy 1961).

2.2.2.2 Hydrogen defects in zircon

Naturally crystalline zircons are reported to generally contain water content of less than 0.01 wt% H_2O (Woodhead et al. 1991b; Nasdala et al. 2001; Bell et al. 2004). However, synthetic zircon (Trail et al. 2011) and latest investigation on natural igneous zircons (De Hoog et al. 2014) showed higher water content, up to 0.14 wt%. Zircon becomes metamict due to accumulation of radiation damage to the crystal caused mainly by alpha decay events of U and Th, which substitute for Zr during crystal growth. The radiation damage introduces point defects and expands the crystal lattice and decreases its crystallinity, finally producing an amorphous glass, which may be largely opened to the infiltration of secondary hydrous species (Woods et al. 1991b). By far, higher amounts of water in natural zircon has been observed in metamict zircon, with structural water up to 0.04 wt% (Woodhead et al. 1991a) and significant amounts of secondary water up to 16.6 wt% (Coleman and Erd 1961; Nasdala et al. 2001).

The nature of hydrous species, only OH^- or both OH^- and H_2O, existing in zircon, has been an early debated topic (Frondel 1953; Mumpton and Roy 1961; Caruba and Iacconi 1983; Lumpkin and Chakoumakos 1988). Nasdala et al. (2001) concluded that OH^- is probably the only way to incorporate hydrous species into zircon during primary growth, while in a second stage water can be incorporated either as OH^- or H_2O molecules. Systematic studies on zircons with varying degrees of crystallinity have been performed by Woodhead et al. (1991b) and Nasdala et al. (2001), and OH absorption features have been analyzed for crystalline, partially metamict, and largely metamict zircons, respectively (Fig. 2.16). OH bands around 3420 cm^{-1} (E // c), 3385 cm^{-1} ($E \perp c$), 3200 cm^{-1} ($E \perp c$), 3100 cm^{-1} ($E \perp c$) and very weak band around 3510 cm^{-1} (E // $c > E \perp c$) are commonly found in crystalline zircon with considerable variability. Partially metamict zircons can also exhibit sharp bands around 3420 cm^{-1}

(E // c), 3385 cm^{-1} (E ⊥ c) and a very weak band around 3510 cm^{-1} (E // c > E ⊥ c), but most commonly show broad peaks around 3400 cm^{-1} (E // c > E ⊥ c) and 3265 cm^{-1} (E ⊥ c > E // c). Metamict zircons show invariably an isotropic very broad band around 3400 cm^{-1}. It should be noted that sharp bands occurring in the range 3550-3700 cm^{-1} are generally related to hydrous species present in inclusions inside zircon (Fig. 2.16). The combination mode triplet around 2750 cm^{-1} (E // c) is considered a rough estimate of crystallinity of zircon: it is very weak or absent in spectra of metamict zircon, but exhibit the strong absorption for crystalline zircon.

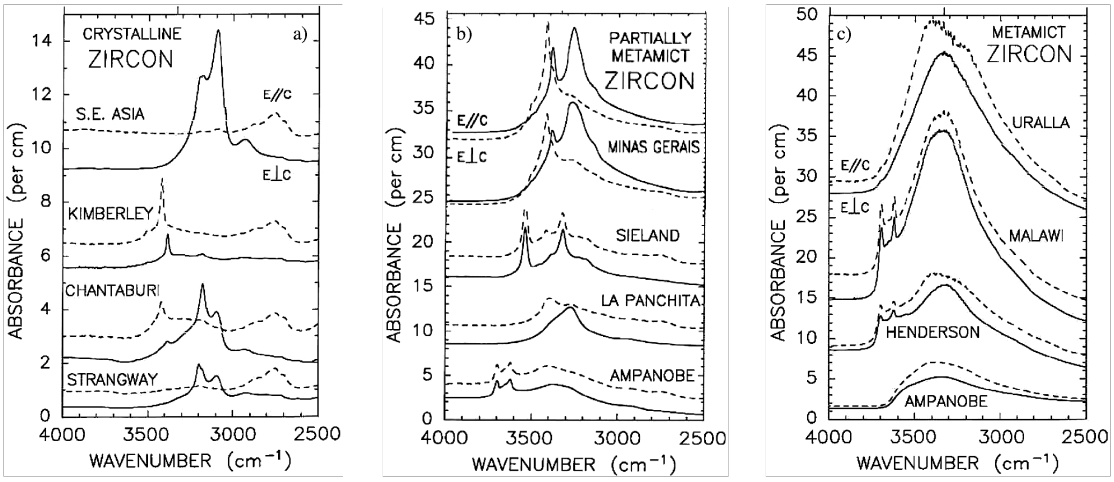

Figure 2.16. Polarized infrared spectra of zircon samples from different localities with a range of occurrences and structural states. a) crystalline zircons; b) partially metamict zircons; c) metamict zircons (modified from Woodhead et al. 1991b).

Several mechanisms have been suggested for the incorporation of H into crystalline zircon, however, the association between OH absorption bands and H incorporation mechanisms vary from one another (Woodhead et al. 1991b; Nasdala et al. 2001; Trail et al. 2011; Botis et al. 2013; Balan et al. 2013; De Hoog et al. 2014). It is partly due to the fact that assignment of OH bands is remains uncertain: It is usually based on the use of the empirical formulas correlating the OH frequency with the H bond (O-H···O) length (Libowitzky 1999), which is not initially made for it and can lead to strong misinterpretation (Ingrin et al. 2013). This approach does not consider

local relaxation around the defect, which can be high for instance in the case of substitution mechanisms.

Five mechanisms involving H incorporation into crystalline zircon have been proposed: 1) hydrogarnet substitution: $[V_{si}^{''''}4H^{\cdot}]^{x}$; 2) H substitution associated with Zr vacancy: $[V_{Zr}^{''''}4H^{\cdot}]^{x}$; 3) coupled substitution associated with trivalent cation replacing Si: $[M_{Si}^{'}H^{\cdot}]^{x}$; and 4) coupled substitution associated with trivalent cation replacing the Zr cation: $[M_{Zr}^{'}H^{\cdot}]^{x}$; and 5) incorporation of a small metal cation in the vacant octahedral site coupled with partial hydroxylation of neighboring vacant tetradron.

Hydrogarnet substitution

The hydrogarnet substitution was originally suggested by Frondel and Collette (1957) as the main mechanism for H incorporation in zircon to compensate for Si vacancies. Caruba et al. (1985) reported synthetic zircon samples, grown in a fluorinated environment, with up to 80% of the SiO_4 tetrahedral replaced by $(OH,F)_4$ groups, where the hydrogarnet substitution mechanism was suggested for the 3515 cm^{-1} band. However, since the band 3505-3515 cm^{-1} commonly occurs rarely and with very low intensity in natural zircon, it is concluded that, although possible, hydrogarnet substitution is probably not energetically favored. Nasdala et al. (2001) proposed a partial hydrogarnet substitution mechanism for the 3420 cm^{-1} band and fully one for the 3505-3515 cm^{-1} band, while Woodhead et al. (1991b) interpreted only the weak 3510 cm^{-1} band to be related to hydrogarnet substitution and 3420 cm^{-1} band to coupled substitution. In an *ab initio* study of zircon, Botis et al. (2013) found that hydrogarnet or partial hydrogarnet substitution would exhibit an IR band around 3420 cm^{-1}. While Balan et al. (2013) reported, from a first-principle study, that the bands at 3420 and 3385 cm^{-1} are associated with a fully protonated Si vacancy. The model of this kind of defect is shown in Figure 2.17, with the theoretical IR absorption bands (3427 cm^{-1} when E // c and 3387 cm^{-1} when $E \perp c$) in good agreement with the naturally observed bands. They also investigated two models of

composite hydrogarnet defects involving H and F atoms: $(OH)_3F$ model and OHF_3 model. The $(OH)_3F$ model leads to three absorptions bands, with one band at 3494 cm^{-1} (the corresponding OH approximately points to the fluoride ion; Fig. 2.18a) and two other bands at 3442 and 3364 cm^{-1} (the corresponding OH groups show H-bonding pattern similar to that observed in the hydrogarnet defect; Fig. 2.18a). The OHF_3 model results in one single band at 3554 cm^{-1} (Fig. 2.18b). Therefore, the consistency between the theoretical bands generated from the models of composite hydrogarnet defects and the band at 3515 cm^{-1} observed in a zircon synthesized in F-rich environment, leads to the suggestion that the naturally observed band at 3505-3515 cm^{-1} are associated with composite hydrogarnet defects involving H and F. Thus, the attribution of the band at 3200 cm^{-1} to hydrogarnet substitution proposed by Trail et al. (2011) is probably not appropriate.

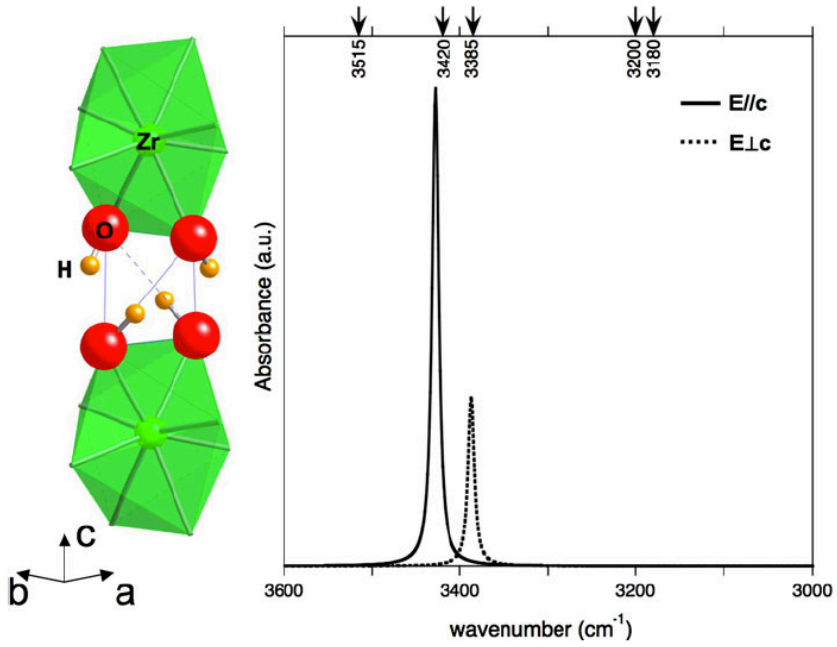

Figure 2.17. Theoretical model and theoretical IR absorption spectrum of hydrogarnet defects, $[V_{si}^{''''}4H^{\bullet}]^{x}$, in zircon (from Balan et al. 2013). The arrows indicate the major OH absorption bands found in natural and synthetic zircon.

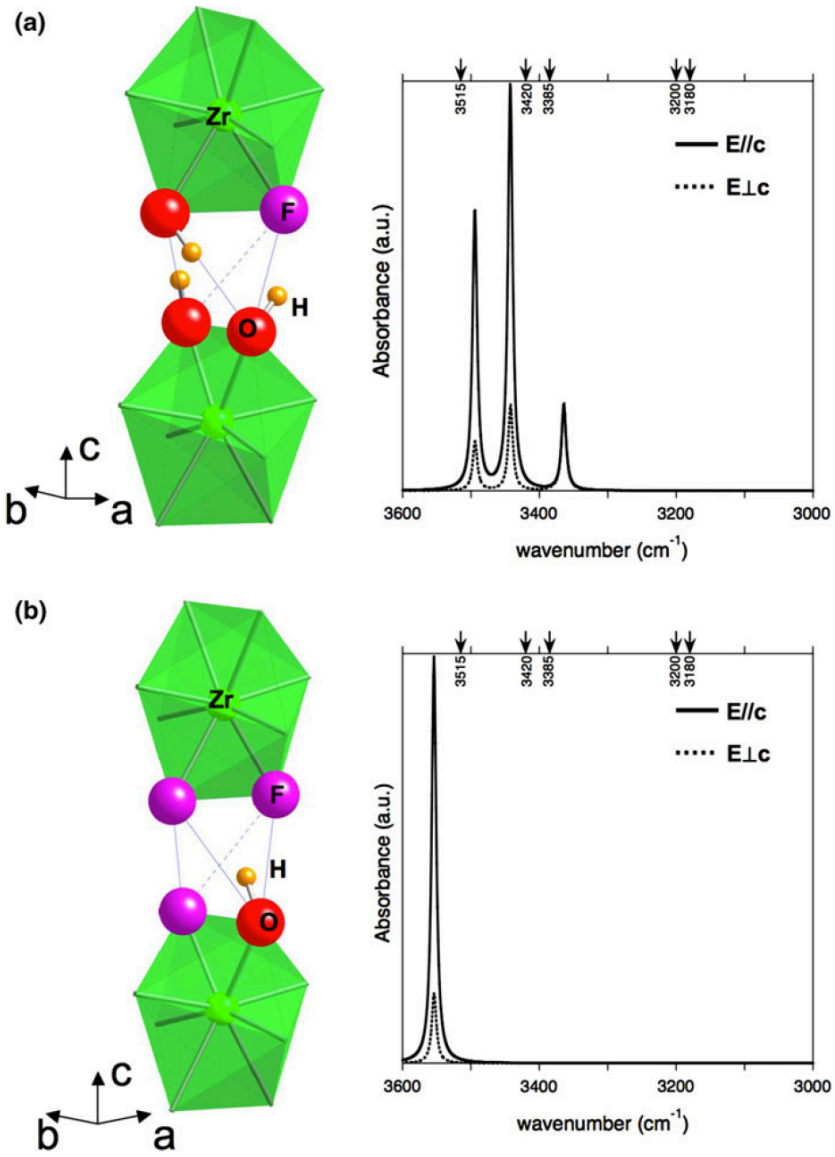

Figure 2.18. Theoretical models and theoretical IR absorption spectra of composite hydrogarnet defects involving H and F atoms in zircon. a) $(OH)_3F$ model; b) OHF_3 model (from Balan et al. 2013). The arrows indicate the major OH absorption bands found in natural and synthetic zircon.

H substitution associated with Zr vacancy

Defect of H associated with Zr vacancy has been earlier proposed by Nasdala et al. (2001) and Trail et al. (2011). However, the former employed this substitution to account for the 3180 cm^{-1} band, while the latter account for the bands at 3415 and 3385 cm^{-1} due to their lower robustness with annealing compared to the band at 3200

cm^{-1}, as well as the fact that the two different Zr-O bond distances would suggest two different frequencies for the OH. In their first-principle study of OH defects in zircon, Balan et al. (2013) investigated also H-defects associated with a Zr vacancy, $[V_{Zr}^{''''}4H^{\cdot}]^{x}$. Two models were proposed, the most stable one has its hydrogen atoms located on the equatorial oxygen atoms of the vacant Zr site and pointing to the apical oxygen atoms (Fig. 2.19). The corresponding absorption bands for this defect are at 3199 cm^{-1} ($E \perp c$) and 3212 cm^{-1} ($E // c$), of which the band at 3199 cm^{-1} is the most intense one (Fig. 2.19). Taking consideration of the similar spectroscopic properties of the band at 3200 cm^{-1} observed in synthetic zircons, the occurrence of this band in synthetic pure samples and its increase in Al-doped samples (Trail et al. 2011), they ascribed the band at 3200 cm^{-1} to fully protonated Zr vacancies.

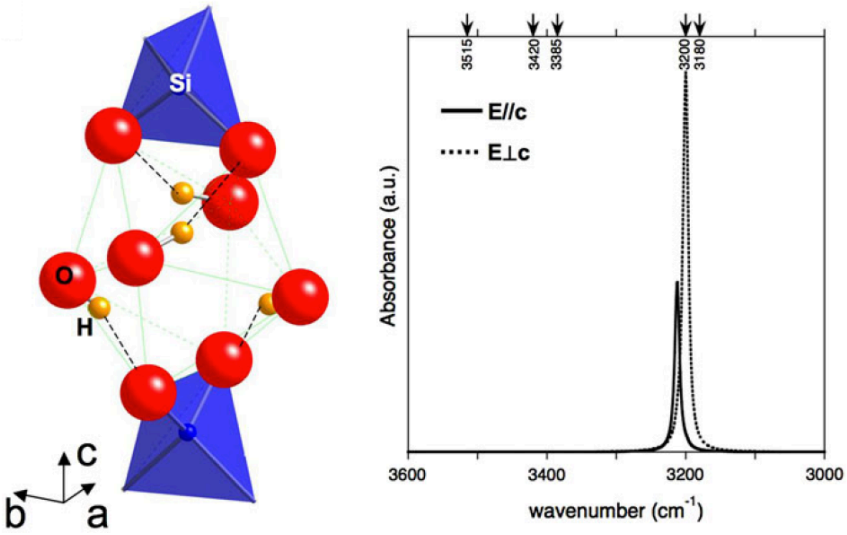

Figure 2.19. Theoretical model and theoretical IR absorption spectrum of a fully protonated Zr vacancies, $[V_{si}^{''''}4H^{\bullet}]^{x}$ (from Balan et al. 2013). The arrows indicate the major OH absorption bands found in natural and synthetic zircon.

Coupled substitution associated with a trivalent cation replacing Si

H-compensating trivalent substitution at Si sites has been proposed only by Botis et al. (2013) through the results of an *ab initio* calculation of OH absorption bands in

zircon. The authors suggested Al as a main candidate for trivalent substitution at Si sites and a $[Al_{Si}^{'}H^{\cdot}]^{x}$ defect would give rise to an OH absorption band at 3385 cm^{-1}.

Coupled substitution associated with a trivalent cation replacing Zr

H-compensated trivalent substitution at Zr site by far are the most prevailing mechanism mentioned in the literature, although several authors attributed varying OH bands to this mechanism. Y^{3+} and REE^{3+} are known to be the dominant trace elements in zircon substituting for the Zr cation, through the xenotime-type substitution, i.e., $[REE_{Zr}^{'}P_{Si}^{\cdot}]^{x}$ (Speer 1980; Finch et al. 2001). In the case of P not in enough concentration to balance charge deficiency, H could play an important role in maintaining charge neutrality. From an ab inito study of OH absorption bands in zircon, Botis et al. (2013) proposed two positions for a charge compensating H, one at the center of a neighboring void of substituted M^{3+} cation and one at the next nearest void. The calculated OH bands for these two configurations are around 3200 cm^{-1} (H close) and 3100 cm^{-1} (H far), respectively. Hoog et al. (2014) observed a large REE excess, around the same amount as H, in addition to those charge compensated by the xenotime-type substitution. These authors concluded that the broad bands located at 3200 and 3100 cm^{-1} in the IR spectra are associated with this kind of substitution mechanism. However, other OH bands have been already attributed to this substitution, including the band at 3385 cm^{-1} (Nasdala et al. 2001) and bands at 3420, 3385 and 3270 cm^{-1} (Woodhead et al. 1991b).

Coupled substitution involving partial hydrogarnet substitution

The substitution mechanism, involving a small metal cation in the vacant octahedral site coupled with a partial hydroxylation of the neighboring vacant tetradron, was suggested only as a possible means of incorporating H by Woodhead et al. (1991b). However, no OH band assignment has been proposed for such substitution.

2.2.2.3 Diffusion in zircon

Numerous studies have been performed to quantify and characterize diffusion in zircon due to its wide range of geochemical application, but studies are mostly limited to cations, oxygen and helium diffusion. To our knowledge no kinetics data involving hydrogen diffusion in zircon have been reported.

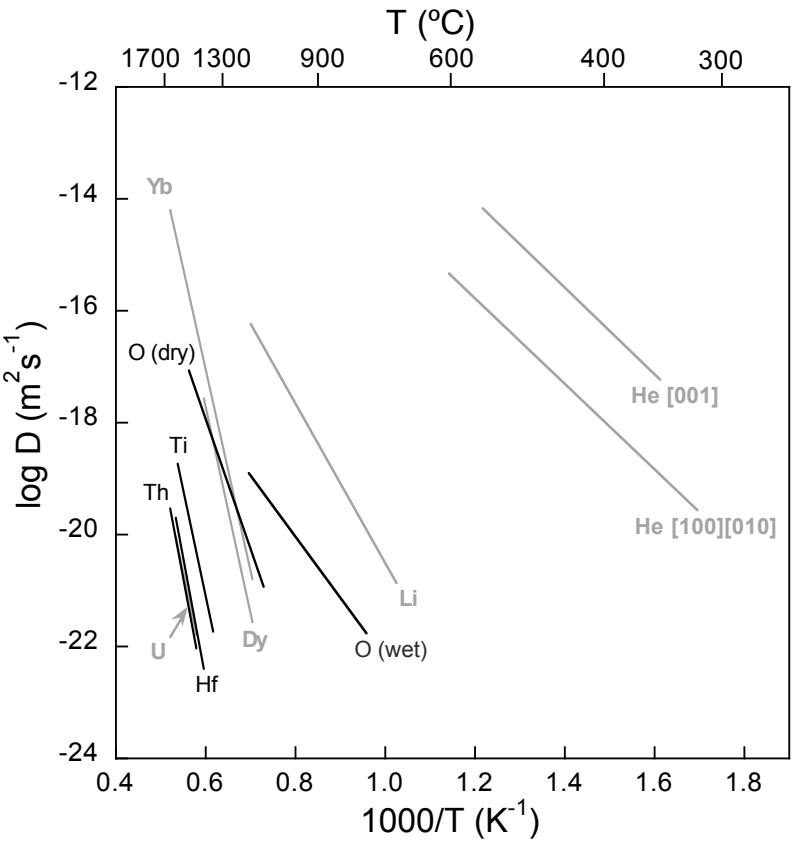

Figure 2.20. Compilation of cations, oxygen and helium diffusion laws in zircon (Li: Cherniak and Watson 2010; He: Cherniak et al. 2009; others: Cherniak and Watson 2003).

Cations and oxygen diffusions in zircon have been shown to exhibit very sluggish kinetics and much higher activation energies compared to other NAMs (Cherniak 1995; Cherniak 1997; Cherniak et al. 1997a, 1997b; Cherniak and Watson 2001; Farver and Yund 1991; Watson and Cherniak 2000, 2002; Fig. 2.10). For example, diffusion of tetravalent cations (Hf, Th and U) shows activation energies around 800

kJ/mol and an upper limit value of diffusivity of 10^{-19} m^2/s at 1600 °C (Hf diffusion). For cations of the same charge, diffusivities increase with decreasing ionic radius. All the cations diffusion in zircon shows isotropic properties. Vacancy mechanism is assumed to be the dominant mechanism. Oxygen diffusion in zircon, with isotropic properties, exhibits two diffusion laws when in absence and in presence of water in the system. Enhanced diffusivity and lower activation energy was found for oxygen diffusion under hydrothermal conditions compared with dry conditions (Fig. 2.20). It was proposed that under dry conditions O diffuse through a vacancy mechanism, while it is through H_2O molecules under hydrothermal conditions (Cherniak and Watson 2003).

Li diffusion exhibit faster diffusivity and lower activation energy compared with other cations in zircon. Since Li signatures will be moderately preserved in zircon at mid-crustal metamorphic temperatures, Li isotopes has been employed to study mineral-fluid interactions at the Earth's surface, to trace process of aqueous alteration and weathering, and as indicator of incorporation of surface-derived material into crustal magmas (Cherniak and Watson 2010; Tomascak 2004; Teng et al. 2004).

He diffuses anisotropically in zircon with fast diffusion directions along *c* axis through an interstitial mechanism (Farley 2007; Reich et al. 2007; Cherniak et al. 2009). The anisotropy is a result of *c*-parallel through-going channels or "pipes" in the structure. Low and comparable activation energies were reported around 147 kJ/mol for directions parallel and perpendicular to the *c* axis. He has been used as a low-temperature chronometer due to its fast diffusivity and consequent low closure temperature.

Chapter 3

Theory and application of diffusion

Diffusion is the fundamental and the only process through which particles (atoms, ions or molecules) move from one location to another within or through a crystalline solid. Diffusion is due to thermally activated atomic-scale random motion of particles in minerals. Looking at diffusion from the atomistic point of view can favor an explanation of the underlying diffusion mechanism. Here the mineral is considered a continuum without a discrete atomic structure. The basic concepts and the application to our experimental approach to hydrogen in minerals will be presented in this chapter.

3.1 Theory of diffusion

3.1.1 Fick's first law

During investigation of diffusive mass transport, the German physiologist Adolf Fick recognized in 1855 the analogy between diffusion and heat transfer by conduction and successfully applied Fourier's law of heat conduction to describe diffusion. Fick proposed that the diffusive flux is proportional to the concentration gradient.

Atomic diffusion in minerals is induced by a driving force, such as chemical potential gradient, temperature gradient, etc. Among them, the chemical potential gradient is the most common driving force occurring in solid earth sciences. When a chemical potential gradient of a component i, $(d\mu/dx)_i$,is present in a crystal, atoms move from one region to another to equilibrate μ and to reduce the Gibbs free energy of the system. The resulting variation due to $(d\mu/dx)_i$ is directly proportional to the concentration gradient, $(dC/dx)_i$, if the activity a_i is proportional to C_i (the activity coefficient r_i is assumed constant in the crystal; see for instance Brady 1993; Doremus 2002). In the case, of gradients involving diluted species or isotopes, without any

applied external forces, the rate of transfer of the diffusing atoms through a unit area of a given plane is only proportional to the gradient of concentration across that plane. This relationship is referred to as "Fick's first law":

$$J = -D\frac{\partial C}{\partial x} \tag{3.1}$$

where the flux J (kg/m^2.s) is the net flow of particles passing through a unit area in unit time, D (m^2/s) is the diffusion coefficient of the diffusing species, C (kg/m^3) is the concentration of the diffusing species, x is the distance (m), $\partial C/\partial x$ is the concentration gradient, and the negative sign indicates that the direction of the diffusive flux is opposite to the direction of the concentration gradient (the diffusive flux goes from high to low concentration).

This is for the case under steady state conditions, where the flux in each point doesn't change with time. However, most of the diffusion processes are under non steady state conditions with the flux in each point varying with time. Then Fick's second law applies.

3.1.2 Fick's second law

Generally, under non steady-state conditions, the flux in each point varies with time (Fig. 3.1). Assuming the flux is one-dimensional along the x direction. During time t, the mass variation in the volume, with thickness of dx and area of S, equals the flux into the volume from the left side (J_xS) minus the flux out of the volume from the right side ($J_{x+dx}S$) (Fig. 3.1):

$$\frac{\partial C}{\partial t}Sdx = J_xS - J_{x+dx}S = -\frac{\partial J_x}{\partial x}Sdx \tag{3.2}$$

where J_x is the flux along x direction. Hence,

$$\frac{\partial C}{\partial t} = -\frac{\partial J_x}{\partial x} \tag{3.3}$$

Combining this equation with Fick's first law leads to Fick's second law:

$$\frac{\partial C}{\partial t} = \frac{\partial}{\partial x}(D\frac{\partial C}{\partial x}) \tag{3.4}$$

In this general law, the diffusion coefficient is a function of concentration. If the concentration of the diffusing species is extremely small or for isotopic diffusion, the diffusion coefficient can be considered independent of the concentration. Then, the above equation can be simplified to:

$$\frac{\partial C}{\partial t} = D\frac{\partial^2 C}{\partial x^2} \tag{3.5}$$

Since the hydrous defect concentrations in garnet and zircon crystal lattice are in trace amounts, it is assumed in this study that D is independent of concentration.

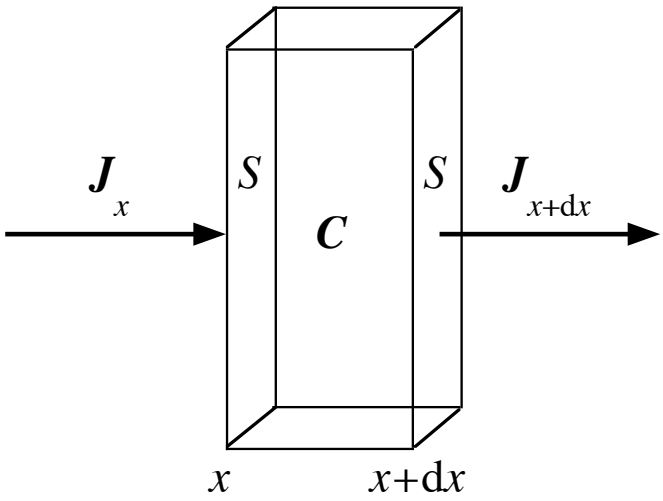

Figure 3.1. Diagram of flux into and out of an element volume. The flux is one dimensional, along the x axis from left to right. The flux at x is J_x while at $x + dx$ is J_{x+dx}.

3.1.3 Microscopic view of diffusion

From the atomistic point of view, diffusion is considered as a result of the random walk of the diffusing particles (atoms, ions or molecules) among sites in the crystal structure. The trajectories they follow involve a series of discrete jumps, and it is generally assumed that each jump is uncorrelated with the previous one. Considering

two adjacent parallel crystallographic planes along x axis, 1 and 2, at distance d apart (Fig. 3.2). Assuming n_1 and n_2 the atoms per unit area in plane 1 and 2, respectively. If the jump frequency of atom under a certain temperature is Γ and the probability for atom to successfully jumps from any particular site on plane 1 to a neighboring site on plane 2, or from plane 2 to plane 1 is P, then the net atom flux from plane 1 to plane 2 is:

$$J = (n_1 - n_2)P\Gamma \tag{3.6}$$

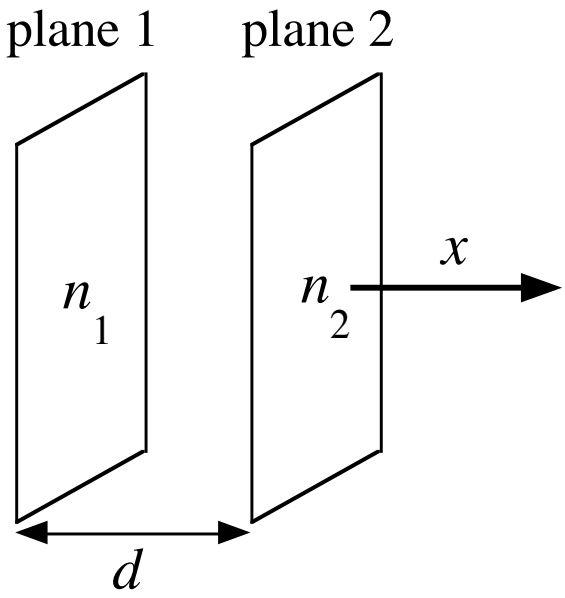

Figure 3.2. Atomic jumps between two crystal atomic planes along one dimension in a mineral. The distance between the crystal plane is d.

Since $n_1 = C_1 d$ and $n_2 = C_2 d$ where C_1 and C_2 are the concentrations of atoms on plane 1 and 2, then

$$J = (C_1 - C_2)dP\Gamma = -d^2 P\Gamma \frac{\partial C}{\partial x} \tag{3.7}$$

Comparing above equation with Fick's first law, we have

$$D = d^2 P\Gamma \tag{3.8}$$

where P, d depends on crystal structure, Γ relates also closely to temperature besides crystal structure. Equation (3.8) provides a basis for the atomic treatment of diffusion coefficient. It establishes the relationship between diffusion coefficient and atomic jump frequency, atomic jump probability as well as crystallographic parameter.

3.2 Various kinds of diffusion

According to diffusion medium involved, thermally activated diffusion can be classified as volume diffusion and grain-boundary diffusion. In present study, only volume diffusion through the crystal lattice is considered.

According to diffusion species, thermally activated diffusion can be classified as self-diffusion (or tracer diffusion) and chemical diffusion (or interdiffusion).

Self-diffusion refers to diffusion of an intrinsic stoichiometric component in the crystal where there is no chemical potential gradient in terms of elemental composition. Generally, the isotope of the component to be studied is introduced into the crystal in order to deduce its self-diffusion coefficient. It is named a tracer diffusion, which is usually assumed to be identical to self-diffusion (assuming no significant isotopic effect). The tracer can be a radioactive or a stable isotope. In this case, the chemical potential gradient presents only in isotopes. The difference in diffusivities of different isotopes is very small (e.g., Richter et al. 2008; Ingrin and Blanchard 2006). For instance, diffusivity of hydrogen is about 1.4 times greater than diffusivity of deuterium, thus, as an approximation, diffusivities of hydrogen and deuterium are considered the same. Hence, hydrogen isotope diffusivities in NAMs and hydrous minerals, obtained by hydrogen-deuterium exchange experiments, are regarded H diffusion through the crystal lattice of the mineral, independently of the original concentration of H impurities in the mineral.

Chemical diffusion refers to diffusion of a species in the crystal where there is chemical potential gradient in major and minor components. It concerns binary diffusion (or interdiffusion), multispecies diffusion and multicomponent diffusion. In the present study, only interdiffusion is involved. Interdiffusion refers to two diffusion

species with different diffusivities move oppositely in a binary system due to the chemical potential gradient (such as Fe-Mg diffusive change in olivine). The effective diffusion of hydrogen determined from H-extraction/incorporation experiments corresponds to interdiffusion between either protons and polarons or protons and vacancies. The relationship between the measured effective diffusivity and the individual diffusivities of the species is governed by the specific reaction involved (see for instance, Kohlstedt and Mackwell 1998). It may depend on the type of H-defects within the crystal (see for instance, Padrón-Navarta et al. 2014).

3.3 Thermodynamics of diffusion

3.3.1 Diffusion mechanism

Diffusion in a crystalline solid refers to jumps of particles (atoms, ions or moleculars) from one crystallographic site to an adjacent one. It proceeds through imperfections in the crystal structure, such as point defects. Point defects can be present in the form of vacancies, interstitials or substituted impurity ions.

In the case of lattice diffusion, referring to atomic diffusion within a crystalline solid, three general kinds of mechanisms have been proposed (Putnis and McConnell, 1980; Mehrer 2007), among which the vacancy mechanism and the direct interstitial mechanism are the most prominent by far.

1) Exchange mechanism

This is a collective mechanism, which involves two neighboring lattice atoms directly exchanging their positions (case a in Fig. 3.3). In a crystalline solid this mechanism will introduce large distortions to squeeze the atoms through, therefore, making this process energetically unfavorable. In general, the ring mechanism, referring to rotation of three or more atoms as a group by one atom distance, requires less lattice distortion than direct exchange (case b in Fig. 3.3). However, this mechanism involves much more atoms moving simultaneously, making it more complex and unlikely for most crystalline solids.

2) Vacancy mechanism

Atom diffuses by jumping from a lattice site to a neighboring vacant lattice site, when enough vacancies are available through the crystal lattice and/or vacancy mobility is large enough (case c in Fig. 3.3). This mechanism has been regarded as the most important diffusion mechanism for the matrix atoms and substitutional atoms in metals.

3) Interstitial mechanism

Atom diffuses by jumping directly from one interstitial site to another of its neighboring interstitial site without introducing much local strain, if the diffusing foreign atom has a smaller size than the inter-lattice space, such as H diffusion in NAMs. This is called a direct interstitial mechanism (case d in Fig. 3.3). When the interstitial atom is of similar size than the lattice atom or is exactly the same, self-interstitial, diffusion may proceed through the interstitialcy mechanism (or indirect interstitial mechanism): the interstitial atom replaces a neighbor lattice atom which will be kicked out into adjacent interstitial site (case e in Fig. 3.3).

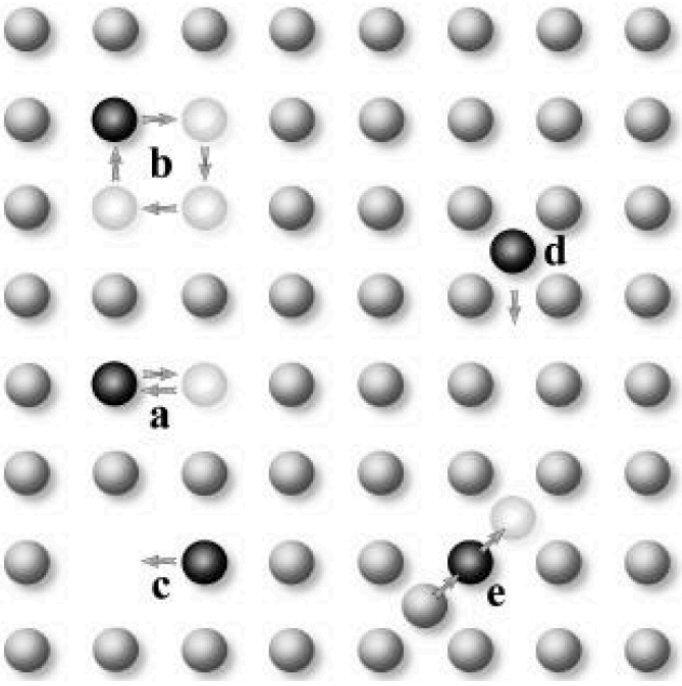

Figure 3.3. Schematic representation showing main diffusion mechanisms: a) direct exchange; b) ring exchange; c) vacancy exchange; d) direct interstitial exchange; e) indirect interstitial exchange (from Kurka 2005).

3.3.2 Diffusion law - Arrhenius law

As a thermally activated process, diffusion generally shows a strong temperature dependence. It is generaly described by an Arrhenius law:

$$D = D_0 \exp(-\frac{E_a}{kT}) \tag{3.9}$$

where D_0 is the pre-exponential factor (m^2/s), E_a is the activation energy of diffusion (kJ/mol), k is the Boltzmann constant (8.31 kJ/mol.K), t is the absolute temperature (K). The above equation can be rewritten as:

$$\ln D = \ln D_0 - \frac{E_a}{R} \cdot \frac{1}{T} \text{ or } \log D = \log D_0 - \frac{E_a}{2.3R} \cdot \frac{1}{T} \tag{3.10}$$

Therefore, a plot of ln$D$ versus 1/T or log$D$ versus 1/T should give a straight line, where the activation energy E_a and the pre-exponential term D_0 can be estimated from the slope and the intercept of the line, respectively.

Even if the Arrhenius law for atomic diffusion is essentially empirical, it has a theoretical justification from the microscopic analysis of diffusion, as we will see below.

To jump from one crystallographic position to another, particles need energy to break inter-atomic bonds with neighbors (that is energy barrier) and to cause the necessary lattice distortions during jump. The energy necessary for motion is called the activation energy of migration. The average thermal energy of an atom is usually smaller than the activation energy of migration and a large fluctuation in energy is needed for a jump. Generally, only atoms possessing energy higher than the activation energy can jump.

Let us consider an interstitial atom diffusing through an interstitial mechanism in a crystalline solid. Assuming that the number of the neighboring interstitial sites around the interstitial atom (coordination number) is z and the frequency for the atom vibrating toward one of the interstitial sites is ν, then the probability of such fluctuation or jump frequency Γ can be expressed as:

$$\Gamma = \nu z \exp(-\frac{\Delta G}{kT}) \tag{3.11}$$

where ΔG is the Gibbs free energy of activation. It should be noted that, since the amount of interstitial atoms is far less than the amount of interstitial sites in a crystal, all the neighboring interstitial sites around an interstitial atom can be considered vacant. Combining the above equation with $D = d^2 P\Gamma$ leads to:

$$D = d^2 P\nu z \exp(-\frac{\Delta G}{kT}) = d^2 P\nu z \exp(\frac{\Delta S}{k})\exp(-\frac{\Delta H}{kT}) \tag{3.12}$$

where ΔS and ΔH are the entropy and enthalpy of migration, respectively. Let

$$D_0 = d^2 P\nu z \exp(\frac{\Delta S}{k}) \text{ and } E_a = \Delta H$$

then equation (3.12) is simplified to equation (3.9). D_0 is related to the crystal structure, jump frequency and jump distance.

Now weconsider an atom located at a lattice site diffusing to one of its neighboring vacancies through a vacancy mechanism. The opportunity to find the right vacancy at the right moment is more difficult than to jump to an interstitial site, since the probability of occurrence of vacancy around an atom is rather small, the atom cannot carry out a new jump until a new vacancy move to its vicinity. Assuming the coordination number of the atom is z, the probability of occurrence of a vacancy around the atom, n_v/N, with n_v the number of vacancies and N the bulk number of atoms in the crystal, can be expressed as:

$$\frac{n_v}{N} = \exp(-\frac{\Delta G_v}{kT}) = \exp(\frac{\Delta S_v}{k})\exp(-\frac{\Delta H_v}{kT}) \tag{3.13}$$

where ΔG_v, ΔS_v and ΔH_v are the Gibbs free energy, the entropy and the enthalpy of vacancy formation, respectively. Assume the frequency for the atom vibrating toward one of its neighboring vacancies is ν, then the jump frequency Γ can be expressed as:

$$\Gamma = \nu z \exp(\frac{\Delta S_v + \Delta S}{k})\exp(-\frac{\Delta H_v + \Delta H}{kT}) \tag{3.14}$$

Combining the above equation with $D = d^2 P\Gamma$ leads to:

$$D = d^2 P\nu z \exp(\frac{\Delta S_v + \Delta S}{k}) \exp(-\frac{\Delta H_v + \Delta H}{kT}) \quad (3.15)$$

Let

$$D_0 = d^2 P\nu z \exp(\frac{\Delta S_v + \Delta S}{k}) \text{ and } E_a = \Delta H_v + \Delta H$$

then equation (3.15) can be expressed also by equation (3.9).

Therefore, whatever the mechanism, interstitial or vacancy mechanism, through which particles diffuse in a crystalline solid, the Arrhenius law always stands, the correlation between diffusion coefficient and activation energy is the same. The activation energy can show different values depending on the involved diffusion mechanism, which gives an indication on the nature of the diffusion process.

With exponential relationship with temperature, the diffusion coefficient increases drastically with increasing temperature. This is because the higher the temperature is, the greater the vibration energy of atoms is. Consequently, the jump frequency for atoms through fluctuation in energy increases. Besides, the concentration of vacancies increases with increasing temperature, which also favors the diffusion of atoms through a vacancy mechanism.

3.3.3 Influential factors for diffusion

In addition to temperature, there are others factors affecting diffusion coefficient, such as pressure, crystal structure, chemical composition, crystal defects, oxygen fugacity and so on.

Pressure

The dependence of diffusion coefficient on pressure, at least for pressures available in laboratory devices, is far less strong than that on temperature. Usually, the diffusion coefficient decreases with pressure not more than a factor of ten for pressures of 1 GPa (Mehrer 2007).

Crystal structure

The crystal structure can be a rough reflection of the atomic packing density. The less closely packed the atoms are, the more "open space" there is in the crystal structure. Diffusion is through random walks of particles. Therefore, a diffusing species is expected to move more rapidly if there is more "open space" present in the crystal, and vice versa. Based on this concept, the dependence of diffusivity on ionic porosity, a direct measure of the "open space" in a mineral, has been suggested by many authors (Dowty 1980; Zhao and Zheng 2007). The ionic porosity of a mineral is defined as the unoccupied volume divided by the total volume. Moreover, the more closed packed the atoms are, the shorter will be the mean atomic spacing in crystals and hence the stronger will be the average M-O bonds. This will enhance the energy barrier to exceed for diffusion, leading to higher activation energy (Brady and Cherniak 2010).

Theoretically, crystallographic anisotropy may result in diffusion anisotropy, which is consistent with the effect of ionic porosity on diffusivity. If the ionic porosity is different for different crystallographic orientations, then diffusion along the orientation with the greatest ionic porosity should be the fastest. In a compilation of anisotropy data for diffusion of various elements in minerals, many of the data with significant anisotropy are found for diffusion of oxygen, suggesting that larger species may be more subjected to diffusion orientation (Brady and Cherniak 2010).

3.4 Analytical solutions for diffusion

Therefore it is essential to control the experiment environment (i.e., temperature, pressure, oxygen fugacity, water fugacity), to study the effect of one variable at the same time. Two kinds of experiments can be performed to get the diffusion coefficient: bulk exchange (using mineral powders) and single crystal experiments. Only the latter one will be briefly described here.

Before starting the diffusion experiments, the single crystal will be cut and polished to get thin slices or cubic crystal, typically with specific crystallographic orientations. Then the sample will be placed with a surrounding gas phase, solution or

fine-grained source, or as a thin-film coating the surface (Farver 2010). Depending on the pressure needed, the experiments can be done at ambient pressure in a furnace, or at elevated pressure using cold-seal pressure vessels, piston cylinder or multi-anvil apparatus. There are two kinds of annealing: sequential annealing and annealing for only one time to get a profile (Ingrin and Blanchard 2006). For the former, there are a series of annealing steps. After each step, the tracer concentration of the thin slices is measured. For the latter, there is only one annealing step, with time long enough to get a full profile. After the annealing, a thin slice is cut from the middle of the cubic crystal and the tracer concentration profile is measured. For H diffusion, concentration is measured most frequently by Fourier Transform Infrared rarely by Spectrometry (FTIR), Secondary Ion Mass Spectrometry (SIMS), or Nuclear Reaction Analysis (NRA).

For samples with a plate shape and a small ratio of thickness to lateral sizes, unidirectional diffusion can be assumed. Solutions of Fick's second law are used to fit the experimental measurements for different geometries and boundary conditions (Carlaw and Jaeger 1959; Crank 1975). Let us consider that the diffusion coefficient is not a function of the concentration. For a semi-infinite solid, with a homogeneous initial concentration C_0 and constant surface concentration C_1 (infinite, well-mixed reservoir), the diffusion profile along the direction x (perpendicular to the surface) can be fitted by the solution:

$$\frac{C_{(x,t)} - C_0}{C_1 - C_0} = 1 - erf\left(\frac{x}{2\sqrt{Dt}}\right) \tag{3.16}$$

where $C_{(x,t)}$ is the concentration at time t and at a distance x from the surface, t is the duration of the annealing, D is the diffusion coefficient, and erf is the error function.

For the present study, our sample slices can be compared to a solid with a homogeneous concentration C_0 bounded by two infinite parallel planes (with thickness 2L), and a constant surface concentration C_1 (continuous flux of gas with constant composition), then equation (3.16) becomes (Ingrin and Blanchard, 2006):

$$C_{(x,t)} = \frac{4C_0}{\pi}\sum_{n=0}^{\infty}\frac{(-1)^n}{2n+1}\exp\left(\frac{-D(2n+1)^2\pi^2 t}{4L^2}\right)\cos\left(\frac{(2n+1)\pi x}{2L}\right) \qquad (3.17)$$

The boundary conditions for the sequential hydrogen-deuterium exchange experiments in present study are the following (Fig. 3.4): For OH species, x = -L, L, C = 0, at any t; -L < x < L, $C = C_0$, at $t = t_0$; -L < x < L, $C = C$ (x, t), at $t > t_0$.

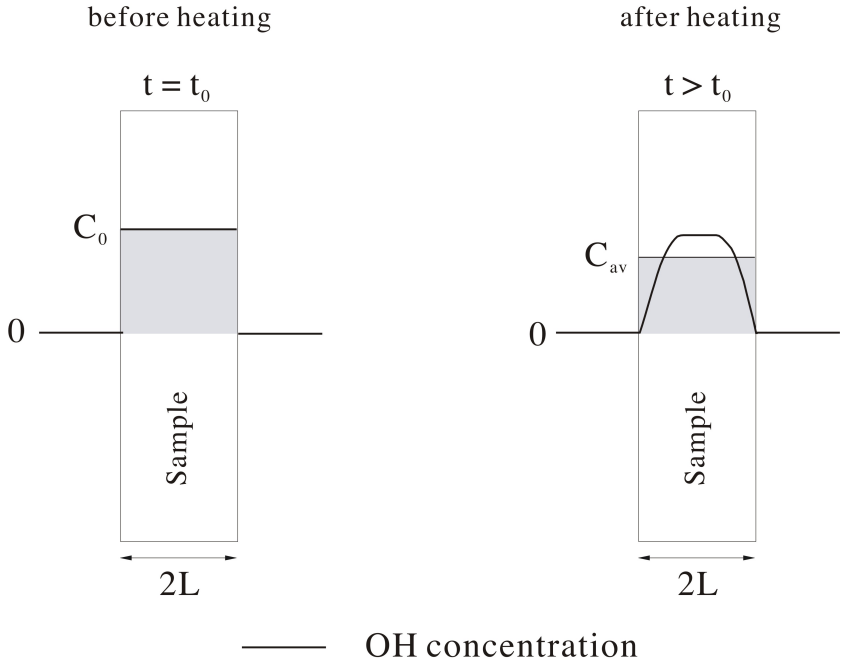

Figure 3.4. Schematic diagram of the boundary conditions for OH species during hydrogen-deuterium exchange experiment in the present study (modified after Kurka 2005).

Since it is the average concentration $C_{av(t)}$ across the whole sample thickness that is deduced from the IR absorption measurements; for the decreasing OH species, the integration of equation (3.17) from –L to L gives $C_{av(t)}$:

$$\frac{C_{av(t)}}{C_0} = \frac{8}{\pi^2}\sum_{n=0}^{\infty}\frac{1}{(2n+1)^2}\exp\left(\frac{-D(2n+1)^2\pi^2 t}{4L^2}\right) \qquad (3.18)$$

$C_{av(t)}$ corresponds to the measured absorbance for progressive annealing time, D is the diffusion coefficient, t is the cumulative duration of the experiment. The approximation of equation (3.18) is:

$$\frac{C_{av(t)}}{C_0} = \frac{8}{\pi^2}[\exp(-\frac{\pi^2 t}{4L^2}D) + \frac{1}{9}\exp(-\frac{9\pi^2 t}{4L^2}D) + \frac{1}{25}\exp(-\frac{25\pi^2 t}{4L^2}D) + \ldots] \quad (3.19)$$

The above series is rapidly convergent and the contribution of the fourth exponential term contributes to less than one percent of the total value. We have calculated the series up to the eighth term, thus the value obtained should be far enough precise.

For the increasing OD species during H-D exchange, the following equation is used:

$$\frac{C_{av(t)}}{C_s} = 1 - \frac{8}{\pi^2}\sum_{n=0}^{\infty}\frac{1}{(2n+1)^2}\exp(\frac{-D(2n+1)^2\pi^2 t}{4L^2}) \quad (3.20)$$

C_s corresponds to the absorbance of OD of the sample saturated with deuterium, i.e. the last deuteration step when the H-D exchange reaction has reached to an equilibrium, and $C_{av(t)}$ corresponds to the measured absorbance for progressive annealing time.

The diffusion coefficient D was determined by fitting numerically the relative concentration C/C_0 and C/C_s versus t for the decreasing and increasing species respectively, where C/C_0 is the ratio of integral absorbance A/A_0 (acquired from the results of FTIR measurements) and C/C_s the ratio of A/A_s, considering only the defects available for the exchange (see later comments). It was assumed in this study that the diffusion coefficient does not change with concentration of OH species. As shown in previous diffusion studies (Ingrin and Blanchard 2006) hydrogen diffusion in garnets is isotropic, we assume the same is true for H-D exchange in andradite.

Chapter 4

Experimental, analytical methods and samples

4.1 Experimental methods

4.1.1 Annealing procedures

In the case of diffusion studies in laboratory though H-D exchange, the duration of experiments need to be feasible at a scale of a thesis. The temperature of the experiments should not be too low for a sample of required thickness (which will lead to very low kinetics and too long time of experiments). Thus the lower limits of the temperatures were set at 400 °C for andradite garnet and 900 °C for zircon, the kinetics of andradite are faster than those of zircon. An upper limit of the temperature is also defined by the minimum time of annealing possible to achieve with a sufficient resolution (duration of the annealing step compared to the time to reach the final temperature). Some limitations can also happen due to the occurrence of concurrent reactions such as hydrogen extraction or decomposition of sample that may occur under higher temperatures. Therefore, the higher limits of temperature are set at 700 °C for andradite and 1150 °C for zircon. Concurrent extraction for andradite happened above 800 °C (Kurka 2005). There is no well-defined temperature for the beginning of decomposition for zircon. A temperature range from 1400 °C to 2000 °C was compiled for zircon decomposition by Peña and de Aza (1984) and Kaiser et al. (2008).

Stepwise annealing experiments, with temperature ranging from 400 to 700 °C for andradite and 800 to 1050 °C for zircon, were carried out in a horizontal furnace with lanthanium chromite heating elements at ambient pressure. The sample was placed in an alumina tube of 18 mm internal diameter located few mm away from the Pt/Pt-$Rh_{10\%}$ thermocouple (Fig. 4.1). The uncertainty in temperature due to gradients in the furnace, fluctuation in room temperature, and uncertainty in the thermocouple measurement is estimated to less than 5 K.

To conduct the H-D (D replacing H) and D-H (H replacing D) exchange experiments, the furnace was continuously flushed with a gas mixture of $Ar_{(90\%)}/D_{2(10\%)}$ flowing through deuterated water (99.9% D_2O, Sigma-Aldrich) and with a gas mixture of $Ar_{(90\%)}/H_{2(10\%)}$ flowing through deionized water, respectively. The alumina tube was flushed with the gas mixture for 30 min before we start the heating procedure to ensure that the tube was completely filled with the gas mixture prior heating. The controller of the heating apparatus for the furnace was programmed in a way to reach the temperature plateau within about 1 h without overshoot.

The sample slice was annealed for a fixed time and was analyzed by FTIR spectroscopy before and after annealing. Then the slice was re-annealed under the same conditions and another FTIR measurement was performed. This procedure was repeated until a steady state absorption value of OH (OD) bands is reached with prolonged annealing time.

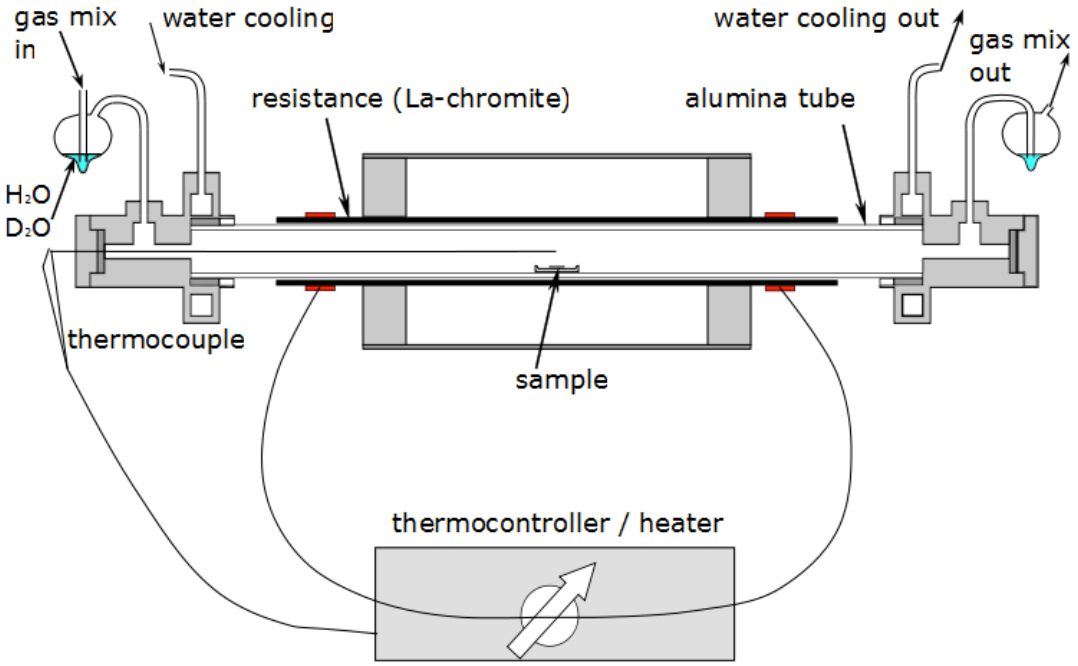

Figure 4.1. Schematic diagram of the high temperature furnace with the attached sockets for the controlled gas flow assemblage on both ends of the alumina tube.

4.1.2 Temperature controlling

The time and temperature ramp necessary to reach the desired temperature, the duration of the annealing and the cooling of the furnace was monitored by a EUROTHERM series 900 regulator. A typical temperature time program is presented in Figure 4.2. There are two ramps and two plateaus. During the first ramp, the sample was heated at a rate of 20 °C/min from 200 °C until a temperature 200 °C lower than the desired temperature was reached, which needs about 20 to 40 minutes depending on the desired temperature. The duration for the first plateau was set for 20 minutes to stabilize the temperature before the second ramp. Then the temperature was raised at the same rate during the second ramp until a temperature 15 °C lower than the desired temperature. Then the rate was reduced to 2 °C/min and the desired temperature is reached and stabilized after about 10 minutes without overshoot. Therefore, a total time of 60 to 80 minutes is needed to arrive to the temperature of the annealing plateau.

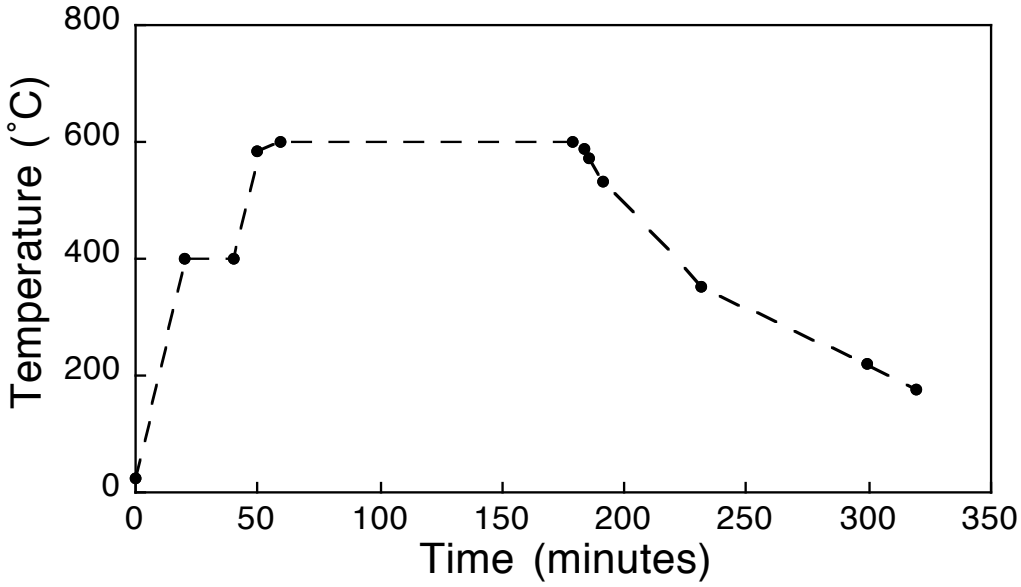

Figure 4.2. Representative temperature/time progression during an annealing experiment.

4.2 Analytical methods

4.2.1 Electron Microprobe Analysis (EMPA)

Major elements compositions of the samples were analyzed with a Camera SX50 automated electron microprobe at the GET laboratory of the University of Toulouse. The operating conditions were set to an accelerating voltage of 15 kV and a beam current of 20 nA. 34 analytical points were recorded on 5 different slices for andradite, while 3 analytical points were recorded on each of the four zircon samples.

4.2.2 LA-ICP-MS

The composition of samples was also measured by LA-ICP-MS at the laboratory of the University of Science and Technology of China to get better estimation of minor elements content. Two sample slices each of andradite and zircon were ablated in situ with a Coherent company GeoLas pro ArF laser system with a beam

wavelength of 193 nm at 10Hz repetition rate and 10J/cm^2 energy per pulse. The ablation crater diameters are 60 μm. The sample aerosol was carried to ICP-MS by high purity Helium at a flow rate of 0.3 L/min. A typical analysis consists of 80-100 replicates within 80-100 s. PerkinElmer DRII ICPMS was used to analyze the aerosol samples with the RF power of 1350 w and nebulized gas flow rate of 0.7 L/min. Sample analysis results were processed with LaTEcalc software. The signal intensity (counts per ppm) for each element was calibrated against a NIST 610 silicate glass and the Si^{29} content of samples was used as an internal standard. Typical analytical precision ranged from 2% to 5%.

4.2.3 Fourier Transform Raman Spectroscopy (FT-Raman)

FT-Raman spectra were recorded at room temperature using a Bruker IFS 66v spectrometer at the laboratory of the Lille 1 University - Science and Technology. Three slices of zircon along the three crystallographic orientations were analyzed before and after annealing to measure the variation of crystallinity upon heating. Raman spectra were acquired with a 514.5 nm line of an Ar^+ laser, with laser power of 45-100 mW, a beam current of 4 nA and a beam diameter of 50 μm.

4.2.4 Fourier Transform Infrared Spectroscopy (FTIR)

IR spectroscopy is ideally suitable for the investigation of traces amount of hydrogen in NAMs due to its high sensitivity to polar O-H bonds in the structure. Furthermore, since the mass of H atom is low, the absorption bands can be readily observed in the high-frequency region of the spectrum in the range 3000-4000 cm^{-1} and thus do not overlap with other peaks from the host lattice in most cases.

4.2.4.1 Basic concepts

Setup of measurements

An IR light source emits a beam of polychromatic IR radiation, it is then modulated in intensity across the frequency range by an interferometer and directed through a plane parallel sample (Fig. 4.3). Certain frequencies of light are absorbed by the sample due to internal molecular vibrations, and the intensity of the transmitted light is recorded by an IR detector. The interferogram observed by the detector is Fourier-transformed to an IR spectrum mathematically. During an analysis, a background is recorded first to measure the intensity of the incident light at any wavenumber and then the sample spectrum is divided by this background spectrum showing the transmittance of the sample. Finally, the transmittance spectrum is converted to an absorbance spectrum.

Basic units and relations

The transmittance (T), defined by the ratio of the transmitted intensity to the incident intensity, is dimensionless and conveniently multiplied by 100%. It is usually exchanged by absorbance (A), which is a negative logarithm of transmittance:

$$T = I / I_0 \tag{4.1}$$

$$A = -\log T = -\log I / I_0 \tag{4.2}$$

where I is the transmitted intensity and I_0 is the intensity of the transmitted light without sample.

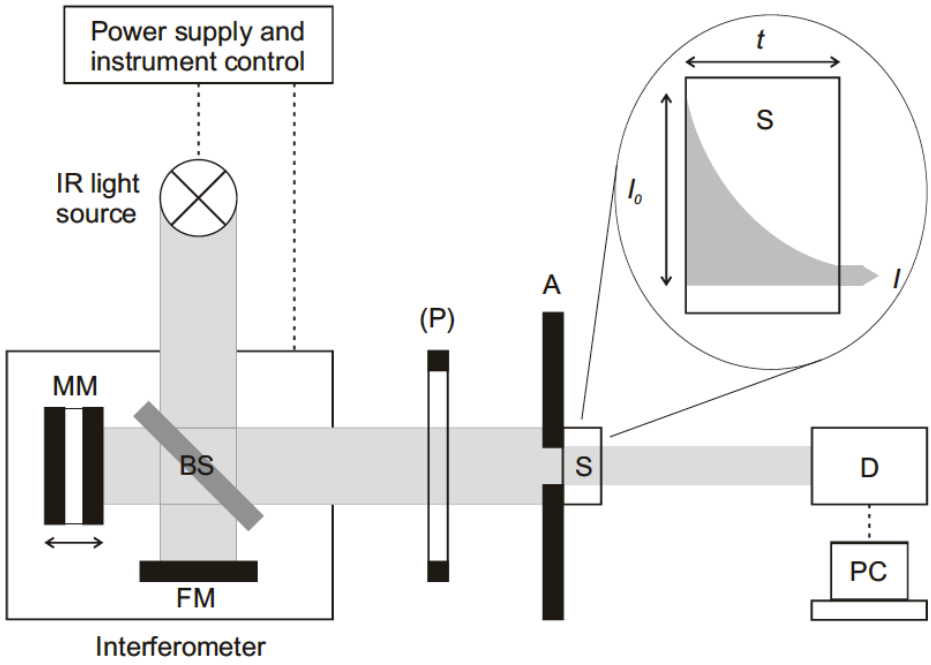

Figure 4.3. Basic experimental setup of an FTIR spectrometer. A = aperture, BS = beam splitter, D = detector, FM = fixed mirror, MM = moving mirror, (P) = polarizer (optional), S = sample. The close-up shows the exponential decrease of light intensity by absorption with increasing sample thickness (from Libowitzky and Beran 2006).

4.2.4.2 Calculation of water content

Integrated absorbance is linearly proportional to the thickness of the sample and the concentration of the absorbing species, which can be expressed by the Beer-Lambert's law:

$$A = \varepsilon \cdot t \cdot c \tag{4.3}$$

where ε is the molar absorption coefficient (L/mol.cm), t is the sample thickness (cm) and c is the concentration of the absorbing species (mol/L).

The hydrogen concentration expressed as ppm H_2O by weight was calculated by the following equation:

$$c(wt\%H_2O) = \frac{A(cm^{-1}) \cdot 1.8015}{t(cm) \cdot D(g/cm^3) \cdot \varepsilon(cm^{-2} permol H_2O/L)} \tag{4.4}$$

where A is the integrated area in the OH stretching region, t is the sample thickness, D is the density of mineral (3.86 g/cm^3 for andradite; 4.7 g/cm^3 for zircon), and ε is the

specific absorption coefficient (Paterson 1982; Libowitzky and Rossman 1997). The value of ε is acquired from calibration using independent analytical methods such as gas extraction manometry and SIMS.

Andradite

In the case of andradite, only unpolarized spectra were recorded to calculate the water content due to its isotropic properties. Several specific absorption coefficients for grossular and other garnets have been proposed, among which a ε value for grossular proposed by Rossman and Aines (1991) is widely adopted. The use of a single absorption coefficient for garnets is still under discussion (Maldener et al. 2003). Malder et al. (2003) investigated various kinds of garnets by nuclear reaction analysis and FTIR spectroscopy, the calculated ε values vary over a large range due to the complexity of the spectra. It leads to a suggestion that reliable ε value for each individual garnet species have probably to be calculated separately. However, for the purpose of this study, to investigate the diffusion kinetics of hydrogen, the uncertainty on the true OH content does not affect the diffusion result itself since it is the relative decrease or increase of OH and OD bands during annealing that is used.

Zircon

In the case of zircon, an anisotropic mineral, things become a bit more complicated. Lets consider a single absorber randomly oriented with respect to the indicatrix axis x, y, z (Fig. 4.4). With polarized light in the three main indicatrix faces, one can obtain component absorbance A_x, A_y and A_z along the principle axes directions. The obtained A_x, A_y and A_z are projections of the absorbance parallel to the absorber onto the axis and are defined by (Libowitzky and Rossman 1996):

$$A_x = A \cdot \cos^2 \alpha; \quad A_y = A \cdot \cos^2 \beta; \quad A_z = A \cdot \cos^2 \gamma \tag{4.5}$$

where α, β, γ are the three angles describing the orientation of the absorber.

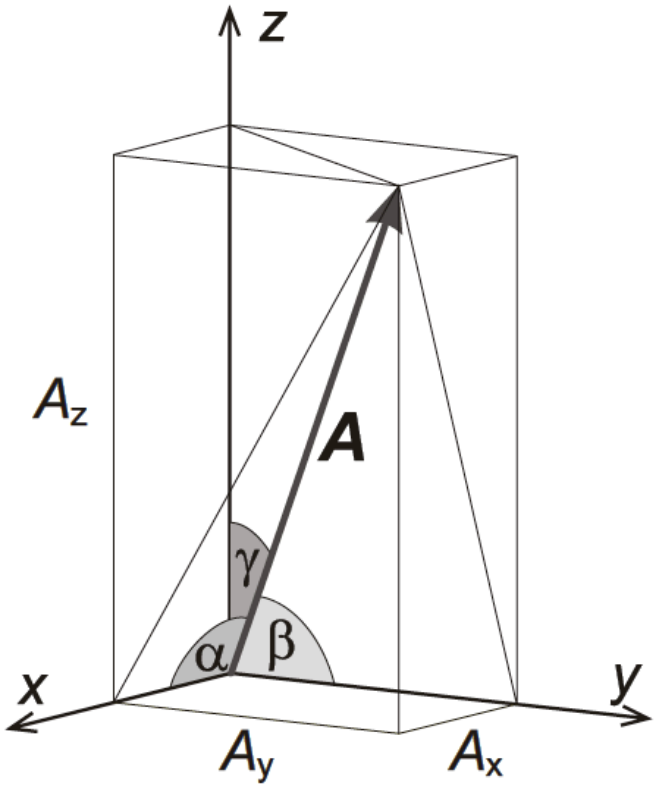

Figure 4.4. Spatial orientation of an absorber A in an orthogonal axis system X, Y, Z (from Libowitzky and Beran 2006).

The total absorbance of an oriented crystal is obtained by summing up the three polarized component absorbance (the electric vector *E* of the light is parallel to the component of the dipole of the absorber):

$$A_{tot} = A_x + A_y + A_z \quad (4.6)$$

As zircon is tetragonal, A is equal to the integral absorbance when the electric vector *E* is parallel to c (*E* // c) plus two times the integral absorbance when *E* // a, that is $A = A_{//c} + 2 \times A_{//a}$. A specific absorption coefficient for zircon was proposed by Bell et al. (2004). Value of 36241 cm^{-2} per mol H_2O/L was deduced from the measurement of the H_2O content in a kimberlitic zircon by nuclear reaction analysis. However, the OH absorption signature of this zircon is quite different from ours, a more common approach for calculation absorption coefficients, proposed by Libowitzky and Rossman (1997), was adopted in this study. A linear relationship is defined between a mineral absorption coefficient and the mean OH stretching band

wavenumber for hydrous minerals with known H_2O contents. Thus, once the mean OH stretching band wavenumber of a mineral is obtained, ε can be calculated. The technique is generally designed and calibrated for application to hydrous minerals with known absorption coefficients, but it has been applied to anhydrous minerals too (Nasdala et al. 2001; Blanchard and Ingrin 2004b; Stalder and Skogby 2007).

The precise water content before annealing is calculated from total absorbance. However, for the purpose of this study, to investigate the diffusion kinetics of zircon where only relative concentration values are necessary, only the unpolarized spectra of diffusion species was recorded during annealing.

4.2.4.3 IR absorption of OH and OD bands

For diatomic molecules or ions, while the energy of IR radiation matches the transition energy of the bond that vibrate, an absorption of IR radiation will occur and result in an absorption band in the IR spectrum with the frequency (ν) determined by:

$$\nu = \frac{1}{2\pi c}\sqrt{\frac{k}{\mu}} \tag{4.7}$$

where c is speed of light in vacuum (m/s), k is the bond force constant (g/s^2), μ is the reduced mass which is defined by:

$$\mu = \frac{m_1 \cdot m_2}{m_1 + m_2} \tag{4.8}$$

where m_1 and m_2 are the masses of the two atoms involved in the vibration.

The stretching vibration of an isolated OH ion will produce theoretically an IR absorption at the frequency of 3735 cm^{-1}. However, in crystalline solids, H atom is usually attracted by other electronegative atoms, usually oxygen atoms, forming hydrogen-bonds (O-H···O) (the first oxygen atom is called the donor and the latter the acceptor atoms). Due to the attractive force of the acceptor atoms, the hydrogen atom is pulled away from the donor atom. This leads to a weakening of the O-H bond

compared with a non-bonded unit and the corresponding decrease of frequency of its stretching vibration.

The correlation between bond length of hydrogen-bond versus the stretching frequency of the OH bond has been investigated theoretically and empirically (Bellamy and Owen 1969; Mikenda 1986). Figure 4.5 shows the typical positive and curved trend line of this correlation through the average distance between O donor and acceptor: OH with stronger hydrogen-bonds will present an IR stretching frequency at lower energies. Moreover, strong hydrogen-bonds tend to present a more linear relationship while weak ones present frequently bent relationship. The OH stretching frequencies for andradite and zircon are in the range 3150-3650 and 2850-3700 cm^{-1}, respectively.

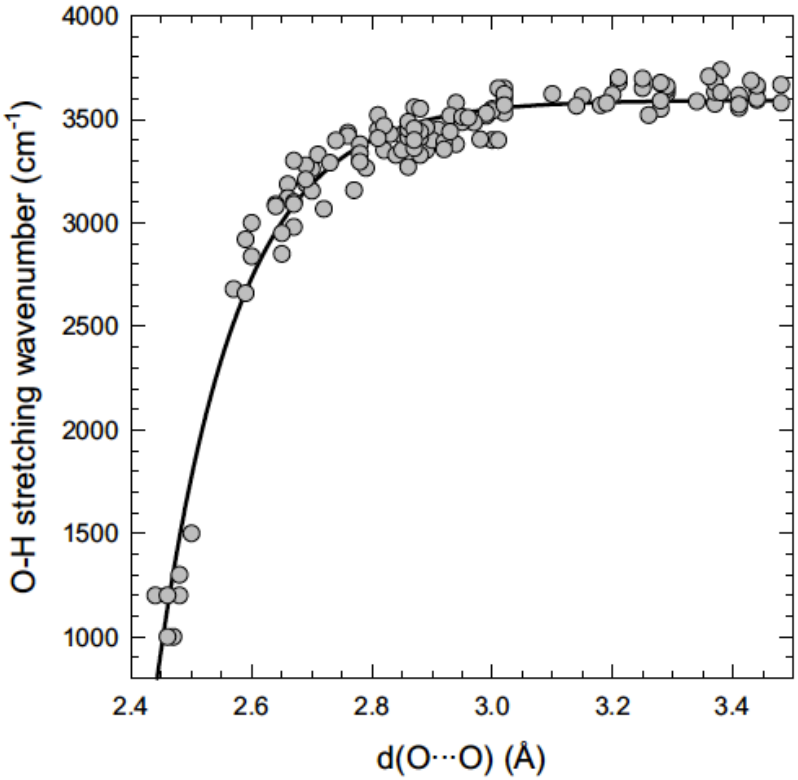

Figure 4.5. Correlation between Hydrogen-bond length and O-H stretching frequency (from libowitzky and Beran 2006).

According to equation (4.7), using the reduced mass, the band shifts of OD bands towards lower wavenumbers can be calculated. The ratio of ν_{OH} to ν_{OD} is given by the

inverse ratio of the square root of reduced mass of OH to OD, resulting in a theoretical factor of 1.374.

4.2.4.4 IR measurements

The H content of each slice was analyzed before annealing and after each annealing. Polarized or unpolarized spectra were acquired at room temperature with a Perkin Elmer 1760X FTIR microscope spectrometer equipped with a liquid nitrogen cooled MCT detector, a KBr beam splitter and a globar IR source, at the laboratory of the Lille 1 University - Science and Technology. A new background was collected when the polarizer was used as well as its orientation was changed. Measurements of multi points from rim to the center of each untreated sample show that hydroxyl content is homogeneous. Several analytical points nearby the center were recorded for each slice, after each annealing steps, with an aperture of 100 μm in diameter and 32 scans at a resolution of 2 cm^{-1}.

Uncertainties in the absorbance measurements were estimated from both the reproducibility of the analysis on a same slice and the variation of the integral absorbance due to a change of the position of the points used to anchor the baseline corrections. The contribution of these errors to the measured integral absorbances corresponds to 3% to 5% for andradite garnet and 6% to 9% for zircon of the maximum value of absorbance of OH (resp. OD) depending on the slice. It is this fixed value of uncertainty, which has been used to plot the evolution with time of the exchange. The errors on the thickness of the slice vary from 0.5% to 2%, depending on the slice. This error has a only a minor effect on the estimation of the water content of the sample and no effect on the determination of the individual diffusion coefficients since the thickness of the slices is kept constant during annealing experiments.

4.3 Samples

The samples used in this experimental study are andradite garnet single crystals from a single origin and zircon single crystals from different localities showing intermediate to low levels of crystallization.

4.3.1 Overview of the samples

Andradite garnet

The andradite garnet single crystal (SER), collected by Andreas Kurka, comes from an iron-skarn deposit on Serifos island, Greece. The crystal is found in large geodes inside an almost monomineralic hedenbergite rock adjacent to a marble layer. It is accompanied by "praseme" quartz (which shows a green color due to very fine hedenbergite inclusions), calcite, ilvaite, hematite and "pyroxene-asbestos". The andradite form idiomorphic crystal up to 5 cm in diameter and shows a prominent zonation with a darker colored rim of about 1 mm thickness. Thin slices of the andradite show a brownish-yellow color.

Zircons

Two zircon single crystals (ZrB and ZrD), of gem quality, with crystallinity at intermediate level, come from Madagascar. Both crystals are light yellow brown in color and cuboid with smooth angles in shape. They have a similar original size of 5 × 5 × 7 mm^3, are free of inclusions and cracks under microscope observations. Detailed geological information and the heating history of the samples were not available. Thin slices of the two zircons are transparent by optical view.

4.3.2 Sample preparation

For the purpose of experimental studies of hydrogen diffusion, transparent slices of good quality without any inclusions and cracks are prepared. Inclusions of other OH-bearing minerals, which have different hydrogen diffusion kinetics than the mineral studied in this thesis (andradite garnet and zircon), could confuse the results

of kinetics studies of andradite garnet and zircon. Any cracks in the slices could provide a quick path for the hydrogen diffusion and thus accelerate the diffusivity.

To have a good signal to noise ratio, the slices should not be too thin; To get an accurate absorbance of OH, the slices should not be too thick (or else, the concentration of defects is no more linearly related to thickness, absorbance saturation effect is observed); To apply a one-dimensional model on hydrogen diffusion, a plate shape with a high length-width over thickness ratio is required (at least larger than three).

Taking consideration of these requirements the sample slices are prepared in the following ways:

Crystals were first cut into slices using a low speed diamond saw along the three crystallographic orientations for zircon (the orientation was determined according to the crystal shape, and was verified through Raman and FTIR analysis) and no consideration of the crystallographic orientation for andradite garnet. The slices have dimensions of 2.0 to 5.0 mm in diameter and 0.1 to 1 mm thickness. The slices were then mounted on a cylinder holder with epoxy and polished on both sides using SIC sand paper (1000 to 4000 grain size) and finally with 1 μm grain size alumina powder. The thickness of the slices after polishing was between 140 to 671 μm for andradite garnet and 111 to 372 μm for zircon. Thickness of platelets was measured with a Mitutoyo digital micrometer (± 3 μm). List of slices with the corresponding experimental conditions are listed in Table 4.1 and Table 4.2.

For the FTIR measurements, the sample slices were put on a sample holder with defined apertures from 1 to 3 mm, depending on the slice size.

Table 4.1. Dimension of slices and experimental conditions for andradite garnet.

Sample No.	Thickness (μm)	Size (mm × mm)	Experiments	T (°C)
SER04	277	3.0 × 2.0	H-D exchange	600
SER04	277	3.0 × 2.0	D-H exchange	600
SER13	273	3.0 × 2.0	H-D exchange	500
SER13	273	3.0 × 2.0	D-H exchange	400
SER13	273	3.0 × 2.0	H-D exchange	550
SER15	671	3.2 × 2.4	H-D exchange	600
SER16-P3	236	4.0 × 2.7	H-D exchange	550
SER16-P6	236	4.0 × 2.7	H-D exchange	550
SER17	182	4.5 × 4.0	H-D exchange	425
SER18	596	4.5 × 3.0	H-D exchange	700
SER19	140	5.0 × 2.8	H-D exchange	500

Table 4.2. Dimension of slices and experimental conditions for zircon.

Sample No.	Thickness (μm)	Size (mm × mm)	Experiments	T (ºC)
ZrB-c2	111	2.0 × 1.4	H-D exchange	900
ZrB-c3	314	2.1 × 2.0	H-D exchange	1000
ZrB-c1	291	2.4 × 1.9	H-D exchange	1150
ZrD-b2	153	2.6 × 2.3	H-D exchange	950
ZrB-b1	139	3.9 × 1.9	H-D exchange	1000
ZrD-b1	204	3.2 × 1.9	H-D exchange	1050
ZrD-b3	372	3.5 × 2.8	H-D exchange	1050
ZrB-b2	385	2.5 × 1.8	H-D exchange	1100
ZrB-a1	199	4.0 × 3.0	H-D exchange	1050
ZrB-a2	184	3.2 × 3.0	H-D exchange	600-900

Chapter 5

Kinetics of hydrogen diffusion in andradite

5.1 Chemical composition

34 analytical points were recorded on 5 different slices by EMPA for major elements (Table 5.1), while 8 analytical points were recorded on 2 different slices by LA-ICP-MS for a better estimation of minor elements content (Table 5.2). The average composition and standard deviation are presented at the last two rows in the tables.

The use of a single absorption coefficient for garnets is still under discussion due to the complexity of the spectra (Maldener et al. 2003). A value of 0.18 (± 0.05) and 0.067 (± 0.013) wt% H_2O is obtained using, respectively, the calibration of Rossman and Aines (1991) for grossular, and the wavenumber-dependent calibration of Libowitzky and Rossman (1997). The absorption coefficient proposed by Maldener et al. (2003) leads to a value of 0.30 (± 0.23) wt% H_2O. It is observed that the uncertainty in the water content is high as no reliable specific calibration for andradite has been proposed. The use of the general calibration of Libowitzky and Rossman (1997) for garnet was highly debated (Maldener et al. 2003). We prefered to be conservative; we used the average of the three values (0.18 ± 0.12) as an estimation of the water concentration in the samples used in this study. However, in this study, the uncertainty in OH content does not affect the diffusion results, which are only dependent on the relative decrease or increase of the integral absorbance of OH and OD bands during annealing.

Taking consideration of the water content of 0.18 (± 0.12) wt% H_2O calculated from FTIR results, the chemical formula of andradite deduced from these measurements is assumed to be: $(Ca_{2.992}Mn_{0.006}Mg_{0.001})_{2.999}(Fe)_{1.992}[Si_{2.981}(4H)_{0.025}]_{3.010}O_{12}$.

Table 5.1. EMPA analysis of andradite samples used in this study.

Points	SiO_2	TiO_2	Al_2O_3	Cr_2O_3	Fe_2O_3	FeO*	MnO	MgO	CaO	Total
1	35.90	0.00	0.00	0.00	30.46	1.38	0.15	0.01	32.31	100.21
2	35.85	0.00	0.00	0.01	30.27	1.14	0.17	0.00	32.44	99.88
3	35.67	0.01	0.00	0.00	30.55	0.96	0.16	0.01	32.41	99.79
4	35.22	0.00	0.00	0.03	31.40	0.04	0.07	0.00	32.78	99.54
5	35.39	0.00	0.00	0.01	31.10	0.00	0.13	0.02	33.06	99.70
6	35.29	0.00	0.00	0.01	30.88	0.00	0.07	0.00	32.96	99.21
7	35.15	0.03	0.00	0.00	31.60	0.00	0.08	0.00	33.19	100.04
8	35.23	0.00	0.00	0.03	31.38	0.00	0.03	0.00	33.37	100.04
9	35.19	0.00	0.00	0.00	32.27	0.00	0.10	0.02	33.70	101.29
10	35.03	0.00	0.00	0.02	31.81	0.00	0.09	0.00	33.90	100.85
11	35.00	0.00	0.00	0.00	31.32	0.00	0.14	0.00	33.42	99.88
12	36.09	0.00	0.00	0.05	32.12	0.00	0.07	0.00	33.74	102.07
13	35.51	0.00	0.00	0.03	31.89	0.00	0.07	0.00	33.41	100.91
14	35.50	0.00	0.00	0.00	31.81	0.00	0.09	0.00	33.76	101.17
15	35.48	0.00	0.00	0.00	31.49	0.00	0.11	0.00	33.36	100.44
16	36.19	0.00	0.00	0.01	31.13	0.82	0.07	0.00	33.08	101.31
17	35.80	0.01	0.00	0.03	32.43	0.00	0.04	0.00	33.47	101.77
18	35.86	0.00	0.00	0.01	31.62	0.00	0.09	0.00	33.52	101.11
19	36.35	0.00	0.00	0.05	31.36	0.60	0.04	0.00	33.43	101.85
20	36.23	0.00	0.00	0.00	32.07	0.26	0.09	0.00	33.54	102.20
21	36.40	0.00	0.00	0.00	31.35	0.44	0.09	0.00	33.56	101.84
22	36.44	0.00	0.00	0.00	31.77	0.08	0.07	0.00	33.89	102.24
23	35.91	0.00	0.00	0.01	31.87	0.00	0.13	0.00	33.47	101.39
24	36.47	0.00	0.00	0.00	31.53	0.77	0.12	0.00	33.34	102.24
25	35.75	0.00	0.18	0.00	31.78	0.21	0.16	0.00	33.08	101.16
26	35.48	0.00	0.17	0.00	32.40	0.17	0.10	0.00	32.91	101.23
27	36.04	0.00	0.75	0.02	30.26	0.01	0.11	0.00	33.54	100.74

Table 5.1. continued

Points	SiO_2	TiO_2	Al_2O_3	Cr_2O_3	Fe_2O_3	FeO*	MnO	MgO	CaO	Total
28	35.91	0.04	0.00	0.05	31.32	0.06	0.20	0.00	33.34	100.93
29	35.61	0.00	0.00	0.01	31.68	0.00	0.08	0.00	33.77	101.16
30	35.61	0.00	0.00	0.00	31.61	0.00	0.14	0.00	33.43	100.79
31	35.28	0.00	0.00	0.03	32.41	0.00	0.17	0.00	33.35	101.25
32	35.71	0.00	0.00	0.00	31.35	0.00	0.12	0.00	33.39	100.57
33	35.64	0.00	0.00	0.02	32.32	0.00	0.06	0.04	33.53	101.60
34	35.73	0.00	0.00	0.03	31.62	0.00	0.10	0.00	33.31	100.79
Average	35.70	0.00	0.03	0.01	31.54	0.20	0.10	0.00	33.32	100.92
STD	0.41	0.01	0.13	0.02	0.58	0.38	0.04	0.01	0.39	0.83

Table 5.2. LA-ICP-MS analysis of andradite samples used in this study.

Points	SiO_2	TiO_2	Al_2O_3	Cr_2O_3	Fe_2O_3	FeO*	MnO	MgO	CaO	Total
1	35.21	0.00	0.02	0.00	30.88	0.00	0.09	0.01	33.25	99.5
2	35.21	0.00	0.04	0.00	30.94	0.00	0.09	0.01	32.90	99.2
3	35.21	0.00	0.02	0.00	31.21	0.00	0.09	0.01	32.99	99.5
4	35.21	0.00	0.02	0.00	31.05	0.00	0.09	0.01	32.97	99.4
5	35.21	0.00	0.02	0.00	30.75	0.00	0.09	0.01	32.70	98.8
6	35.21	0.00	0.02	0.00	30.94	0.00	0.09	0.01	32.46	98.7
7	35.21	0.00	0.03	0.00	31.50	0.00	0.09	0.01	32.50	99.3
8	35.21	0.00	0.20	0.00	30.93	0.00	0.11	0.01	32.84	99.3
Average	35.21	0.00	0.04	0.00	31.03	0.00	0.09	0.01	32.83	99.21
STD	0.00	0.00	0.06	0.00	0.23	0.00	0.01	0.00	0.27	0.30

5.2 Baseline correction

The integration region of OH and OD were from 3750 to 3150 cm^{-1} and from 2700 to 2500 cm^{-1} respectively. The baseline correction for OH and OD absorption bands were performed by two different ways. For OH, a linear baseline was used (Fig. 5.1a), while for OD, the spectrum of the sample at $t = 0$ was systematically subtracted (Fig. 5.1b): The bands located at 2466 cm^{-1} and 2640 cm^{-1} are related to crystal structural internal vibrations, these two bands remain constant during annealing.

The OH homogeneity of the slices was systematically checked; slices SER04, SER15, SER17 and SER18 were perfectly homogeneous, but slices SER13, SER16 and SER19 display sectors with different concentrations. The extreme case occurs in SER16, which shows one sector with more than twice the concentration of the other (see SER-P3 and SER-P6 in Table 5.4). For these slices, only sectors of more than 500 μm in diameter, with almost constant concentration were selected for measurements.

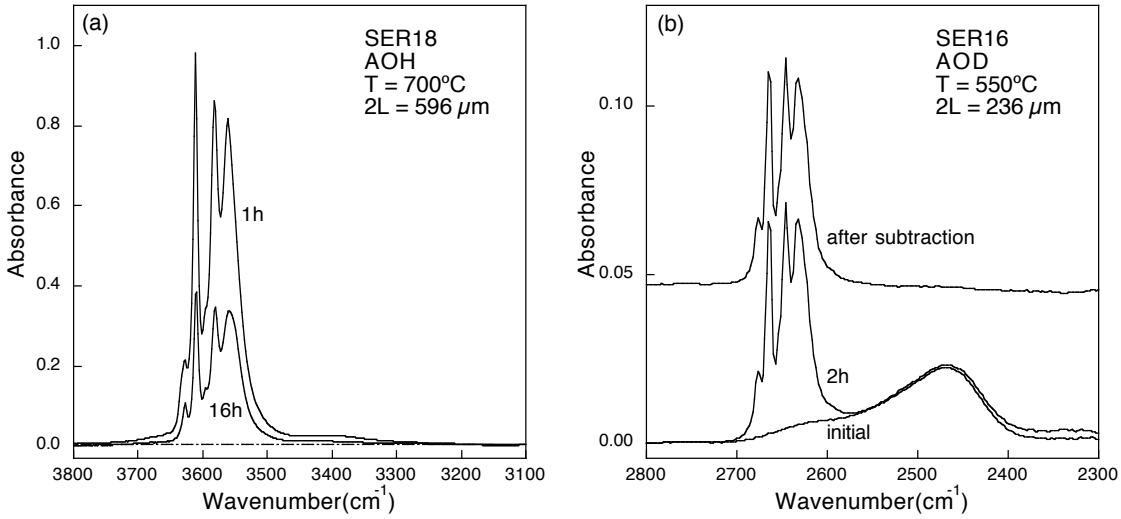

Figure 5.1. Examples showing the baseline correction of OH and OD absorption region: a) OH stretch region (3750 to 3150 cm^{-1}); Slice SER18, annealed at 700 °C, with a thickness 2L of 596 μm and b) OD stretch region (2700 to 2500 cm^{-1}); Slice SER16, annealed at 550 °C, with a thickness 2L of 236 μm.

5.3 IR spectroscopic characterization of OH and OD bands

Annealing of OH-bearing andradite in $Ar_{(90\%)}/D_{2(10\%)}$ leads to a replacement of hydrogen by deuterium. Due to twice the mass of deuterium atom than that of hydrogen atom, the IR absorption bands of OD can be found at lower frequency. Figure 5.2 shows a representative evolution of FTIR absorption during H-D exchange at 500°C for SER13 where OH bands were gradually replaced by OD bands. It has most prominent bands at 3612, 3583, 3564 cm^{-1} and a minor band at 3634 cm^{-1}. The OH absorption features are representative of andradite from skarn (Amthauer and Rossman 1998), which resembles that of Ti-bearing andradite in Armbruster et al. (1998) and the KPK54-9 An_{99} andradite from Phu Kha Hill, Thailand used by Phichaikamjornwut et al. (2012) for the study of hydrogen dehydration and rehydration.

Using a Gaussian and occasionally a Lorentzian shape (bands at 3641 and 3526 cm^{-1}), a peak-deconvolution of the spectrum with the Peakfit software (SPSS Inc.) leads to 12 different peaks located at 3641, 3634, 3628, 3621, 3612, 3605, 3596, 3583, 3575, 3564, 3547, 3526 and a small broad band of water at 3406 cm^{-1}, probably due to the presence of some fluid inclusions (Fig. 5.3a). The deconvolution of the weakest bands is guided by the results of the dehydration experiments of Kurka et al. (2005) and an in situ IR experiments at varying temperatures down to -150°C (see end of this chapter). The decomposition of the corresponding OD absorption bands is also shown in Figure 5.3b. The ν_{OH}/ν_{OD} ratio for each band is listed in Table 5.3.

The frequency shift due to the isotopic replacement (ν_{OH}/ν_{OD} close to 1.355) is in agreement with previous observations in anhydrous minerals and hydrates during H-D exchange (Hercule and Ingrin, 1999; Blanchard and Ingrin 2004a; Kurka et al. 2005; Mikenda, 1986; see also Figure 5.4a). The dependence of the isotropic ratios (ν_{OH}/ν_{OD}) on the OH stretching frequencies shows some deviation from the correlation proposed by Mikenda (1986) (Fig. 5.4b). All the values for garnets and diopside lie below this curve. A stronger decreasing of the isotropic frequencies ratios with decreasing frequencies is confirmed.

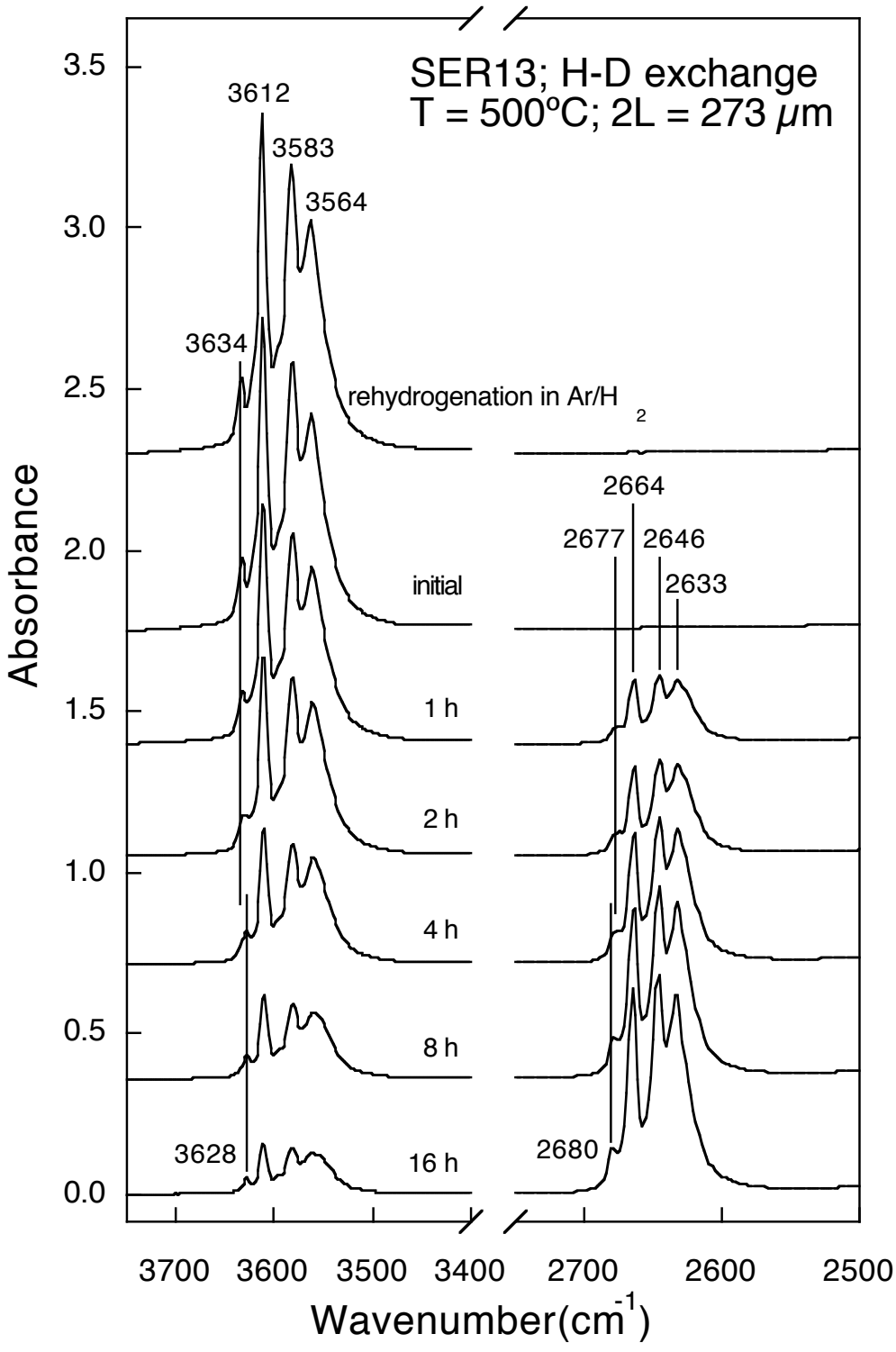

Figure 5.2. Representative evolution of andradite spectra during annealing under Ar/D_2 atmosphere showing the replacement of OH bands by OD bands. Slice SER13, annealed at 500 °C, with a thickness 2L of 273 μm. The uppermost spectrum shows the result after rehydrogenation in Ar/H_2 atmosphere at 400 °C.

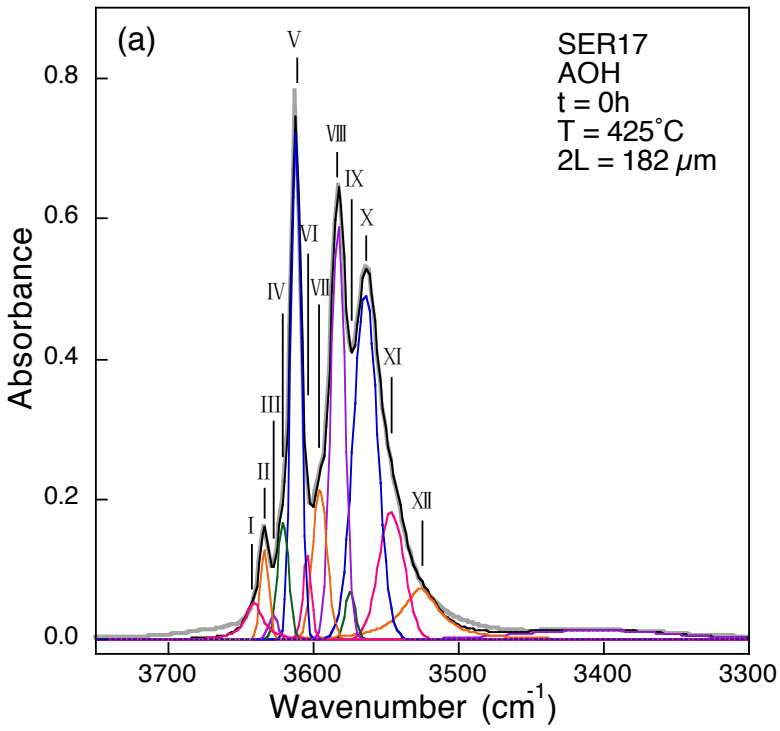

No.	Band
I	3641
II	3634
III	3628
IV	3621
V	3612
VI	3605
VII	3596
VIII	3583
IX	3575
X	3564
XI	3547
XII	3526

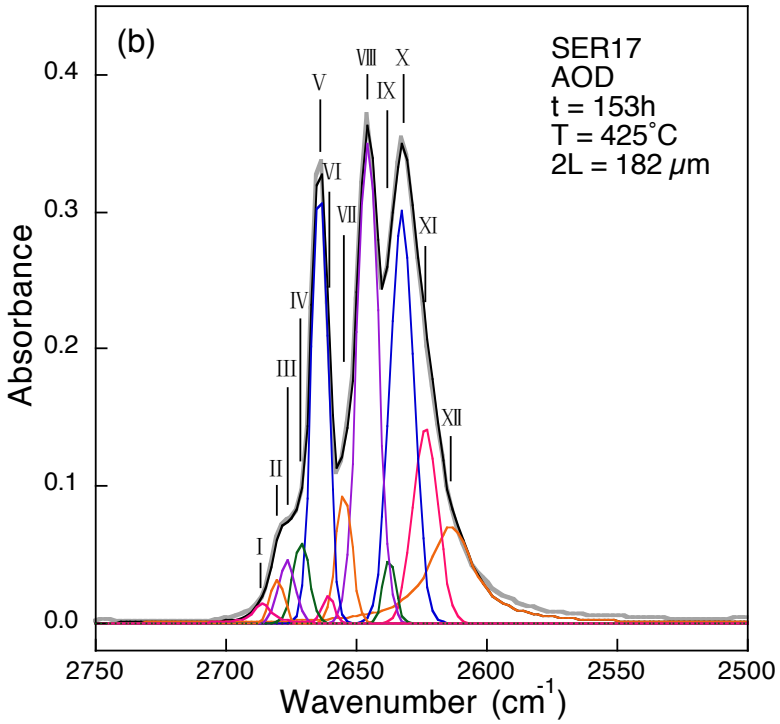

No.	Band
I	2686
II	2680
III	2677
IV	2671
V	2664
VI	2661
VII	2655
VIII	2646
IX	2638
X	2633
XI	2624
XII	2614

Figure 5.3. Representative IR absorption spectrum of the a) OH and b) OD stretching regions of andradite. The peak-deconvolution of the spectra leads to 12 peaks of OH/OD. Slice SER17, with a thickness 2L of 182 μm.

Table 5.3. Peak-deconvolution results of OH and OD absorption bands from spectra measured at a resolution of 2 cm^{-1}.

No.	ν_{OH} (cm^{-1})	ν_{OD} (cm^{-1})	ν_{OH}/ν_{OD}
I	3641	2686	1.356
II	3634	2680	1.356
III	3628	2677	1.355
IV	3621	2671	1.356
V	3612	2664	1.356
VI	3605	2661	1.355
VII	3596	2655	1.354
VIII	3583	2646	1.354
IX	3575	2638	1.355
X	3564	2633	1.354
XI	3547	2624	1.352
XII	3526	2614	1.349

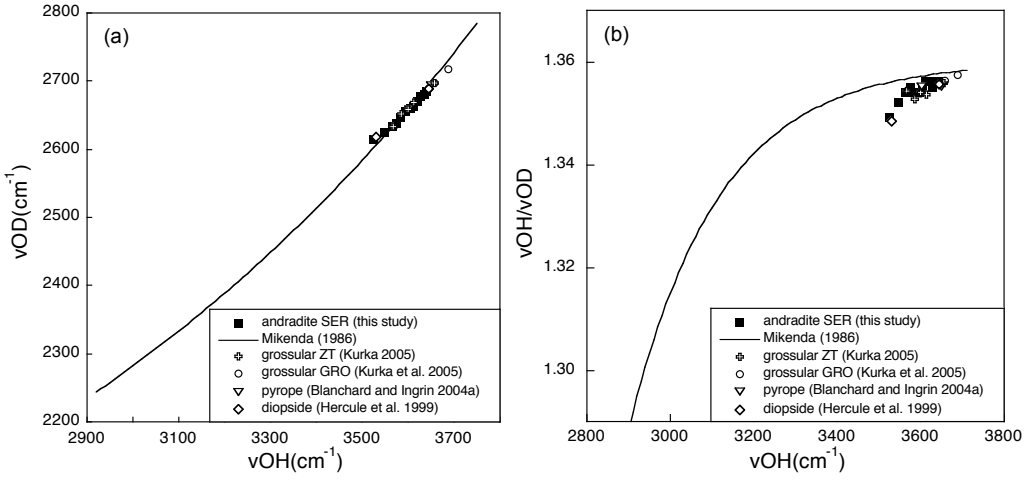

Figure 5.4. Correlation between a) OH and OD stretching frequencies b) ν_{OH}/ν_{OD} ratios and OH stretching frequencies in solid hydrates and minerals.

5.4 Bands transfer

At first glance, the shape and relative absorbances of OD bands remain the same as OH bands, which is a regular behavior for H-D exchange in minerals (Ingrin and Blanchard 2006). A closer look at the spectra shows that if the match between OH and OD bands is true for the majority of bands the OH bands at 3634 cm^{-1} and 3628 cm^{-1} which are coupled respectively with OD bands at 2680 cm^{-1} and 2677 cm^{-1} have a different behavior (Fig. 5.5).

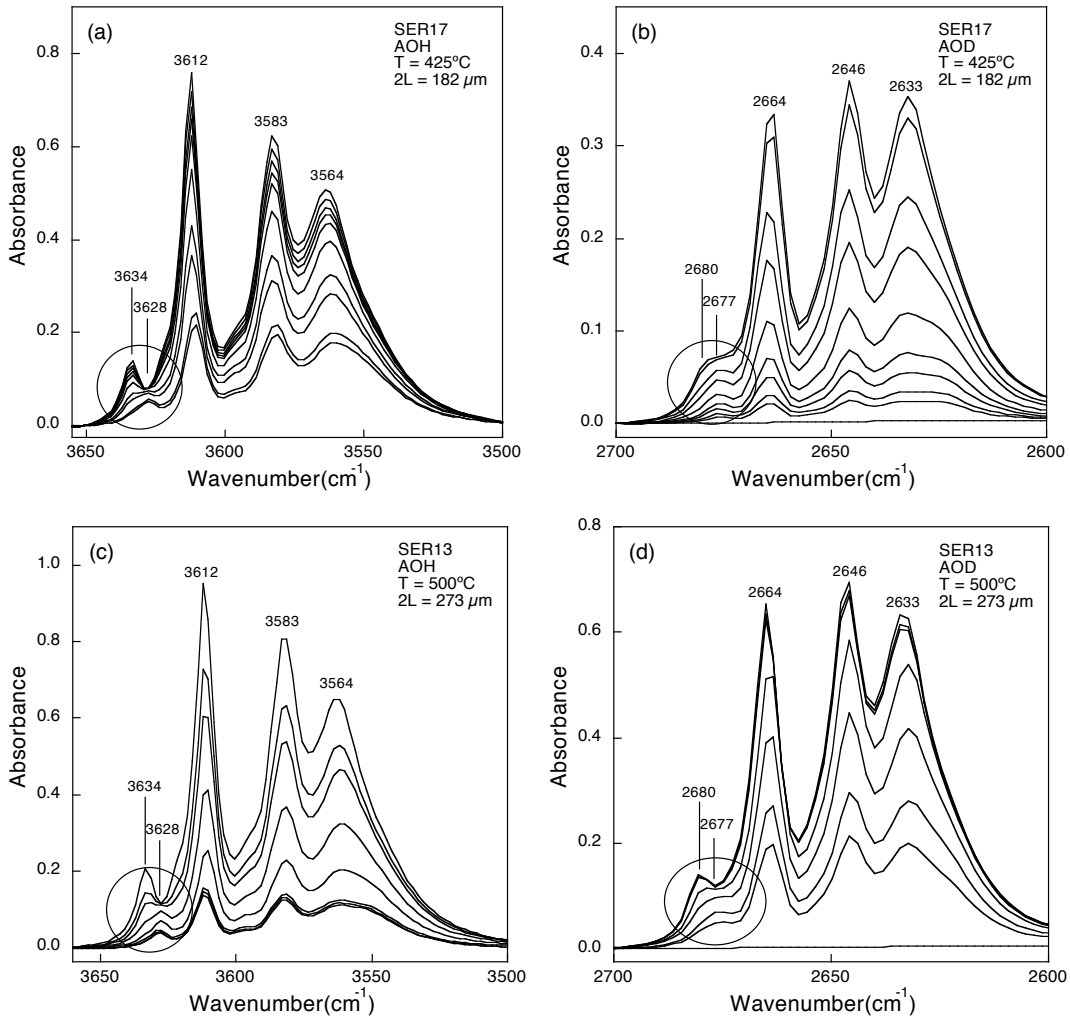

Figure 5.5. Detail of the evolution of spectra during annealing showing the specific behavior for **(a, c)** OH bands at 3634 and 3628 cm^{-1}, time of annealing increase with decreasing bands intensity **(b, d)** corresponding OD bands at 2680 and 2677 cm^{-1}, time of annealing increase with decreasing bands intensity. Slice SER17, annealed at 425°C, with a thickness 2L of 182 μm; slice SER13, annealed at 500 °C, with a thickness 2L of 273 μm.

On the OH side, the band at 3634 cm^{-1} decreases continuously during the exchange and it almost disappears when the overall OH reach an equilibrium value and changes very little with prolonged annealing, while the band at 3628 cm^{-1} reveals itself gradually and shows limited decrease. On the OD side, the lower-frequency band at 2677 cm^{-1} is the first to appear and it grows progressively, while the higher-frequency band at 2680 cm^{-1} increase gradually and even overtake 2677 cm^{-1} band (Fig. 5.5d), both bands stop change when the overall OD reach an equilibrium value.

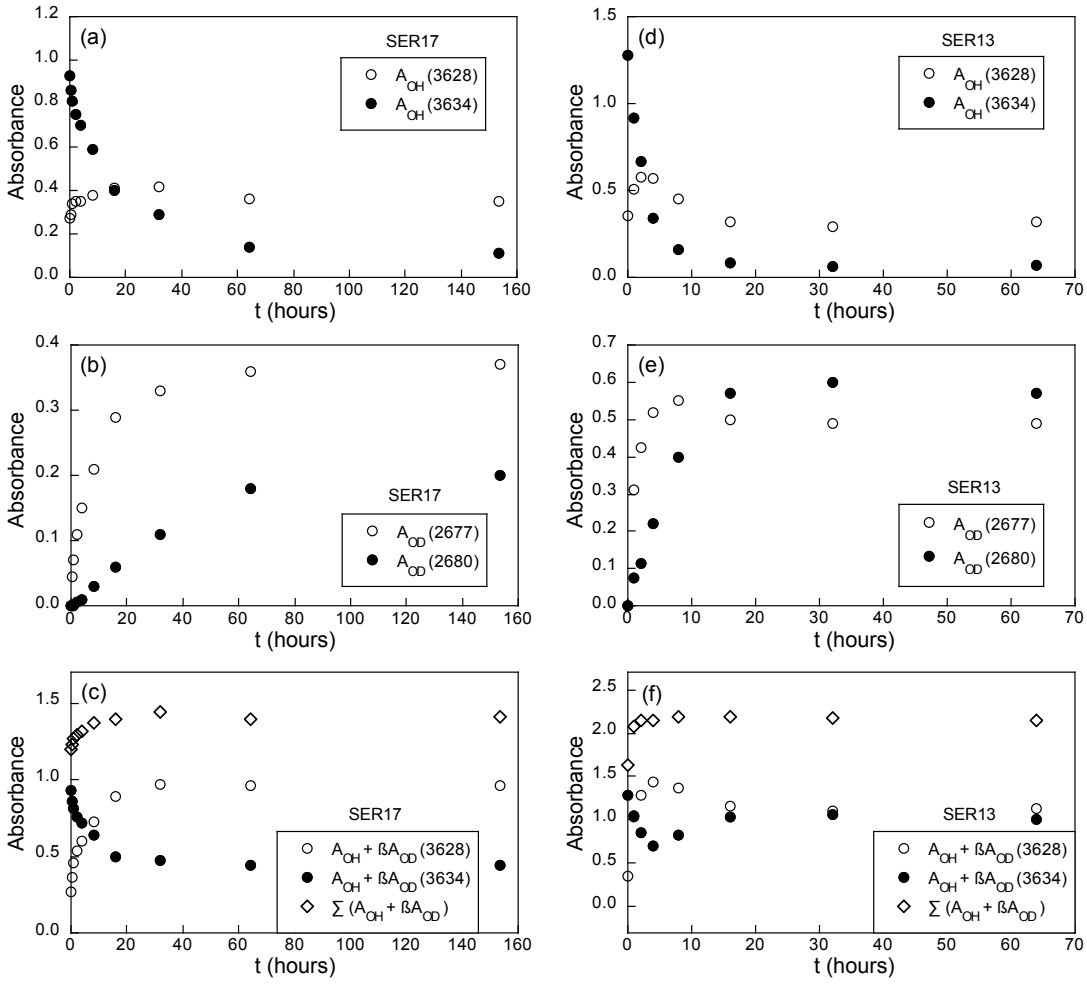

Figure 5.6. Evolution of the integral absorbance of **(a, d)** OH bands at 3628 and 3634 cm^{-1} and **(b, e)** corresponding OD bands at 2677 and 2680 cm^{-1} and **(c, f)** the sum of OH and OD bands (A_{OH} + βA_{OD}) with time of annealing. Slice SER17, annealed at 425°C, with a thickness of 182 μm; slice SER13, annealed at 500 °C, with a thickness of 273 μm.

To have a better understanding of the behavior of this bands transfer, peak deconvolutions of the evolution spectra were performed. Figure 5.6 shows the quantitative evolution of the four bands and the two associated H-defects. The latter can be followed by plotting the evolution of the sum of OH and OD integral absorbance, taking account of the difference of the extinction coefficient of the two isotopes ($A_{OH} + \beta A_{OD}$; see more explanations in the description of Table 5.4). The interesting feature is that the total concentration of the defects associated to the two bands remains constant overall the experiment and only their relative proportions adjust during the exchange (sum of the absorbances; Fig. 5.6c, f). This suggests that the two defects are probably two configurations (giving rise to lower-frequency and higher-frequency bands) of a same defect with very similar energies.

We plotted for all the slices the evolution of relative proportion of these two configurations, in the form of OH, OD bands and the sum of OH and OD bands, against the fraction of remaining OH in the sample during H-D exchange. For clarity, evolution data were shown for SER17 and SER13, while only the relative proportion at the final step was shown for the other slices (Fig. 5.7). We found that the proportion of the two configurations associated with the same species correlates to the fraction of remaining OH, that mark the progress of the exchange (for OH species, $A_{3628}/(A_{3628} + A_{3634})$ is positively proportional to A_{OH}/A_{OH0}; for OD species, $A_{2677}/(A_{2677} + A_{2680})$ is positively proportional to A_{OD}/A_{OD}; Fig. 5.7a, b). It is completely reversible comparing H-D and D-H exchange for the same sample (SER04 and SER13). It is not simply correlated to temperature, thickness or initial concentration of H, for the seven slices. The H-defects tend to present configuration giving rise to higher-frequency bands when its overall content is high and lower-frequency bands when it is low (i.e. for OH species, 3634 cm^{-1} and 3628 cm^{-1} bands are favored respectively when overall OH content is high and low; for OD species, 2688 cm^{-1} and 2677 cm^{-1} bands are favored respectively when overall OD content is high and low). It is expected that, if a total H-D exchange could be completed the ratio of $A_{2677}/(A_{2677} + A_{2680})$ and $(A_{3628} + \beta A_{2677})/[(A_{3628} + \beta A_{2677}) + (A_{3628} + \beta A_{2677})]$ would be the same as $A_{3628}/(A_{3628} + A_{3634})$ at the beginning (Fig. 5.7c).

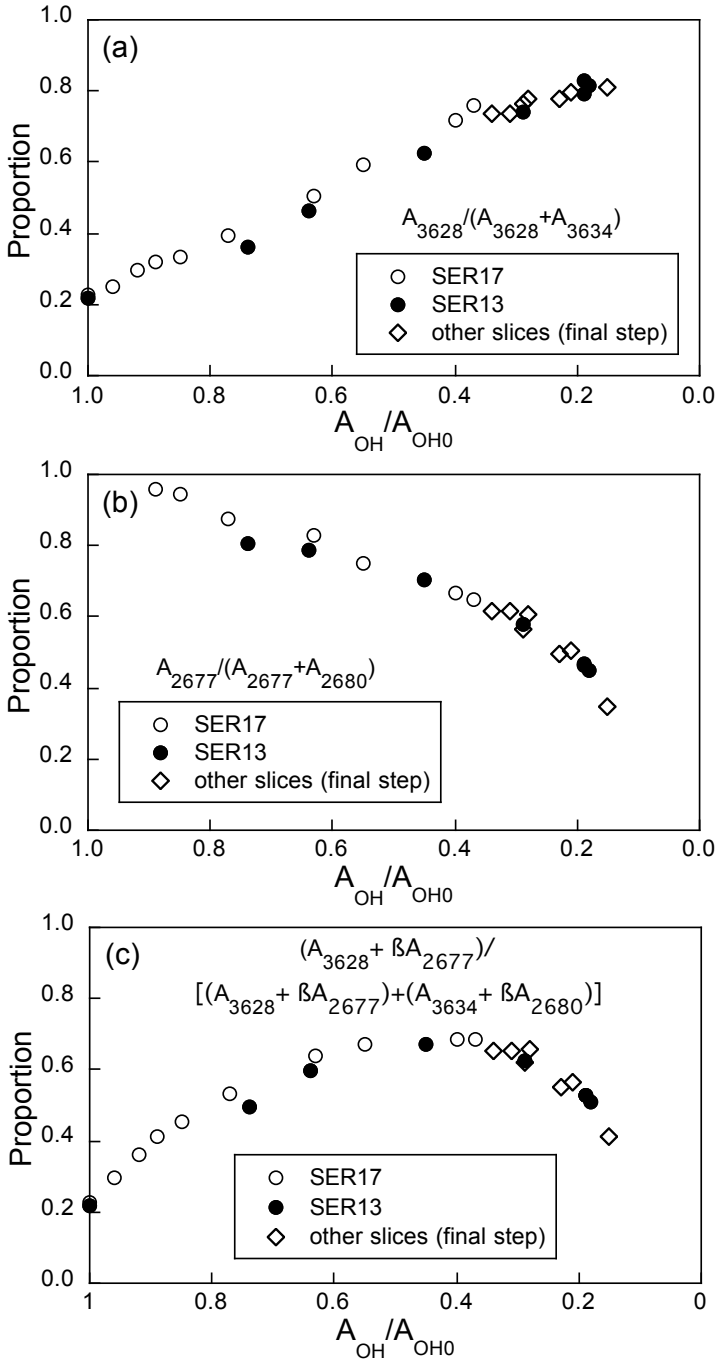

Figure 5.7. Relationship between the relative proportion of the two configurations for a) OH bands, b) OD bands, (c) sum of OH and OD bands and the fraction of remaining OH (A_{OH}/A_{OH0}) during H-D exchange.

The particular behavior of these bands shows that some local adjustment occurs during annealing but it does not affect the overall diffusion process and the measured diffusion coefficients.

5.5 Diffusion kinetics

Diffusion kinetics for H-D exchange

Another important specific feature of H-D exchange in andradite is that, like for the extraction experiments performed earlier (Kurka 2005, Phichaikamjornwut et al. 2012), the exchange is never complete, 15 to 35% of the original OH bands absorbance remains after H-D exchange (Table 5.4). Even if the annealing time is prolonged by a factor of 4, the absorbance of OH and OD bands remains constant within error uncertainties.

As the absorbance of OH bands A_{OHf} at the final stage of the exchange is not null, it was considered that the corresponding amount of H-defects is not available for the H-D exchange. For the exchange we only considered the H-defects corresponding to the difference between the initial absorbance, at time $t = 0$ and the final absorbance ($A_{OH0} - A_{OHf}$) when a steady state is reached (Table 5.4). Therefore, the evolution with time t of OH and OD bands during H-D exchange is best represented by the normalized values: $(A_{OH} - A_{OHf})/(A_{OH0} - A_{OHf})$ and A_{OD}/A_{ODf} (Table 5.4); where A_{OH} and A_{OD} are the absorbances of OH and OD bands at time t and A_{ODf} is the absorbance of OD bands at the final stage of exchange when A_{OD} has reached a steady state maximum value (Table 5.4). For reverse experiments, D-H exchanges, the evolution with time of the exchange is represented by the normalized values: $(A_{OH} - A_{OH0})/(A_{OHf} - A_{OH0})$ and A_{OD}/A_{OD0}, where A_{OH0} and A_{OD0} are here the absorbances of the bands at the beginning of the D-H exchange ($t = 0$) and A_{OHf} is here the value of A_{OH} at the end of D-H exchange.

Table 5.4. Experimental data from H-D and D-H exchange.

H-D exchange

t (h)	A_{OH}	A_{OD}	$A_{OH}-A_{OHf}$	$(A_{OH}-A_{OHf})/(A_{OH0}-A_{OHf})$	A_{OD}/A_{ODf}	$A_{OH}+\beta A_{OD}$
SER04; 600 °C; 2L = 277 μm; size = 3.0 × 2.0 mm^2; $A_{OH0} - A_{OHf}$ = 42.78 - 5.77 = 37.01; A_{ODf} = 22.42						
0.00	42.78	0.00	37.01	1.00	0.00	42.78
1.00	9.05	20.62	3.28	0.09	0.92	43.28
3.00	6.52	23.02	0.75	0.02	1.03	44.73
7.00	9.62	20.94	3.85	0.10	0.93	44.37
15.00	6.80	21.88	1.03	0.03	0.98	43.13
31.00	5.77	22.42	0.00	0.00	1.00	42.98
63.00	6.30	22.28	0.53	0.01	0.99	43.28
SER13; 500 °C; 2L = 273 μm; size = 3.0 × 2.0 mm^2; $A_{OH0} - A_{OHf}$ = 60.13 - 10.78 = 49.35; A_{ODf} = 29.81						
0.00	60.13	0.00	49.35	1.00	0.00	60.13
1.00	44.50	9.40	33.72	0.68	0.32	60.10
2.00	38.58	13.62	27.80	0.56	0.46	61.19
4.00	27.30	19.91	16.52	0.33	0.67	60.35
8.00	17.56	25.29	6.78	0.14	0.85	59.54
16.00	11.60	28.98	0.82	0.02	0.97	59.71
32.00	10.78	29.81	0.00	0.00	1.00	60.26
64.00	11.33	29.16	0.55	0.01	0.98	59.74
SER13; 550 °C; 2L = 273 μm; size = 3.0 × 2.0 mm^2 (second annealing); $A_{OH0} - A_{OHf}$ = 57.92 - 17.05 = 40.87; A_{ODf} = 25.46						
0.00	57.92	0.30	40.87	1.00	0.00	58.42
0.50	48.87	6.69	31.82	0.78	0.25	59.98
1.00	41.71	11.10	24.66	0.60	0.43	60.14
2.00	29.88	17.45	12.83	0.31	0.68	58.85

Table 5.4. continued.

H-D exchange

t (h)	A_{OH}	A_{OD}	A_{OH}-A_{OHf}	(A_{OH}-A_{OHf})/ (A_{OH0}-A_{OHf})	A_{OD}/A_{ODf}	$A_{OH}+\beta A_{OD}$
4.00	21.08	23.17	4.03	0.10	0.91	59.54
8.00	18.23	25.05	1.18	0.03	0.98	59.81
16.10	24.88	21.34	7.83	0.19	0.84	60.30
32.10	19.84	23.90	2.79	0.07	0.94	59.51
64.10	17.05	25.46	0.00	0.00	1.00	59.31
SER15; 600 °C; 2L = 671 μm; size = 3.2 × 2.4 mm^2; A_{OH0} - A_{OHf} = 159.87 - 33.54 = 126.33; A_{ODf} = 74.34						
0.00	159.87	0.00	126.33	1.00	0.00	159.87
0.50	138.01	12.30	104.47	0.83	0.17	158.43
1.00	129.85	19.46	96.31	0.76	0.26	162.15
2.00	121.94	24.99	88.40	0.70	0.34	163.42
4.00	117.57	26.71	84.03	0.67	0.36	161.91
8.00	100.83	38.74	67.29	0.53	0.52	165.14
16.00	80.84	51.13	47.30	0.37	0.69	165.72
32.00	53.74	64.27	20.20	0.16	0.86	160.43
64.25	37.63	68.89	4.09	0.03	0.93	151.99
105.25	33.54	74.34	0.00	0.00	1.00	156.94
183.25	40.71	67.40	7.17	0.06	0.91	152.59
SER16-P3; 550 °C; 2L = 236 μm; size = 4.0 × 2.7 mm^2; A_{OH0} - A_{OHf} = 16.33 - 5.57 = 10.76; A_{ODf} = 6.32						
0.00	16.33	0.00	10.76	1.00	0.00	16.33
0.50	11.24	3.16	5.67	0.53	0.50	16.49
1.00	8.36	4.50	2.79	0.26	0.71	15.83
2.07	5.65	6.32	0.08	0.01	1.00	16.14

Table 5.4. continued.

H-D exchange

t (h)	A_{OH}	A_{OD}	A_{OH}-A_{OHf}	(A_{OH}-A_{OHf})/ (A_{OH0}-A_{OHf})	A_{OD}/A_{ODf}	$A_{OH}+\beta A_{OD}$
4.07	5.93	6.22	0.36	0.03	0.98	16.26
8.07	5.57	6.32	0.00	0.00	1.00	16.06
SER16-P6; 550 °C; 2L = 236 μm; size = 4.0 × 2.7 mm^2; A_{OH0} - A_{OHf} = 36.04 - 11.10 = 24.94; A_{ODf} = 14.58						
0.00	36.04	0.00	24.94	1.00	0.00	36.04
0.50	27.56	5.46	16.46	0.66	0.37	36.62
1.00	21.40	8.87	10.30	0.41	0.61	36.12
2.07	12.87	13.47	1.77	0.07	0.92	35.23
4.07	11.96	14.18	0.86	0.03	0.97	35.50
8.07	11.10	14.58	0.00	0.00	1.00	35.30
SER17; 425°C; 2L = 182 μm; size = 4.5 × 4.0 mm^2; A_{OH0} - A_{OHf} = 42.30 - 15.58 = 26.72; A_{ODf} = 15.93						
0.00	42.30	0.00	26.72	1.00	0.00	42.30
0.50	40.61	1.05	25.03	0.94	0.07	42.35
1.00	39.06	1.53	23.48	0.88	0.10	41.60
2.00	37.81	2.63	22.23	0.83	0.17	42.18
4.00	36.13	3.60	20.55	0.77	0.23	42.11
8.00	32.52	5.65	16.94	0.63	0.35	41.90
16.00	26.45	8.85	10.87	0.41	0.56	41.14
32.08	23.27	11.35	7.69	0.29	0.71	42.11
64.18	16.97	14.95	1.39	0.05	0.94	41.79
153.32	15.58	15.93	0.00	0.00	1.00	42.02

Table 5.4. continued.

H-D exchange

t (h)	A_{OH}	A_{OD}	A_{OH}-A_{OHf}	(A_{OH}-A_{OHf})/ (A_{OH0}-A_{OHf})	A_{OD}/A_{ODf}	A_{OH}+βA_{OD}
SER18; 700 °C; 2L = 596 μm; size = 4.5 × 3.0 mm^2; A_{OH0} - A_{OHf} = 117.92 - 26.92 = 91.00; A_{ODf} = 53.71						
0.00	117.92	0.00	91.00	1.00	0.00	117.92
1.00	61.99	35.80	35.07	0.39	0.67	121.42
2.00	44.24	45.59	17.32	0.19	0.85	119.92
4.00	27.97	53.13	1.05	0.01	0.99	116.17
8.00	29.72	51.98	2.80	0.03	0.97	116.01
16.00	26.92	53.71	0.00	0.00	1.00	116.08
SER19; 500 °C; 2L = 140 μm; size = 5.0 × 2.8 mm^2; A_{OH0} - A_{OHf} = 34.17 - 9.69 = 24.48; A_{ODf} = 14.53						
0.00	34.17	0.00	24.48	1.00	0.00	34.17
0.50	22.85	6.62	13.16	0.54	0.46	33.84
1.00	18.68	9.44	8.99	0.37	0.65	34.35
2.00	15.05	11.46	5.36	0.22	0.79	34.07
4.00	12.32	13.05	2.63	0.11	0.90	33.98
8.12	10.83	14.05	1.14	0.05	0.97	34.15
32.00	9.69	14.53	0.00	0.00	1.00	33.81

Table 5.4. continued.

D-H exchange

t (h)	A_{OH}	A_{OD}	$A_{OH}-A_{OH0}$	$(A_{OH}-A_{OH0})/(A_{OHf}-A_{OH0})$	A_{OD}/A_{OD0}	$A_{OH}+\beta A_{OD}$
SER04; 600 °C; 2L = 277 μm; size = 3.0 × 2.0 mm^2; A_{OHf} - A_{OH0} = 43.43 - 6.30 = 37.13; A_{OD0} = 22.28						
0.00	6.30	22.28	0.00	0.00	1.00	43.28
1.00	41.60	1.66	35.30	0.95	0.07	44.35
2.00	43.43	0.47	37.13	1.00	0.02	44.21
6.00	38.31	2.75	32.01	0.86	0.12	42.87
14.00	43.09	0.32	36.79	0.99	0.01	43.62
SER13; 400 °C; 2L = 273 μm; size = 3.0 × 2.0 mm^2; A_{OHf} - A_{OH0} = 57.92 - 11.33 = 46.59; A_{OD0} = 29.16						
0.00	11.33	29.16	0.00	0.00	1.00	59.74
8.00	23.94	21.87	12.61	0.27	0.75	60.24
16.00	30.12	17.76	18.79	0.40	0.61	59.60
32.00	38.01	13.44	26.68	0.57	0.46	60.32
64.33	49.83	6.91	38.50	0.83	0.24	61.30
128.33	57.28	1.68	45.95	0.99	0.06	60.07
178.00	57.92	0.30	46.59	1.00	0.01	58.42

Notes: *t* is the time of annealing at nominal temperature; 2L is the thickness of the slice; A_{OH} and A_{OD} are the integral absorbance of the OH and OD respectively; A_{OH0} and A_{OHf} are the integral absorbance of OH bands at $t = 0$ and at the final stage of exchange; A_{OD0} and A_{ODf} are the integral absorbance of OD bands at $t = 0$ and at the final stage of exchange, respectively; ($A_{OH} + \beta A_{OD}$) is the total integral absorbance considering both OH and OD bands adjusted by the ratio of the extinction coefficients $\beta = \varepsilon_{OH}/\varepsilon_{OD}$. *The two points of analysis P3 and P6 correspond to the concentration of the two sectors observed in SER16 (see text). It was used to test the possible impact of concentration on the result of H-D exchange.

The last column of Table 5.4 shows the value of ($A_{OH} + \beta A_{OD}$), where β is the ratio of the extinction coefficient of OH and OD, $\varepsilon_{OH}/\varepsilon_{OD}$. ($A_{OH} + \beta A_{OD}$) represents the total concentration of H-defects present in the sample during the H-D exchange. β is deduced from the value ($A_{OH0} - A_{OHf}$)/A_{ODf} for each H-D exchange and ($A_{OHf} - A_{OH0}$)/A_{OD0} for each D-H exchange (Table. 5.5). An average value of 1.66 ± 0.03 was measured. The almost constant value of ($A_{OH} + \beta A_{OD}$), which accounts to the total value of integral absorbance of OH and OD bands, indicates that there is no loss of hydrous species during the experiments. It must be noted also that at the end of two D-H exchange experiments (SER04 and SER13) the exchange is almost complete with A_{OD} almost at zero.

Table 5.5. Deduced β value for each H-D and D-H exchange.

Sample No.	β (H-D)	β (D-H)	β (total)
SER04	1.65		1.65
SER04		1.68	1.68
SER13	1.66		1.66
SER13		1.61	1.61
SER13	1.62		1.62
SER15	1.68		1.68
SER16-P3	1.70		1.70
SER16-P6	1.71		1.71
SER17	1.68		1.68
SER18	1.64		1.64
SER19	1.69		1.69
Average			1.66

The evolution with time *t* of the normalized values of the H-D and D-H are presented in Figure 5.8. For each experiment, a diffusion coefficient *D* is deduced from the fit by equation (2.1) for the decreasing species and equation (2.2) for the increasing species (solid line; Fig. 5.8). The error bars on *D* are estimated from the extreme values that still fit the data within the experimental uncertainties (dashed lines; Fig. 5.8). The diffusion coefficients deduced from the two reverse experiments (D-H exchange) are close to the ones deduced from H-D exchange showing that the kinetics is the same for the two processes (Fig. 5.8; Table 5.7).

For SER15 and SER18 each, initial IR spectrum has saturated OH bands due to large thickness and the OH absorbance was no longer proportional to thickness. Thus we used, a posteriori, the average value of $(A_{OH} + \beta A_{OD})$ at each step, as initial value. A complete restoration of OH bands after rehydrogenation during D-H exchange demonstrates the reversibility of the exchange experiments. A steady-state was reached for all the runs at the end of the exchange experiments, which can be readily seen from the integral absorbance ratio versus *t* plot where the data points for the longer durations slightly fluctuate around an equilibrium value (Fig. 5.8).

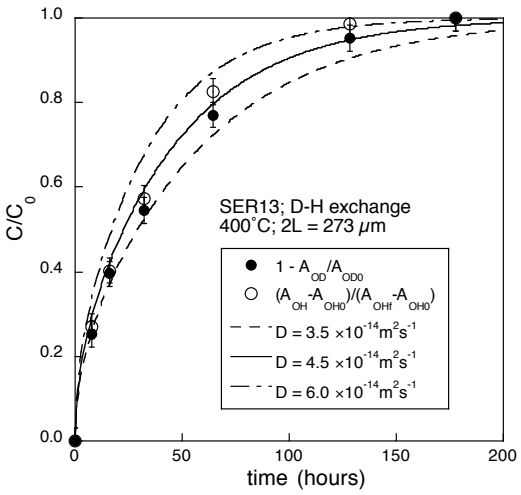

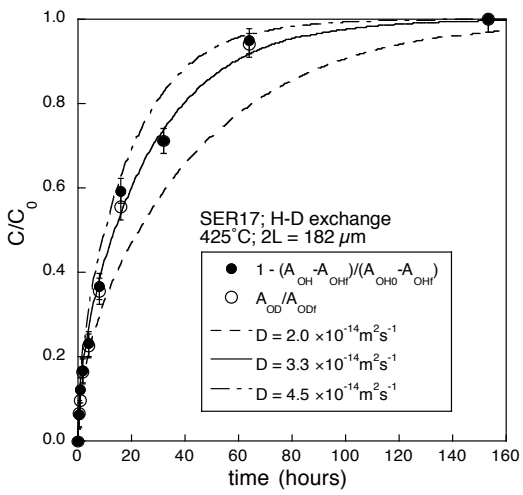

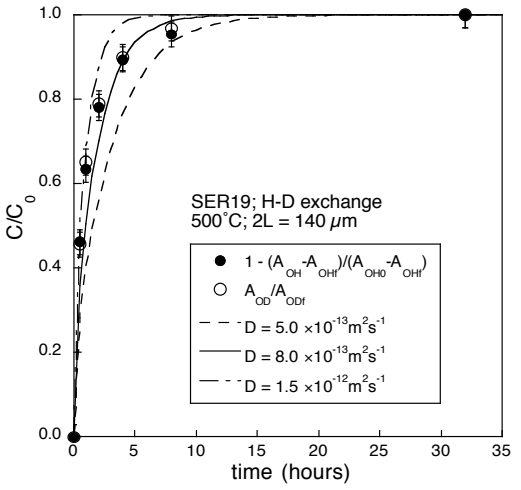

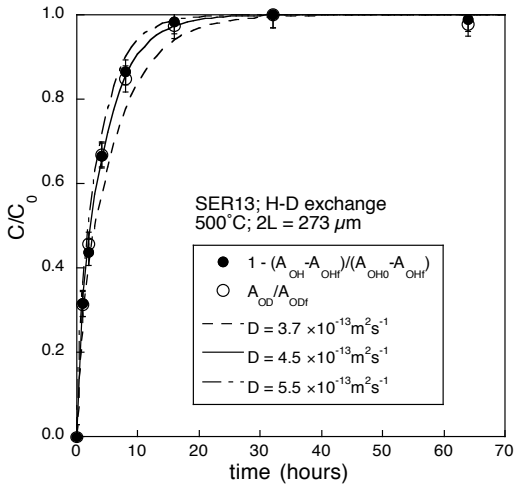

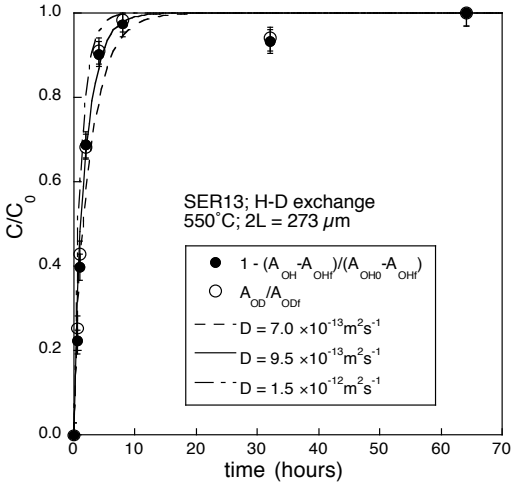

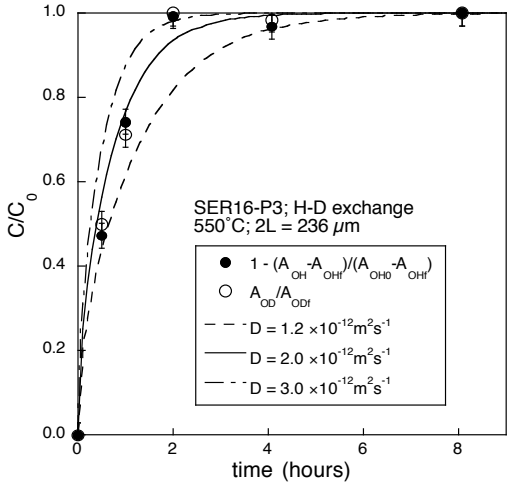

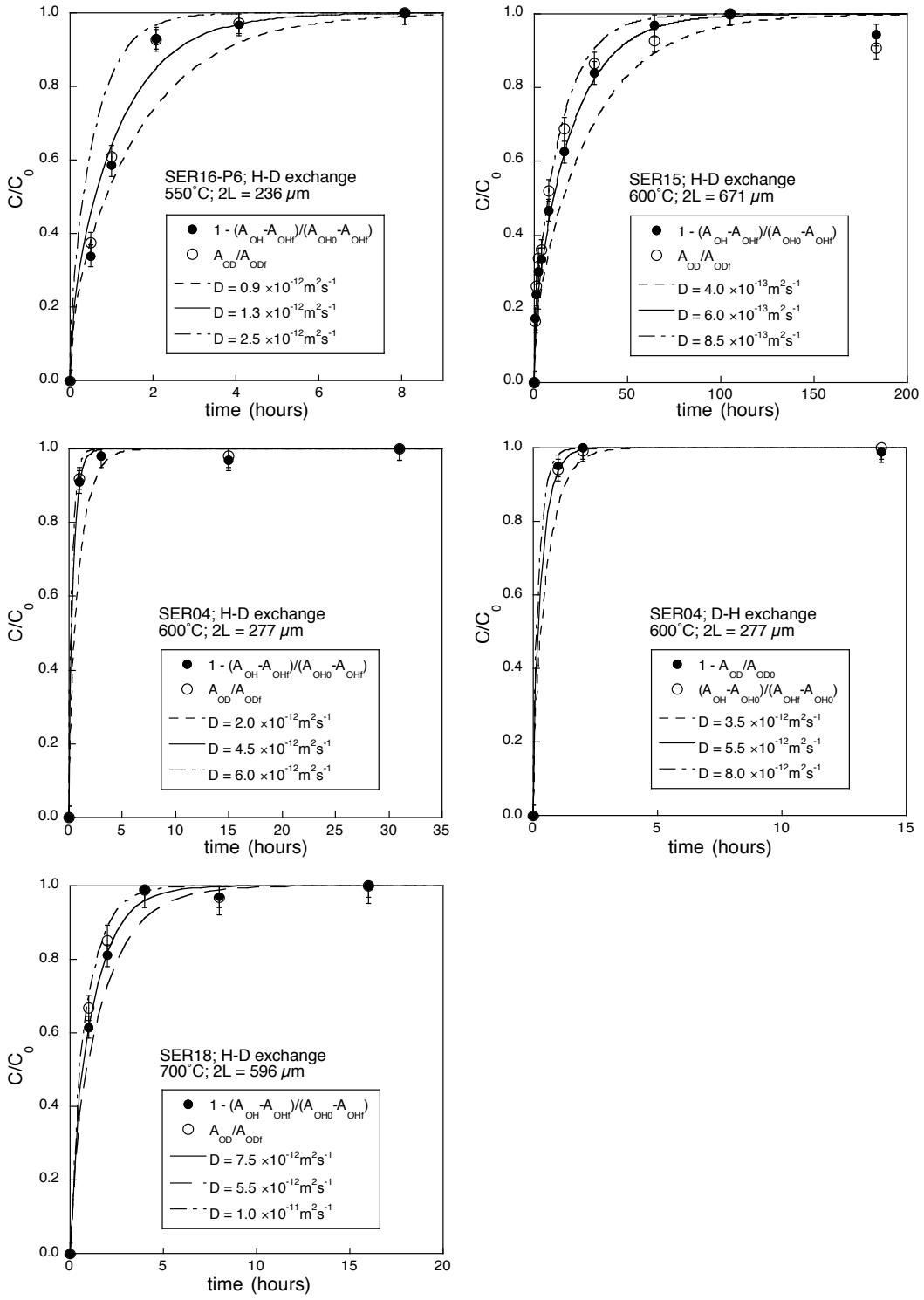

Figure 5.8. Fits of data by equation (3.18) and (3.20) for H-D and D-H experiments at temperatures between 400 and 700 °C (continuous line). Empty circles represent the evolution of the increasing species: OD bands for H-D exchange (resp. OH bands for D-H exchange). Solid circles represent the evolution of the decreasing species: OH bands for H-D exchange (resp. OD bands for D-H exchange). Error bars on *D* are deduced from the range of *D* values that still fit the data (discontinuous lines).

Diffusion kinetics for H-extraction

Further annealing for SER16, conducted at 800 °C under the same atmosphere, leads to gradually loss of hydrogen from the crystal since (A_{OH} + βA_{OD}) decreased with time (Table. 5.6), which means that extraction occurs concurrently with H-D exchange at this temperature. It should be noted that the values at t = 0 in Table 5.6 are the values for the last step of annealing at 700 °C. Extraction kinetics was calculated for SER16-P3 and P6 using the progressive decrease of all the hydrous species (OH and OD) represented by the quantity (A_{OH} + βA_{OD}) (Fig. 5.9).

It should be noted that a small area of dark coating appeared on the surface when the slice was annealing at 800 °C for 52 min and the dark coating grew with prolonged annealing. Slight change in color to a darker color was also observed in grossular annealed in air at higher temperature (Kurka 2005). An oxidation of Fe^{2+} was suggested by this author. However, it cannot be the case in our sample since there is no Fe^{2+} present. Extraction occurs concurrently with H-D exchange only at higher temperature, indicating that mechanism involved in extraction has a higher activation energy, than H-D exchange.

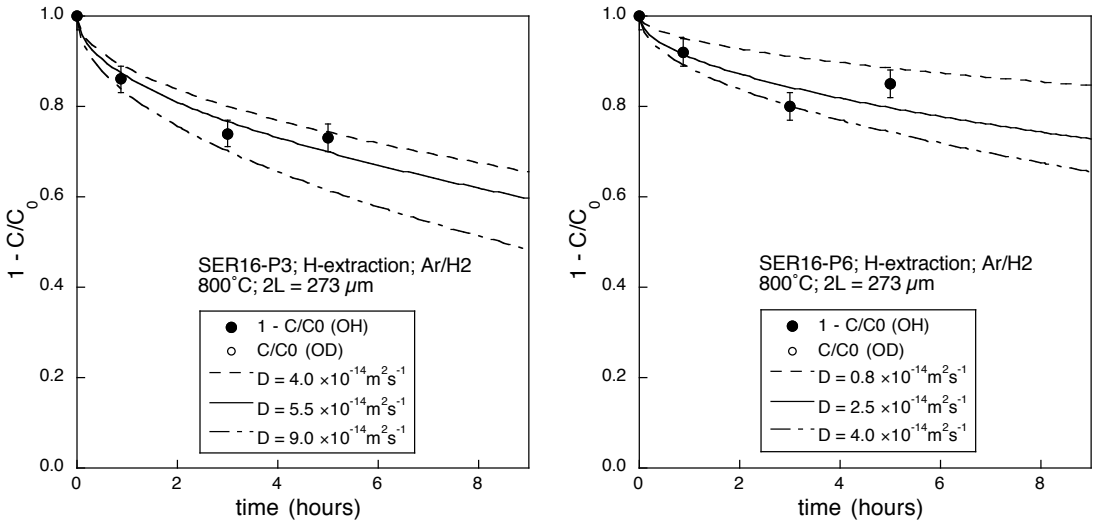

Figure 5.9. Decreasing of value of (A_{OH} + βA_{OD}) as a function of time for SER16 further annealing at 800 °C under the same atmosphere as for H-D exchange at 700 °C.

Table 5.6. Experimental data for further annealing of SER16 at 800 °C under the same atmosphere as for 700 °C.

t (h)	A_{OH}	A_{OD}	$A_{OH}+\beta A_{OD}$	$(A_{OH}+\beta A_{OD})/(A_{OH}+\beta A_{OD})_i$
SER16-P3; 800 °C				
0.00	5.57	6.32	16.06	1.00
0.87	3.10	6.54	13.96	0.87
3.00	2.42	5.78	12.01	0.75
5.00	2.42	5.61	11.73	0.73
SER16-P6; 800 °C				
0.00	11.10	14.58	35.30	1.00
0.87	6.52	15.81	32.76	0.93
3.00	6.28	13.42	28.56	0.81
5.00	6.39	14.41	30.31	0.86

Note: The values at $t = 0$ are the values for the last step of annealing at 700 °C.

5.6 Diffusion law

All bands follow the same kinetics regarding exchange of H by D or D by H. It is also true for the bands at 3634 and 3628 cm^{-1} mentioned above if the global evolution of the couple of bands is considered. The deduced diffusion coefficients, listed in Table 5.7, are fitted to an Arrhenius law (Fig. 5.10). Following the least-square cubic method proposed by York (1966), the least-square fits lead to the diffusion law:

$$D = D_0 \exp\left[-\frac{(96 \pm 11) kJ/mol}{RT}\right] \text{with } \log D_0 \text{ (in } m^2/s) = -5.9 \pm 0.7. \qquad (5.2)$$

The uncertainties correspond to the uncertainties of the least-square fitting taking account of the uncertainty on T (fixed at 5 °C) and the individual uncertainties on D.

The diffusion coefficients deduced from the two points of SER16 (P3 and P6), are similar within the uncertainty of the experiments. It confirms that kinetics of H-D exchange is not strongly dependent on the concentration of H-defects. H-D and D-H

experiments performed in a same slice show also that the kinetics of the reverse experiment is not affected by the duration of the previous H-D experiment. It was observed that a fast exchange starts immediately with the annealing in D-rich atmosphere (see SER04 experiments, Table 5.4). It demonstrates that the incomplete exchange in the H-D experiment is not due to a slow down of the kinetics linked to a dependence of the diffusion coefficient with H concentration but that a steady-state is reached for the exchange. It looks as if a fraction of the H in the structure was not accessible for the H-D exchange. The shape of the remaining OH spectrum at the end of the H-D exchange experiments is identical to the original spectrum, except for the small changes affecting the bands at 3634 and 3628 cm^{-1} (Fig. 5.1, 5.5). Thus, the fraction of H not accessible for H-D exchange is linked to a specific H-defect but affect all the types of OH bands. The complete rehydrogenation (SER04 and SER13) shows also that no irreversible change occurs in the sample during annealing (Fig. 5.1; Table 5.4). Slices with different thicknesses performed at the same temperature (SER 04 and SER15 at 600 °C; SER13 and SER19 at 500 °C) give similar diffusion.

Table 5.7. Summary of diffusion coefficients from H-D and D-H exchanges.

Sample No.	T (°C)	Experiments	D (m^2s^{-1})
SER04	600	H-D exchange	$(4.5 \pm 2.5) \times 10^{-12}$
SER04	600	D-H exchange	$(5.5 \pm 2.5) \times 10^{-12}$
SER13	500	H-D exchange	$(4.5 \pm 1.0) \times 10^{-13}$
SER13	400	D-H exchange	$(4.5 \pm 1.5) \times 10^{-14}$
SER13	550	H-D exchange	$(9.5 \pm 2.0) \times 10^{-13}$
SER15	600	H-D exchange	$(6.0 \pm 2.5) \times 10^{-13}$
SER16-P3	550	H-D exchange	$(2.0 \pm 1.0) \times 10^{-12}$
SER16-P6	550	H-D exchange	$(1.3 \pm 1.2) \times 10^{-12}$
SER17	425	H-D exchange	$(3.3 \pm 1.3) \times 10^{-14}$
SER18	700	H-D exchange	$(7.5 \pm 2.5) \times 10^{-12}$
SER19	500	H-D exchange	$(8.0 \pm 3.5) \times 10^{-13}$

Note: The error bars on *D* are estimated from the extreme values deduced from Fig. 5.8.

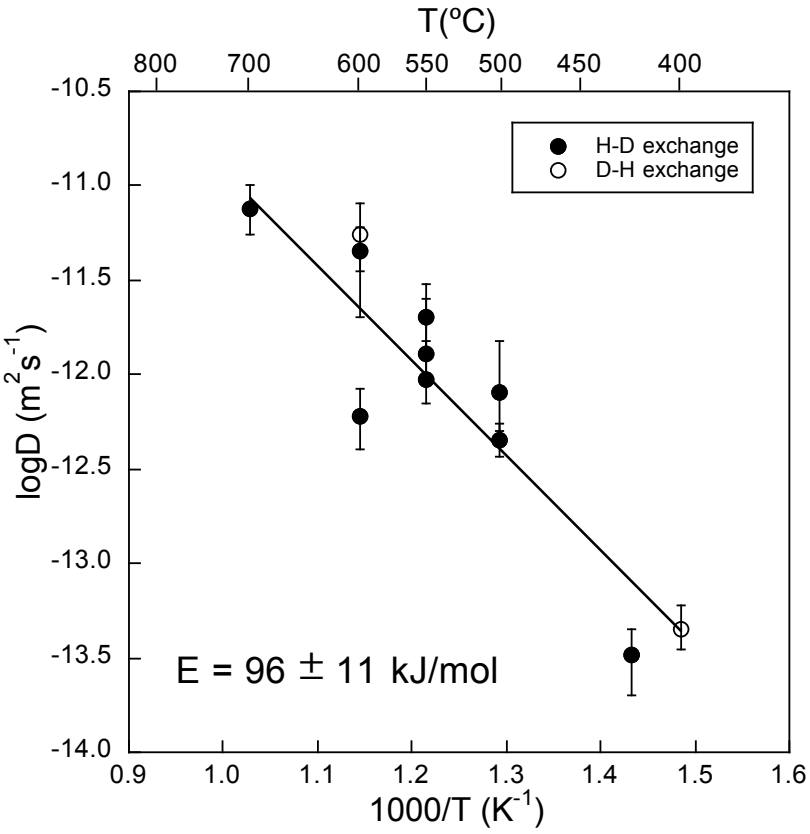

Figure 5.10. Arrhenius plot showing diffusion data for H-D and D-H exchange and the associated fit law.

5.7 Discussion

5.7.1 Comparison with H-extraction with oxidizing conditions

Kinetics of H-extraction in andradite under oxidizing conditions have been measured by Kurka (2005) in an andradite sample (SER12) similar to ours and by Phichaikamjornwut et al. (2012) whose andradite sample (KPK54-9) has composition very close to ours. The reducing condition of our ($Ar/D_{2(10\%)}$) experiments at 800°C corresponds to a pO_2 of 10^{-20} atm., far from the oxidizing condition of experiments in air (Table 5.8).

Figure 5.11 represents the plot of the dependence of the diffusion coefficient of H-extraction in andradite as a function of pO_2. The deduced dependence follows relation:

$$D_{H-extr} \propto pO_2^{0.05\pm0.01} \quad (5.3)$$

Table 5.8. Diffusion coefficients for H-extraction performed at 800 °C for andradite with different values of oxygen partial pressure (pO_2).

Sample No.	Atmosphere	pO_2 (atm)	D (m^2s^{-1})
SER12	air	0.21	$(4.0 \pm 2.0) \times 10^{-13}$
KPK54-9	air	0.21	$(2.0 \pm 2.0) \times 10^{-13}$
SER16-P3	Ar/D_2	1.0×10^{-20}	$(5.5 \pm 3.0) \times 10^{-14}$
SER16-P6	Ar/D_2	1.0×10^{-20}	$(2.5 \pm 1.5) \times 10^{-14}$

Notes: SER12, Kurka (2005); KPK54-9, Phichaikamjornwut et al. (2012); SER16-P3, P6, this study.

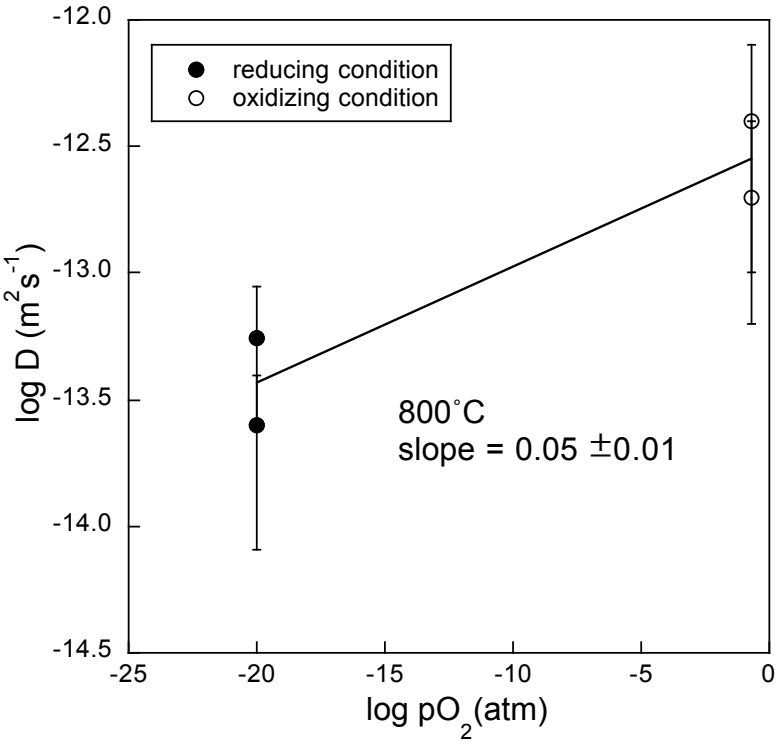

Figure 5.11. Kinetics of H-extraction in andradite plotted against oxygen partial pressure.

A dependence on pO_2 with an exponent of 0.22 (± 0.04) was found by Kurka (2005) for two grossulars, with composition of $Gr_{83}An_{14}$ and $Gr_{73}An_{23}$ respectively. Thus, H-extraction for andradite shows less dependence on pO_2 compared to that for grossular.

5.7.2 Comparison with H-D exchange diffusion laws in NAMs

Figure 5.12 shows a comparison between the diffusion laws for H-D exchange in andradite and several other NAMs. With 96 ± 11 kJ/mol, the activation energy of andradite falls in the lowest range of activation energy of hydrogen diffusion in NAMs, close to the value measured for grossular $Gr_{83}An_{14}$. The activation energies deduced for NAMs are in the range 100-190 kJ/mol (grossular $Gr_{83}An_{14}$: 102 kJ/mol, Kurka et al. 2005; grossular $Gr_{73}An_{23}$: 190 kJ/mol, Kurka 2005; Dora Maria pyrope: 140 kJ/mol, Blanchard and Ingrin 2004a; diopside: 145 kJ/mol, Hercule and Ingrin 1999; olivine // a: 140 kJ/mol, Du Frane et al. 2012; forsterite // c: 134 kJ/mol, Ingrin and Blanchard (2006); quartz // c: 176 kJ/mol, Kats et al. 1962). It is also the fastest diffusion rate in NAMs and it is two orders of magnitude faster than in other garnets, at 700°C (Fig. 5.12). Data of H-D exchange are generally assumed to represent the mobility of hydrogen as a single proton hopping from one oxygen site to another (see for instance, Hercule and Ingrin 1999 and Ingrin et al. 2001 for diopside). The activation energy of hydrogen diffusion in andradite is comparable to the one of other NAMs; a similar mechanism for hydrogen diffusion is highly probable.

A possible explanation for the lower activation energy for H diffusion in grossualr and andradite than for pyrope (102 and 96 compared to 140 kJ/mol). Armbruster and Geiger (1993) calculated bond valences for numbers of end-member and nearly end-member silicate garnets using the constants given by Brese and O'Keefe (1991). In accord with the crystal chemical interpretation of Shannon and Rossman (1992), these calculations reveal that Ca on the dodecahedral (X) site in grossular and andradite is strongly overbonded (2.51 and 2.32 valence units, respectively), while Mg and Fe in pyrope and almandine are underbonded (1.72 and 1.79 valence units,

respectively). Nearly ideal bond valences are gained for the octahedral (Y) and tetrahedral (Z) site in pyrope, almandine and andradite. In garnet, every oxygen atom is coordinated by 2X-, 1Y- and 1Z-cation. According to Pauling's rules, the electrostatic valence for oxygen is sum of electrostatic bond strength of adjacent cations, 2X, 1Y and 1Z. The deduced electrostatic valences for oxygen are 2.13, 2.08, 1.93 and 1.95 for end-member grossular, andradite, pyrope and almandine, respectively. Hence, oxygen in grossular and andradite is overbonded while in pyrope and almandine is underbonded.

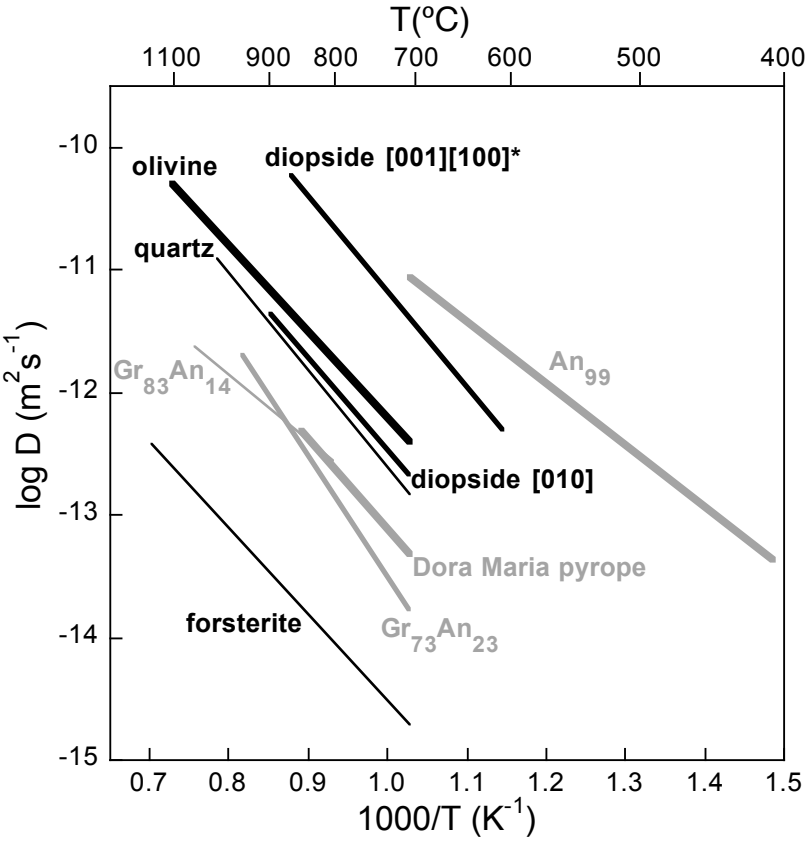

Figure 5.12. Compilation of diffusion laws for H-D exchange in NAMs. $Gr_{83}An_{14}$: Kurka et al. (2005); $Gr_{73}An_{23}$: Kurka (2005); Dora Maira pyrope: Blanchard and Ingrin (2004a); diopside: Hercule and Ingrin (1999); olivine // a: Du Frane et al. (2012); forsterite // c: Ingrin and Blanchard (2006); quartz // c: Kats et al. (1962); An_{99}: this study.

In view of hydrogen diffusion as a single proton hopping from one oxygen site to another, Weaker forces of attraction should be expected between proton and overbonded oxygen (in grossular and andradite) compared to proton and underbonded oxygen (in pyrope and almandine). Therefore, a lower activation energy of migration of protons could be expected in grossular and andradite compared to pyrope and almandine. Some authors also propose that more closely packed structure would increase the potential energy barrier to diffusion when considered ionic porosity, the fraction of the unit-cell volume in a mineral not occupied by ions (mostly oxygen atoms; e.g., Brady and Cherniak 2010; Zhao and Zheng 2007). Grossular and andradite have a larger ionic porosity than pyrope. It may also account for the lower activation energy observed for H diffusion.

5.7.3 Comparison with H-extraction/incorporation laws in andradite and garnets of the grossular-andradite series

Figure 5.13 shows the chemical diffusion coefficients for H as calculated from extraction experiments in andradite with similar compositions to those described here (An_{99}) compared to the results of H-D and D-H exchanges (Kurka 2005; Ingrin and Blanchard 2006; Phichaikamjornwut et al. 2012). Extraction experiments in air show atleast two distinct diffusivities: hydrogens associated with bands at frequencies below3580 cm^{-1} have a faster diffusion law than the ones associated with bands at frequencies above 3600 cm^{-1} (laws I and II respectively; Fig. 5.13). The activation energies of the extraction laws are higher than those of the H-D exchange (271 and 209 kJ/mol, respectively compared to 96 kJ/mol). This is common in garnets (Kurka 2005; Ingrin and Blanchard, 2006). The diffusivities for H-extraction in An_{99} are one to three orders of magnitude lower than the diffusivity deduced from H-D exchange at 800°C. This means that in An_{99} the process of chemical diffusion involved in H-extraction experiments in air at below 1000°C is not limited by H diffusion, but by a slower mechanism (Fig. 5.13).

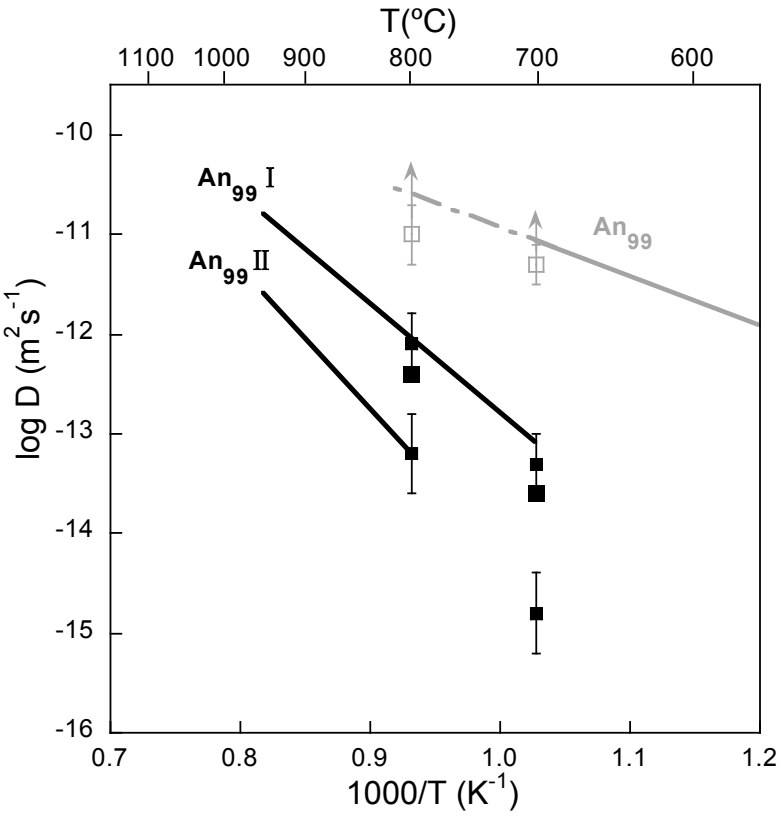

Figure 5.13. Comparison of H-D exchange kinetics with H-extraction and H-incorporation kinetics in An_{99}. Solid and empty squares correspond to the H-extraction and H-incorporation data of An_{99} respectively from Phichaikamjornwut et al. (2012), with the larger ones the original data when taking overall OH bands as a whole and smaller ones the distinct data when separating OH bands into higher-frequency and lower-frequency bands; arrows indicate that these values are probably underestimated; the gray line represent H diffusion law deduced from H-D exchange experiments in this study; the black lines represent H diffusion laws deduced from H-extraction experiments, with An_{99} I for the faster kinetics corresponding to OH bands at lower frequencies and An_{99} II for the slower kinetics corresponding to OH bands at higher frequency bands (Kurka 2005).

An interesting point is that in H-incorporation experiments in H_2 at 700 and 800°C, on the same slices as were used for H-extraction in air, Phichaikamjornwut et al. (2012) observed a diffusion rate one to two orders of magnitude faster than for extraction (empty squares compared to solid squares in Fig. 5.13). The values

measured by Phichaikamjornwut et al. (2012) are lower limits since both slices were completely rehydrogenated after the first annealing step (steps of 20 minutes and 1h, respectively). This suggests that the mechanism that controls H incorporation must be different from the one controlling extraction and that H incorporation is potentially fast enough to be limited by the mobility of hydrogen as defined by the diffusion law deduced from H-D exchange.

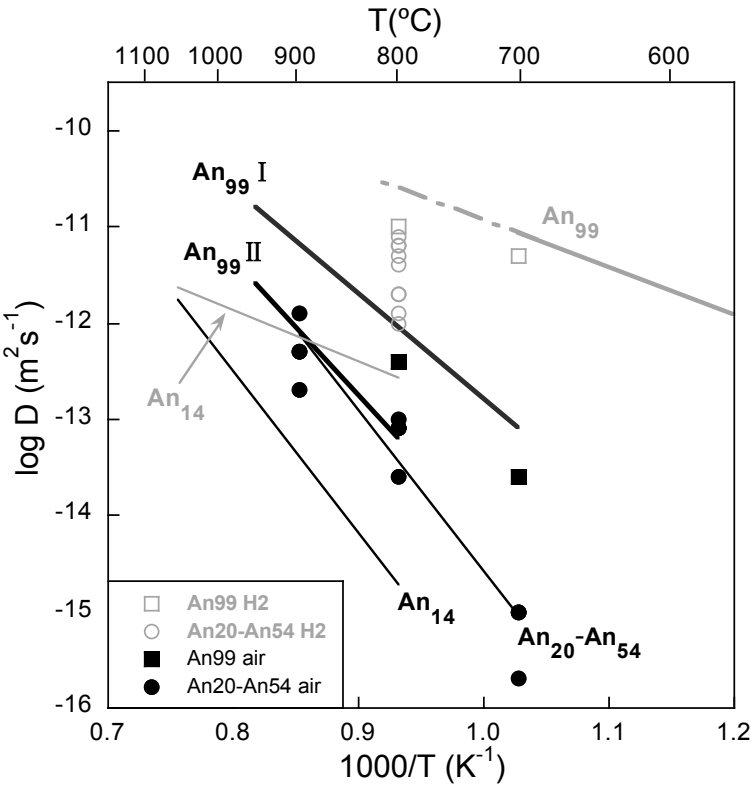

Figure 5.14. Comparison of H-D exchange kinetics with H-extraction and H-incorporation kinetics in the grossular-andradite series. Solid and empty squares correspond to the H-extraction and H-incorporation data of An_{99} while solid and empty circles correspond to the H-extraction and H-incorporation data of An_{20}-An_{45}, respectively from Phichaikamjornwut et al. (2012); the gray lines represent H diffusion laws deduced from H-D exchange experiments (An_{14}: $Gr_{83}An_{14}$, Kurka et al. 2005; An_{99}: this study); the black lines represent H diffusion laws deduced from H-extraction experiments (An_{14}: $Gr_{83}An_{14}$, Kurka et al. 2005; An_{20}–An_{45}, Phichaikamjornwut et al. 2012; An_{99} I (lower-frequency bands), II (higher-frequency bands): Kurka 2005).

Phichaikamjornwut et al. (2012) also showed that the kinetics of H incorporation are faster than kinetics of extraction for other compositions in the grossular-andradite series where iron exists mostly as Fe^{3+} (Fig. 5.14). The activation energies for H-extraction in these garnets are also high compared to the activation energies for H diffusion, 96 – 102 kJ/mol against around 320 – 340 kJ/mol (An_{14}: $Gr_{83}An_{14}$, 323 kJ/mol, Kurka et al. 2005; An_{20} -An_{45}: 338 kJ/mol, Phichaikamjornwut et al. 2012). It is interesting to note that hydrogen diffusivity in the grossular-andradite series increases dramatically with the andradite component: by two orders of magnitude from An_{14} to An_{99} (Fig. 5.14). Since no H-D exchange experiments have been conducted on intermediate compositions it is difficult to say if the rate of diffusion evolves smoothly with the andradite content or if a sharp increase occurs at a critical composition.

In their study of H-extraction in andradite Phichaikamjowut et al. (2012) explained the apparent decrease of the dehydrogenation rate in long experiments by two effects: a dependence of diffusion rate on hydrogen concentration (Wang et al. 1996) and the difference of kinetics between the OH bands that compose the IR spectra (Kurka et al. 2005). These two effects can significantly affect the kinetics of H-extraction but they cannot explain why the same phenomenon is observed in H-D exchange; the concentration of hydrous defects remains constant and OH bands behave globally the same during exchange experiments. The fraction of H-defects that does not participate to the H-D exchange (15 to 35%) cannot be associated with a specific defect since overall shape of the spectrum remains the same during the exchange. These hydrogens must be dispersed in the bulk of the sample: the proportion of these “relict” hydrogens and the quality of the fit of the H-D exchange by a single diffusion process are independent of the thickness of the slices (Fig. 5.8). The exact nature of these heterogeneities in andradite (clustering of H-defects, presence of 2D or 3D defects …) is not completely understood but they are good candidates to explain the specific behavior observed during H-extraction experiments in andradite-rich garnets by previous authors (Kurka 2005; Phichaikamjorn et al. 2012).

The mechanisms of H-extraction and H-incorporation in andradite are still unknown. Phichaikamjornwut et al. (2012) have shown that the redox-reaction Fe^{2+} + OH^{-} = Fe^{3+} + O^{2-} + $1/2H_2$ alone cannot control H-extraction, since most of the time there is not enough Fe^{2+} available in the crystal to remove all the hydrogen atoms. However, there is plenty of Fe^{3+} available for the reverse reaction (H-incorporation). It may explain why H-incorporation is generally faster than H-extraction in andradite and is limited by the mobility of hydrogen. Even if Phichaikamjornwut et al. (2012) did not find evidence of reduction of Fe^{3+} into Fe^{2+} from Mössbauer measurement, Fe^{3+} offers short pathways to balance charges during rehydrogenation.

Determination of the absolute hydrogen concentration in andradite shows a high uncertainty due to the lack of specific calibration (0.18 ± 0.12 wt% H_2O in this andradite). It is difficult in these conditions to estimate the contribution of Fe^{2+} and others multivalent cations such as Mn in the mechanism of H-extraction. The potential role of minor cations in the extraction process of hydrogen in andradite should not be underestimated. Electrical conduction in pyrope-almandine garnets is generally assumed to be controlled by the mobility of small polarons. However, the activation energy of conduction is much lower than the activation energy of H-extraction (120-130 $kJmol^{-1}$; Dai et al. 2012, 2013 compared to 200-300 $kJmol^{-1}$). Therefore, redox reactions cannot alone explain the chemical diffusion of hydrogen in garnet. This strongly suggests that another process with a higher activation energy must be involved. Diffusion of cation vacancies is a good candidate for the control of this process. It is known that the activation energy of diffusion of cations in the X site of garnets (Ca, Fe, Mg, Mn) are comparable to the activation energy of H-extraction (230 – 300 $kJmol^{-1}$; Carlson 2006; Ganguly 2010). Therefore, it is possible that the mobility of this type of vacancies controls H-extraction in andradite. The number of experiments performed on andradite is limited and many issues remain to be answered. We do not know if the kinetics of extraction remains the same after a full cycle of H-extraction and H-incorporation on the same sample. It would not be the case, for instance, if the first H-extraction involves cations reorganizing around the defects allowing local charge balance after H removing (for instance, Mn diffusion at

a neighbor site). No reorganizing would be then needed for the second extraction experiment.

5.7.4 Geological applications

The present results suggest that the kinetics of H-D exchange in andradite is much faster than for other NAMs, and especially faster than the ones of other garnets (Fig. 5.12). This means that the capacity of andradite to retain hydrogen isotropic information about fluid-rock interaction is weaker than in other garnets.

Andradite is a rock-forming garnet typically found in skarns, which are often mined as ore deposits and found in contact metamorphic assemblages like serpentine. The hydrogen isotope information collected from andradite, if preserved during cooling, could be used to indicate the origin of the H_2O in the fluid with which the crystal grew.

We consider here a simple model in which the andradite grain is a sphere with radius a, an initial homogenous concentration C_i and is in contact to a medium with constant concentration C_0. The solution to the diffusion equation at the center of the sphere can then be deduced though the equation (Crank 1975):

$$\frac{C - C_1}{C_0 - C_1} = 1 + 2\sum_{n=1}^{\infty}(-1)^n \exp(-Dn^2\pi^2 t / a^2) \qquad (5.4)$$

We assumed that the concentration at the center of the sphere can be preserved if the dimensionless parameter Dt/a^2 is less than or equal to 0.03. Curves of $Dt/a^2 = 0.03$ for the temperature range 100-700 °C and mineral grains from 1 mm to 10 cm was plotted in Figure. 5.15. These curves give the time-grain radius limits under which initial hydrogen isotope information will be preserved in the center of the grain. For times and grain radius below the curves, concentrations at the center will remain unaffected, but will be changed when above the curves.

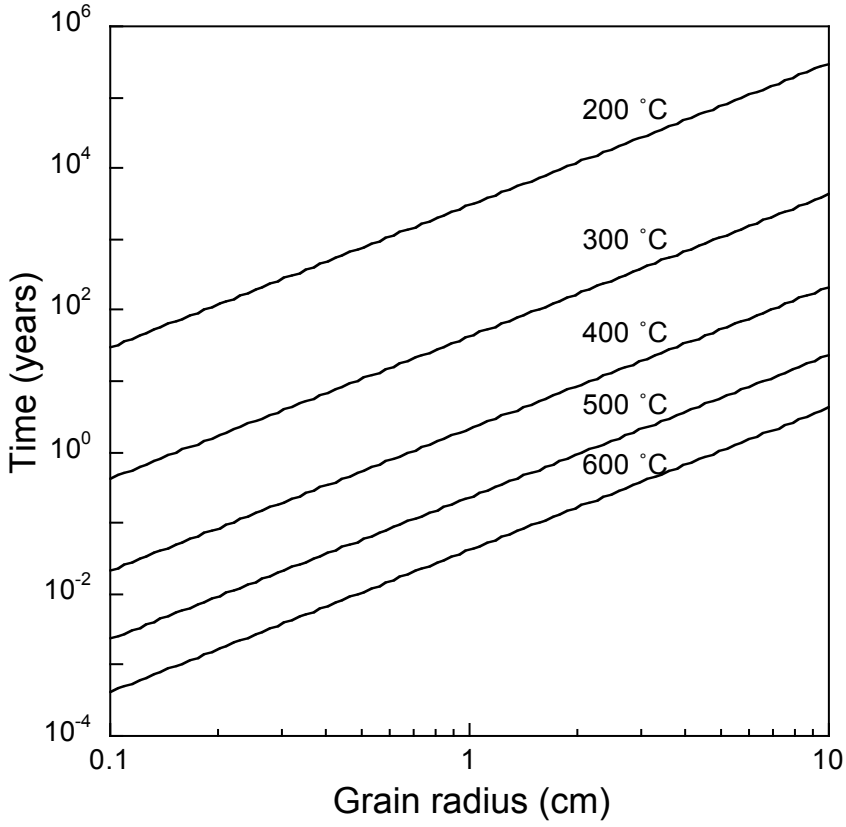

Figure 5.15. Curves representing time-grain radius conditions under which hydrogen isotope signature at the center of grain will be preserved. For times and temperatures below the curves, concentrations at the center will remain unaffected, but will be changed when above the curves.

Using the diffusion law deduced in this study, the isotope ratio in the center of a 5 cm diameter andradite grain would not survive more than 1) few months at a temperature of 600 °C, 2) 10 years at 400 °C and 3) less than 30000 years at 200 °C. Therefore, hydrogen isotope memory of andradite is efficient only to record low-grade metamorphic and metasomatic events, mostly short events at shallow depth and below 400°C. For higher temperatures and deeper events, the ability of garnet to retain isotopic information will strongly depend on its andradite content: change of composition from $Gr_{86}An_{14}$ to An_{99}, has the same effect on H mobility as a temperature increase of 500°C (see the shift of diffusion laws in Fig. 5.14). The same effect is expected on the closure temperature of garnet for hydrogen isotopes.

It is essential to consider the results of H-D diffusion experiments to discuss the isotopic signature of garnets because the diffusion of hydrogen in garnet is always faster than the chemical diffusion. In addition, these differences increase at lower temperature due to the difference of the activation energies. The fast diffusion of hydrogen in garnet may explain the large heterogeneity in δD value observed and their difference of behavior compared to $\delta^{18}O$ values (Zheng et al. 2003; Chen et al. 2011; Sheng et al. 2007). More data from H-D exchange experiments on garnets of various compositions is needed to better understand the significance of the measured isotopic data (Gong et al. 2007).

Chapter 6

Kinetics of hydrogen diffusion in Zircon

6.1 Chemical composition

3 EPMA analyses were performed on ZrB and ZrD zircons (Table 6.1) and 5 analytical points were recorded on the same slices by LA-ICP-MS (Table 6.2). The average compositions and standard deviations are presented also in the tables.

Analytical results show that the two crystals are homogeneous with similar composition: $Zr_{0.9949}Hf_{0.0095}Sc_{0.0011}Y_{0.0020}Yb_{0.0002}Th_{0.0002}U_{0.0003}Pb_{0.0001}Si_{0.9887}Ti_{0.0029}O_{3.9994}$ for ZrB and $Zr_{0.9944}Hf_{0.0100}Sc_{0.0012}Y_{0.0031}Yb_{0.0004}Th_{0.0004}U_{0.0003}Pb_{0.0001}Si_{0.9847}Ti_{0.0029}O_{4.0006}$ for ZrD.

Table 6.1. EMPA analysis of zircon samples used in this study.

Sample	Points	SiO_2	P_2O_5	TiO_2	Fe_2O_3	Y_2O_3	ZrO_2	Ce_2O_3	HfO_2	ThO_2	UO_2	Total
ZrB	1	31.59	0.00	0.00	0.00	0.00	65.69	0.00	1.37	0.00	0.00	98.66
	2	32.47	0.00	0.00	0.04	0.00	66.54	0.00	1.45	0.00	0.00	100.51
	3	32.28	0.03	0.00	0.01	0.00	66.22	0.00	1.48	0.09	0.00	100.11
	Average	32.11	0.01	0.00	0.02	0.00	66.15	0.00	1.44	0.03	0.00	99.76
	STD	0.46	0.02	0.00	0.02	0.00	0.43	0.00	0.06	0.05	0.00	0.97
ZrD	1	31.92	0.00	0.00	0.05	0.00	66.00	0.00	1.36	0.10	0.00	99.42
	2	32.19	0.00	0.00	0.10	0.00	66.56	0.00	1.36	0.02	0.00	100.23
	3	32.05	0.01	0.00	0.00	0.00	66.23	0.01	1.44	0.05	0.00	99.78
	Average	32.05	0.00	0.00	0.05	0.00	66.26	0.00	1.39	0.06	0.00	99.81
	STD	0.14	0.01	0.00	0.05	0.00	0.28	0.00	0.05	0.04	0.00	0.41

6.2 Baseline correction and water content

The integration of OH and OD bands were done between 3700 to 2850 cm^{-1} and 2700 to 2200 cm^{-1}, respectively. The OH and OD regions are separated by bands (centered at 2750 cm^{-1}) that partly overlap with them which are associated with three phonon combination modes of internal SiO_4 stretch vibration (Nasdala 1995; Woodhead 1991). For OH, the baseline fit was made first for the spectrum at the final step, using a polynomial interpolation from several points taken on both sides of OH region (Fig. 6.1a). The spectra from final step of dehydrogenation are the ones that exhibit the best contribution of the SiO_4 stretching vibration. Then, this baseline was applied for all the spectra of the same slice at different annealing steps. For OD, the spectrum of the sample at $t = 0$ was systematically subtracted (Fig. 6.1b).

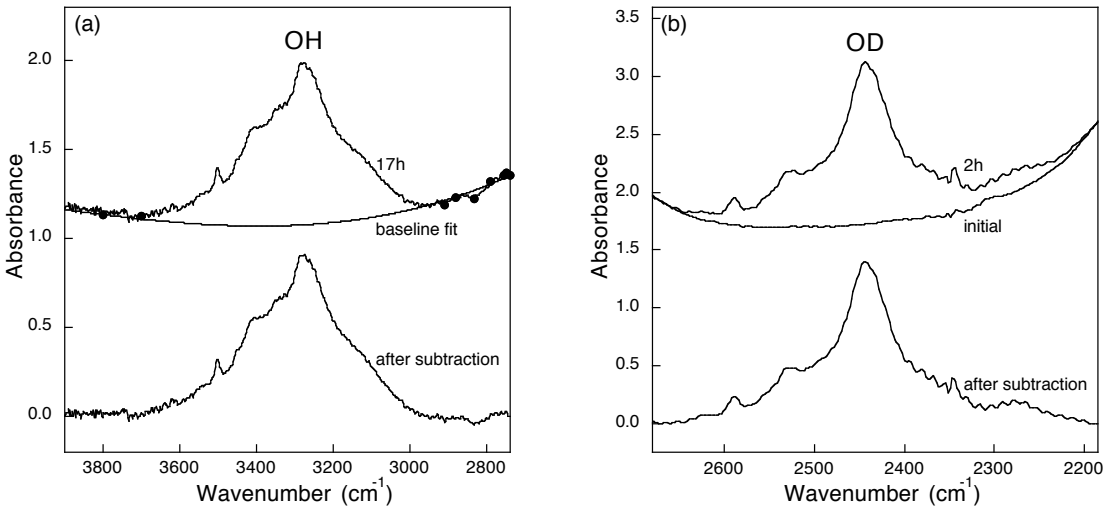

Figure 6.1. Examples showing the baseline correction of OH and OD absorption regions: a) OH stretching region (3700 to 2850 cm^{-1}); and b) OD stretching region (2700 to 2200 cm^{-1}). Slice ZrB-a1, annealed at 1050 °C, with a thickness 2L of 199 μm.

The use of a single absorption coefficient for zircon is still under discussion due to the shape variation of spectra. The commonly used general wavenumber-dependent calibration for absorption coefficients, proposed by Libowitzky and Rossman (1997),

was adopted in this study. The ε_i values was obtained through the correlation line: ε_i (cm^{-2}permolH_2O/L) = 246.6 × [3753 - ν(cm^{-1})], where ν is the area-weighted average wavenumber of the individual absorption bands. The resulting ε_i is the same for ZrB and ZrD; it is equal to 115655 cm^{-2} per mol H_2O/L. Using this value, the same average value of 86 ppm H_2O was obtained for both crystals ZrB and ZrD.

6.3 Raman spectroscopic characterization

FT-Raman analyses were conducted on slices ZrB-a1, ZrB-b2, ZrB-c3 and ZrD-b2 before and after annealing to gain information on the variation of crystallinity upon annealing (Table 6.3, Fig. 6.2). The band located at 1000 cm^{-1}, defined as a ν3 band, is related to internal SiO_4 stretching vibration. The half-width (Full width at half maximum) and position of this intense band is widely used to estimate the crystallinity of zircon (Nasdala et al. 1995; Wang et al. 2006). The change of degree of crystallinity was estimated according to Nasdala et al. (1995). Crystallinity of ZrB and ZrD samples were initially at intermediate level (but close to well crystallized) and reach the well-crystallized level upon annealing. The higher the temperature (and the longer the time) of annealing, the higher the level of crystallinity reached at the end of experiment (Mainz 2007). Overall, the change in crystallinity remains relatively minor and we assume that this change do not affect notably the diffusion rate of these zircons (Table 6.3).

Table 6.1. Changes of ν_3 band of Raman spectra in zircon samples before and after annealing and related change of the degree of crystallinity (Nasdala et al. 1995).

Sample No.	T (ºC)	Structural state	ν_3 (SiO_4) / FWHM (cm^{-1})	
		before / after annealing	before annealing	after annealing
ZrD-b2	950	Intermediate / well crystallized	1004.0 / 6.1	1004.5 / 5.2
ZrB-c3	1000	Intermediate / well crystallized	1003.3 / 6.1	1004.0 / 4.0
ZrB-a1	1050	Intermediate / well crystallized	1003.0 / 6.0	1004.5 / 3.7
ZrB-b2	1100	Intermediate / well crystallized	1003.3 / 6.9	1005.5 / 3.5

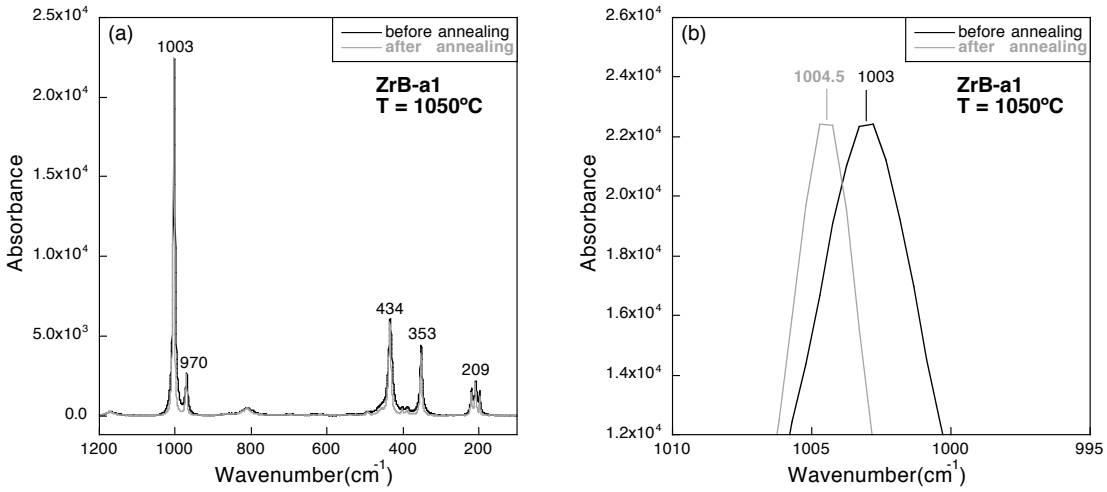

Figure 6.2. Comparison of Raman spectra of ZrB-a1 showing increasing degree of crystallinity upon annealing at 1050°C. a) Principal absorption Raman bands of zircon before and after annealing. Bands located at 1003 and 970 cm^{-1} represent internal SiO_4 stretching modes while that for internal bending modes are at 434 cm^{-1}. The bands located at 353, 220, 209 and 198 cm^{-1} represent external vibrations of rigid SiO_4 tetrahedron. b) Enlargement of band ν3 (around 1000 cm^{-1}) showing clearly the frequency shifts to higher wavenumber and band sharpening upon annealing.

6.4 IR spectroscopic characterization of OH and OD bands

6.4.1 IR spectroscopic characterizeation

Figure 6.3 and Figure 6.4 shows the evolution of FTIR absorption spectra during H-D exchange and rehydrogenation result for a representative slice. Since there is no evidence of absorption bands of H_2O at 1600 cm^{-1} corresponding to H-O-H bending mode or 5200 cm^{-1} corresponding to H-O-H combination mode before annealing and after annealing, we conclude that OH is the only hydrous species present in these zircons and there is no H_2O formed during annealing. Absorption features from 3700 to 2850 cm^{-1} and from 2700 to 2200 cm^{-1} are due to OH and OD ions respectively, while the small broad bands centered around 2750 cm^{-1} (*E* // *c*) are characteristic for three-phonon processes in zircon (Nasdala 1995, Woodhead 1991, Zhang 2010). Zhang et al. (2010) reported for partially metamict zircon, which gradually

recrystallized during high temperature annealing, that the broad 2700-2900 cm^{-1} feature gradually split into several narrow bands located at 2875, 2751 and 2700cm^{-1} (E // c). They were assigned to structural vibrations. A systematic decrease of OH bands along with an increase of OD bands upon heating can be easily identified from Fig. 6.3 and Fig. 6.4.

At the beginning of annealing, a rearrangement of OH bands occurs with a decrease of the band at 3406 cm^{-1} (E // $c > E \perp c$) accompanied by an increase of the band at 3265 cm^{-1} ($E \perp c > E$ // c). Besides, the band at 3503 cm^{-1} with a polarization nearly parallel to c axis, become more and more distinct upon heating, although tiny in absorbance, the band remains stable after a long annealing. With H-D exchange, the OD area gradually show absorption bands that are not necessarily corresponding one to one to those in the OH area, among which sharp bands at 2687 and 2673 cm^{-1} (with corresponding bands at 3621 and 3641cm^{-1} in the OH area) become clearly visible when the H-D exchange reach approximately 40%.

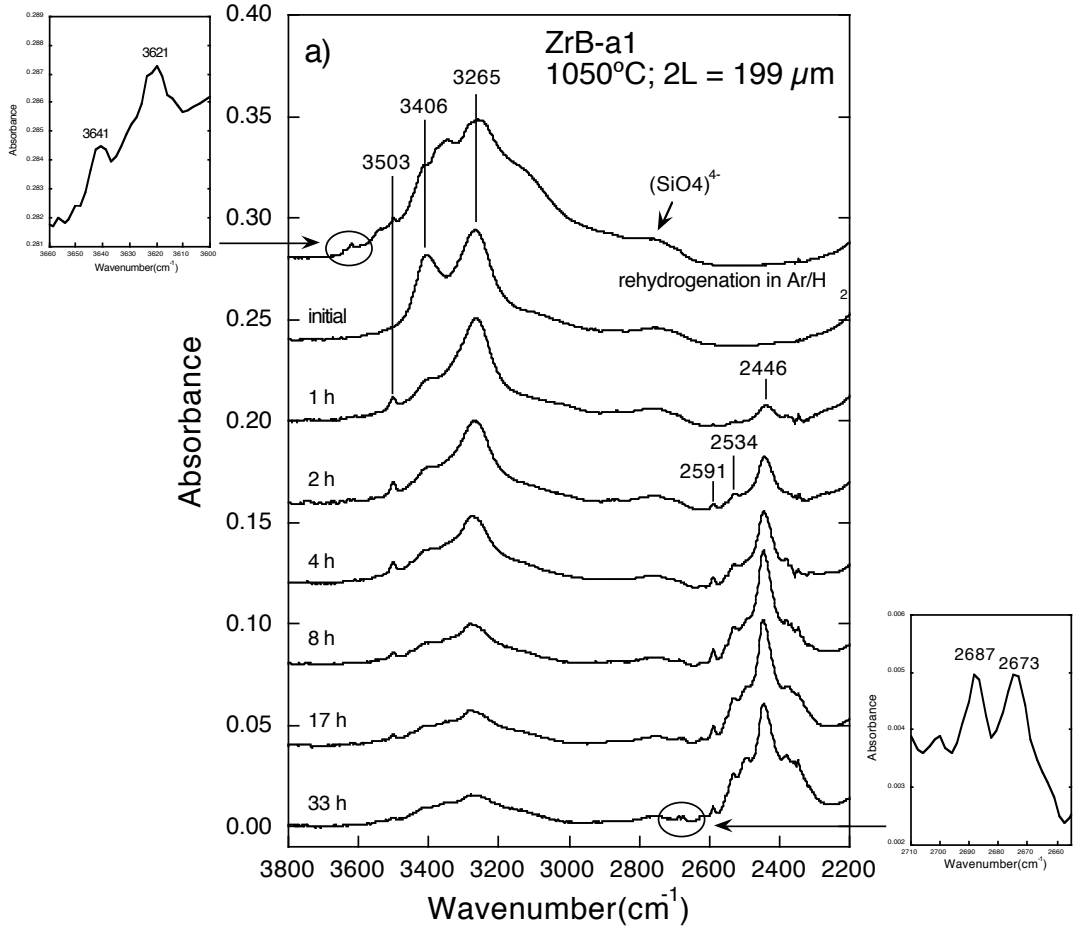

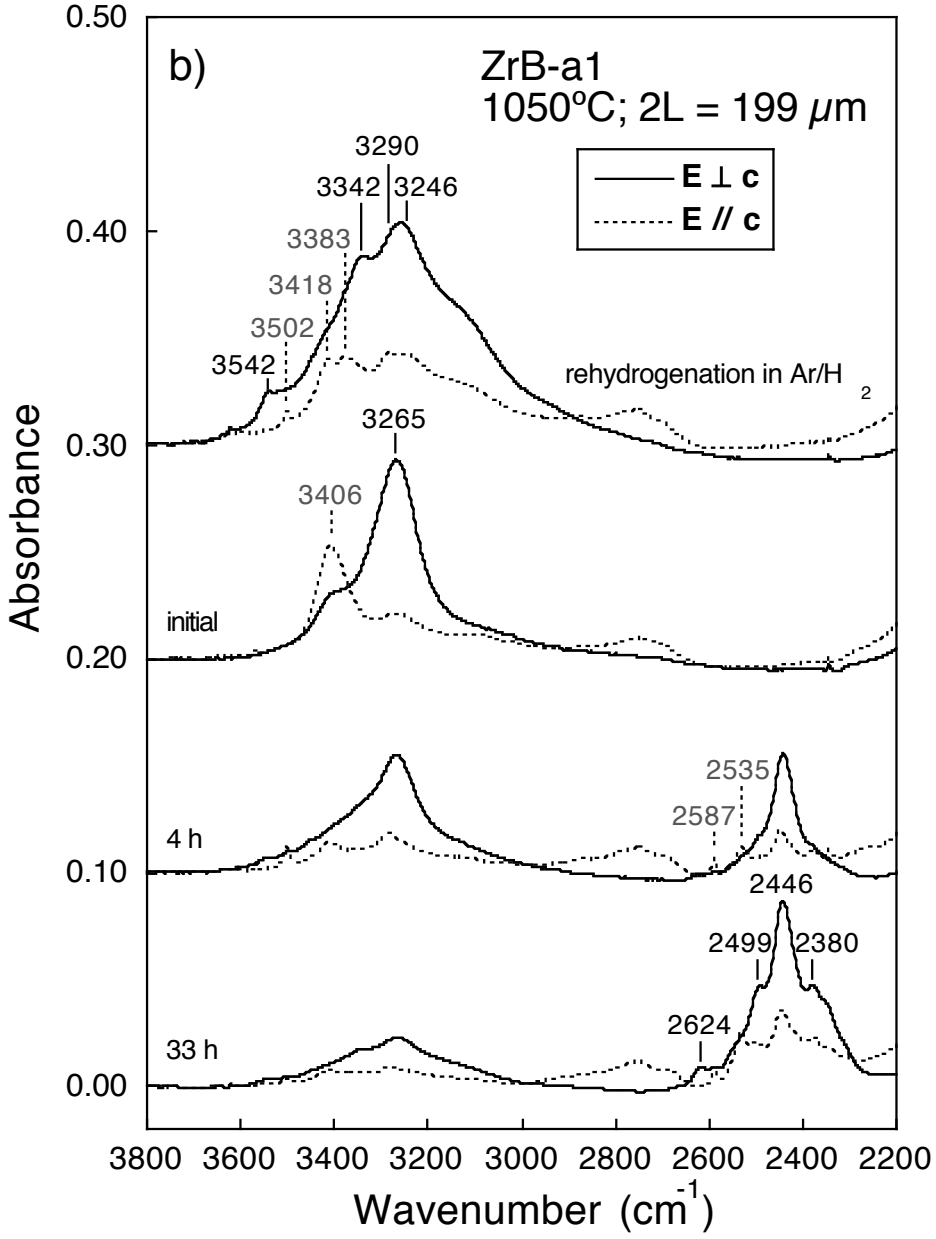

Figure 6.3. a) Representative unpolarized FTIR evolution of zircon (slices parallel to *c* axis) with annealing in Ar/D_2 atmosphere in the region 3800-2200 cm^{-1}, showing the replacement of OH bands by OD bands. The uppermost spectrum shows the result after rehydrogenation in Ar/H_2 atmosphere for 42.5 h. The two small plots are the enlargement of the bands indicated by the arrows. b) Polarized spectra showing the polarization of the respective absorption bands. ZrB-a1, annealed at 1050 °C, with a thickness 2L of 199 μm.

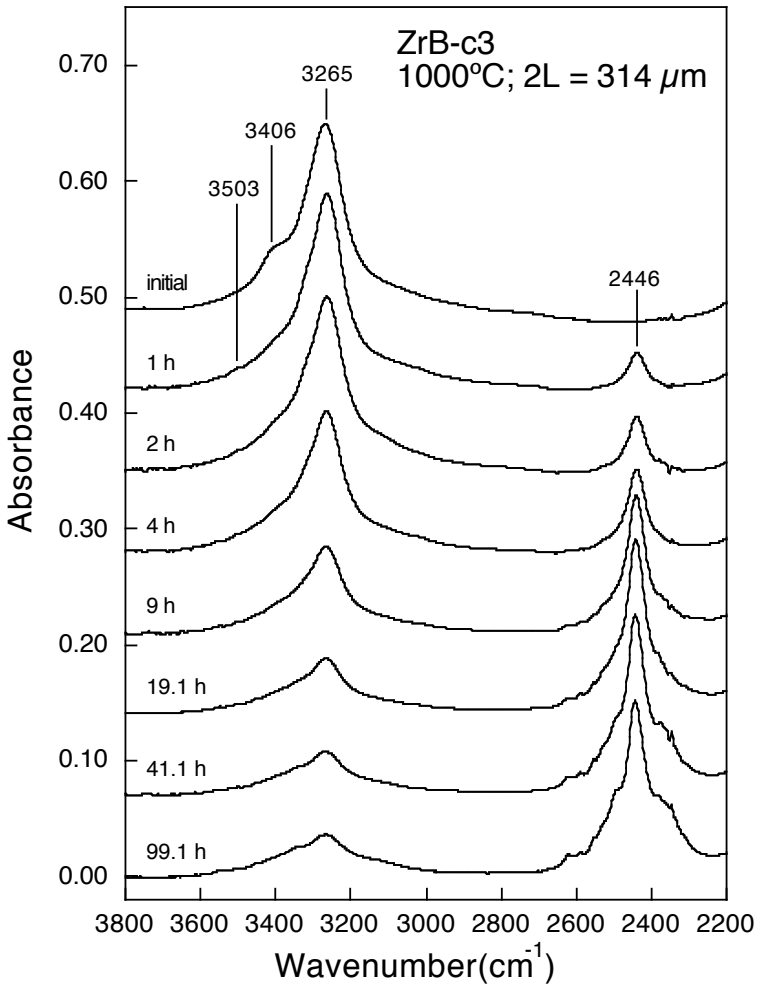

Figure 6.4. Representative unpolarized FTIR evolution of zircon (slices perpendicular to *c* axis) with annealing in Ar/D_2 atmosphere in the region 3800-2200 cm^{-1}, showing the replacement of OH bands by OD bands. ZrB-c3, annealed at 1000 °C, with a thickness 2L of 314 μm. Note that since the slice is perpendicular to *c* axis, unpolarized spectra and polarized spectra are the same with both being similar to spectra when $E \perp c$ for slices parallel to *c* axis.

To see the influence of the rearrangement on the total integral absorbance, two slices (ZrB-a2 and ZrD-b3) were used to undergo stepwise heating from 600 °C to 900 °C in an $Ar/D_{2(10\%)}$ atmosphere at an interval of 50 °C for 1h at each step (Fig. 6.5). The rearrangement does not start significantly before 850 °C. At this temperature the H-D exchange remains moderate. During this first step of rearrangement, the total OH integral absorbance decrease of 27% when the electric vector *E* is parallel to *c*, but increase of 8% when *E* is perpendicular to *c*. Therefore, it

contributes an increase of 8% to integral absorbance of OH bands for slices perpendicular to *c* (that is 108% of the initial A_{OH}) while a decrease of 10.6% in unpolarized spectra of slices parallel to *c* (that is 89.4% of the initial A_{OH}). This suggests that changes in absorbance are due to local rearrangement without any loss of OH. The rearrangement of bands has been reported in previous studies on several NAMs with change of intensities of bands upon heating (zircon, Woodhead et al. 1991b; Trail et al. 2011; Zhang et al. 2010; pyrope, Blanchard and Ingrin 2004b; pyroxene, Skogby and Rossman 1989; enstatite, Stalder and Skogby 2007; kyanite, Wieczorek et al. 2004; forsterite Libowitzky and Beran 1995). For zircon, it was hypothesized that H migration during heating may be a result of the change of degree of crystallinity (Woodhead et al. 1991a). Alternatively, Blanchard and Ingrin (2004b) suggested for pyrope that migration of H from relatively unstable site to more stable site may account for the phenomenon. In our case, the rearrangement occurs at the beginning of annealing while the evolution of crystallinity is progressive and evolves all along the annealing history of samples. Thus we favor here a rapid local rearrangement of some OH defects upon heating.

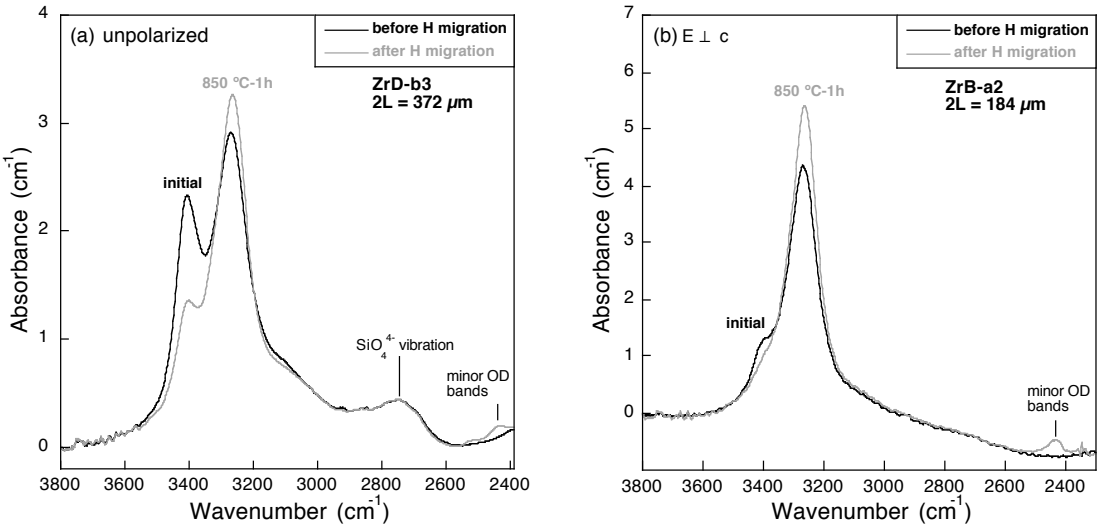

Figure 6.5. Evolution of FTIR absorption spectra of ZrD-b3 and ZrB-a2 showing the rearrangement of OH bands at the beginning of annealing. a) Unpolarized spectra of ZrD-b3 with a thickness 2L of 372 μm; b) polarized spectra ($E \perp c$) of ZrB-a2 with a thickness 2L of 184 μm.

The uppermost spectrum in Fig. 6.3a, which represents the result of rehydrogenation in $Ar/H_{2(10\%)}$ atmosphere of a sample after an almost complete deuteration, shows an absorbance about twice greater than the initial value while we know that the initial rearrangement of bands already reduced the absorbance of unpolarized bands by 10.6%. In total, compared to integral absorbance just after the initial rearrangement of spectra bands it corresponds to up to 118% increase of the integral absorbance after 42.5 h annealing (A_{OH} of 26.18 versus 12.03). This increase prove that extra hydrogen/deuterium have been added to the crystals concurrently with exchange of deuterium and/or hydrogen in the crystal. The faster way to incorporate hydrogen in mineral containing multivalent cations is through the reduction of these cations like in olivine (Kohlstedt and Mackwell, 1998) or pyroxene (Hercule and Ingrin, 1999). The concurrent reduction of U^{5+} to U^{4+} during H-D exchange is proven by the observed evolution of electronic absorption bands related to these species, which will be shown later (see § 6.5).

6.4.2 Wavenumber shift (ν_{OH}/ν_{OD})

A comparison between the shape of the initial spectrum and that of the rehydrogenated one in Fig. 6.3a indicates that new OH bands appeared. To check if there is indeed some new bands occurring, peak-deconvolution of the unpolarized spectra (the initial one, nearly completely deuterated one and rehydrogenated one for ZrB-a1) were performed with the Peakfit software (SPSS Inc.) where a Gaussian and occasionally a Lorentzian shape (bands at 3503 cm^{-1}) was used. The deconvolution lead to 14 different peaks for the initial spectrum and 17 different peaks for the rehydrogenated one, wherein the three bands located at 2876, 2759 and 2684 cm^{-1} are associated with SiO_4 vibrations and the three bands located at 3641, 3621 and 3596 cm^{-1} occurring in the latter spectrum are essentially new bands (Fig. 6.6a, b; Table 6.4). The remaining bands are correlated well with each other in the two spectra. The deconvolution of the initial spectrum is guided by the spectra from final step of dehydrogenation, where the weaker bands are more clearly visible due to the large

decrease of the stronger bands (removing of the larger overlap), and by the comparison between the unpolarized and polarized spectra, where bands exhibit different behavior with different polarizations. The deconvolution of the rehydrogenated spectrum (and also the nearly completely deuterated one) is guided by the comparison between the unpolarized and polarized spectra. The deconvolution for the nearly completely deuterated spectrum leads to 14 different bands, corresponding one to one to the bands in the rehydrogenated spectrum (Fig. 6.6c; Table 6.4). Dawson et al. (1971) also reported the complexity of the bands in zircon with more than 20 peaks at temperature of 100 K. Due to the very complex spectra with broadly overlapping single bands, the result of the deconvolution must be interpreted with caution. Slight deviations from our deconvolution are likely. The deconvolution results and the ν_{OH}/ν_{OD} ratio for each band are shown in Table. 6.4.

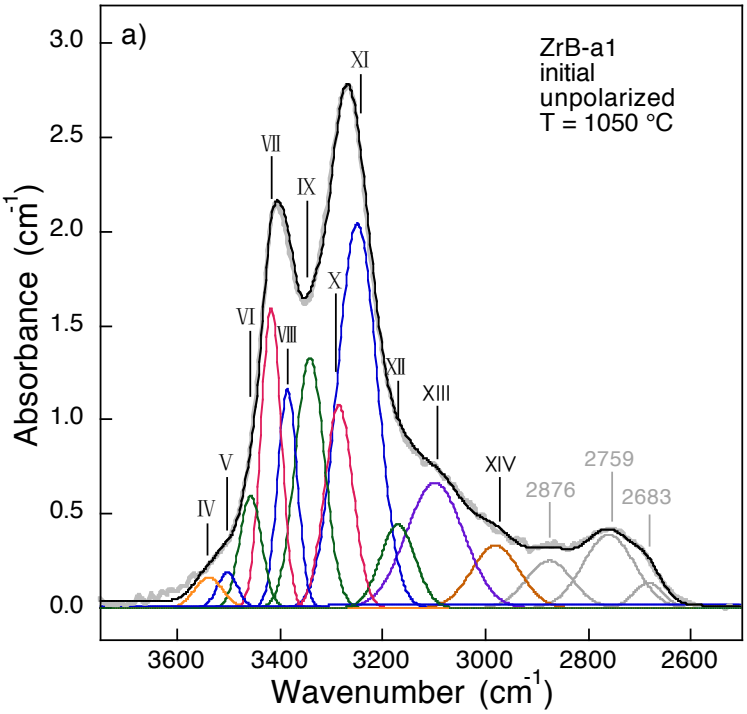

IV	3540
V	3503
VI	3458
VII	3418
VIII	3386
IX	3343
X	3286
XI	3250
XII	3171
XIII	3099
XIV	2981

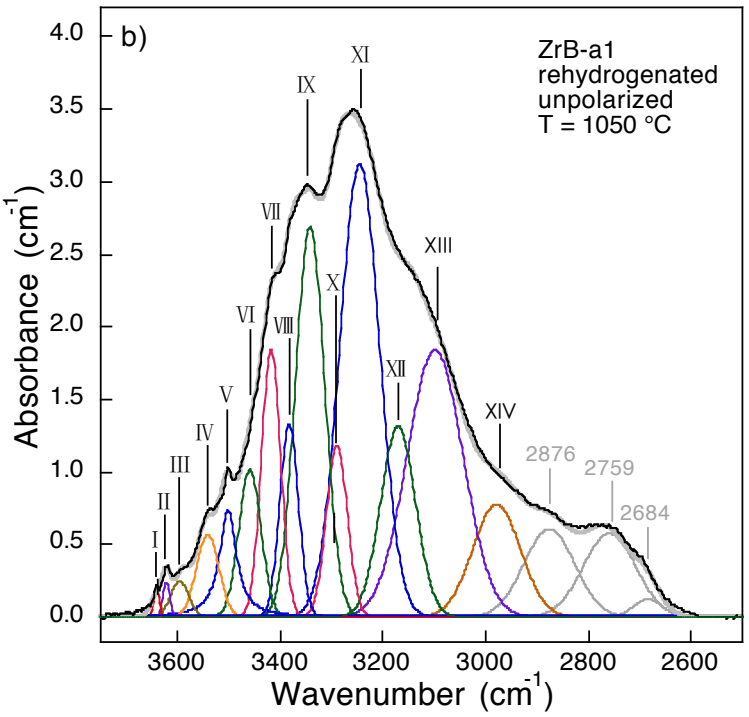

I	3641
II	3621
III	3596
IV	3542
V	3502
VI	3460
VII	3418
VIII	3383
IX	3342
X	3290
XI	3246
XII	3171
XIII	3099
XIV	2979

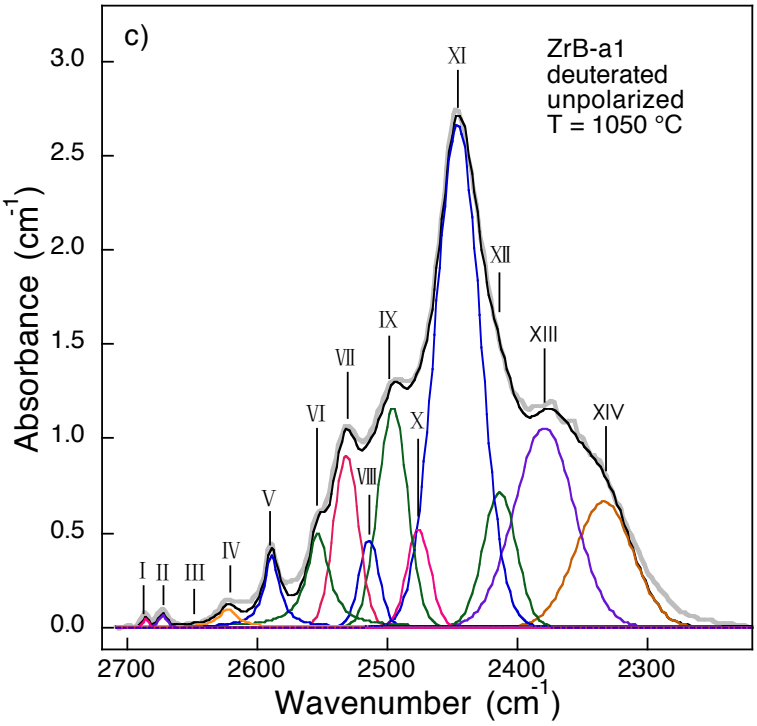

I	2687
II	2673
III	2649
IV	2623
V	2589
VI	2554
VII	2532
VIII	2515
IX	2497
X	2477
XI	2447
XII	2414
XIII	2380
XIV	2334

Figure 6.6. Results of deconvolution of unpolarized IR spectra for slice ZrB-a1. a) OH area of the initial spectrum; b) OH area of the rehydrogenated spectrum; c) OD area of the nearly completely deuterated spectrum. The three bands in gray are not linked to hydrous species but to SiO_4 vibrations. The thick gray line is the original spectrum and the black line is the generated one.

Table 6.4. Results of deconvolution of unpolarized IR spectra for slice ZrB-a1 at initial stage (ν_{OHi}), after rehydrogenation (ν_{OH}) and after deuteration (ν_{OD}) (ratio of OH/OD frequencies collected from the two last steps are also reported).

No.	ν_{OHi} (cm^{-1})	ν_{OH} (cm^{-1})	ν_{OD} (cm^{-1})	ν_{OH}/ν_{OD}
I		3641	2687	1.355
II		3621	2673	1.355
III		3596	2649	1.357
IV	3540	3542	2623	1.350
V	3503	3502	2589	1.352
VI	3458	3460	2554	1.355
VII	3418	3418	2532	1.350
VIII	3386	3383	2515	1.345
IX	3343	3342	2497	1.339
X	3286	3290	2477	1.328
XI	3250	3246	2447	1.327
XII	3171	3171	2414	1.313
XIII	3099	3099	2380	1.302
XIV	2981	2979	2334	1.276

By summarizing the deconvolution data and the data from literature (synthetic zircon, Trail et al. 2011; annealed metamict zircon, unpublished data; grossular, Kurka et al. 2005; andradite, this thesis; pyrope, Blanchard and Ingrin, 2004a; diopside, Hercule et al. 1999; forsterite, Ingrin, personnal communication; wadsleyite, Vigouroux 2014; rutile, (Ingrin, personnal communication) in a ν_{OH}/ν_{OD} versus ν_{OH} plot (Fig. 6.7), we found that data of zircon deviate from the correlation presented by Mikenda (1986) while the data of other NAMs seem to roughly follow that correlation. For zircon, the frequency shift due to the isotopic replacement shows deviation from the correlation proposed by Mikenda (1986) (Fig. 6.7a); a much stronger decreasing of the isotropic frequencies ratios with decreasing frequencies is found compared with

that proposed by Mikenda (1986) (Fig. 6.7b). The reason for the different behavior of zircon from other NAMs is unknown, but its particular closely packed crystal structure may be a possible reason since different structural environments may exhibit different evolution of isotopic ratios. We propose a new correlation for zircon, which may be useful for estimating ν_{OH} from ν_{OD} frequencies in zircon: $\nu_{OH}/\nu_{OD} = -1.0931 + 0.001345 \times \nu_{OH}$ (cm^{-1}) $- 1.8467e\text{-}7 \times (\nu_{OH})^2$ (cm^{-2}), with R = 0.99401.

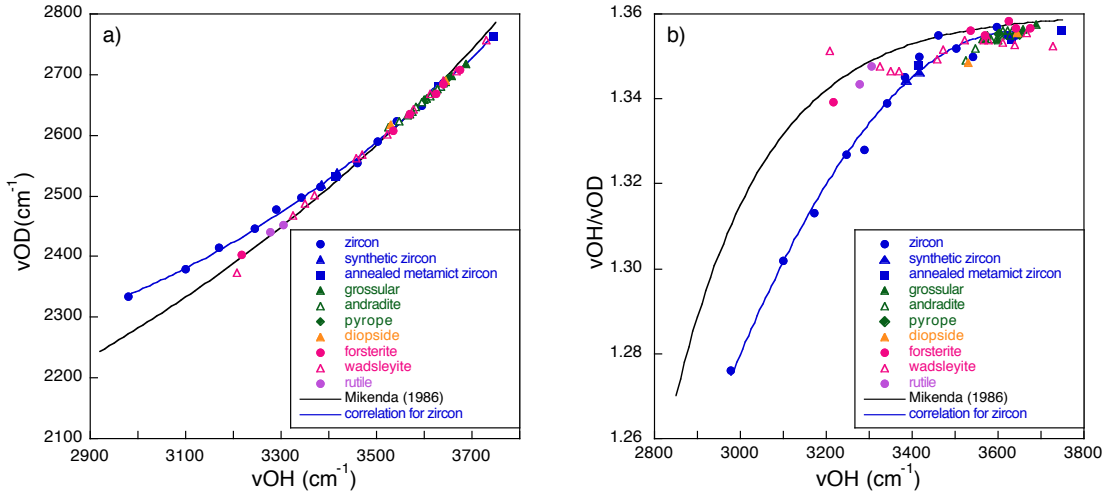

Figure 6.7. Correlation between a) OH and OD stretching frequencies and b) ν_{OH}/ν_{OD} ratios and OH stretching frequencies. Black line: correlation curve by Mikenda (1986) for solid hydrates and minerals; blue line: new correlation for zircon using data from present study and from the literature (full blue circles: deconvolution data from zircon in the present study; full blue triangles: synthetic zircon in the presence of H_2O and D_2O, Trail et al. 2011; full blue squares: metamict zircon after annealing at 1000 °C in Ar/D_2 for 96 h, unpublished data). Full green triangles: grossular, kurka et al. 2005; empty green triangles: andradite, this theis; full green diamond: pyrope, Blanchard and Ingrin 2004a; full orange triangles: diopside, Hercule et al. 1999; full red circles: forsterite, Ingrin personnal communication; empty red triangles: wadsleyite, Vigouroux 2014; full purple circles: rutile, Johnson et al. 1975).

6.4.3 OH sites and orientation

Taking consideration of the results from previous studies performed on OH in zircon, suggestions about the site location of OH group giving rise to bands occurring

in the zircons of this study are given below.

1) OH groups associate with a Si vacancy

Since 3420 cm^{-1} (E // c) and 3385 cm^{-1} ($E \perp c$) bands always occur concurrently and has been confirmed to be associated with the hydrogarnet substitution mechanism (4OH replacing SiO_4) through a first-pinciples study of OH in zircon by Balan et al. (2013b), we favor this assignment of the two bands.

It has been suggested previously that the defects corresponding to the band at 3515 cm^{-1} could involve both OH and F ions (Caruba et al. 1985; Trail et al. 2011; Botis et al. 2013; Balan et al. 2013b). Since no F element was observed above the detection limit in our chemical analysis, we can not confirm this assignment. Nevertherless, if this assignment is true, the increase of the band at 3503 cm^{-1} band with the decrease of the band at 3406 cm^{-1} at the first step of annealing would be probably due to moving of some interstitial F ions and their association with hydrozircon defects.

For the bands at 3621 and 3641 cm^{-1}, they do not exist in the original spectra, they appear during annealing (and also the corresponding OD bands at 2673 and 2687 cm^{-1}), they are clearly visible after 40% of exchange. They must correspond to new defects or new configuration of defects, most probably introduced through the oxidation-reduction of uranium ions. The band at 3621 cm^{-1} has also been observed previously (Dawson et al. 1971; Nasdala et al. 2001; Zhang et al. 2010). For the two intermediate zircon studied by Nasdala et al. (2001), the band at 3621 cm^{-1} is observed in zircon K2 with prominent U^{4+} bands present while it is absent in zircon Z18 with only minor U^{4+} bands present. We performed H-D exchange and rehydrogenation experiments under 1100 °C for another zircon sample (ZrF; not shown in present study) with little U ions and observed no occurrence of band at 3621 cm^{-1}. Zhang et al. (2010) investigated metamict zircons undergoing thermal annealing. They found in a crystal annealed at 1300 K for 1 h in N_2 that an extra band at 3621 cm^{-1} occurs concurrently with the U^{4+} band at 4832 cm^{-1}, and in another crystal (with both U^{5+} and U^{4+} bands present originally) undergoing stepwise annealing in air that the band at 3621 cm^{-1} occurs at 1200 K and its integral absorbance remains nearly constant till 1800 K at which temperature it disappeared, while in the case of U ions,

the integral absorbance of U^{5+} bands increase linearly from 1200 K and the integral absorbance of U^{4+} bands decreases drastically from 1400 K and they disappeared at 1700 K. After the last annealing step at 1150 °C for ZrB-c1 (present study), the U^{4+} ions are completely reoxidized to U^{5+} ions while the bands at 2673 and 2687 cm^{-1} are still present with an integral absorbance half the original (the total OD integral absorbance decrease by 50%; see § 6.5, 6.6). Considering these observations from literature and the present study, we propose that the bands at 3621 and 3641 cm^{-1} are related to some new defects introduced during U^{5+}-U^{4+} oxidation-reduction reaction, but not bound with U^{4+} ions. Considering that, in NAMs such as olivine, garnet and pyroxene, the OH absorption bands at high wavenumbers are commonly relate to defects involving Si vacancy (e.g., olivine, Lemaire et al. 2004; garnet, Rossman and Aines 1991; pyroxene, Balan et al. 2013a), it is probable that the bands at 3621 and 3641 cm^{-1} are also linked to Si vacancies.

2) OH groups associate with Zr-unoccupied defects

The band at 3200 cm^{-1} was observed by Trail et al. (2011) in pure and Ti-, Th-, Al-doped crystalline zircons. Balan et al. (2013b) obtained bands at 3199 cm^{-1} (E // c) and 3212 cm^{-1} ($E \perp c$) for defects of four OH replacing Zr cation through theoretical calculations, and demonstrated that the band at 3200 cm^{-1} found in natural and synthetic zircons are very probably associated with a Zr vacancy. We adopt this assignment for this band.

The bands at 3180 and 3100 cm^{-1} are always present concurrently in natural and synthetic crystalline zircons (Dawson et al. 1971; Woodhead et al. 1991b; Nasdala et al. 2001). The band at 3200 cm^{-1} can occur with or without accompany of these two bands; it always form a band doublet with band at 3180 cm^{-1} in the second case (Trail et al. 2011; Woodhead et al. 1991b; De Hoog et al. 2014). Although only the bands at at 3200 and 3100 cm^{-1} were reported to be present in zircons, in fact, the band at 3180 cm^{-1} was also present forming a band doublet with the 3200 cm^{-1} band (Woodhead et al. 1991b; De Hoog et al. 2014). These three bands show also a stronger stability than the band at 3420 cm^{-1} upon high temperature annealing (Woodhead et al. 1991; Nasdala et al. 2001; unpublished data in this study). This suggests a strong link

between these three bands. Therefore, these bands are probably all related to the Zr-unoccupied defects, that is, alternatively, the band at 3200 cm^{-1} is related to a Zr vacancy (Balan et al. 2013b) while the bands at 3180 and 3100 cm^{-1} are associated to a coupled substitution by REE and H (Belan et al. 2013; De Hoog et al. 2014).

3) The bands located near 3265 cm^{-1}

The protons giving rise to the bands near 3265 cm^{-1} (3290 and 3246 cm^{-1}) are highly mobile: They can either exchange with Si-vacancy related protons, or with Zr-unoccupied related protons (Zhang et al. 2010; present study). The precise assignment of these bands is unknown. Zhang et al. (2010) found for a metamict zircon (Cam25) that the band near 3270 cm^{-1} disappears between 1600 and 1700 K accompanied by a simultaneous occurrence of extra bands at 3189, 3099 and 2993 cm^{-1} bands. We also observed in our samples a transfer from the band at 3420 cm^{-1} toward the band at 3265 cm^{-1} at the beginning of annealing. In our extra high temperature annealing on another zircon sample at 1100 °C (ZrF; not shown in present study), the transfer from band near 3265 cm^{-1} to 3200 and 3100 cm^{-1} bands was also observed.

Therefore, maybe the protons in zircon are highly mobile, this can partly account for the diversity and complexity of OH absorption bands found in natural zircons.

6.5 Redox reaction of U ions

A reduction of U^{5+} to U^{4+} during annealing is evidenced through the evolution of near-infrared (NIR) absorption bands (Fig. 6.8). In zircon, the Zr^{4+} site can be occupied by uranium ions. Since the Zr^{4+} site is noncentrosymmetric, D_{2d}, the electronic transitions for U ions paramagnetic impurities are possible. Several theoretical and experimental studies have been performed to investigate the energy levels of U ions, and the spectra of U^{4+} and U^{5+} ranging from 4000 to 30000 cm^{-1} in U-doped zircon and natural zircon have been reported (Judd and Runciman 1976; Richman et al.1967; Mackey et al.1975; Vance and Mackey 1974, 1975, 1978; Zhang et al. 2002, 2003, 2004). There are five irreducible representations of the D_{2d} point

group: Γ_1, Γ_2, Γ_3 and Γ_4 are nondegenerate (singlet); Γ_5 is doubly degenerate (doublet). The degenerate $5f_2{}^SL_J$ terms split into 70 levels: $16\Gamma_1$, $9\Gamma_2$, $12\Gamma_3$, $12\Gamma_4$, $21\Gamma_5$ (Richman et al.1967). A Γ_4 singlet is assumed as the U^{4+} ground state, and the large number of strong lines in the σ and π spectra are due to $\Gamma_4 \rightarrow \Gamma_5$ and $\Gamma_4 \rightarrow \Gamma_1$ transitions (zero-phonon transitions), respectively (Richman et al.1967; Mackey et al.1975; Vance and Mackey 1978). Not all the levels can be observed due to the selection rules. More than 30 lines of U^{4+} in zircon were observed (Richman et al.1967; Mackey et al.1975; Vance and Mackey 1978) and all the lines appeared to be intensity correlated in samples with different concentrations (Mackey et al.1975). Although the point symmetry of the U^{5+} ions could be less than D_{2d} because of local charge compensation, Vance and Mackey (1974) adopted D_{2d} symmetry as a reasonable approximation for the crystal-field calculations. They showed that, in D_{2d} symmetry, the $^2F_{7/2}$ excited state of U^{5+} would split into $2\Gamma_6$ doublets and $2\Gamma_7$ doublets and the $^2F_{5/2}$ ground state would split into $2\Gamma_6$ doublets and $1\Gamma_7$ doublets (the $^2F_{7/2}$ excited state would be separated from the $^2F_{5/2}$ ground state by around 7000 cm^{-1} for a free U^{5+} ion). Only bands near 9030 cm^{-1} (under 15 K) and 6700 cm^{-1} (under 15 K; 6668 cm^{-1} under 300 K) for U^{5+} in zircon were observed (Vance and Mackey 1974, 1975, 1978) and the intensities of these bands were found to vary linearly with U^{5+} concentration. They were suggested to be associated with $\Gamma_6 \rightarrow \Gamma_6$ and $\Gamma_7 \rightarrow \Gamma_7$ transitions by Judd and Runciman (1976), which was experimentally confirmed by Vance and Mackey (1978).

Figure 6.8 shows evolution of uranium electronic absorption bands ranging from 4500 to 6900 cm^{-1} with annealing in zircon under reducing condition from unpolarized and polarized FTIR spectra. The decreasing bands at 6677 and 6644 cm^{-1} ($E \perp c > E // c$) have been assigned to U^{5+}, of which the band at 6644 cm^{-1} is the most prominent one (Vance and Mackey 1974, 1975, 1978; Zhang et al. 2002, 2003). The bands at 6776, 6520, 6027 and 4580 cm^{-1} ($E \perp c$) as well as 5864 and 4837 ($E // c$), showing increasing intensities, have been assigned to U^{4+}; the band at 4837 cm^{-1} is the most prominent one (Richman et al. 1967, Vance and Mackey 1975; Vance and Mackey 1978; Zhang et al. 2002, 2003, 2004). The uranium ions in these zircon

samples are dominated by U^{5+} ions with U^{4+} ions occurring in minor quantity. The reduction process of uranium was almost achieved at the time of completion of deuteration since there was no evidence for any change of uranium during the rehydrogenation in Ar/H_2. This suggests that the redox reaction has reached an equilibrium.

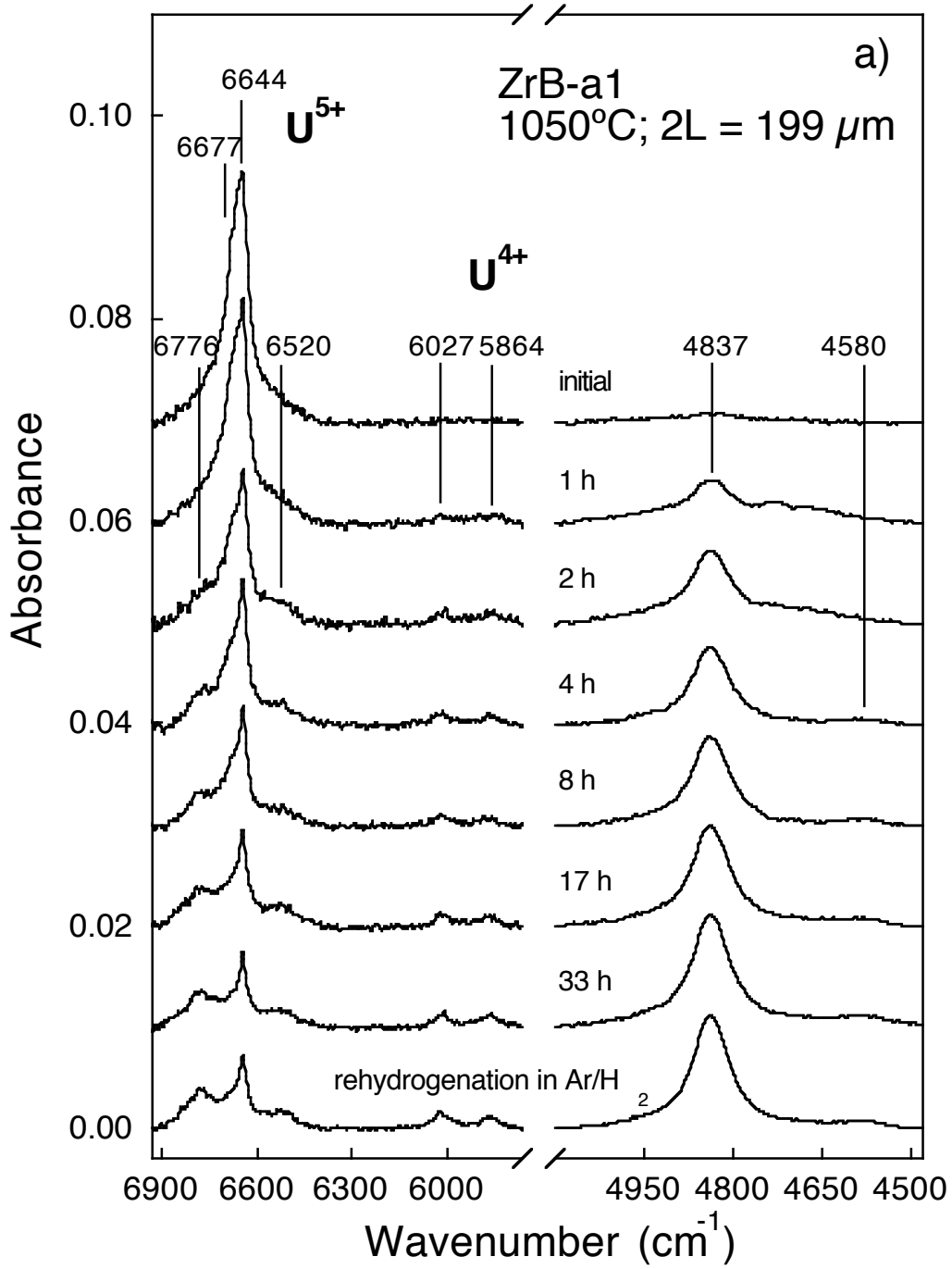

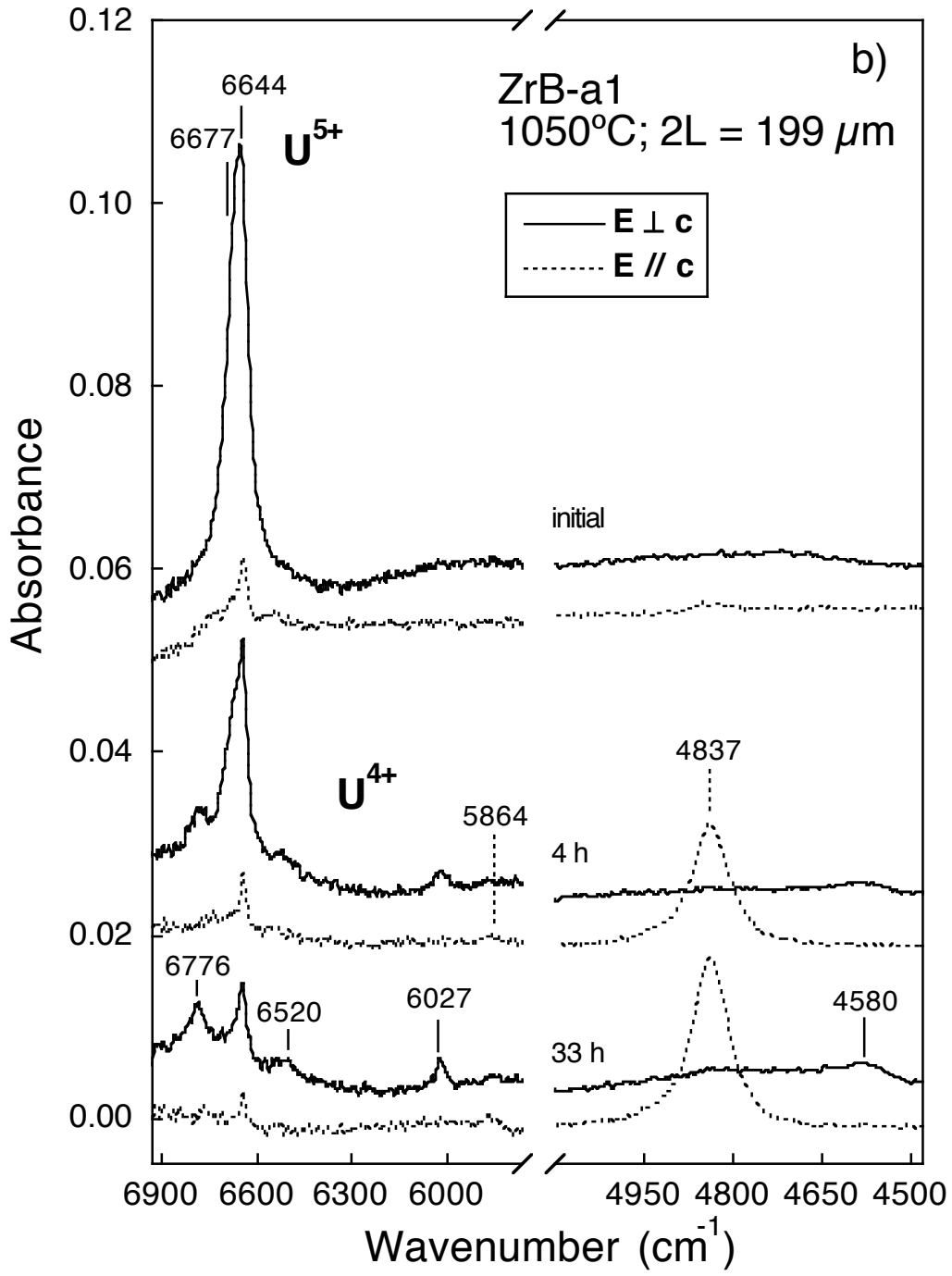

Figure 6.8. a) Representative unpolarized FTIR evolution of zircon in the range 4500-6900 cm^{-1} showing stepwise reduction of U^{5+} to U^{4+} with time of heating under reducing condition. b) Polarized spectra showing the polarization of the respective absorption bands. Bands located at 6644 and 4837 cm^{-1} are the most characteristic absorption features of U^{5+} and U^{4+} respectively. Slice ZrB-a1, annealed at 1050 °C, with a thickness 2L of 199 μm.

Since the U^{4+} bands spread on a large frequency range, assuming a common absorption coefficient for all the bands is probably not feasible. It is assumed in this study that the integral absorbance of each band is proportional to the concentration of U ions. The 6677 and 6644 cm^{-1} bands (U^{5+}, $E \perp c$) and the 4837 cm^{-1} band (U^{4+}, $E // c$) were used for spectra analysis considering their relatively intense absorption (the same method was adopted by Zhang et al. 2003). The baseline correction for U^{5+} bands (6677 and 6644 cm^{-1}) and U^{4+} band (4837 cm^{-1}) were performed by two different ways. For U^{5+} bands, two approaches have been tried in order to separate the U^{5+} bands from the U^{4+} bands (6776 and 6520 cm^{-1}): direct integration and peakfit deconvolution. Since direct integration gives value with large uncertainty, the peakfit deconvolution was adopted (see Fig. 6. 9a for ZrB-a1). Using a Gaussian shape for bands at 6776 and 6520 cm^{-1} and a Lorentzian shape for bands at 6677 and 6644 cm^{-1}, a peak-deconvolution of the spectrum in 6850 to 6440 cm^{-1} region with the Peakfit software (SPSS Inc.) was performed (Fig. 6.9a). The sum of absorbance of U^{5+} bands at 6677 and 6644 cm^{-1} was used to deduce the diffusivity. For the U^{4+} band, the spectrum at $t = 0$ was systematically subtracted to obtain directly the increase value of integral absorbance (Fig. 6.9b). Uncertainties in the absorbance measurements were estimated from both the reproducibility of the analysis on a same slice and the variation of the integral absorbance due to a slight change of the integrated region. The contribution of these errors to the measured integral absorbances corresponds to 6% to 9% of the maximum value of absorbance of U^{5+} (resp. U^{4+}) depending on the slice.

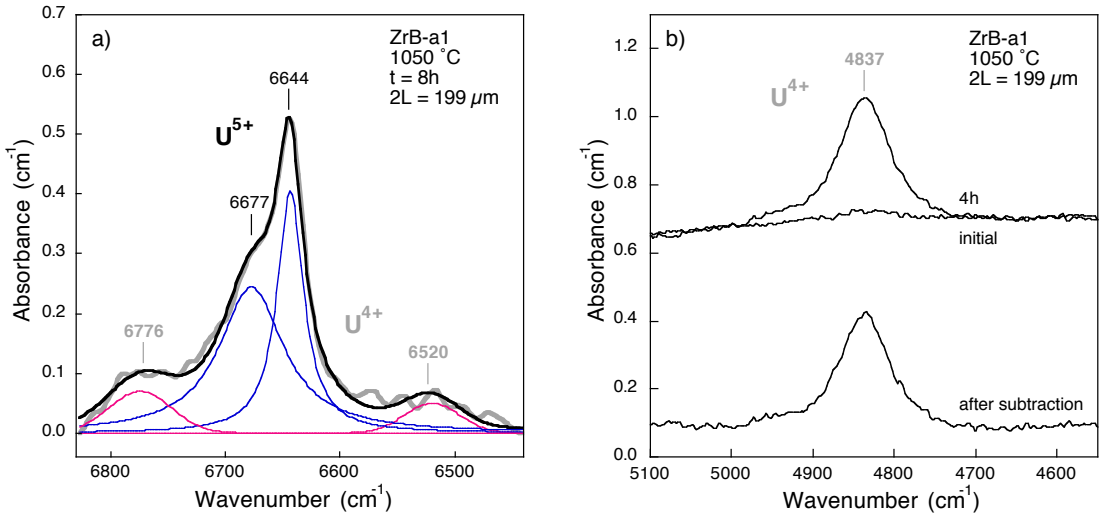

Figure 6.9. Examples showing the baseline correction of U^{5+} bands (6677 and 6644 cm^{-1}) and U^{4+} band (4837 cm^{-1}) region. a) U^{5+} absorption region (6850 to 6440 cm^{-1}). The thick gray line is the original spectrum and the black line is the generated one. The deconvoluted bands at 6677 and 6644 cm^{-1} are U^{5+} bands while the bands at 6776 and 6520 cm^{-1} are U^{4+} bands. b) U^{4+} absorption region (5000 to 4600 cm^{-1}). Slice ZrB-a1, annealed at 1050 °C, with a thickness 2L of 199 μm.

The integrated area of the U^{5+} bands and U^{4+} bands are shown in Table 6.5. Since no diffusion of uranium out of the crystal is expected at these temperatures (diffusion rate of U is lower than 3.6×10^{-27} m^2s^{-1} at 1150 °C; Cherniak et al. 1997b), the decrease of U^{5+} is assumed to be proportional to the increase of U^{4+}. Therefore, the ratio of molar absorption coefficients, $\varepsilon_U^{5+}/\varepsilon_U^{4+}$, was calculated from $(A_U^{5+}{}_0 - A_U^{5+})/(A_U^{4+} - A_U^{4+}{}_0)$, where A_U^{5+} and A_U^{4+} are the integral absorbances of U^{5+} and U^{4+} bands at time t respectively; $A_U^{5+}{}_0$ and $A_U^{4+}{}_0$ are the integral absorbances of U^{5+} and U^{4+} at $t = 0$ respectively; $A_U^{5+}{}_0 - A_U^{5+}$ is the decreasing integral absorbance of U^{5+} and $A_U^{4+} - A_U^{4+}{}_0$ is the increasing integral absorbance of U^{4+}. The deduced value of $\varepsilon_U^{5+}/\varepsilon_U^{4+}$ is 2.16 ± 0.05 (Table 6.5, Fig. 6.10). Note that for sample ZrB-c1 annealed at 1150 °C, further annealing after the completion of H-D exchange (A_U^{5+} increases, Table 6.5; A_{OH} remains unchanged while A_{OD} decreases, Table 6.6) implies that U^{4+} was reoxidized to U^{5+} and D was extracted from the sample. The final integral absorbance of U^{5+} is even greater than the initial one (8.97 versus 7.30) indicating that

not only the original U^{5+} has been restored, but also the original minor U^{4+} has been oxidized to U^{5+}. Another direct evidence is that there is no U^{4+} bands at 6776 and 6520 cm^{-1} present in the spectrum at this stage.

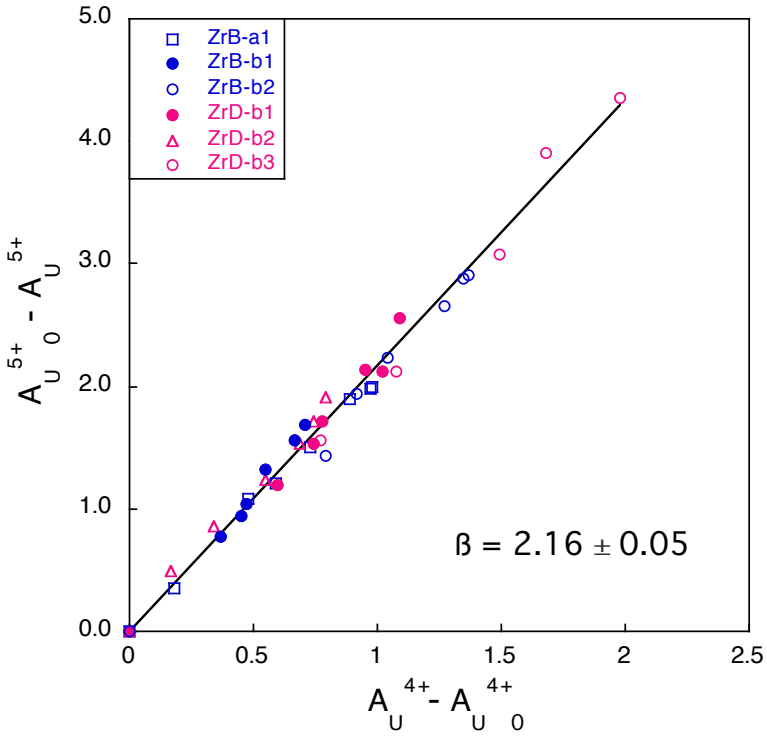

Figure 6.10. Changes of integral absorbance of U^{5+} and U^{4+} bands upon heating. The slope of the linear dependency of $A_U{}^{5+}{}_0$ - $A_U{}^{5+}$ versus $A_U{}^{4+}$ - $A_U{}^{4+}{}_0$ corresponds to the ratio of the molar absorption coefficients, $\varepsilon_U{}^{5+}/\varepsilon_U{}^{4+}$. $A_U{}^{5+}{}_0$ and $A_U{}^{4+}{}_0$ are the integral absorbances of U^{5+} and U^{4+} at $t = 0$; $A_U{}^{5+}$ and $A_U{}^{4+}$ are the integral absorbances of U^{5+} and U^{4+} bands at time t respectively; $A_U{}^{5+}{}_0$ - $A_U{}^{5+}$ is the decreasing integral absorbance of U^{5+} and $A_U{}^{4+}$ - $A_U{}^{4+}{}_0$ is the increasing integral absorbance of U^{4+}.

Table 6.5. Changes of integral absorbance of U^{5+} bands (6677 and 6644 cm^{-1}) and U^{4+} band (4837 cm^{-1}) upon heating.

t (h)	A_U^{5+}	$A_U^{4+} - A_U^{4+}{}_0$	$A_U^{5+} - A_U^{5+}{}_f$	$(A_U^{5+} - A_U^{5+}{}_f)/(A_U^{5+}{}_0 - A_U^{5+}{}_f)$	$(A_U^{4+} - A_U^{4+}{}_0)/(A_U^{4+}{}_f - A_U^{4+}{}_0)$	$A_U^{5+}{}_0 - A_U^{5+}$
ZrB-c2; 900°C; 2L = 111 μm; $A_U^{5+}{}_0 - A_U^{5+}{}_f = 2.52 - 0.34 = 2.18$						
0.00	2.52		2.10	1.00		0.00
1.00	2.10		1.68	0.80		0.42
4.00	1.38		0.96	0.46		1.14
8.00	1.17		0.75	0.36		1.35
16.00	0.96		0.54	0.26		1.56
33.00	0.78		0.36	0.17		1.74
75.00	0.62		0.20	0.10		1.90
131.00	0.36		0.00	0.00		2.16
ZrB-c3; 1000°C; 2L = 314 μm; $A_U^{5+}{}_0 - A_U^{5+}{}_f = 6.78 - 1.90 = 4.88$						
0.00	6.78		4.88	1.00		0.00
1.00	5.75		3.85	0.79		1.03
2.00	4.75		2.85	0.58		2.03
4.00	4.35		2.45	0.50		2.43
9.00	3.74		1.84	0.38		3.04
19.10	3.13		1.23	0.25		3.65
44.10	2.45		0.55	0.11		4.33
92.10	1.90		0.00	0.00		4.88
ZrB-c1; 1150°C; 2L = 291 μm; $A_U^{5+}{}_0 - A_U^{5+}{}_f = 6.55 - 2.18 = 4.37$						
0.00	6.55		4.37	1.00		0.00
1.00	2.68		0.50	0.11		3.87
2.00	2.18		0.00	0.00		4.37
4.00	7.72		5.54	1.27		

Table 6.5. continued.

t (h)	A_U^{5+}	$A_U^{4+} - A_U^{4+}{}_0$	$A_U^{5+} - A_U^{5+}{}_f$	$(A_U^{5+} - A_U^{5+}{}_f)/(A_U^{5+}{}_0 - A_U^{5+}{}_f)$	$(A_U^{4+} - A_U^{4+}{}_0)/(A_U^{4+}{}_f - A_U^{4+}{}_0)$	$A_U^{5+}{}_0 - A_U^{5+}$
ZrD-b2; 950°C; 2L = 153 μm; $A_U^{5+}{}_0 - A_U^{5+}{}_f = 2.31 - 0.40 = 1.91$; $A_U^{4+}{}_0 = 0.03$; $A_U^{4+}{}_f - A_U^{4+}{}_0 = 0.79$						
0.00	2.31	0.00	1.91	1.00	0.00	0.00
1.00	1.82	0.17	1.42	0.74	0.22	0.49
3.00	1.45	0.34	1.05	0.55	0.43	0.86
10.00	1.08	0.55	0.68	0.35	0.70	1.23
22.42	0.78	0.69	0.38	0.20	0.87	1.53
44.00	0.60	0.74	0.20	0.10	0.94	1.71
90.00	0.40	0.79	0.00	0.00	1.00	1.91
ZrB-b1; 1000°C; 2L = 139 μm; $A_U^{5+}{}_0 - A_U^{5+}{}_f = 1.87 - 0.18 = 1.69$; $A_U^{4+}{}_0 = 0.03$; $A_U^{4+}{}_f - A_U^{4+}{}_0 = 0.71$						
0.00	1.87	0.00	1.69	1.00	0.00	0.00
1.00	1.10	0.37	0.92	0.54	0.52	0.77
2.00	0.93	0.45	0.75	0.44	0.63	0.95
6.00	0.83	0.47	0.65	0.39	0.66	1.04
12.00	0.55	0.55	0.37	0.22	0.77	1.32
32.00	0.31	0.67	0.13	0.08	0.94	1.56
73.00	0.18	0.71	0.00	0.00	1.00	1.69
ZrD-b1; 1050°C; 2L = 204 μm; $A_U^{5+}{}_0 - A_U^{5+}{}_f = 3.15 - 0.60 = 2.55$; $A_U^{4+}{}_0 = 0.05$; $A_U^{4+}{}_f - A_U^{4+}{}_0 = 1.09$						
0.00	3.15	0.00	2.55	1.00	0.00	0.00
1.00	1.96	0.60	1.36	0.54	0.55	1.19
2.00	1.62	0.74	1.02	0.40	0.68	1.53
4.00	1.43	0.78	0.83	0.32	0.72	1.72
8.08	1.03	1.02	0.43	0.17	0.94	2.12
16.22	0.60	1.09	0.00	0.00	1.00	2.55
26.28*	1.01	0.95	0.41	0.16	0.87	2.14

Table 6.5. continued.

t (h)	A_U^{5+}	$A_U^{4+} - A_U^{4+}{}_0$	$A_U^{5+} - A_U^{5+}{}_f$	$(A_U^{5+} - A_U^{5+}{}_f)/(A_U^{5+}{}_0 - A_U^{5+}{}_f)$	$(A_U^{4+} - A_U^{4+}{}_0)/(A_U^{4+}{}_f - A_U^{4+}{}_0)$	$A_U^{5+}{}_0 - A_U^{5+}$
ZrD-b3; 1050°C; 2L = 372 μm; $A_U^{5+}{}_0 - A_U^{5+}{}_f = 5.84 - 1.49 = 4.35$; $A_U^{4+}{}_0 = 0.06$; $A_U^{4+}{}_f - A_U^{4+}{}_0 = 1.98$						
0.00	5.84	0.00	4.35	1.00	0.00	0.00
1.20	4.28	0.77	2.79	0.64	0.39	1.56
2.20	3.72	1.08	2.23	0.51	0.55	2.12
6.20	2.76	1.49	1.27	0.29	0.75	3.08
15.20	1.93	1.68	0.44	0.10	0.85	3.91
32.20	1.49	1.98	0.00	0.00	1.00	4.35
ZrB-b2; 1100°C; 2L = 385 μm; $A_U^{5+}{}_0 - A_U^{5+}{}_f = 4.22 - 1.31 = 2.91$; $A_U^{4+}{}_0 = 0.21$; $A_U^{4+}{}_f - A_U^{4+}{}_0 = 1.37$						
0.00	4.22	0.00	2.91	1.00	0.00	0.00
1.00	2.79	0.79	1.48	0.51	0.58	1.43
2.00	2.28	0.92	0.97	0.33	0.67	1.94
4.00	1.98	1.04	0.67	0.23	0.76	2.24
8.00	1.56	1.27	0.25	0.09	0.93	2.66
15.00	1.31	1.37	0.00	0.00	1.00	2.91
31.00	1.34	1.35	0.03	0.01	0.99	2.88
ZrB-a1; 1050°C; 2L = 199 μm; $A_U^{5+}{}_0 - A_U^{5+}{}_f = 2.32 - 0.43 = 1.89$; $A_U^{4+}{}_0 = 0.06$; $A_U^{4+}{}_f - A_U^{4+}{}_0 = 0.98$						
0.00	2.32	0.00	1.99	1.00	0.00	0.00
1.00	1.97	0.18	1.64	0.83	0.18	0.35
2.00	1.24	0.48	0.91	0.46	0.49	1.08
4.00	1.12	0.59	0.79	0.39	0.60	1.21
8.00	0.81	0.73	0.48	0.24	0.74	1.51
17.00	0.43	0.89	0.10	0.05	0.91	1.89
33.00	0.33	0.98	0.00	0.00	1.00	1.99
rehydr	0.34	0.97	0.01	0.01	0.99	1.98

Notes: t is the time of annealing; A_U^{5+} and A_U^{4+} are the integral absorbances of U^{5+} and U^{4+} bands at time t respectively; $A_U^{5+}{}_0$ and $A_U^{4+}{}_0$ are the integral absorbances of U^{5+} and U^{4+} at $t = 0$ respectively; $A_U^{5+}{}_f$ and $A_U^{4+}{}_f$ are the integral absorbances of U^{5+} and U^{4+} bands at the final stage of exchange when $A_U^{5+}$and A_U^{4+} have reached a steady state maximum value. $A_U^{5+}{}_0$ - A_U^{5+} is the decreasing integral absorbance of U^{5+} and A_U^{4+}- $A_U^{4+}{}_0$ is the increasing integral absorbance of U^{4+}; "rehydr" for ZrB-a1 represents the result of rehydrogenation of the sample in Ar/H_2 atmosphere for 42.5 h; during the last annealing of ZrD-b1 (26.28*), extraction of OH (OD) species occurred and U^{4+} was oxidized into U^{5+}, thus the data of this step was not used for the calculation of diffusivity.

6.6 Diffusion kinetics

During annealing in deuterated environment (i.e., during H-D exchange), the evolution of the OH integral absorbance relates only to the H-D exchange process. These data can be used to deduce the kinetics of deuteration. However, at the same time as the reduction of uranium, incorporation of deuterium into the crystal structure occurs concurrently with deuteration. It is necessary to separate in the increase of OD bands, the part due to the H-D exchange from the part due to D incorporation. To do it, it is necessary to determine the ratio of molar absorption coefficients of OH to OD, β, that is $\varepsilon_{OH}/\varepsilon_{OD}$. This was calculated from the value of the integral absorbance of OH bands at saturation, A_{OHs} (integral absorbance of OH bands after completion of rehydrogenation) compared to that of OD bands at saturation, A_{ODs} (integral absorbance of OD bands if all H contributing to A_{OHs} were replaced by D). Since there is no further reduction of uranium during rehydrogenation (U absorption spectrum does not change; Fig. 6.9), no incorporation of H species is expected to occur during rehydrogenation. A_{ODs} is equals to the value of A_{OD} at the completion of the H-D exchange (A_{ODf}) plus a value corresponding to the contribution of OH that remains unexchanged after completion of the H-D experiment (A_{OHf}/β): $A_{ODs} = A_{ODf} + A_{OHf}/\beta$. According to $A_{OHs} = \beta A_{ODs} = \beta(A_{ODf} + A_{OHf}/\beta)$, values of β of 2.16 and 2.36 were obtained, from the experiments on ZrB-a1 (unpolarized spectra and polarized spectra

perpendicular to c, respectively). A mean value of 2.27 ± 0.11 was adopted. $A_{OH0} - A_{OH}$ corresponds to the decreasing absorbance of OH, with A_{OH0} the absorbance at time $t = 0$ considering the initial rearrangement and A_{OH} the absorbance at time t. A_{OD} is the absorbance of OD at time t. Then $A_{OD(H-D)}$, A_{OD} related to H-D exchange, was calculated from $(A_{OH0} - A_{OH})/\beta$, while $A_{OD(inc)}$, A_{OD} related to D incorporation, was obtained from $A_{OD} - A_{OD(H-D)}$. Another important specific feature of H-D exchange in zircon is that, like for the same experiments performed on garnets (grossular, Kurka 2005; grossular, Kurka et al. 2005; andradite, this thesis), the exchange is never complete, 27 to 48% of the original OH bands absorbance remains after H-D exchange (Table 6.6). During the final steps, the change of absorbance of OH and OD bands is rather limited or remains constant within error uncertainties, showing an equilibrium of the reaction and accomplishment of the exchange.

Since the absorbance of OH bands at the final stage of the exchange, A_{OHf}, is not null, we consider that the corresponding amount of H-defects is not available for the H-D exchange; only H-defects corresponding to the difference between the absorbance at time $t = 0$ and the final absorbance $(A_{OH0} - A_{OHf})$ when a steady state is reached, can be considered for the exchange (Table 6.6). Therefore, the evolution with time t of OH bands during H-D exchange is best represented by the normalized value: $(A_{OH} - A_{OHf})/(A_{OH0} - A_{OHf})$ (Table 6.6), while for OD bands related to deuterium incorporation is represented by $A_{OD(inc)}/A_{OD(inc)f}$, where $A_{OD(inc)}$ is the absorbance of OD bands related to D incorporation at time t and $A_{OD(inc)f}$ is the absorbance of OD bands at the final stage of incorporation when A_{OD} has reached a steady state maximum value (Table 6.6). The kinetics of redox reaction of uranium was calculated using data of integral absorbances of U^{5+} (bands at 6677 and 6644 cm^{-1}) and U^{4+} (band at 4837 cm^{-1}). The same method for data processing as H diffusion was applied on uranium redox reaction. The evolution with time t of U^{5+} and U^{4+} bands is represented by the normalized values: $(A_U{}^{5+} - A_U{}^{5+}{}_f)/(A_U{}^{5+}{}_0 - A_U{}^{5+}{}_f)$ and $(A_U{}^{4+} - A_U{}^{4+}{}_0)/(A_U{}^{4+}{}_f - A_U{}^{4+}{}_0)$, where $A_U{}^{5+}$ and $A_U{}^{4+}$ are the integral absorbances of U^{5+} and U^{4+} bands at time t and $A_U{}^{5+}{}_f$ and $A_U{}^{4+}{}_f$ is the absorbances of U^{5+} and U^{4+} bands at the final stage of exchange when $A_U{}^{5+}$and $A_U{}^{4+}$ have reached a steady state maximum value (Table 6.5).

Table 6.6. Experimental integral absorbance from H-D exchange experiments.

t (h)	A_{OH}	A_{OD}	A_{OH}- A_{OHf}	$(A_{OH}-A_{OHf})/(A_{OH0}-A_{OHf})$	A_{OH0}- A_{OH}	A_{OD} (H-D)	A_{OD} (inc)	$A_{OD(inc)}/A_{OD(inc)f}$
ZrB-c2; 900 °C; 2L = 111 μm; A_{OH0} = 9.01 × 1.08 = 9.74; A_{OH0} - A_{OHf} = 9.74 - 3.04 = 6.69; $A_{OD(inc)f}$ = 5.75; A_{ODf} = 8.70								
0.00	9.01 (9.74)	0.00	6.69	1.00	0.00	0.00	0.00	0.00
1.00	9.28	0.54	6.24	0.93	0.45	0.20	0.34	0.06
4.00	8.60	2.02	5.56	0.83	1.13	0.50	1.53	0.27
8.00	7.70	3.25	4.66	0.70	2.04	0.90	2.35	0.41
16.00	5.78	5.08	2.74	0.41	3.96	1.74	3.34	0.58
33.00	3.69	6.85	0.65	0.10	6.05	2.66	4.19	0.73
75.00	3.04	8.70	0.00	0.00	6.69	2.95	5.75	1.00
131.00	3.46	8.32	0.42	0.06	6.27	2.76	5.56	0.97
ZrB-c3; 1000 °C; 2L = 314 μm; A_{OH0} = 31.21 × 1.08 = 33.71; A_{OH0} - A_{OHf} = 33.71 - 8.86 = 24.85; $A_{OD(inc)f}$ = 10.92; A_{ODf} = 21.80								
0.00	31.21 (33.71)	0.00	24.85	1.00	0.00	0.00	0.00	0.00
1.00	29.20	3.16	20.34	0.82	4.51	1.99	1.18	0.11
2.00	28.40	4.25	19.54	0.79	5.31	2.34	1.91	0.17
4.00	23.14	7.31	14.28	0.57	10.57	4.66	2.65	0.24
9.00	15.35	11.99	6.49	0.26	18.36	8.09	3.90	0.36
19.10	10.12	16.90	1.26	0.05	23.59	10.39	6.51	0.60
44.10	8.86	20.90	0.00	0.00	24.85	10.95	9.95	0.91
92.10	9.02	21.80	0.16	0.01	24.69	10.88	10.92	1.00

Table 6.6. continued.

t (h)	A_{OH}	A_{OD}	A_{OH}- A_{OHf}	$(A_{OH}-A_{OHf})/(A_{OH0}-A_{OHf})$	A_{OH0}- A_{OH}	A_{OD} (H-D)	A_{OD} (inc)	$A_{OD(inc)}/A_{OD(inc)f}$
ZrB-c1; 1150 °C; 2L = 291 μm; A_{OH0} = 26.23 × 1.08 = 28.33; A_{OH0} - A_{OHf} = 28.33 - 11.76 = 16.57; $A_{OD(inc)f}$ = 6.90; A_{ODf} = 14.20								
0.00	26.23 (28.33)	0.00	16.57	1.00	0.00	0.00	0.00	0.00
1.00	12.47	13.64	0.71	0.04	15.86	6.99	6.65	0.96
2.00	11.76	14.20	0.00	0.00	16.57	7.30	6.90	1.00
4.00	11.76	7.30	0.00	0.00	16.57	7.30	0.00	
ZrD-b2; 950 °C; 2L = 153 μm; A_{OH0} = 10.92 × 0.895 = 9.76; A_{OH0} - A_{OHf} = 9.76 - 4.09 = 5.67; $A_{OD(inc)f}$ = 6.06; A_{ODf} = 8.56								
0.00	10.92 (9.76)	0.00	5.67	1.00	0.00	0.00	0.00	0.00
1.00	9.23	1.02	5.14	0.91	0.53	0.23	0.79	0.13
3.00	9.09	1.50	5.00	0.88	0.66	0.29	1.20	0.20
10.00	8.31	3.22	4.22	0.74	1.45	0.64	2.59	0.43
22.42	6.95	4.80	2.85	0.50	2.81	1.24	3.56	0.59
44.00	4.53	7.46	0.44	0.08	5.23	2.30	5.15	0.85
90.00	4.09	8.56	0.00	0.00	5.67	2.50	6.06	1.00
ZrB-b1; 1000 °C; 2L = 139 μm; A_{OH0} = 10.12 × 0.895 = 9.05; A_{OH0} - A_{OHf} = 9.05 - 3.75 = 5.30; $A_{OD(inc)f}$ = 5.35; A_{ODf} = 7.51								
0.00	10.12 (9.05)	0.00	5.30	1.00	0.00	0.00	0.00	0.00
1.00	7.74	1.87	3.99	0.75	1.31	0.58	1.29	0.24
2.00	7.41	2.60	3.66	0.69	1.64	0.72	1.88	0.35
6.00	5.53	3.71	1.78	0.34	3.52	1.55	2.16	0.40
12.00	4.22	5.95	0.47	0.09	4.83	2.13	3.82	0.71
32.00	3.75	7.26	0.00	0.00	5.30	2.33	4.93	0.92
73.00	4.14	7.51	0.39	0.07	4.91	2.16	5.35	1.00

Table 6.6. continued.

t (h)	A_{OH}	A_{OD}	A_{OH}- A_{OHf}	$(A_{OH}-A_{OHf})/(A_{OH0}-A_{OHf})$	A_{OH0}- A_{OH}	A_{OD} (H-D)	A_{OD} (inc)	$A_{OD(inc)}/A_{OD(inc)f}$
ZrD-b1; 1050 °C; 2L = 204 μm; A_{OH0} = 14.77 × 0.895 = 13.20; A_{OH0} - A_{OHf} = 13.2 - 6.97 = 6.23; $A_{OD(inc)f}$ = 6.10; A_{ODf} = 8.70								
0.00	14.77 (13.20)	0.00	6.23	1.00	0.00	0.00	0.00	0.00
1.00	11.75	2.92	4.78	0.77	1.45	0.64	2.28	0.37
2.00	10.26	4.39	3.29	0.53	2.94	1.29	3.10	0.51
4.00	9.17	5.56	2.20	0.35	4.03	1.78	3.78	0.62
8.08	6.97	7.89	0.00	0.00	6.23	2.74	5.15	0.84
16.22	7.29	8.70	0.32	0.05	5.91	2.60	6.10	1.00
ZrD-b3; 1050 °C; 2L = 372 μm; A_{OH0} = 26.57 × 0.895 = 23.75; A_{OH0} - A_{OHf} = 23.75 - 11.4 = 12.35; $A_{OD(inc)f}$ = 9.74; A_{ODf} = 15.18								
0.00	26.57 (23.75)	0.00	12.35	1.00	0.00	0.00	0.00	0.00
1.20	22.01	3.23	10.61	0.86	1.74	0.77	2.46	0.25
2.20	21.51	4.27	10.11	0.82	2.24	0.99	3.28	0.34
6.20	17.72	8.11	6.32	0.51	6.03	2.66	5.45	0.56
15.20	12.20	13.68	0.80	0.06	11.55	5.09	8.59	0.88
32.20	11.40	15.18	0.00	0.00	12.35	5.44	9.74	1.00
ZrB-b2; 1100 °C; 2L = 385 μm; A_{OH0} = 29.28 × 0.895 = 26.18; A_{OH0} - A_{OHf} = 26.18 - 7.52=18.66; $A_{OD(inc)f}$ = 10.05; A_{ODf} = 18.27								
0.00	29.28 (26.18)	0.00	18.66	1.00	0.00	0.00	0.00	0.00
1.00	19.38	3.93	11.86	0.64	6.80	3.00	0.93	0.09
2.00	17.10	7.91	9.58	0.51	9.08	4.00	3.91	0.39
4.00	11.02	14.23	3.50	0.19	15.16	6.68	7.55	0.75
8.00	8.57	16.05	1.05	0.06	17.61	7.76	8.29	0.83

15.00	7.52	18.27	0.00	0.00	18.66	8.22	10.05	1.00
31.00	8.35	16.98	0.83	0.04	17.83	7.85	9.13	0.91

Table 6.6. continued.

t (h)	A_{OH}	A_{OD}	A_{OH}- A_{OHf}	$(A_{OH}-A_{OHf})/(A_{OH0}-A_{OHf})$	A_{OH0}- A_{OH}	A_{OD} (H-D)	A_{OD} (inc)	$A_{OD(inc)}/A_{OD(inc)f}$
ZrB-a1; 1050 °C; 2L = 199 μm; A_{OH0} = 13.46 × 0.895 = 12.03; A_{OH0} - A_{OHf} = 12.03 - 4.85 = 7.18; $A_{OD(inc)f}$ = 6.71; A_{ODf} = 9.87								
0.00	13.46 (12.03)	0.00	7.18	1.00	0.00	0.00	0.00	0.00
1.00	11.00	1.00	6.15	0.86	1.03	0.45	0.55	0.08
2.00	9.42	3.28	4.57	0.64	2.61	1.15	2.13	0.32
4.00	8.50	5.05	3.65	0.51	3.53	1.56	3.49	0.52
8.00	5.52	8.04	0.67	0.09	6.52	2.87	5.17	0.77
17.00	5.10	9.25	0.25	0.03	6.93	3.05	6.20	0.92
33.00	4.85	9.87	0.00	0.00	7.18	3.16	6.71	1.00
rehydr	26.18	0						

Notes: *t* is the time of annealing at nominal temperature; A_{OH} is the integral absorbance of the OH bands and A_{OD} the integral absorbance of the total OD bands ($A_{OD(H-D)}$ and $A_{OD(inc)}$ related to H-D exchange and deuterium incorporation respectively); A_{OH0} is the modulated integral absorbance of OH bands at t = 0 after consideration of the rearrangement of OH bands in the initial annealing, that is 89.4% of the initial A_{OH} for slices parallel to *c* axis and 108% for slices perpendicular to *c* axis; A_{OHf} and A_{ODf} are the integral absorbance of OH and total OD bands at the final stage of experiment, respectively; $A_{OD(inc)f}$ is the integral absorbance of OD bands related to deuterium corporation at the final stage of experiment; "rehydr" for ZrB-a1 represents the result of rehydrogenation of the sample in Ar/H_2 atmosphere for 42.5 h; ZrB-c, ZrB-b, ZrB-a represent slices perpendicular to *c*, *b*, *a* axis of zircon B respectively; ZrD-b represent slices perpendicular to *b* axis of Zircon D.

The evolutions with time *t* of the normalized ratios of absorbance of the diffusing species are presented in Figure 6.11 - 6.13, with diffusion coefficients *D* deduced from the fit by equation (3.18) for the decreasing species and equation (3.20) for the increasing species (continuous line). The error bars on *D* are estimated from the extreme values that still fit the data within the experimental uncertainties (continuous lines). The similarity of kinetics between uranium redox reaction and deuterium incorporation for each slice (Fig. 6.11, 6.12; Table 6.7), confirms that deuterium incorporated into the zircon structure through the following redox reaction: $U^{5+} + 1/2H_2 + O^{2-} = U^{4+} + OH^-$. Redox reaction mechanism involving Fe has been confirmed during H-incorporation/extraction process in other NAMs through Mössbauer spectroscopy (e.g., diopside: Skogby 1994, Forneris and Skogby 2004; and garnet: Kurka 2005). In zircon, we found that H-D exchange exhibit diffusivities nearly identical to those of deuterium incorporation processes associated to uranium reduction (Fig. 6.12, 6.13; Table 6.7). The diffusion coefficients deduced from slices parallel to *a* and *b* axes at 1050 °C (ZrB-a1, ZrD-b1 and ZrD-b3), are identical within uncertainty (Fig. 6.12, 6.13; Table 6.7). It demonstrates that there is no anisotropy of H diffusion between *a* and *b* axes.

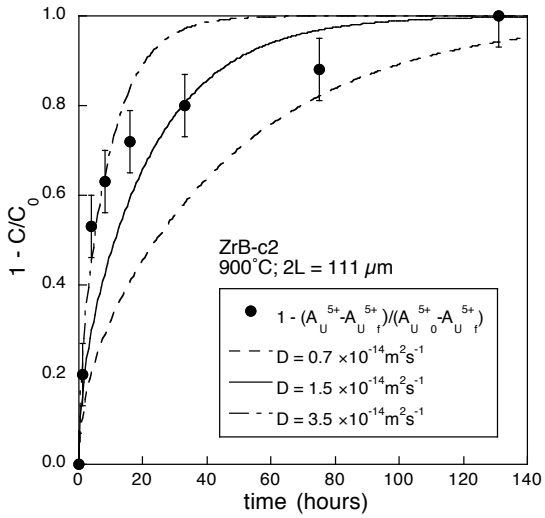

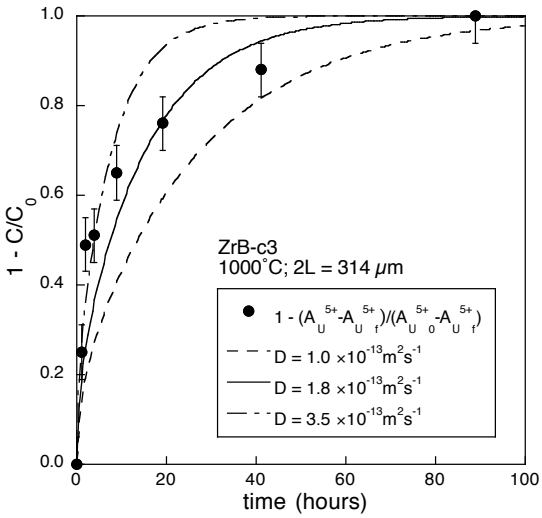

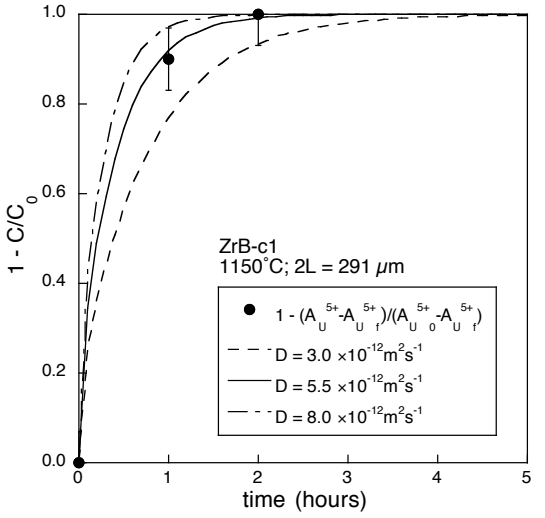

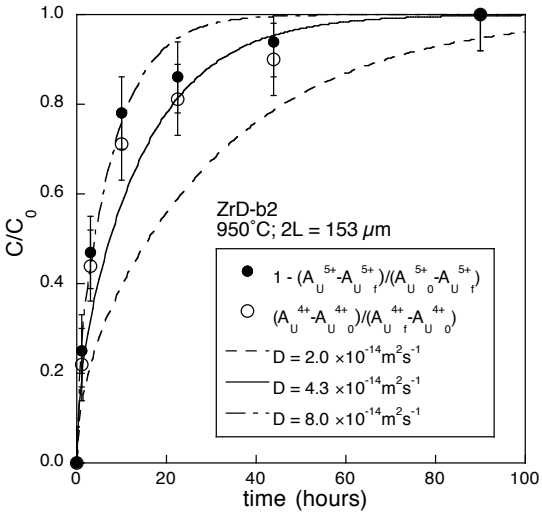

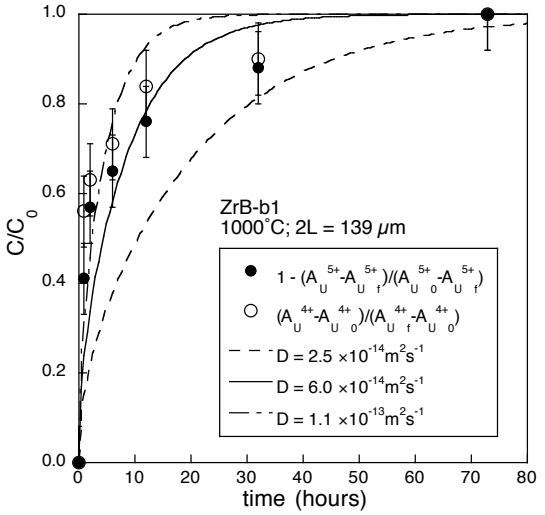

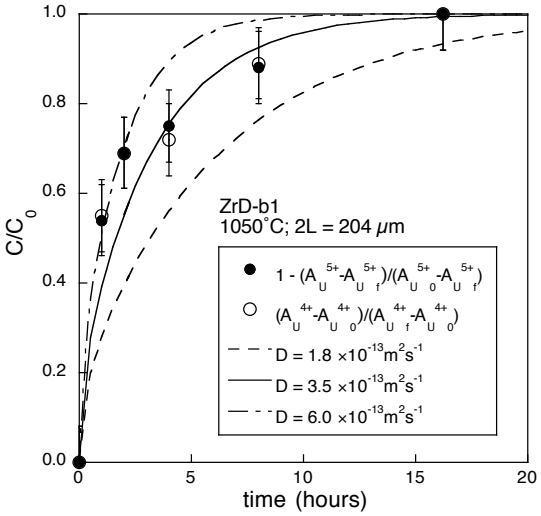

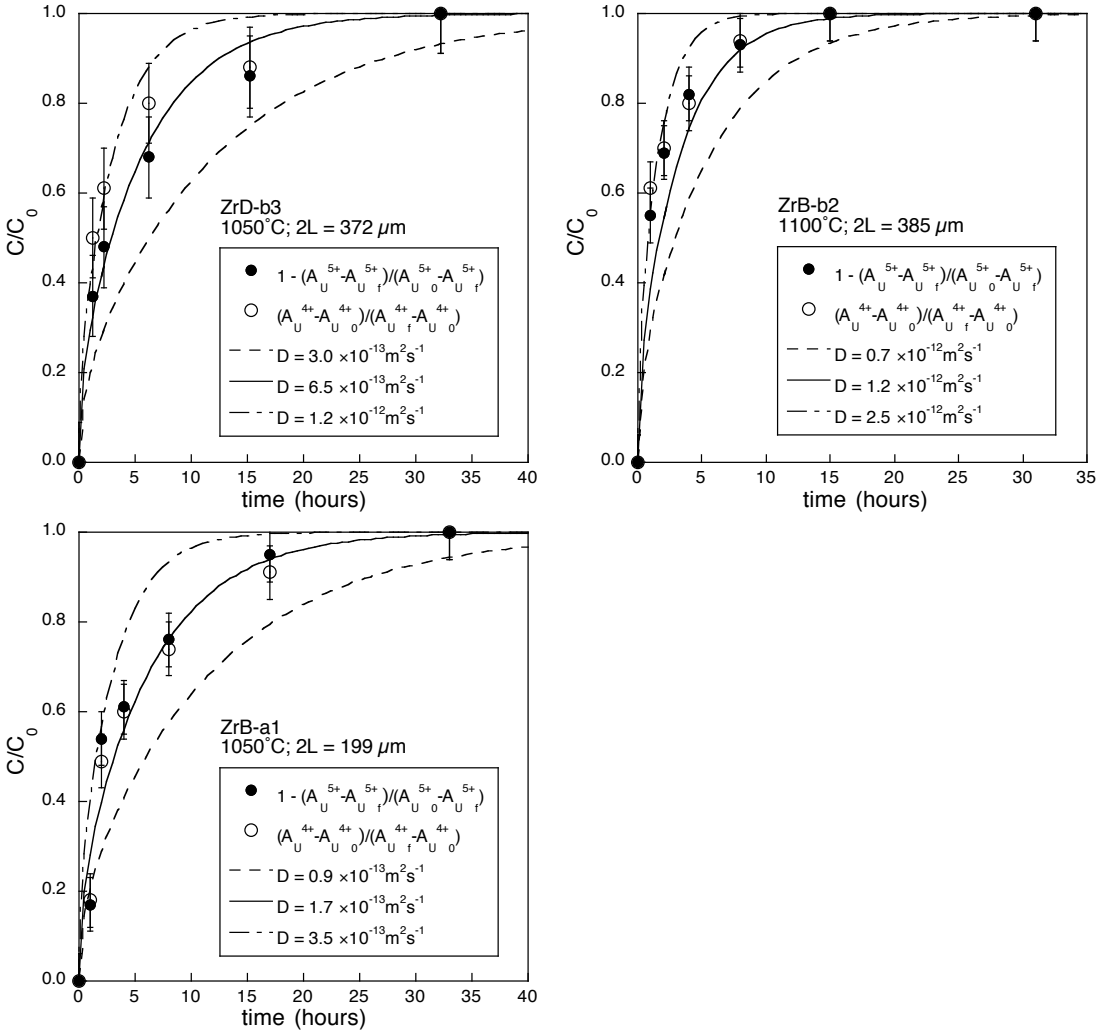

Figure 6.11. Fits of data by equation (3.18) and (3.20) for U-redox reactions in the experimental temperature range from 900 to 1150 °C (continuous line). Solid circles represent the normalized ratios of U^{5+} absorbance: $1 - (A_U{}^{5+} - A_U{}^{5+}{}_f)/(A_U{}^{5+}{}_0 - A_U{}^{5+}{}_f)$, empty circles represent the normalized ratios of U^{4+} absorbance: $(A_U{}^{4+} - A_U{}^{4+}{}_0)/(A_U{}^{4+}{}_f - A_U{}^{4+}{}_0)$. Error bars on *D* are deduced from the range of *D* values that still fit the data (discontinuous lines).

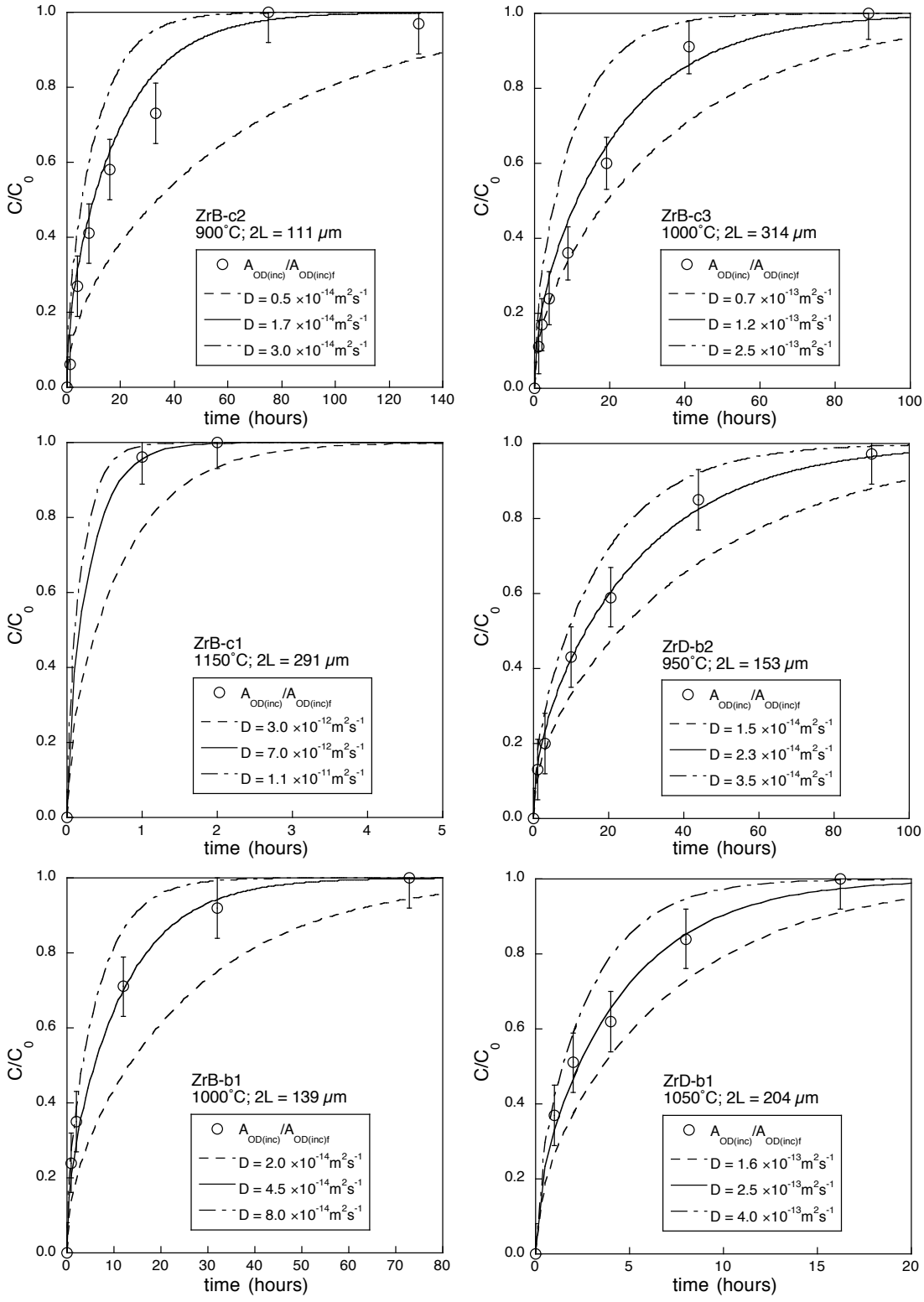

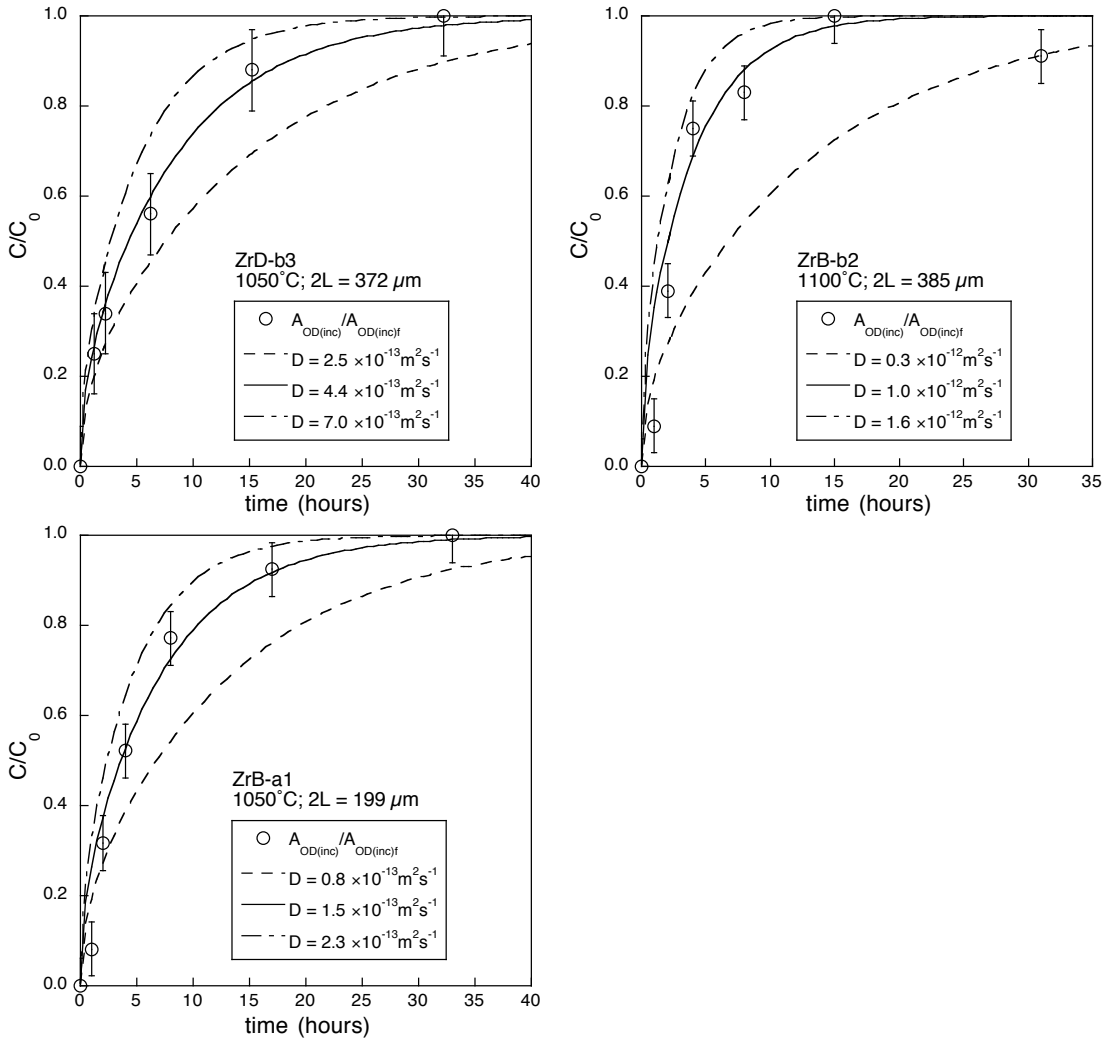

Figure 6.12. Fits of diffusion data by equation (3.20) for different values of diffusivities of deuterium incorporation at temperatures ranging from 900 to 1150 °C along the three crystallographic orientations (continuous line). Empty circles represent the normalized ratios of OD absorbance: $A_{OD(inc)}/A_{OD(inc)f}$. $A_{OD(inc)}$ is the absorbance of OD bands related to D incorporation at time *t* and $A_{OD(inc)f}$ is the absorbance of OD bands at the final stage of incorporation when A_{OD} has reached a steady state maximum value. Error bars on *D* are deduced from the range of *D* values that still fit the data (discontinuous lines).

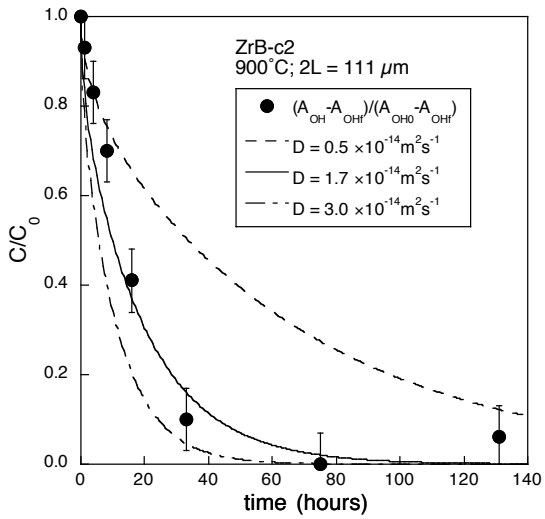

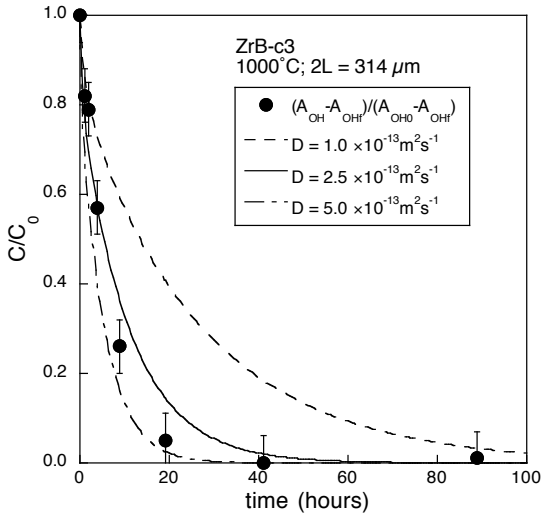

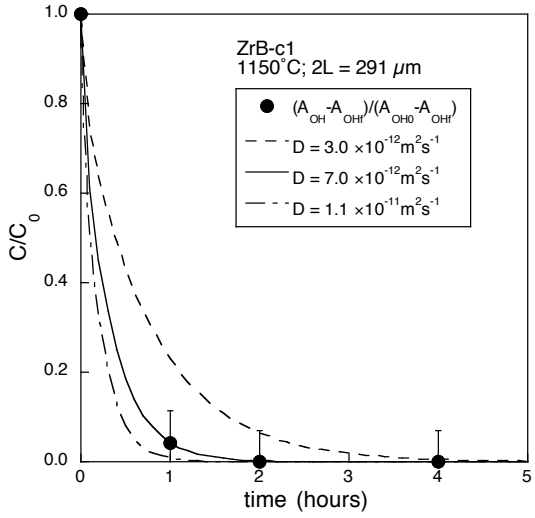

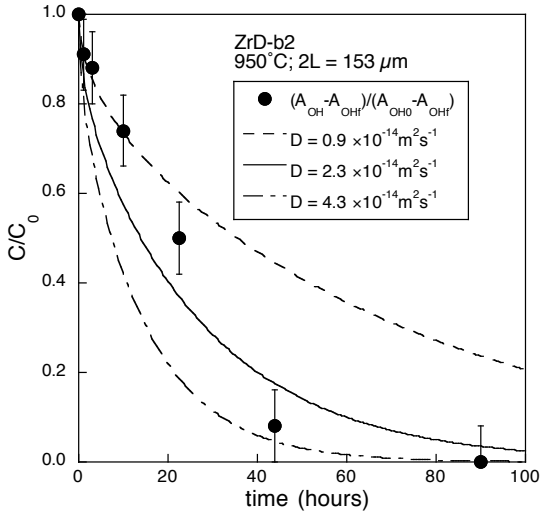

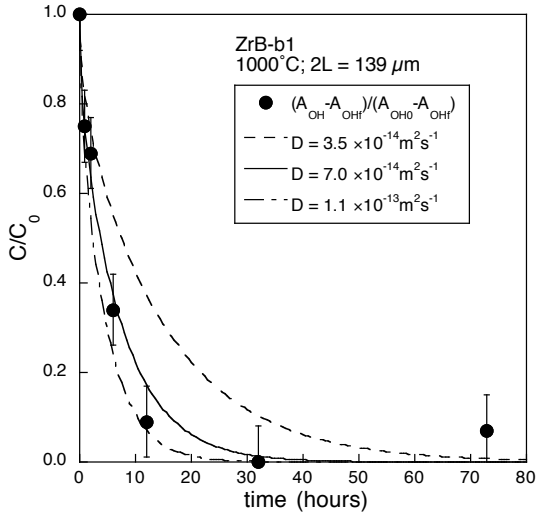

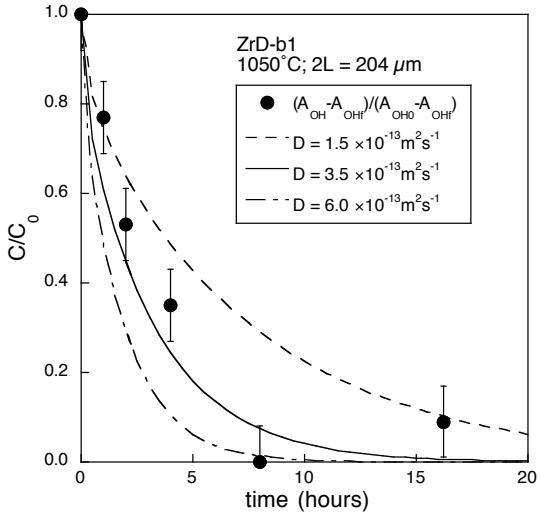

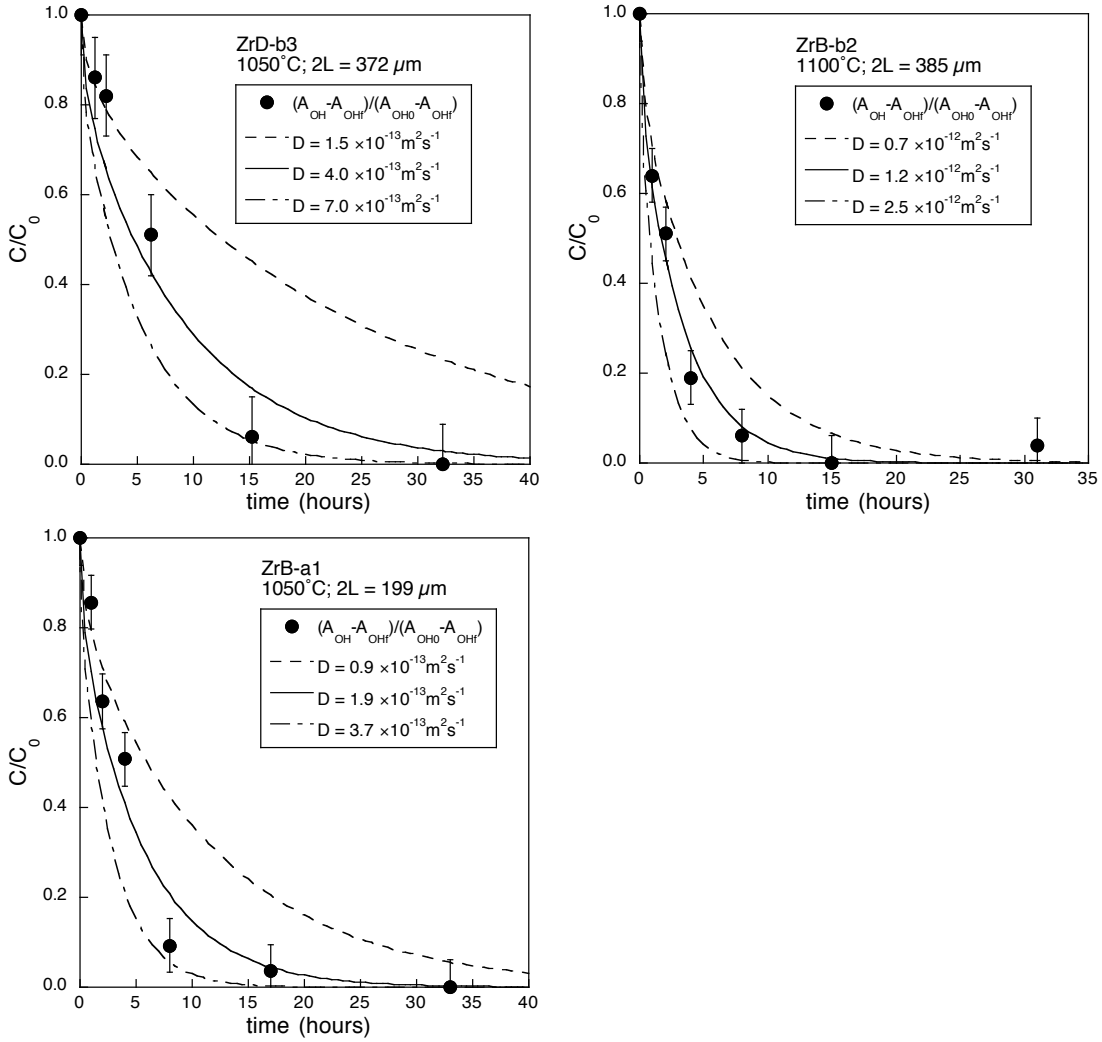

Figure 6.13. Fits of diffusion data by equation (3.18) for different values of diffusivities of H-D exchange at temperatures ranging from 900 to 1150 °C along the three crystallographic orientations (continuous line). Solid circles represent the normalized ratios of OH absorbance: $(A_{OH} - A_{OHf})/(A_{OH0} - A_{OHf})$. Error bars on *D* are deduced from the range of *D* values that still fit the data (discontinuous lines).

6.7 Diffusion law

The calculated diffusivities for H diffusion in zircon along the three crystallographic orientations are listed in Table 6.7 and plotted in an Arrhenius diagram (Fig. 6.14). A least-squares fit, following the "least-square cubic" method proposed by York (1969), leads to two diffusion laws along *a* or *b*, and *c* axes:

$$D_{[100][010]} = D_0 \exp\left[\frac{-(374 \pm 39)kJ/mol}{RT}\right] \quad (6.1)$$

with log D_0 (m^2s^{-1}) = 2.24 ± 1.57.

$$D_{[001]} = D_0 \exp\left[\frac{-(334 \pm 49)kJ/mol}{RT}\right] \quad (6.2)$$

with log D_0 (m^2s^{-1}) = 1.11 ± 0.22.

The uncertainties correspond to the uncertainties of the least-squares fitting taking account of the uncertainty on *T* (fixed at 5 °C) and the individual uncertainties on *D*. In comparison with diffusion along *a* or *b* axis, diffusion along *c* axis possesses comparable activation energy but diffusivities 2-4 times faster in the temperature range of the experiments (900-1150 °C). We assume that the diffusion laws above represent the "self-diffusion" of H-defects in zircon.

Table 6.7. Diffusivities corresponding to H-D exchange, D incorporation and U reduction in zircon for all the slices at temperatures ranging from 900 to 1150 °C along the three crystallographic orientations.

Sample No.	T (°C)	$D_{H\text{-}D}$ (m^2s^{-1})	$D_{D\text{-}inc}$ (m^2s^{-1})	$D_{U\text{-}redox}$ (m^2s^{-1})
ZrB-c2	900	$(1.7 \pm 1.3) \times 10^{-14}$	$(1.7 \pm 1.3) \times 10^{-14}$	$(1.5 \pm 2.0) \times 10^{-14}$
ZrB-c3	1000	$(2.5 \pm 2.5) \times 10^{-13}$	$(1.2 \pm 1.3) \times 10^{-13}$	$(1.8 \pm 1.2) \times 10^{-13}$
ZrB-c1	1150	$(7.0 \pm 4.0) \times 10^{-12}$	$(6.0 \pm 4.0) \times 10^{-12}$	$(5.5 \pm 2.5) \times 10^{-12}$
ZrD-b2	950	$(2.3 \pm 2.0) \times 10^{-14}$	$(2.3 \pm 1.2) \times 10^{-14}$	$(4.5 \pm 3.5) \times 10^{-14}$
ZrB-b1	1000	$(7.0 \pm 4.0) \times 10^{-14}$	$(4.5 \pm 3.5) \times 10^{-14}$	$(6.0 \pm 5.0) \times 10^{-14}$
ZrD-b1	1050	$(3.5 \pm 2.5) \times 10^{-13}$	$(2.5 \pm 1.5) \times 10^{-13}$	$(3.5 \pm 3.0) \times 10^{-13}$
ZrD-b3	1050	$(4.0 \pm 3.0) \times 10^{-13}$	$(4.4 \pm 2.6) \times 10^{-13}$	$(6.5 \pm 5.5) \times 10^{-13}$
ZrB-b2	1100	$(1.2 \pm 1.3) \times 10^{-12}$	$(1.0 \pm 0.7) \times 10^{-12}$	$(1.2 \pm 1.3) \times 10^{-12}$
ZrB-a1	1050	$(1.9 \pm 1.8) \times 10^{-13}$	$(1.5 \pm 0.8) \times 10^{-13}$	$(1.7 \pm 1.8) \times 10^{-13}$

Notes: ZrB-c, ZrB-b, ZrB-a represent slices perpendicular to *c*, *b*, *a* axes of zircon B, respectively; ZrD-b represent slices perpendicular to *b* axis of Zircon D; The error bars on *D* are estimated from the extreme values deduced from Fig. 6.11.- 6.13.

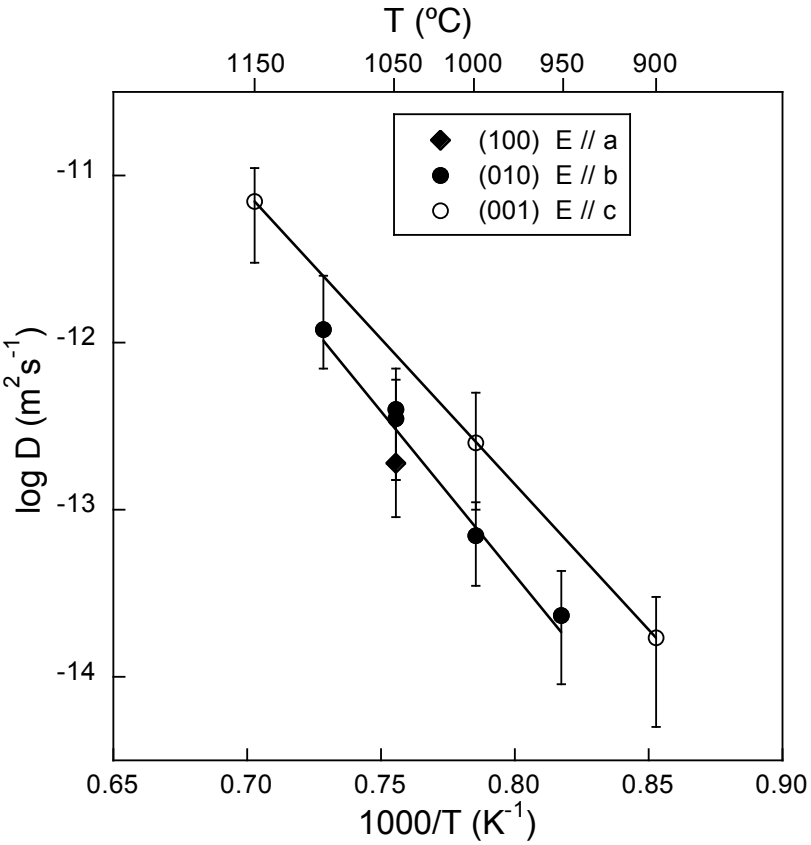

Figure 6.14. Arrhenius diagrams showing the two diffusion laws for Hmobility in zircon along different crystallographic orientations. Solid diamonds represent diffusion along *a* axis, solid circles along *b* axis, empty circles along *c* axis.

6.8 Discussion

6.8.1 Comparison between H-D exchange and D-incorporation in zircon

For the zircon investigated in this study, D-incorporation through a redox reaction has almost the same kinetics than H diffusion. The effective diffusivities obtained from H-incorporation/extraction in Fe-bearing minerals, like olivine, pyroxene and garnet, correspond to chemical diffusion of interstitial protons coupling with counter flux of electron holes localized on iron atoms, following the reaction: $Fe^{3+} + O^{2-} + 1/2H_2 = Fe^{2+} + OH^-$ (e.g., olivine: Mackwell and Kohlstedt 1990; diopside: Skogby 1994, Hercule and Jannick 1999; enstatite: Stalder et al. 2007; grossular: Kurka 2005). The change of oxidation state of Fe during H-incorporation/extraction in diopside has

been confirmed by Mössbauer spectroscopy, demonstrating parallel changes in the contents of Fe^{2+} and OH^- considering the uncertainty of molar absorptivity, while other mechanisms involving in H-incorporation/extraction are possible (Skogby and Rossman 1989; Kurka 2005). With increasing Fe content thus parallel increasing electron holes content, the diffusivity of H-incorporation/extraction will increase up to be equal to H diffusion coefficient (that is limited by H diffusion) when a critical value of Fe content is reached. A critical value of 6-8% Fe/(Fe + Mg) for natural diopside and 10-12% for synthetic enstatite, respectively, was suggested (Hercule and Ingrin, 1999; Stalder et al. 2007). In our zircon sample, the concentration of Fe is very limited (values), but the concentration of U is significant (values) and a U redox reaction mechanism was confirmed for D-incorporation during the H-D exchange experiments. Therefore, D-incorporation in zircon is due to a coupled diffusion of interstitial protons with electron holes localized on uranium atoms. Since the kinetics of D-incorporation is nearly identical to that of H-D exchange, we suggest that a critical value of uranium content (or electron holes content) was already reached in our samples and the mobility of the polarons is much faster than the mobility of hydrogen atoms. Therefore, the kinetics of the incorporation reaction is limited by the mobility of hydrogen atoms in the structure of zircon. At our knowledge, it is the first time that a redox reaction involving in H-incorporation related to uranium is evidenced in minerals.

6.8.2 Comparison with H diffusion laws in NAMs

Figure 6.15 shows a compilation of H diffusion laws in zircon and other NAMs, which were deduced from H-D exchange and suggested to represent true H mobility. Compared with other NAMs, the activation energy for hydrogen diffusion in zircon exhibits much higher values (334-374 kJ/mol). The activation energies obtained for other NAMs are in the range 100-190 kJ/mol (diopside: 145 kJ/mol, Hercule and Ingrin 1999; olivine // a: 140 kJ/mol, Du Frane et al. 2012; quartz // c: 176 kJ/mol, Kats et al. 1962; Dora Maria pyrope: 140 kJ/mol, Blanchard and Ingrin 2004a; grossular (GRO and ZT): 155 kJ/mol, Kurka 2005) and an interstitial mechanism (H

moves as interstitial proton) was suggested for these NAMs. In the temperature range investigated, zircon exhibits diffusivities one to four orders of magnitude lower than for other NAMs. At our knowledge, it is the first time that such a high activation energy is observed for H-D diffusion in minerals.

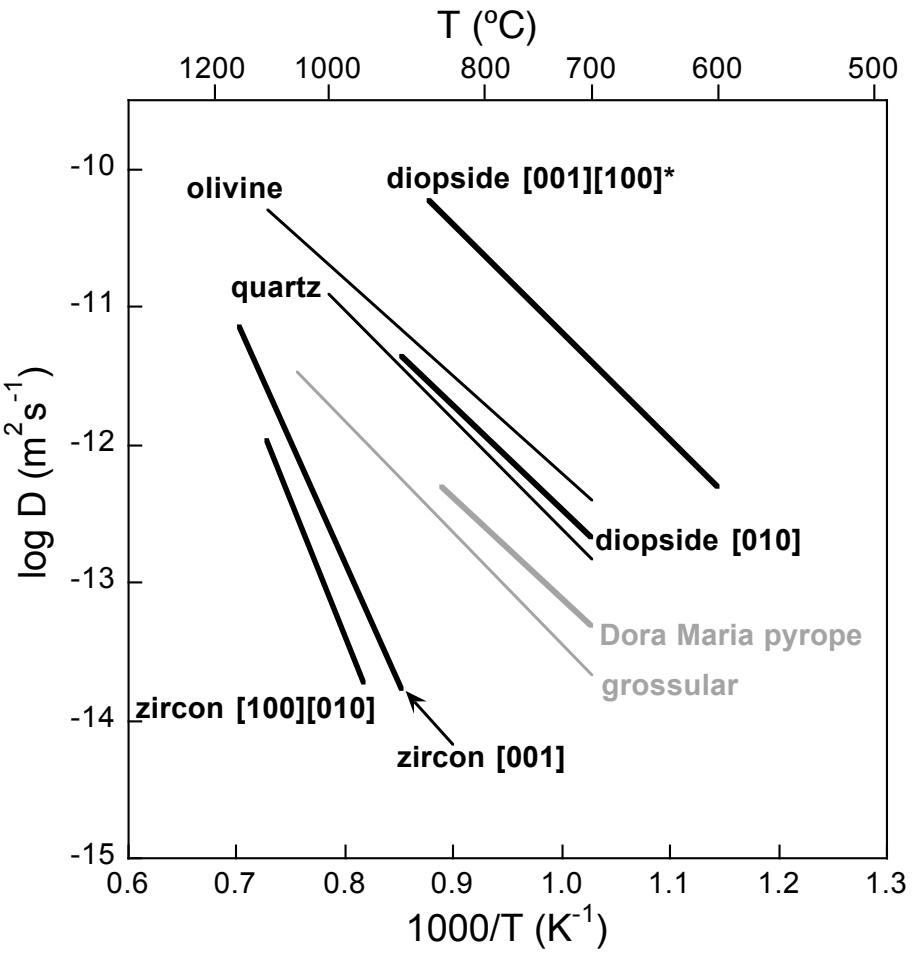

Figure 6.15. Arrhenius diagrams showing diffusion laws for H-D exchange in zircon and other NAMs. Diopside: Hercule and Ingrin (1999); olivine: Du Frane et al. (2012); quartz: Kats et al. (1962); Dora Maira pyrope: Blanchard and Ingrin (2004a); grossular: Kurka (2005); zircon: this study.

For diffusion data available, highly charged cations and oxygen diffusion in zircon have been found to exhibit much higher activation energies and slower diffusivities than in other NAMs (U: 726 kJ/mol, Th: 792 kJ/mol, Hf: 812 kJ/mol, Cherniak et al. 1997b; Ti: 754 kJ/mol, Cherniak and Watson 2007; Si: 738 kJ/mol, Cherniak et al. 2008; Yb: 691 kJ/mol, Dy: 734 kJ/mol, Cherniak et al. 1997a; O under dry conditions:

448 kJ/mol, Watson and Cherniak 1997; Fig. 6.16), while monovalent cation and neutral molecules have comparable activation energies than in other NAMs (Li: 275 kJ/mol, Cherniak and Watson 2010; He: 148 kJ/mol for diffusion along *c* axis and 146 kJ/mol for diffusion perpendicular to *c* axis, Cherniak et al. 2009; O through H_2O molecule under hydrothermal conditions: 210, Watson and Cherniak 1997; Fig. 6.16). However, H diffusion exhibits much higher activation energy and slower diffusivity than in other NAMs. It is highly probable that either the diffusion mechanism or the diffusion species in zircon is different from in other NAMs.

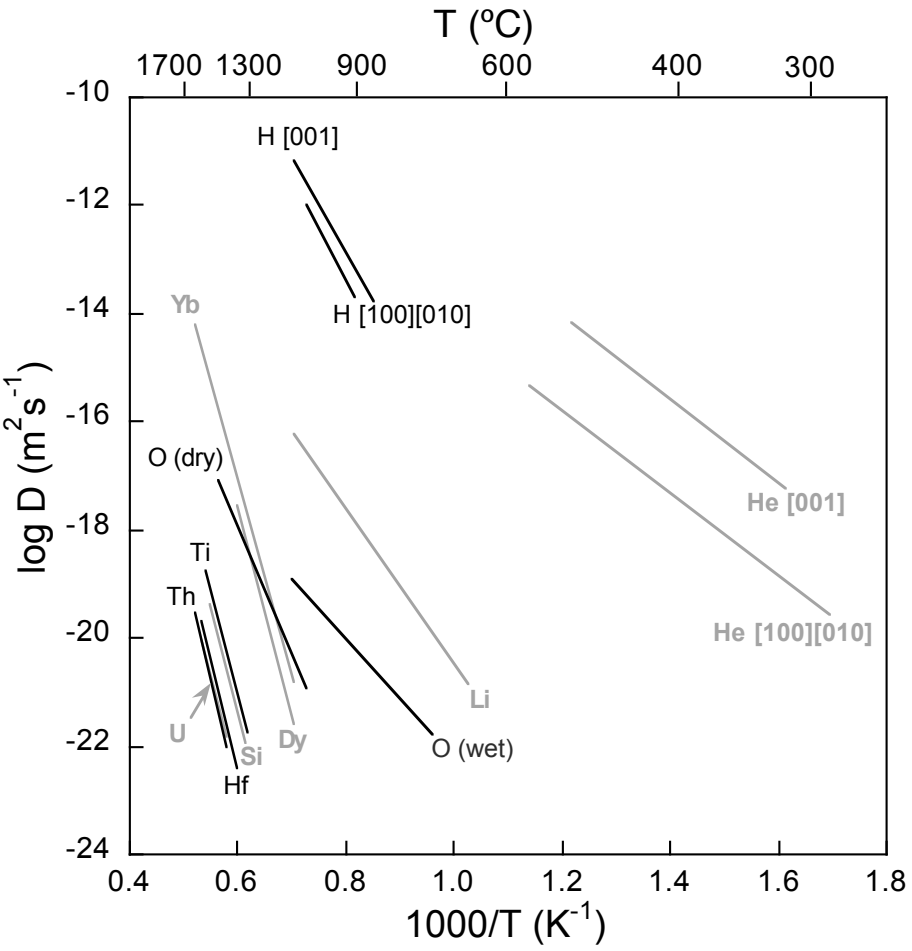

Figure 6.16. Compilation of results of diffusion studies in zircon. U, Th, Hf: Cherniak et al. 1997b; Ti: Cherniak and Watson 2007; Si: Cherniak et al. 2008 (from Rutherford backscattering spectrometry measurements); Yb, Dy: Cherniak et al. 1997a; O: Watson and Cherniak 1997; Li: Cherniak and Watson 2010; He: Cherniak et al. 2009; H: present study.

Diffusion of cations and oxygen (dry conditions) in zircon are generally assumed to be through an intrinsic vacancy mechanism. If we consider Hf as a proxy for Zr, similar diffusivities are expected for these two elements given their similar charges and sizes. Considering the significantly low diffusion rate of Hf (Zr), Si and O diffusion in zircon and their isotropic diffusion properties, an intrinsic vacancy mechanism or mechanism associated with oxygen atom (under dry conditions) for H diffusion in zircon can be reasonably ruled out. H and He diffusion in zircon present the same anisotropic properties. The diffusion of He in zircon show strong anisotropy with diffusivity along *c* axis (146 kJ/mol) nearly two orders of magnitude faster than that perpendicular to *c* axis (148 kJ/mol) (Cherniak et al. 2009). The same anisotropy and similar diffusivities for He diffusion in zircon was also found by Reiners et al. (2004) with activation energies ranging from 163 to 174 kJ/mol. Reich et al. (2007) simulated the diffusion of He in perfectly crystallized zircon using molecular dynamics simulations and empirical force field and quantum mechanical calculations. A strong anisotropy with diffusion was confirmed and an interstitial mechanism was proposed. They suggested that the anisotropy is a result of diffusion through *c*-parallel open channels (the four-coordinated interstice parallel to *c* axis) in the structure, which lead to less of impediment to move than in other crystallographic directions. Moreover, Farley (2007) investigated systematically He diffusion in zircon structure phosphates (with HREE and Y) and found the same strong anisotropy for He diffusion. They demonstrated that the shorter the distance between diagonally opposed atoms of the interstice (the narrower the interstice) from $TbPO_4$ to $LuPO_4$, the slower the diffusivity for interstitial He moves through the channel. Therefore, an interstitial mechanism for H diffusion in zircon is probable considering the similar strong anisotropy behavior.

Zhang et al. (1991b) compared the diffusivities of molecular H_2O in rhyolitic glasses with that of noble gases and proposed a correlation between the activation energy and the radii of the neutral molecular species: $E = 94(r - 0.31)^2$. The greater the radius of the diffusion neutral species, the higher the activation for diffusion is. The ionic radius of H (H^+) is 8.768×10^{-6} Å, the covalent radius of H is between 0.29

and 0.37 Å, the radius of H_2 molecule is about 0.6-0.7 Å. The atomic radius of He is 0.31 Å (Wolfram Research, Inc.). Therefore, if an interstitial H_2 molecule mechanism is proposed for H diffusion in zircon, it is understandable that He diffusion in zircon has a lower activation energy and fast diffusivity than H diffusion. In this case, diffusion of H_2 and He molecule in zircon are facilitated by the relatively large size of the open voids (2.4×2.4 Å^2 cross-section) along *c* axis.

Oxygen diffusion in zircon under hydrothermal conditions shows much lower activation energy and fast diffusivity than under dry conditions. This kind of behavior is common in NAMs, such as diopside (Ryerson and McKeegan 1994; Farver 1989), quartz (Dennis 1984; Giletti and Yund 1984) and anorthite (Ryerson and McKeegan 1994; Giletti et al. 1978). It is generally argued that molecule H_2O is the dominant species transporting oxygen under hydrothermal conditions, and that the neutral H_2O molecule migrates faster than highly charged oxygen anions (e.g., Farver and Yund 1990, 1991; Zhang et al. 1991a). Likely, it was also suggested that oxygen diffuses in zircon through interstitial molecular H_2O under hydrothermal conditions (Cherniak and Watson 2003). The radius of H_2O molecule is about 1.38 Å. It is estimated from distance of oxygen atoms in hexagonal ice structure (Pauling 1960), and it is not much different from the ionic radius of oxygen anions (1.40 Å). As the radius of H_2O is greater than that of H_2 molecule, the diffusivity of oxygen in zircon under hydrothermal conditions is slower than H diffusion. However, the dissociation energy of H-H is greater than that of H-O (436 kJ/mol versus 428 kJ/mol; Darwent 1970). Thus, maybe it can partly account for the reason why H diffusion exhibits a higher activation energy than oxygen diffusion under hydrothermal conditions. Moreover, since the radius of H_2O molecule is quite large compared with the voids along the *c* axis in zircon, the predominance of diffusion along the *c* axis become weak, leading to an isotrope behavior of oxygen diffusion.

6.8.3 Geological application

Using the present H diffusion data, we can determine the conditions under which H signatures in zircon would be retained or lost through diffusion. For spherical

geometry and the simple case of isothermal heating, the criterion that determines the retention of H at the center of the crystal is the dimensionless parameter Dt/a^2 (Crank 1975). It is assumed that the concentration at the center of the sphere can be preserved if Dt/a^2 is less than or equal to 0.03. However, due to the anisotropy of H diffusion in zircon, simple calculations assuming spherical geometry and isotropic diffusion cannot adequately describe behavior of H diffusion. We considered that the diffusion is in a cylinder of finite length with different diffusivities in the axial and radial directions. Following analytical expressions presented by Watson et al. (2010) for diffusion in cylindrical geometry with isothermal heating, we can define a "spherical equivalent" D_s/R^2, with D_s the effective diffusivity for spherical geometry and R the effective radius of the sphere:

$$\frac{D_s}{R^2} = \frac{4}{9}\left(\frac{D_{11}}{a^2} + \frac{D_{33}}{h^2} + 2\sqrt{\frac{D_{11}D_{33}}{a^2h^2}}\right) \tag{6.3}$$

where a and h are the radius and height of the cylinder, respectively, and D_{11} and D_{33} are the radial and axial diffusivities at a given temperature. Values of D_s/R^2 can then be determined from the expression for given aspect ratio (ratio of length to diameter of zircon), temperature and diffusion parameters. We consider here only a 1:1 aspect ratio and radius equal to that of the sphere, that is $R = a = 1/2h$, then the expression becomes:

$$D_s = \frac{4}{9}\left(D_{11} + \frac{D_{33}}{4} + \sqrt{D_{11}D_{33}}\right) \tag{6.4}$$

Using values of axial diffusivity and radial diffusivity at a given temperature, the effective diffusivity for a sphere of radius $R = a$ can be deduced. This effective diffusivity, falling between diffusivities for different orientations, would be the estimated value in a mineral with anisotropic diffusion, if spherical geometry and isotropic diffusion are assumed. Adoption of the effective diffusivities deduced, curves of $Dt/a^2 = 0.03$ for the temperature range 200-600 °C and mineral grains from 100 μm to 1 cm is plotted in Figure. 6.17. These curves give the time-grain radius limits under which initial hydrogen isotope information will be preserved in the center

of the grain. For times and grain radius below the curves, concentrations at the center will remain unaffected, but will be changed when above the curves.

At 650 °C, H information at the center of 100 μm radius zircons will be altered by diffusion in less than ten years. H would remain over a million years in zircons at this temperature if radius is higher than 3.2 cm. At lower temperatures, such as 400-500 °C, H signatures will be retained for considerably longer times: at 500 °C, 100 and 300 μm radii zircons will retain H signatures at their center for more than 0.1 Ma and 1 Ma, while at 400 °C these values would be 0.4 Ga and 3.5 Ga for the same radii. Hence, zircons will be moderately retentive of H signatures at mid-crustal metamorphic temperatures but unlikely to retain this information for geologically significant times under high-grade metamorphism.

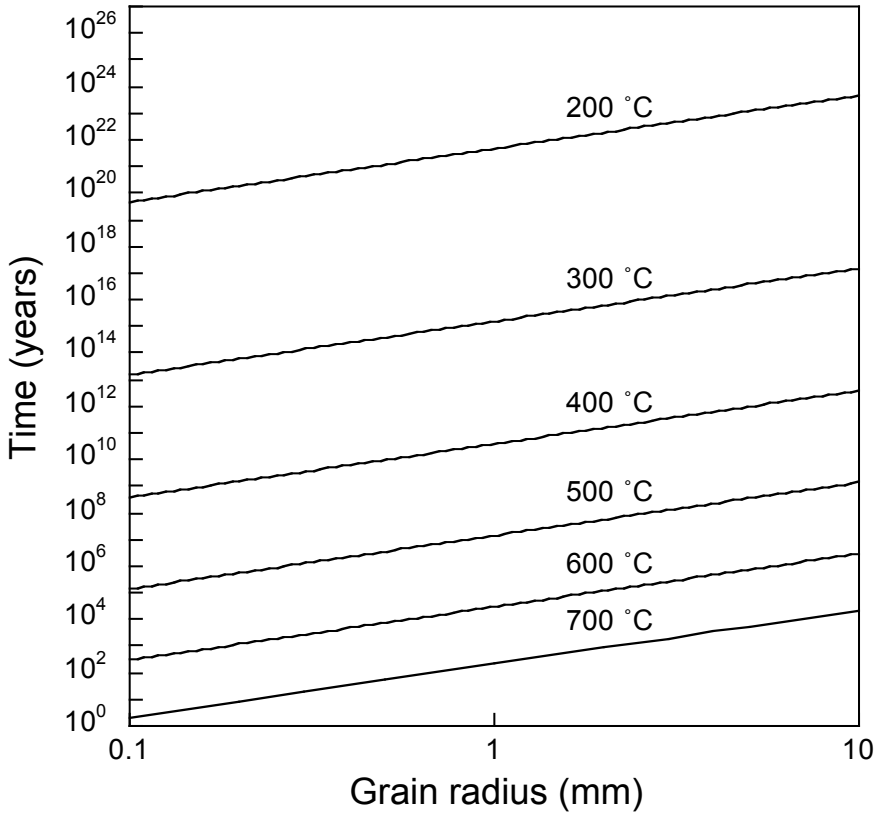

Figure 6.17. Curves representing time-grain radius conditions under which hydrogen isotope signature at the center of grain will be preserved. For times and temperatures below the curves, concentrations at the center will remain unaffected, but will be changed above the curves.

Under conditions where zircons are somewhat retentive of H, we can also calculate the percentage of loss of initial H contents from 100 μm radii grains undergoing isothermal heating through the redox process (Fig. 6.18). This simple example, which models zircons as spheres, assumes an initial uniform H content in the zircon and zero concentration of H in the surrounding medium. Zircons will retain 90% of their initial H composition over 3000 years at 500 °C and 8 Ma at 400 °C; 75% will be retained over 20, 000 years and 50 Ma at these respective temperatures. Of course, this calculation assumes that the redox conditions are favorable (oxidizing conditions) and that enough multivalent cations (Fe^{2+}, U^{4+}) are available.

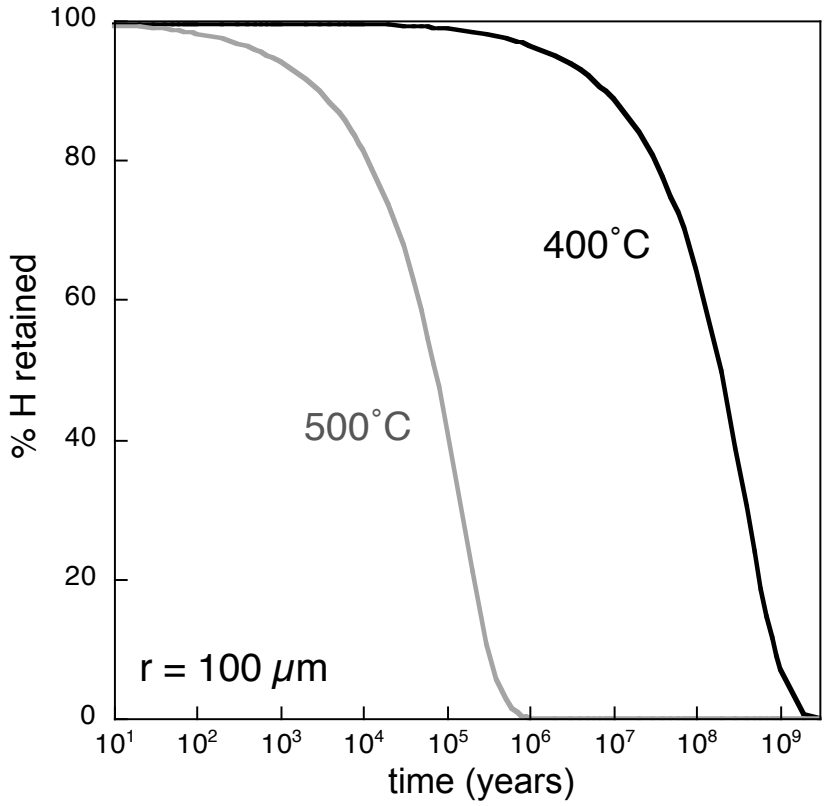

Figure 6.18. Percentage of H retained in zircons in cylindrical symmetry with effective radius of sphere of 100 μm under isothermal heating at 400 and 500 °C.

The present results suggest that the kinetics of H-D exchange in zircon is much slower than for other NAMs. The difference will even increase with decreasing

temperature because of the comparatively high activation energy for H diffusion in zircon.

Chapter 7

Conclusion and perspectives

7.1 Conclusion

Kinetics of hydrogen diffusion in andradite and zircon were studied by performing H-D exchange experiments through sequential annealing. The andradite samples are single crystals from an iron-skarn deposit on Serifos island, Greece, while the zircon samples are single crystals from Madagascar. The change of the content of OH (or OD) of the samples is analyzed by FTIR spectroscopy. The main conclusions of this study are summarized in the following.

7.1.1 Andradite garnet

1) The andradite samples show complex IR absorption features with most prominent bands at 3612, 3582, 3562 cm^{-1} and a minor band at 3634 cm^{-1}. The OH absorption features are representative of andradite from skarn and resemble that of Ti-bearing andradite in Armbruster et al. (1998). An average value for water content of 0.18 ± 0.12 wt% H_2O was deduced combining different calibration methods.

2) A local adjustment of defects associated with the little bands located at 3634 and 3628 cm^{-1} (as well as corresponding bands at 2680 and 2677 cm^{-1} in the OD area) occurs during annealing. On the OH side, the band at 3634 cm^{-1} decreases continuously during the exchange until it almost disappears while the band at 3628 cm^{-1} shows a more limited decrease. On the OD side, the lower-frequency band at 2677 cm^{-1} is the first to appear and it grows until its overtaken by the higher-frequency band at 2680 cm^{-1}. The total concentration of the defects at the origin of the two bands remains constant overall the experiment; only their relative proportions adjust during the exchange. This suggests that the two defects are

probably two configurations (giving rise to lower-frequency and higher-frequency bands) of a same defect with very similar energy. The little local adjustment during annealing does not affect the overall diffusion process and the deduced diffusion coefficients.

3) All bands follow the same kinetics regarding exchange of H by D (H-D exchange) or D by H (D-H exchange), with diffusion law (Fig. 7.1):

$$D = D_0 \exp\left[-\frac{(96 \pm 11) kJ/mol}{RT}\right] \text{with } \log D_0 \text{ (in } m^2/s) = -5.9 \pm 0.7.$$

It is also true for the bands at 3634 and 3628 cm^{-1} if the global evolution of the couple of bands is considered.

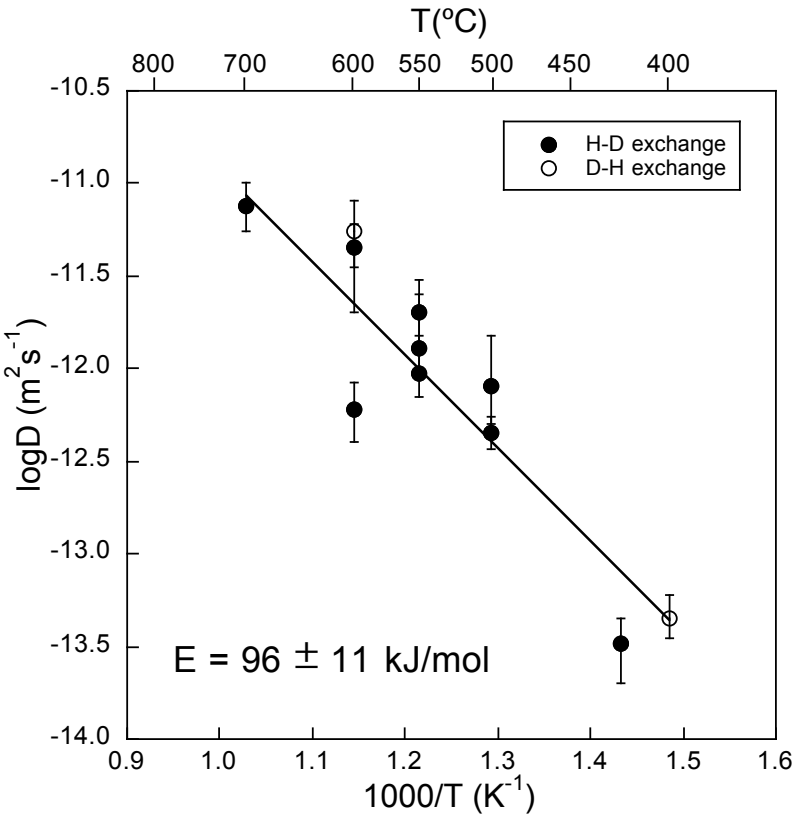

Figure 7.1. Arrhenius plot showing diffusion data for H-D and D-H exchange and the associated fit law in andradite.

With 96 ± 11 kJ/mol, the activation energy of andradite falls in the lowest range of activation energy of hydrogen diffusion in NAMs (100-190 kJ/mol), close to the value

measured for grossular $Gr_{83}An_{14}$ (Fig. 7.2a). It is also the fastest diffusion rate in NAMs with two orders of magnitude faster than in other garnets, at 700 °C (Fig. 7.2a). Considering that the activation energy of hydrogen diffusion in andradite is comparable to the one of other NAMs, where H was proposed to move as a single proton hopping from one oxygen site to another, a similar mechanism for hydrogen diffusion in andradite is highly probable.

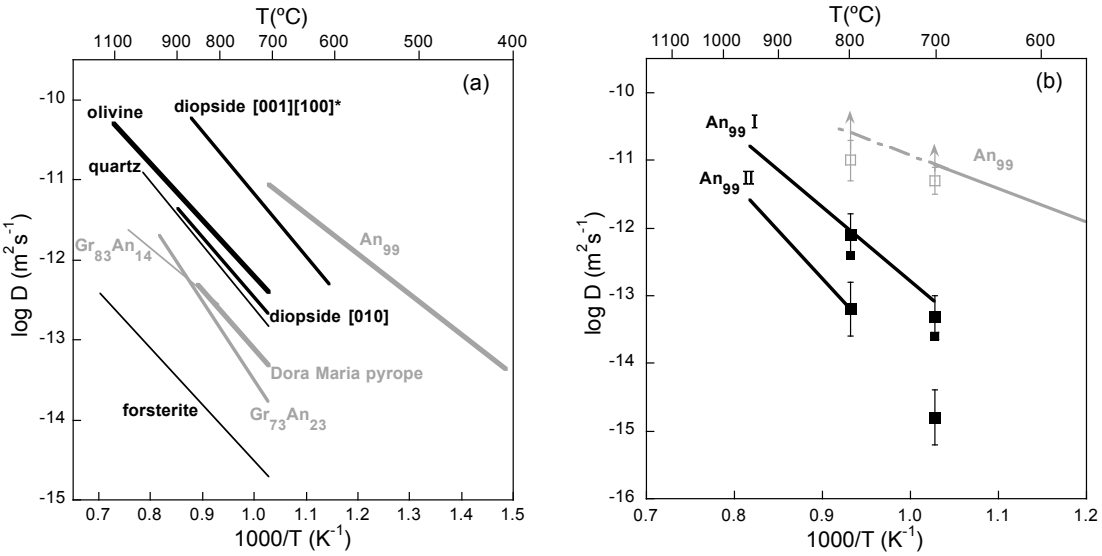

Figure 7.2. a) Compilation of diffusion laws for H-D exchange in NAMs. $Gr_{83}An_{14}$: Kurka et al. (2005); $Gr_{73}An_{23}$: Kurka (2005); Dora Maira pyrope: Blanchard and Ingrin (2004a); diopside: Hercule and Ingrin (1999); olivine // a: Du Frane et al. (2012); forsterite // c: Ingrin and Blanchard (2006); quartz // c: Kats et al. (1962); An_{99}: this study. b) Comparison of kinetics of H-D exchange with H-extraction/incorporation in An_{99}. The gray line represent H diffusion law deduced from H-D exchange experiments in this study and the two balck lines represent H diffusion laws deduced from H-extraction experiments (An_{99} I (lower-frequency bands), II (higher-frequency bands); Kurka 2005). Solid and empty squares correspond to the H-extraction and H-incorporation data of An_{99} from Phichaikamjornwut et al. (2012). The smaller square are the original data when taking overall OH bands as a whole while the larger squares are the distinct data when

separating OH bands into higher-frequency and lower-frequency bands. Arrows indicate that these values are probably underestimated.

The diffusivity deduced from H-D exchange in An_{99} is one to three orders of magnitude higher than the diffusivities for H-extraction (Fig. 7.2b), leading to the conclusion that in An_{99} the chemical diffusion involved in H-extraction experiments in air is not limited by H diffusion but by a slower mechanism than H diffusion.

4) One data of H-extraction diffusivity under reducing condition at 800°C was deduced in this study. When compared with H-extraction data under oxidizing conditions, the dependence of the diffusivity of H-extraction in andradite as a function of pO_2 is suggested to be: $D_{H-extr} \propto pO_2^{0.05\pm0.01}$. A dependence on pO_2 with an exponent of 0.22 (± 0.04) was found by Kurka (2005) for grossular. Thus, H-extraction for andradite shows less dependence on pO_2 compared to that for grossular.

5) Due to the very fast diffusion rate deduced from our study, the isotope memory of andradite is limited only to low-grade metamorphic events, below 400 °C. For higher temperatures, the ability of garnet to retain isotopic information will strongly depend on its andradite content: change of composition from $Gr_{86}An_{14}$ to An_{99}, has the same effect on H mobility as a temperature increase of 500 °C. The same effect is expected on the closure temperature of garnet for hydrogen isotopes.

7.1.2 Zircon

1) The IR absorption features of the two zircon samples studied (ZrB and ZrD) are nearly identical, with main bands located at 3406 and 3265 cm^{-1}. The average water content of both zircons is around 86 ppm H_2O according to the calibration proposed by Libowitzky and Rossman (1997).

2) The crystallinity of the two samples were before annealing at intermediate level (but close to well crystallized) and reach the well crystallized level upon annealing. The higher the temperature of annealing, the higher the level of crystallinity reached at the end of experiments. Overall, the change in crystallinity remains relatively minor

and we assume that it did not affect notably the diffusion rates measured.

3) At the beginning of annealing, a rearrangement of OH bands occurs with a decrease of the band at 3406 cm^{-1} (E // $c > E \perp c$) accompanied by an increase of the band at 3265 cm^{-1} ($E \perp c > E$ // c). This leads to an increase of 8% of the integral absorbance of OH abnds for slices perpendicular to c (that is 108% of the initial A_{OH}) and a decrease of 10.6% in unpolarized spectra of slices parallel to c (that is 89.4% of the initial A_{OH}). Besides, the band at 3503 cm^{-1} reveals itself distinctly upon heating with polarization nearly parallel to c axis. This indicates that the hydrogen in zircon is highly mobile.

4) The frequency shift (ν_{OH}/ν_{OD}) due to the isotopic replacement for zircon and other NAMs shows deviation from the correlation proposed by Mikenda (1986), and a new relation was proposed: $\nu_{OH}/\nu_{OD} = -0.68349 + 0.0010952 \times \nu_{OH}$ (cm^{-1}) $- 1.4699e\text{-}7 \times (\nu_{OH})^2$ (cm^{-2}), with R = 0.99007.

5) Due to reduction of U^{5+} to U^{4+}, additional deuterium incorporates into the crystal structure during H-D exchange, leading to hydrous species content about twice the initial value after almost complete H-D replacement. The deduced rate of uranium redox reaction is similar to that of deuterium incorporation (the process of deuterium incorporation was followed up by separating the absorbance of OD related to D incorporation from that related to H-D exchange: $A_{OD(inc)}$ was acquired from A_{OD} - $A_{OD(H\text{-}D)}$ with $A_{OD(H\text{-}D)}$ calculated from $(A_{OH0} - A_{OH})/\beta$), confirming the uranium redox reaction: $U^{5+} + 1/2H_2 + O^{2-} = U^{4+} + OH^-$.

6) H-D exchange processes exhibit diffusivities nearly identical to that of deuterium incorporation processes. Thus, common diffusion laws were deduced for both processes (Fig. 7.3a):

$$D_{[100][010]} = D_0 \exp\left[\frac{-(374 \pm 39) kJ/mol}{RT}\right] \text{with log } D_0 \ (m^2s^{-1}) = 2.24 \pm 1.57.$$

$$D_{[001]} = D_0 \exp\left[\frac{-(334 \pm 49) kJ/mol}{RT}\right] \text{with log } D_0 \ (m^2s^{-1}) = 1.11 \pm 0.22.$$

H diffusion along *a* and *b* axes follow the same diffusion law, while H diffusion along the *c* axis follow a faster diffusion law. The H-D exchange process is suggested to follow an interstitial mechanism through H_2 molecule. The anisotropy is probably the result of *c*-parallel through-going channels or "pipes" in the structure which lead to easier move along *c* axis than along any other crystallographic directions. The D incorporation mechanism is a coupled diffusion of protons and polarons localized on uranium ions, following the uranium redox reaction which is similar to iron redox reaction observed in other NAMs, such as olivine, diopside and garnet but with Fe^{3+} polarons.

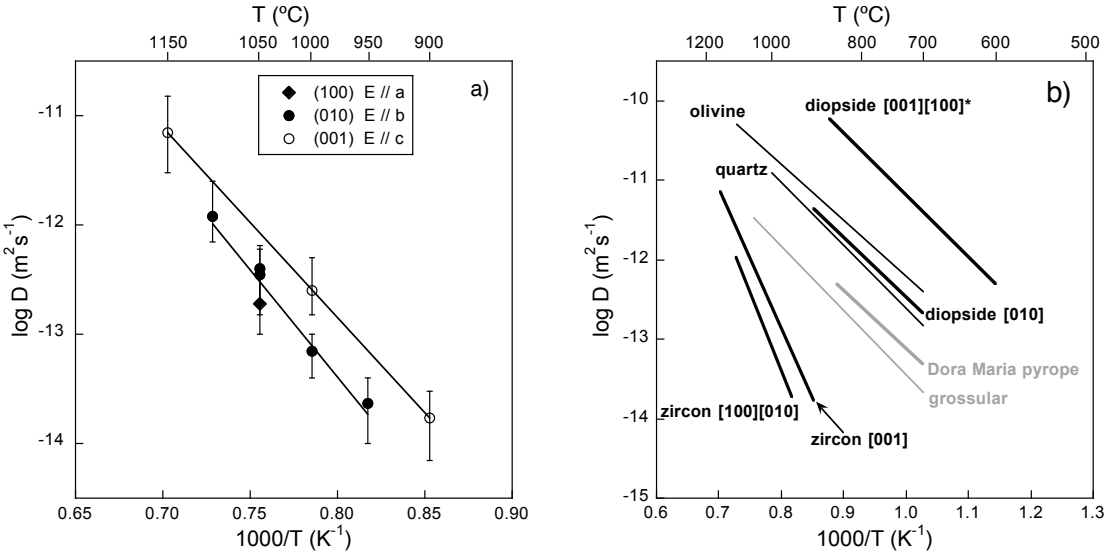

Figure 7.3. a) Arrhenius diagrams showing two diffusion laws for H diffusion in zircon along different crystallographic orientations. Solid diamond represents diffusion along *a* axis, solid circles along *b* axis, empty circles along *c* axis. b) Arrhenius diagrams showing diffusion laws for H-D exchange in zircon and other NAMs. Diopside: Hercule and Ingrin (1999); olivine: Du Frane et al. (2012); quartz: Kats et al. (1962); Dora Maira pyrope: Blanchard and Ingrin (2004a); grossular: Kurka (2005); zircon: this study.

The activation energy for H diffusion in zircon exhibits higher values than those observed in other NAMs ranging from 100 to 190 kJ/mol. In the temperature range

investigated in the present study, zircon exhibits diffusivities one to four orders of magnitude slower when compared with other NAMs (Fig. 7.3b).

7) Although H diffusion in zircon remains rapid compared to diffusion of other cations, zircons will be moderately retentive of H signatures at mid-crustal metamorphic temperatures, but they are unlikely to retain this information for geologically significant times under high-grade metamorphism unless the grain size is large enough (at 650 °C, H would be retained over a million years only in zircons with radius of 3.2 cm or larger).

8) The 3420 and 3385 cm^{-1} bands are attributed to the hydrogarnet substitution with 4OH replacing SiO_4 tetrahedra. The 3641 and 3621 cm^{-1} bands are suggested to be OH groups involving a Si vacancy. The 3200 cm^{-1} band is interpreted to be related to a Zr vacancy, while the 3180 and 3100 cm^{-1} bands are proposed to be related to a Zr-unoccupied defect, probably the substitution of REE for Zr charge compensating by H.

7.2 Perspectives

1) In-situ FTIR analysis at varying temperatures has been used to investigate the H incorporation mechanisms in NAMs based on the shift and broadening of the absorption bands, which is governed by the anharmonic properties of the corresponding vibrational modes (e.g., Lu and Keppler 1997; Yang et al. 2010; Ingrin et al. 2013).

We have attempted to perform in-situ IR experiments on andradite and zircon, and different behaviors of the absorption bands upon heating have been found. Thus, systematic in-situ IR experiments in andradite and zircon samples would be a good way to investigate the different H incorporation mechanisms.

2) Hydrogen diffusivity in the grossular-andradite series increase drastically with the andradite component in garnet: by two orders of magnitude from An_{14} to An_{99}. Thus, H-D exchange experiments for intermediate composition is necessary to understand the influence of andradite content on H diffusion: For instance, we do not

know at the moment if the diffusion increases smoothly with the andradite content or if a sharp increase occurs at a critical composition.

3) Considering that garnet with varying composition and IR absorption bands shows different H diffusion laws, diffusion laws of zircon could also be affected by varying composition and IR absorption. One H-D exchange experiment has been performed on another zircon with different IR absorption features from the ones used in this study, and a higher H diffusion kinetics was observed. Thus, further diffusion studies are needed to verify the hypothesis especially in zircon with no unranium.

4) Last but not the least, extensive studies on metamict zircons have been undergone with respect to the formation process, OH groups, structure and morphonology (e.g., Woodhead et al. 1991a; Zhang et al. 2000; Geisler et al. 2003; Nasdala et al. 2009). It would be very important to know how H diffusion is affected by metamictization of zircon. Is diffusion faster or slower? Diffusion experiments at low temperature would be the only way to reply to these questions and understand how metamict zircon are affected by water.

References

Aines, R.D. and Rossman, G.R. (1984) The hydrous component in garnets: pyralspites. American Mineralogist, 69, 1116–1126.

Aines, R.D. and Rossman, G.R. (1985) The high temperature behavior of trace hydrous components in silicate minerals. American Mineralogist, 70, 1169-1179.

Amthauer, G. and Rossman, G.R. (1998) The hydrous component in andradite garnet. American Mineralogist, 83, 835-840.

Andrut, M. and Wildner, M. (2002) The crystal chemistry of birefringent natural uvarovites: Part IV. OH defect incorporation mechanisms in non-cubic garnets derived from polarized IR spectroscopy. European Journal of Mineralogy, 14, 1019-1026.

Armbruster, T. (1995) Structure refinement of hydrous andradite, $Ca_3Fe_{1.54}Mn_{0.20}Al_{0.26}(SiO_4)_{1.65}(O_4H_4)_{1.35}$, from the Wessels mine, Kalahari manganese field, South Africa. European Journal of Mineralogy, 7, 1221-1225.

Armbruster, T. and Geiger, C.A. (1993) Andradite crystal chemistry, dynamic X-site disorder and structural strain in silicate garnets. European Journal of Mineralogy, 5, 59–71.

Armbruster, T., Birrer, J., Libowitzky, E. and Beran, A. (1998) Crystal chemistry of Ti-bearing andradites. European Journal of Mineralogy, 10, 907-921.

Arredondo, E.H., Rossman, G.R. and Lumpkin G.R. (2001) Hydrogen in spessartine-almandine garnets as a tracer of granitic pegmatite evolution. American Mineralogist, 86, 485-490.

Balan, E., Blanchard, M. and Lazzeri, M. (2014) Contribution of interstitial OH groups to the incorporation of water in forsterite. Physics and Chemistry of Minerals, 41(2), 105-114.

Balan, E., Ingrin, J., Delattre, S., Kovács, I. and Blanchard, M. (2011) Theoretical infrared spectrum of OH-defects in forsterite. European Journal of Mineralogy, 23, 285-292.

Balan, E., Yi, H.H., and Blanchard, M. (2013) First-principle study of OH defects in zircon. Physics and Chemistry of Minerals, 40, 547-554.

Bayer, G. (1972) Thermal expansion of ABO_4 compounds with zircon and scheelite structures. J Less Common Metals, 26,255-262.

Behrens, H., Johannes, W. and Schmalzried, H. (1990) On the mechanisms of cation diffusion processes in ternary feldspars. Physics and Chemistry of Minerals, 17, 62–78.

Bell, D.R. (1993) Hydroxyl in mantle minerals. 389 p. California Institute of Technology, Pasadena, CA, United States, Ph.D. thesis.

Bell, D.R. and Rossman, G.R. (1992a) Water in Earth's mantle: The role of nominally anhydrous minerals. Science, 255, 1391-1397.

Bell, D.R. and Rossman, G.R. (1992b) The distribution of hydroxyl in garnets from the subcontinental mantle of southern Africa. Contributions to Mineralogy and Petrology, 111, 161-178.

Bell, D.R., Rossman, G.R. and Moore, R.O. (2004) Abundance and partitioning of OH in a high-pressure magmatic system: Megacrysts from the Monastery kimberlite South Africa. Journal of Petrology, 45, 1539–1564.

Bellamy, L.J. and Owen, A.J. (1969) A simple relationship between the infrared stretching frequencies and the hydrogen bond distances in crystals. Spectrochimica Acta, A25, 329-333.

Belousova, E.A., Griffin, W.L., O'Reilly, S.Y. and Fisher, N.I. (2002) Igneous zircon: Trace element composition as an indicator of source rock type. Contributions to Mineralogy and Petrology, 143, 602–622.

Beran, A. (1999) Contribution of IR spectroscopy to the problem of water in the Earth's mantle. In: Microscopic Properties and Processes in Minerals. Wright K, Catlow R (eds) NATO Science Series. Kluwer Acad. Publishers, p 523-538.

Beran, A. and Libowitzky, E. (2006) Water in Natural Mantle Minerals II: Olivine, Garnet and Accessory Minerals. In: Keppler, H., and Smyth, J.R. (eds) Water in nominally anhydrous minerals, vol 62. Reviews in Mineralogy and Geochemistry, Mineralogical Society of America and Geochemical Society, Washington, pp 169–192.

Blanchard, M. and Ingrin, J. (2004a) Kinetics of deuteration in pyrope. European Journal of Mineralogy, 16, 567-576.

Blanchard, M. and Ingrin, J. (2004b) Hydrogen diffusion in Dora Maira pyrope. Physics and Chemistry of Minerals, 31, 593-605.

Botis, S.M., Pan, Y. and Ewing, R.C. (2013) Hydrogen incorporation in crystalline zircon: insight from ab initio calculations. American Mineralogist, 98, 745–751.

Bowring S. A. (1995) The Earth's early evolution. Science, 269, 1535-1540.

Bowring S. A. and Schmitz M. D. (2003) High-precision U-Pb zircon geochronology and the stratigraphic record (in Zircon) Reviews in Mineralogy and Geochemistry, 53, 305-326.

Bowring, S. A., Erwin, D.H., Jin, Y.G., Martin, M.W., Davidek, K. and Wang, W. (1998) U/Pb zircon geochronology and tempo of the end-Permian mass extinction. Science, 280, 1039-1045.

Bowring, S.A. (1995) The Earth's early evolution. Science, 269, 1535-1540.

Bowring, S.A. and Schmitz, M.D. (2003) High-precision U-Pb zircon geochronology and the stratigraphic record. In Hanchar, J. M. and Hoskin, P. W. O. (eds.), Zircon, 53, 305-326, Reviews in Mineralogy and Geochemistry, Mineralogical Society of America, Washington, D.C.

Brady, J.B. (1993) Diffusion data for silicate minerals, glasses, and liquids. In: Handbook of Physical Constants. Vol 2. Arhens T.J. (ed) American Geophysical Union, p 269-290.

Brady, J.B. and Cherniak, D.J. (2010) An overview of published experimental diffusion data. In Zhang, Youxue and Cherniak, Daniele, Diffusion in minerals and melts, 72, 899-920, Reviews in Mineralogy and Geochemistry, Mineralogical Society of America, Chantilly, Virginia.

Brese, N.E. and O'Keefe, M.O. (1991) Bond-valence parameters for solids. Acta Crystallographica Section B: Structural Science, 47, 192-197.

Burakov, B.E., Hanchar, J.M., Zamoryanskaya, M.V., Garbuzov, V.M. and Zirlin, V.A. (2002) Synthesis and investigation of Pu-doped single crystal zircon, $(Zr,Pu)SiO_4$. Radiochima Acta, 89, 1-3.

Carlson, W.D. (2006) Rates of Fe, Mg, Mn and Ca diffusion in garnet. American Mineralogist, 91, 1-11.

Carslaw, H.S. and Jaeger, J.C. (1959) Conduction of heat in solids. Clarendon, Oxford, UK, pp 510.

Caruba, R., Baumer, A., Ganteaume, M. and Iacconi, P. (1985) An experimental study of hydroxyl groups and water in synthetic and natural zircons: a model of the metamict state. American Mineralogist, 70, 1224–1231.

Chen, R.X., Zheng, Y.F. and Gong, B. (2011) Mineral hydrogen isotopes and water contents in ultrahigh-pressure metabasiteand metagranite: Constraints on fluid flow during continentalsubduction-zone metamorphism. Chemical Geology, 281, 103-124.

Cherniak, D.J. (1995) Diffusion of lead in plagioclase and K-feldspar: an investigation using Rutherford Backscattering and resonant nuclear reaction analysis. Contributions to Mineralogy and Petrology, 120, 358-371.

Cherniak, D.J. (2000) Rare earth element diffusion in apatite. Geochimica et Cosmochimica Acta, 64, 3871-3885.

Cherniak, D.J. (2002) REE diffusion in feldspar. Chemical Geology, 193, 25-41.

Cherniak, D.J. (2008) Si diffusion in zircon. Physics and Chemistry of Minerals, 35, 179-187.

Cherniak, D.J., Hanchar, J.M. and Watson, E.B. (1997a) Rare-Earth diffusion in zircon. Chemical Geology, 134, 289-301.

Cherniak, D.J., Hanchar, J.M. and Watson, E.B. (1997b) Diffusion of tetravalent cations in zircon. Contributions to Mineralogy and Petrology, 127, 383-390.

Cherniak, D.J. and Watson, E.B. (2001) Pb diffusion in zircon. Chemical Geology, 172, 5–24.

Cherniak, D.J. and Watson, E.B (2007) Ti diffusion in zircon. Chemical Geology, 242, 473–486.

Cherniak, D.J., Watson, E.B. and Thomas, J.B. (2009) Diffusion of helium in zircon and apatite. Chemical Geology, 268, 155–166.

Cherniak, D.J. and Watson, E.B (2003) Diffusion in zircon. In: Hanchar JM, Hoskin PWO (eds) Zircon, reviews in mineralogy and geochemistry, vol 53. Mineralogical Society of America, Washington, DC, pp 113–143.

Cherniak, D.J. and Watson, E.B. (2010) Li diffusion in zircon. Contributions to Mineralogy and Petrology, 160, 383-390.

Cho, H. and Rossman, G.R. (1993) Single crystal NMR studies of low-concentration hydrous species in minerals: grossular garnet. American Mineralogist, 78, 1149-1164.

Cohen-Addad, C., Ducros, P. and Bertaut, E.F. (1967) Étude de la substitution du groupement SiO_4 par $(OH)_4$ dans les composés $Al_2Ca_3(OH)_{12}$ et $Al_2Ca_3(SiO_4)_{2.16}(OH)_{3.36}$ de type grenat. Acta Crystallographica, 23, 220-230 (in French).

Coleman, R.G. and Erd, R.C. (1961). Hydrozircon from the wind river formation, Wyoming. U.S. Geological Survey Research**,** 424-C, 297–300.

Costa, F. and Chakraborty, S. (2008) The effect of water on Si and O diffusion rates in olivine and implications for transport properties and processes in the upper mantle. Physics of the Earth and Planetary Interiors, 166, 11-29.

Crank, J. (1956) The mathematics of diffusion. Oxford Science Publications, Oxford University Press, Second Edition, 1976, pp 414.

Crank, J, (1975) The Mathematics of Diffusion, 2nd ed. Oxford University Press, Oxford. pp 414.

Cygan, R.T. and Lasaga, A.C. (1985) Self-diffusion of magnesium in garnet at 750°C to 900°C. American Journal of Science, 285, 328-350.

Darwent, B.deB. (1970) Bond dissociation energies in simple molecules. National bureau of standards, Branscomb, L.M., director, The Catholic University of America, Washington, D.C, P52.

Davis, D., Williams, I.S. and Krogh, T.E. (2003) Historical development of zircon geochronology. In Hanchar, J. M. and Hoskin, P. W. O. (eds.), Zircon, 53, 145-181, Reviews in Mineralogy and Geochemistry, Mineralogical Society of America, Washington, D.C.

Dawson, P., Hargreave, M.M., and Wilkinson, G.R. (1971) The vibrational spectrum of zircon ($ZrSiO_4$). Journal of Physics C: Solid State Physics, 4, 240-256.

De Hoog, J.C.M., Lissenberg, C.J., Brooker, R.A., Hinton, R., Trail, D., Hellebrand, E. and EIMF (2014) Hydrogen incorporation and charge balance in natural zircon. Geochimica et Cosmochimica Acta, 141, 472-486.

Deer, W.A., Howie, R.A. and Zussman, J. (1982) Andradite. In Rock-forming minerals, vol. IA.Orthosilicates (2nd edition), p. 617-641. Longman, London.

Demouchy, S. and Mackwell, S. (2006) Mechanisms of hydrogen incorporation and diffusion in iron-bearing olivine. Physics and Chemistry of Minerals, 33, 347-355.

Demouchy, S. and Mackwell, S.J. (2003) Water diffusion in synthetic iron-free forsterite. Physics and Chemistry of Minerals, 30, 486-494.

Dennis, P.F. (1984) Oxygen self-diffusion in quartz under hydrothermal conditions. Journal of Geophysical Research B: Solid Earth and Planets, 89, 4047-4057.

Derdau, D., Freer, R. and Wright, K. (1998) Oxygen diffusion in anhydrous sanidine feldspar. Contributions to Mineralogy and Petrology, 133, 199-204.

Doremus, R.H. (1998) Comment on “Stationary and mobile hydrogen defects in potassium feldspar” by AK Kronenberg, RA Yund and GR Rossman. Geochimica et Cosmochimica Acta, 62, 377-378.

Doremus, R.H. (2002) Diffusion of Reactive Molecules in Solids and Melts, Wiley.

Dowty, E. (1980) Crystal-chemical factors affecting the mobility of ion in minerals. American Mineralogist, 65, 174–182.

Du Frane, W.L. and Tyburczy, J.A. (2012) Deuterium-hydrogen exchange in olivine: Implications for point defects and electrical conductivity. Geochemistry, Geophysics, Geosystems, 13, 3, doi:10.1029/2011GC003895.

Ewing, R.C. and Lutze, W. (1997) Disposing of plutonium. Science, 275, 737.

Ewing, R.C., Meldrum, A., Wang, L.M., Weber, W.J. and Corrales, L.R. (2003) Radiation effects in zircon. In Hanchar, J. M. and Hoskin, P. W. O. (eds.), Zircon, 53, 387-426, Reviews in Mineralogy and Geochemistry, Mineralogical Society of America, Washington, D.C.

Farley, K.A. (2007) He diffusion systematics in minerals; evidence from synthetic monazite and zircon structure phosphates. Geochimica et Cosmochimica Acta, 71(16), 4015-4024.

Farver, J.R. (1989) Oxygen self-diffusion in diopside with application to cooling rate determinations. Earth and Planetary Science Letters, 92, 386-396.

Farver, J.R. (1994) Oxygen self-diffusion in calcite: Dependence on temperature and water fugacity. Earth and Planetary Science Letters, 121, 575-587.

Farver, J.R. (2010) Oxygen and hydrogen diffusion in minerals. In Diffusion in minerals and melts, 72(1), 447-507, Reviews in Mineralogy and Geochemistry, Mineralogical Society of America, Chantilly, Virginia.

Farver, J.R. and Yund, R.A. (1990) The effect of hydrogen, oxygen, and water fugacity on oxygen diffusion in alkali feldspar. Geochimica et Cosmochimica Acta, 54, 2953-2964.

Farver, J.R. and Yund, R.A. (1991) Oxygen diffusion in quartz: dependence on temperature and water fugacity. Chemical Geology, 90, 55-70.

Finch, R.J. and Hanchar, J.M. (2003) Structure and chemistry of zircon and zircon group minerals. In Hanchar, J. M. and Hoskin, P. W. O. (eds.), Zircon, 53, 1-25, Reviews in Mineralogy and Geochemistry, Mineralogical Society of America, Washington, D.C.

Foreman, D.W. (1968) Neutron and X-ray diffraction study of $Ca_3Al_2(O_4D_4)_3$, a garnetoid. Joumal of Chemical Physics, 48, 3037- 3041.

Forneris, J.F. and Skogby, H. (2004) Is hydrogen loss via ion oxidation an important mechanism in nominally anhydrous minerals? Goldschmidt Geochemistry 2004 Conference Abstracts.

Freer, R. and Ed wards, A. (1999) An experimental study of Ca-(Fe,Mg) interdiffusion in silicate garnets, Contributions to Mineralogy and Petrology, 134, 370-379.

Frondel, C. (1953) Hydroxyl substitution in thorite and zircon. American Mineralogist, 38, 1007–1018.

Frondel, C. and Collette, R.L. (1957) Hydrothermal synthesis of zircon, thorite and huttonite. American Mineralogist, 42, 759–765.

Gaetani, G.A., Grove, T.L. (1998)The influence of water on melting of mantle peridotite. Contributions to Mineralogy and Petrology, 131, 323–346.

Ganguly, J. (2010) Cation diffusion kinetics in aluminosilicate garnets and geological applications. In Y. Zhang and D.J. Cherniak, Eds.,Diffusion in minerals and melts, 72, p. 559-601, Reviews in Mineralogy and Geochemistry, Mineralogical Society of America, Chantilly, Virginia.

Geiger, C.A., Langer, K., Bell, D.R., Rossman, G.R. and Winkler, B. (1991) The hydroxide component in synthetic pyrope. American Mineralogist, 76, 49-59.

Geisler, T., Rashwan, A.A., Rahn, M.K.W., Poller, U., Zwingmann, H., Pidgeon, R.T., Schleicher, H. and Tomaschek, F. (2003). Low-temperature hydrothermal alteration of natural metamict zircons from the Eastern Desert, Egypt. Mineralogical Magazine, 67(3), 485-508.

Giletti, B.J. and Yund, R.A. (1984) Oxygen diffusion in quartz. Chemical effects of water on the strength and deformation of crustal rocks. Journal of Geophysical Research B: Solid Earth and Planets, 89, 4039-4046.

Giletti, B.J., Semet, M.P. and Yund, R.A. (1978) Studies in diffusion: III, Oxygen and feldspars, an ion microprobe determination. Geochimica et Cosmochimica Acta, 42, 45-57.

Gong, B., Zheng, Y.F. and Chen, R.X. (2007) TC/EA-MS online determination of hydrogen isotope composition and water concentration in eclogitic garnet. Physics and Chemistry of Minerals, 34, 687-698.

Green, D.H. (1973) Experimental melting studies on a model upper mantle composition at high pressure under H_2O saturated and H_2O undersaturated conditions. Earth and Planetary Science Letters, 19, 37–45.

Hanchar, J.M., Finch, R.J., Hoskin, P.W.O., Watson, E.B., Cherniak, D.J. and Mariano, A.N. (2001) Rare earth elements in synthetic zircon: Part 1. Synthesis, and rare earth element and phosphorus doping. American Mineralogist, 86, 667–680.

Harrison, T.M. Schmitt, A.K., McCulloch, M.T. and Lovera, O.M. (2008) Early (P4.5 Ga) formation of terrestrial crust: Lu–Hf, delta O^{-18}, and Ti thermometry results for Hadean zircons. Earth and Planetary Science Letters, 268, 476–486.

Hazen, R.M., Finger, L.W. (1979) Crystal structure and compressibility of zircon at high pressure. American Mineralogist, 64, 196-201.

Henmi, Ch., Kusachi, I. and Henmi, K. (1995) Morimotoite, $Ca_3TiFe^{2+}Si_3O_2$, a new titanian garnet from Fuka, Okayama Prefecture, Japan. Mineralogical Magazine, 59, 115-120.

Hercule, S. and Ingrin, J. (1999) Hydrogen in diopside: Diffusion, kinetics of extraction-incorporation and solubility. American Mineralogist, 84, 1577-1587.

Hier-Majumder, S., Anderson, I.M. and Kohlstedt, D.L. (2005) Influence of protons on Fe-Mg interdiffusion in olivine. Journal of Geophysical Research: Solid Earth, 110, issue B2.

Hinton, R., Macdonald, R., MacGarvie, D., Tindle, A. and Harley, S. (2003) The Possible Role of Hydrogen in the Substitution of Rare Earth Elements into Zircon (abstract). EGS-AGU-EUG Joint Assembly, European Geophysical Society, Nice, France, p. 05968.

Hirose, K. and Kawamoto, T. (1995) Hydrous partial melting of lherzolite at 1 GPa: the effect of H_2O on the genesis of basaltic magmas. Earth and Planetary Science Letters, 133, 463–473.

Hofmeister, A.M. (2004) Enhancement of radiative transfer in the upper mantle by OH in minerals. Physics of the Earth and Planetary Interiors, 146, 483–495.

Hoskin, P.W.O. and Schaltegger, U. (2003) The Composition of Zircon and Igneous and Metamorphic Petrogenesis. In Hanchar, J. M. and Hoskin, P. W. O. (eds.), Zircon, 53, 27-62, Reviews in Mineralogy and Geochemistry, Mineralogical Society of America, Washington, D.C.

Hurley P. M. (1952) Alpha ionization damage as a cause of low He ratios. Trans. American Geophysical Union, 33, 174–183.

Ingrin, J. and Blanchard, M. (2006) Diffusion of hydrogen in minerals. In H. Keppler and J.R. Smyth, Eds.,Water in Nominally Anhydrous Minerals, 62, p. 291-320, Reviews in Mineralogy and Geochemistry, Mineralogical Society of America, Chantilly, Virginia.

Ingrin, J. and Skogby, H. (2000) Hydrogen in nominally anhydrous upper-mantle minerals: concentration levels and implications. European Journal of Mineralogy, 12, 543-570.

Ingrin, J., Hercule, S. and Charton, T. (1995) Diffusion of hydrogen in diopside: results of dehydration experiments. Journal of Geophysical Research, 100, 15489-15499.

Ingrin, J., Kovács, I., Deloule, E., Balan, E., Blanchard, M., Kohn, S.C. and Hermann, J. (2014) Identification of hydrogen defects linked to boron substitution in synthetic forsterite and natural olivine. American Mineralogist, 99, 2138-2141.

Ingrin, J., Liu, J., Depecker, C., Kohn, S.C., Balan, E. and Grant, K.J. (2013) Low-temperature evolution of OH bands in synthetic forsterite, implication for the nature of H defects at high pressure. Physics and Chemistry of Minerals, 40, 499-510.

Ingrin, J., Pacaud, L. and Jaoul, O. (2001) Anisotropy of oxygen diffusion in diopside. Earth and Planetary Science Letters, 192, 347-361.

Ireland, T.R. and Williams, I.S. (2003) Considerations in zircon geochronology by SIMS. In Hanchar, J. M. and Hoskin, P. W. O. (eds.), Zircon, 53, 215-241,

Reviews in Mineralogy and Geochemistry, Mineralogical Society of America, Washington, D.C.

Jacobsen, S.D. and van der Lee, S. (Eds) (2006) Earth's Deep Water Cycle. American Geophysical Union MonogrSer.

Johnson, E.A. (2003) Hydrogen in nominally anhydrous crustal minerals. PhD Dissertation, California Institute of Technology, Pasadena, USA.

Johnson, E.A. and Rossman, G.R. (2013) The diffusion behavior of hydrogen in plagioclase feldspar at 800–1000 °C: Implications for re-equilibration of hydroxyl in volcanic phenocrysts. American Mineralogist, 98, 1779-1787.

Johnson, O.W., Paek, S.H. and Deford, J.W. (1975) Diffusion of H and D in TiO_2: Suppression of internal fields by isotope exchange. Journal of Applied Physics, 46, 1026-1033.

Jung, H. and Karato, S. (2001) Water-induced fabric transitions in olivine. Science, 293, 1460–1463.

Kaiser, A., Lobert, M. and Telle, R. (2008) Thermal stability of zircon ($ZrSiO_4$). Journal of the European Ceramic Society, 28, 2199–2211.

Karato, S. (1990) The role of hydrogen in the electrical conductivity of the upper mantle. Nature, 347, (6290), 272–273.

Karato, S. (2004) Mapping water content in the upper mantle. In: Eiler, J. (Ed.), Inside the Subduction Factory. Geophysical Monograph Series, American Geophysical Union.

Karato, S. (2006) Remote sensing of hydrogen in Earth's mantle. In: Keppler, H., Smyth, J.R. (Eds.), Water in Nominally Anhydrous Minerals. Reviews in Mineralogy and Geochemistry. Mineralogical Society of America, Chantilly, VA, pp. 343–375.

Kats, A., Haven, Y. and Stevels, J.M. (1962) Hydroxyl groups in α-quartz. Physics and Chemistry of Glasses, 3, 69-76.

Keppler, H. and Smyth, J.R. (2006) Water in Nominally Anhydrous Minerals. In Reviews in Mineralogy and Geochemistry, volume 62, Mineralogical Society of

America and the Geochemical Society, p 478, Chantilly, VA and Washington, D.C., USA.

Khomenko, V.M., Langer, K., Beran, A., Koch-Müller, M. and Fehr, T. (1994) Titanium substitution and OH-bearing defects in hydrothermally grown pyrope crystals. Physics and Chemistry of Minerals, 20, 483-488.

Kobayashi, S. and Shoji, T. (1987) Infrared spectra and cell dimensions of hydrothermally synthesized grandite-hydrograndite series. Mineralogical Journal, 13, 490-499.

Kohlstedt, D.L. and Mackwell, S.J. (1998) Diffusion of hydrogen and intrinsic point defects in olivine. Zeitschrift fur Physikalische Chemie, 207, 147– 162.

Kohlstedt, D.L. (2006) The role of water in high-temperature rock deformation. Reviews in Mineralogy & Geochemistry, 62, 377-396.

Kohlstedt, D.L. and Mackwell, S.J. (1998) Diffusion of hydrogen and intrinsic point defects in olivine. Zeitschrift fur Physikalische Chemie, 207,147-162.

Kroger, F.A. and Vink, H.J. (1956) Relations between the Concentrations of Imperfections in Crystalline Solids. Solid State Physics.

Kronenberg, A.K., Kirby, S.H., Aines, R.D. and Rossman, G.R. (1986) Solubility and diffusional uptake of hydrogen in quartz at high water pressure: implications for hydrolytic weakening. Journal of Geophysical Research, 91, 12723-12744.

Kronenberg, A.K. and Wolf, G.H. (1990) Fourier transform infrared spectroscopy determinations of intragranular water content in quartz-bearing rocks: implications for hydrolytic weakening in the laboratory and within the earth. Tectonophysics, 172, 255-271.

Kronenberg, A.K., Yund, R.A. and Rossman, G.R. (1996) Stationary and mobile hydrogen defects in potassium feldspar. Geochimica et Cosmochimica Acta, 60, 4075-4094.

Kronenberg, A.K., Yund, R.A. and Rossman, G.R. (1998) Reply to the comment by Robert H. Doremus on “Stationary and mobile hydrogen defects in potassium feldspar.” Geochimica et Cosmochimica Acta, 62, 379-382.

Kühberger, A., Fehr, T., Huckenholz, H.G. and Amthauer, G. (1989) Crystal chemistry of a natural schorlomite and Ti-andradite synthesized at different oxygen fugacities. Physics and Chemistry of Minerals, 16, 734-740.

Kurka, A. (2005) Hydrogen in Ca-rich Garnets: diffusion and Stability of OH-defects. 145 p. Ph.D. thesis, Université de Toulouse, France.

Kurka, A., Blanchard, M. and Ingrin, J. (2005) Kinetics of hydrogen extraction and deuteration in grossular. Mineralogical Magazine, 69, 359-371.

Lager, G.A., Armbruster, T. and Faber, J. (1987) Neutron and X-ray diffraction study of hydrogarnet$Ca_3Al_2(O_4H_4)$. American Mineralogist, 72, 756-765.

Lager, G.A., Armbruster, T., Rotella, F.J. and Rossman, G.R. (1989) The OH substitution in garnets: X-ray and neutron diffraction, infrared, and geometric-modeling studies. American Mineralogist, 74, 840-851.

Lathe, C., Koch-Müler, M., Wirth, R., van Westrenen, W., Mueller, H-J., Schilling, F. and Lauterjung, J. (2005) The influence of OH in coesite on the kinetics of the coesite-quartz phase transition. American Mineralogist, 90, 36-43.

Le Claire, A.D. (1966) Some comments on the mass effect in diffusion. Philosophical Magazine, 14, 1271–1284.

Lemaire, C., Kohn, S.C. and Brooker, R.A. (2004) The effect of silica activity on the incorporation mechanism of water in synthetic forsterite: a polarized infrared spectroscopic study. Contribution to Mineralogy and Petrology, 147, 48-57.

Libowitzky, E. (1999) Correla tion of O-H stretching frequencies and O-H-O hydrogen bond lengths in minerals. Monatshefte fur Chemie, 130, 1047-1059.

Libowitzky, E. and Beran, A. (1995) OH defects in forsterite. Physics and Chemistry of Minerals, 22, 387-392.

Libowitzky, E. and Beran, A. (2006) The Structure of Hydrous Species in Nominally Anhydrous Minerals: Information from Polarized IR Spectroscopy. In: Keppler, H., and Smyth, J.R. (eds) Water in nominally anhydrous minerals, vol 62. Reviews in Mineralogy and Geochemistry, Mineralogical Society of America and Geochemical Society, Washington, pp 29–52.

Libowitzky, E. and Rossman, G.R. (1996) Principles of quantitative absorbance measurements in anisotropic crystals. Physics and Chemistry of Minerals, 23, 319-327.

Libowitzky, E. and Rossman, G.R. (1997) An IR absorption calibration for water in minerals. American Mineralogist, 82, 1111-1115.

Liu, Y., Gao, S., Hu, Z., Gao, C., Zong, K. and Wang, D. (2010) Continental and oceanic crust recycling-induced melt-peridotite interactions in the trans-north China Orogen: U-Pb dating, Hf isotopes and trace elements in zircons from mantle xenoliths. Journal of Petrology, 51, 537–571.

Locock, A., Luth, R.W., Cavell, G.G., Smith, D.G.S. and Duke, M.J.M. (1995) Spectroscopy of the cation distribution in the schorlomite species of garnet. American Mineralogist, 80, 27-38.

Lu, R. and Keppler, H (1997) Water solubility in pyrope to 100 kbar. Contributions to Mineralogy and Petrology, 129, 35-42.

Lumpkin, G. R. and Chakoumakos, B. C. (1988) Chemistry and radiation effects of thorite-group minerals from the Harding pegmatite, Taos County, New Mexico: American Mineralogist, 73, 1405-1419.

Luo, Y. and Ayers, J.C. (2009) Experimental measurements of zircon/melt trace-element partition coefficients. Geochimica et Cosmochimica Acta, 73, 3656–3679.

Mackwell, S.J. and Kohlstedt, D.L. (1990) Diffusion of hydrogen in olivine: Implications for water in the mantel. Journal of Geophysical Research, 95, 5079-5088.

Maldener, J., Ho sch, A., Langer, K. and Rauch, F. (2003) Hydrogen in some natural garnets studied by nuclear reaction analysis and vibrational spectroscopy. Physics and Chemistry of Minerals, 30, 337-344.

Matveev, S., O'Neill, H.St.C., Ballhaus, C., Taylor, W.R. and Green, D.H. (2001) Effect of silica acitivity on OH - IR spectra of olivine: Implications for low $aSiO_2$ mantle metasomatism. Journal of Petrology, 42, 721-729.

Mehrer, H. (2007). Diffusion in solids: fundamentals, methods, materials, diffusion-controlled processes (Vol. 155), Springer.

Mei, S. and Kohlstedt, D.L. (2000a) Influence of water on plastic deformation of olivine aggregates 1. Diffusion creep regime. Journal of Geophysical Research, 105, 21457–21469.

Mei, S. and Kohlstedt, D.L. (2000b) Influence of water on plastic deformation of olivine aggregates 2. Dislocation creep regime. Journal of Geophysical Research, 105, 21471–21481.

Menzer, G. (1926) Die Kristallstruckture von Granat. Zeitschrift fur Kristallograhie, 63, 157-158.

Menzer, G. (1929) Die Kristallstruktur der Granate. Zeitschrift fur Kristallograhie, 69, 300-396.

Mikenda, W. (1986) Stretching frequency versus bond distance correlation of O–D(H)…Y(Y = N, O, S, Se, Cl, Br, I) hydrogen bonds in solid hydrates. Journal of Molecular Structure, 147, 1-15.

Mosenfelder, J.L., Schertl, H.P., Smyth, J.R. and Liou, J.G. (2005) Factors in the preservation of coesite: The importance of fluid filtration. American Mineralogist, 90, 779-789.

Mumpton, F.A. and Roy, R. (1961) Hydrothermal stability studies of the zircon–thorite group. Geochimica et Cosmochimica Acta, 21, 217–238.

Nasdala, L., Beran, A., Libowitzky, E. and Wolf, D. (2001) The incorporation of hydroxyl groups and molecular water in natural zircon ($ZrSiO_4$). American Journal of Science, 301, 831–857.

Nasdala, L., Kronz, A., Wirth, R., Váczi, T., Perez-Soba, C., Willner, A. and Kennedy, A.K. (2009) The phenomenon of deficient electron microprobe totals in radiation-damaged and altered zircon. Geochimica et Cosmochimica Acta, 73/6, 1637–1650.

Nasdala, L., Wolf, D. and Irmer, G. (1995): The degree of metamictization in zircon: a Raman spectroscopic study. European Journal of Mineralogy, 7, 471-478.

Nobes, R.H., Akhmatskaya, E.V., Milman, V., White, J.A., Winkler, B. and Pickard, C.J. (2000) An ab initio study of hydrogarnets. American Mineralogist, 85, 1706 - 1715.

Novak, G.A. and Gibbs, G.V. (1971) The crystal chemistry of the silicate garnets. American Mineralogist, 56, 791-825.

Nyman, H., Hyde, B.G. and Andersson, S. (1984). Zircon, anhydrite, scheelite and some related structures containing bisdisphenoids. Acta Crystallographica Section B: Structural Science, 40, 441-447.

Ohtani, E. (2005) Water in the mantle. Elements, 1, 25-30.

Padrón-Navarta, J.A., Hermann, J. and O'Neill, H.St.C. (2014) Site-specific hydrogen diffusion rates in forsterite. Earth and Planetary Science Letters, 392, 100-112.

Page, F.Z., Fu, B., Kita, N.T., Fournelle, J., Spicuzza, M.J., Schulze, D.J., Viljoen, V., Basei, M.A.S. and Valley, J.W. (2007) Zircons from kimberlites: New insights from oxygen isotopes, trace elements, and Ti in zircon thermometry. Geochimica et Cosmochimica Acta, 71, 3887–3903.

Paterson, M.S. (1982) The determination of hydroxyl by infrared absorption in quartz, silicate glasses and similar materials. Bulletin of Mineralogy, 105, 20-29.

Pauling, L. (1960) The Nature of the Chemical Bond. Cornell University Press.

Peña, P. and de Aza, S. (1984) The zircon thermal behavior: effect of impurities. Part 1. Journal of Materials Science, 19, 135–142.

Phichaikamjornwut, B., Skogby, H., Ounchanum, P., Limtrakun P. and Boonsoong, A. (2012) Hydrous components of grossular-andradite garnets from Thailand: thermal stability and exchange kinetics. European Journal of Mineralogy, 24, 107-121.

Prandl, W. (1966) Verfeinerung der Kristallstruktur des GrossularsmitNeutronen und Röntgenstrahlbeugung. Zeitschrift fur Kristallograhie, 123, 81-116.

Putnis, A. and McConnel, J.D.C. (1980) Principles of Mineral Behaviour. Blackwell Science, Publications.

Reich, M., Ewing, R.C., Ehlers, T.A. and Becker, U. (2007) Low-temperature anisotropic diffusion of heliumin zircon: implications for zircon (U–Th)/He thermochronometry. Geochimica et Cosmochimica Acta, 71, 3119–31.

Richman I. and Kisliuk P. (1975) Absorption spectrum of U^{4+} in zircon ($ZrSiO_4$). Physical Review, 155, 262-267.

Richman I., Kisliuk, P. and Wong E. Y. (1967) Absorption Spectrum of U^{4+} in Zircon ($ZrSiO_4$). Physical Review, 155, 262-267.

Richter, R.M., Watson, E.B., Mendybaev, R.A., Teng, F.Z. and Janney, P.E. (2008) Magnesium isotope fractionation in silicate melts by chemical and thermal diffusion. Geochimica et Cosmochimica Acta, 72, 206-220.

Robinson, K., Gibbs, G.V. and Ribbe, P.H. (1971) The structure of zircon: A comparison with garnet. American Mineralogist, 56, 782–790.

Rossman, G.R. (1990) Hydrogen in "anhydrous" minerals. Nuclear Instruments and Methods in Physical Research Section B, 45, 41-45.

Rossman, G.R. and Aines, R.D. (1991) The hydrous components in garnets: Grossular-hydrogrossular. American Mineralogist, 76, 1153–1164.

Ryerson, F.J. and McKeegan, K.D. (1994) Determination of oxygen self-diffusion in akermanite, anorthite, diopside, and spinel: implications for oxygen isotopic anomalies and the thermal histories of Ca-Al-rich inclusions. Geochimica et Cosmochimica Acta, 58, 3713-3734.

Sacerdoti, M. and Passaglia, E. (1985) The crystal structure of katoite and implications within the hydrogrossular group of minerals. Bulletin de Minéralogie, 108, l-8.

Shannon, R.D. and Rossman, G.R. (1992) Dielectric constants of silicate garnets and the oxide additivity rule. American Mineralogist, 11, 94-100.

Sheng, Y.M., Xia, Q.K., Dallai, L., Yang, X.Z. and Hao, Y.T. (2007) H_2O contents and D/H ratios of nominally anhydrous minerals from ultrahigh-pressure eclogites of the Dabie orogen, eastern China. Geochimica et Cosmochimica Acta, 71, 2079-2103.

Shuster, D.L., Flowers, R.M. and Farley, K.A. (2006) The influence of natural radiation damage on helium diffusion kinetics in apatite. Earth and Planetary Science Letters, 249, 148–161.

Shuster, D.L., Vasconcelos, P.M., Heim, J.A. and Farley, K.A. (2005) Weathering geochronology by (U–Th)/He dating of goethite. Geochimica et Cosmochimica Acta, 69, 659–673.

Skogby, H. (1994) OH incorporation in synthetic clinopyroxene. American Mineralogist, 79,240-249.

Skogby, H. and Rossman, G.R. (1989) OH- in pyroxene: an experimental study of incorporation mechanism and stability. American Mineralogist, 74, 1059–1069.

Smyth, J.R., Bell, D.R. and Rossman, G.R. (1991) Incorporation of hydroxyl in upper-mantle clinopyroxenes. Nature, 351, 732-735.

Speer, J.A. (1980) Zircon In Orthosilicates (First ed.) (ed. P. H. Ribbe), Reviews in Mineralogy, 5, 67–112.

Speer, J.A. (1982) Zircon, in: Ribbe, P.H., editor, Orthosilicates, 2nd edition, Reviews in Mineralogy, v. 5: Washington, D.C., Mineralogical Society of America, p 67-112.

Stalder, R. and Behrens, H. (2006) D/H exchange in pure and Cr-doped enstatite: implications for hydrogen diffusivity. Physics and Chemistry of Minerals, 33, 601-611.

Stalder, R. and Skogby, H. (2003) Hydrogen diffusion in natural and synthetic orthopyroxene. Physics and Chemistry of Minerals, 30, 12-19.

Stalder, R. and Skogby, H. (2007) Dehydration mechanisms in synthetic Fe-bearing enstatite. European Journal of Mineralogy, 19, 201–216.

Stalder, R., Purwin, H. and Skogby, H. (2007) Influence of Fe on hydrogen diffusivity in orthopyroxene. European Journal of Mineralogy, 19, 899–903.

Subbarao, E.C., Agrawal, D.K., McKinstry, H.A., Sallese, C.W. and Roy, R. (1990) Thermal expansion of compounds of zircon structure. Journal of the American Ceramic Society, 73, 1246-1252.

Sundvall, R., Skogby, H. and Stalder, R. (2009a) Dehydration-hydration mechanisms in synthetic Fe-poor diopside. European Journal of Mineralogy, 21, 17–26.

Sundvall, R., Skogby, H. and Stalder, R. (2009b) Hydrogen diffusion in synthetic Fe-free diopside. European Journal of Mineralogy, 21, 963-970.

Teng, F.Z., McDonough, W.F., Rudnick, R.L., Dalpe, C., Tomascak, P.B., Gao, S. and Chappell, B.W. (2004) Lithium isotopic composition and concentration of the upper continental crust. Geochimica et Cosmochimica Acta, 68, 4167–4178.

Thomas, J.B., Bodnar, R.J., Shimizu, N. and Sinha, A.K. (2002) Determination of zircon/melt trace element partition coefficients from SIMS analysis of melt inclusions in zircon. Geochimica et Cosmochimica Acta, 66, 2887–2901.

Thompson, A.B. (1992) Water in the Earth's upper mantle. Nature, 358, 295-302.

Tomascak, P.B. (2004) Developments in the understanding and applications of lithium isotopes in the Earth and planetary sciences. In: Johnson C, Beard B, Albarede F (eds) Geochemistry of non-traditional isotope systems, reviews in mineralogy and geochemistry, vol 55. Mineralogical Society of America, Washington, DC, pp 153–195.

Trail, D., Bindeman, I.N., Watson, E.B. and Schmitt, A.K. (2009) Experimental calibration of oxygen isotope fractionation between quartz and zircon. Geochimica et Cosmochimica Acta, 73, 7110–7126.

Trail, D., Mojzsis, S.J., Harrison, T.M., Schmitt, A.K., Watson, E.B. and Young, E.D. (2007) Constraints on Hadean zircon protoliths from oxygen isotopes Ti-thermometry, and rare earth elements. Geochemistry Geophysics Geosystems, 8, Q06014.

Trail, D., Thomas, J.B. and Watson, E.B. (2011) The incorporation of hydroxyl into zircon. American Mineralogist, 96, 60–67.

Ushikubo, T., Kita, N.T., Cavosie, A. J., Wilde, S.A., Rudnick R. L. and Valley, J. W. (2008) Lithium in Jack Hills zircons: evidence for extensive weathering of Earth's earliest crust. Earth and Planetary Science Letters, 272, 666–676.

Váczi, T.A. (2009) Mineralogical studies on zircon. Dissertation, Universität Wien. FakultätfürGeowissenschaften, Geographie und Astronomie.

Valley, J.W. (2003) Oxygen isotopes in zircon. In Hanchar, J. M. and Hoskin, P. W. O. (eds.), Zircon, 53, 343-385, Reviews in Mineralogy and Geochemistry, Mineralogical Society of America, Washington, D.C.

Valley, J.W., Bindeman, I.L. and Peck, W.H. (2003) Empirical calibration of oxygen isotope fractionation in zircon. Geochimica et Cosmochimica Acta, 67, 3257–3266.

Van, Westrenen, W., Frank, M.R., Hanchar, J.M., Fei, Y., Finch, R.J. and Zha, C-S. (2004) In situ determination of the compressibility of synthetic pure zircon (ZrSiO4) and the onset of the zircon-reidite phase transition. American Mineralogist, 89, 197-203.

Vance, E.R. and Mackey, D.J. (1974) Optical study of U^{5+} in zircon. Journal of Physics C: Solid State Physics, 7, 1898-1907.

Vance, E.R. and Mackey, D.J. (1975) Further studies of the optical absorption spectrum of U^{5+} in zircon. Journal of Physics C: Solid State Physics, 8, 3439-3447.

Vervoort, J.D., Patchett, P.J., Gehrels, G.E. and Nutman, A.P. (1996) Constraints on early Earth differentiation from hafnium and neodymium isotopes. Nature, 379, 624-627. Vol. 3, edited by Seitz, F. and Turnbull, D., Academic Press Inc, New York, p. 307.

Vigouroux, E. (2014) Diffusivite de l'hydrogene dans la wadsleyite: estimation de la teneur en eau dans manteaux de transition. 228 p. Ph.D. thesis, Université Lille 1: Sciences et Technologies, France.

Wang, D., Li, H., Yi, L. and Shi, B. (2008) The electrical conductivity of upper-mantle rocks: water content in the upper mantle. Physics and Chemistry of Minerals, 35, 157–162.

Wang, D., Mookherjee, M., Xu, Y. and Karato, S. (2006) The effect of water on the electrical conductivity of olivine. Nature, 443 (26), 977–980.

Wang, L., Zhang, Y. and Essene, E. (1996) Diffusion of the hydrous component in pyrope. American Mineralogist, 81, 706-718.

Watson, E.B. and Cherniak, D.J. (1997) Oxygen diffusion in zircon. Earth and Planetary Science Letters, 148, 527-544.

Watson, E.B., Wanser, K.H. and Farley, K.A. (2010) Anisotropic diffusion in a finite cylinder, with geochemical applications. Geochimica et Cosmochimica Acta, 74 (2). pp 614-633. ISSN 0016-7037.

Watson, E.B. (1996) Dissolution, growth and survival of zircons during crustal fusion: Kinetic principles, geological models and implications for isotopic inheritance. Transactions of the Royal Society of Edinburgh. Earth Sciences, 87, 43–56.

Watson, E.B. and Harrison, T.M. (2005) Zircon thermometer reveals minimum melting conditions on earliest Earth. Science, 308, 841–844.

Watson, E.B.,Wark, D.A. and Thomas, J.B. (2006) Crystallization thermometers for zircon and rutile. Contributions to Mineralogy and Petrology, 151, 413–433.

Wieczorek, A., Libowitzky, E. and Beran, A. (2004) A model for the OH defect incorporation in kyanite based on polarised IR spectroscopic investigations. Schweizerische Mineralogische und Petrographische Mitteilungen: eine europäische Zeitschrift für Mineralogie, Geochemie und Petrographie, Band 84, 333-343.

Wilde, S.A., Valley, J.W., Peck, W.H. and Graham, C.M. (2001) Evidence from detrital zircons for the existence of continental crust and oceans on the Earth 4.4 Gyr ago. Nature, 409, 175–178.

Wilkins, R.W.T. and Sabine, W. (1973) Water content of some nominally anhydrous silicates. American Mineralogist, 58, 508–516.

Williams, I.S. (1992) Some observations on the use of zircon U-Pb geochronology on the study of granitic rocks. Transactions of the Royal Society of Edinburgh. Earth Sciences, 83, 447-458.

Winchell, H. (1958) The composition and physical properties of garnet. American Mineralogist, 43, 595-600.

Woodhead, J. A., Rossman, G. R., and Thomas, A. P. (1991b) Hydrous species in zircon. American Mineralogist, 76, 1533-1546.

Woodhead, J., Rossman, G. and Silver, L.T. (1991a) The metamictization of zircon: Radiation dose-dependensttructural characteristics. American Mineralogist, 76, 74-82.

Woods, S.C., Mackwell, S.J. and Dyar, D. (2000) Hydrogen in diopside: Diffusion profiles. American Mineralogist, 85, 480-487.

Xia, Q.K., Sheng, Y.M., Yang, X.Z. and Yu, H.M. (2005) Heterogeneity of water in garnets from UHP eclogites, eastern Dabieshan, China. Chemical Geology, 224, 237-246.

Yang, Y., Xia, Q.K., Feng, M. and Zhang, P.P. (2010) Temperature dependence of IR absorption of OH species in clinopyroxene. American Mineralogist, 95, 1439-1443.

York, D. (1966) Least-squares fitting of a straight line. Canadian Journal of Physics, 44, 1079-1086.

Yoshino, T., Matsuzaki, T., Yamashita, S. and Katsura, T. (2006) Hydrous olivine unable to account for conductivity anomaly at the top of the asthenosphere. Nature, 443 (26), 973–976.

Zabinski, W. (1966) Hydrogarnets. PolskaAkademiaNauk, OddzialKrakowie, KomisjaNaukMineralogicznych, Prace Mineralogiczne, 72, 89–101.

Zhang, M., Salje, E.K.H. and Ewing, R.C. (2002) Infrared spectra of Si-O overtones, hydrous species, and U ions in metamict zircon: radiation damage and recrystallization. Journal of Physics: Condensed Matter, 14, 3333-3352.

Zhang, M., Salje, E.K.H. and Ewing, R.C. (2003) Oxidation state of uranium in metamict and annealed zircon: near-infrared spectroscopic quantitative analysis. Journal of Physics: Condensed Matter, 15, 3445-3470.

Zhang, M., Salje, E.K.H., Ewing, R.C., Daniel, P. and Geisler, T. (2004) Applications of near-infrared FT-Raman spectroscopy in metamict and annealed zircon: oxidation state of U ions. Physics and Chemistry of Minerals, 31, 405-414.

Zhang, M., Salje, E.K.H. and Ewing, R.C. (2010) OH species, U ions, and CO/CO_2 in thermally annealed metamict zircon ($ZrSiO_4$). American Mineralogist, 95. pp. 1717-1724.

Zhang, Y., Stolper, E.M. and Wasserburg, G.J. (1991a) Diffusion of a multi-species component and its role in the diffusion of water and oxygen in silicates. Earth and Planetary Science Letters, 103, 228-240.

Zhang, Y.X., Stolper, E.M. and Wasserburg, G.J. (1991b) Diffusion of water in rhyolitic glasses. Geochimica et Cosmochimica Acta, 55, 441-456.

Zhang, Z. and Saxena, S.K. (1991b) Thermodynamic properties of andradite and application to skarn with coexisting andradite and hedenbergite. Contributions to Mineralogy and Petrology, 107, 255-263.

Zhao, Z.F. and Zheng, Y.F. (2007) Diffusion compensation for argon, hydrogen, lead, and strontium in minerals: Empirical relatioinships to crystal chemistry. American Mineralogist , 92, 289-308.

Zheng, Y.F., Fu, B., Gong, B. and Li, L. (2003) Stable isotope geochemistry of ultrahigh pressure metamorphic rocks from the Dabie-Sulu orogen in China: implications for geodynamics and fluid regime. Earth Science Reviews, 62, 105-161.

Related Publications

Zhang, P.P. and Liu, J. (2013) The incorporation mechanisms and diffusion kinetics of hydrogen in olivine. Acta Petrologica Et Mineralogica, 32 (5), 708-732 (in Chinese with English abstract).

Zhang, P.P., Ingrin, J., Depecker, C. and Xia, Q.K. (2015) Kinetics of deuteration in andradite. American Mineralogist, in press.

Zhang, P.P., Ingrin, J., Depecker, C. and Xia, Q.K. Kinetics of H diffusion in zircon. In preparation for Geology.